Evolution & dynamics of neutron stars : from microphysics to astrophysics

Morgane Fortin

N. Copernicus Astronomical Center
Polish Academy of Sciences
&
Paris Observatory
École doctorale Astronomie et Astrophysique d'Île de France (ED 127)

Thesis for the titles of
Doktor nauk fizycznych
w zakresie
Astronomii
&
Docteur de l'Observatoire de Paris
Spécialité
Astronomie et Astrophysique

Evolution & dynamics of neutron stars : from microphysics to astrophysics

by
Morgane Fortin

Publicly defended on
May 25, 2012
at N. Copernicus Astronomical Center
in front of the jury composed by :

Nils Andersson	Reviewer
Didier Barret	Reviewer
Tomasz Bulik	Reviewer
Michał Jaroszyński	Examiner
Jérôme Margueron	Examiner
Eric Gourgoulhon	Ph.D. supervisor
Julian Leszek Zdunik	Ph.D. supervisor

"Niczego w życiu nie należy się bać,
należy to tylko zrozumieć."
Maria Skłodowska-Curie

« Dans la vie, rien n'est à craindre,
tout est à comprendre. »
Marie Sklodowska-Curie

Streszczenie

W 1967 zaobserwowano w promieniowaniu radiowym pulsary, obiekty, które okazały się potwierdzeniem przewidywań teoretycznych z lat trzydziestych XX wieku dotyczących możliwości istnienia gwiazd neutronowych. Gwiazdy neutronowe rodzą się w wybuchu supernowej, końcowym stadium życia gwiazd o masie ponad ośmiokrotnie przewyższającej masę Słońca. Dotychczas znamy dwa tysiące gwiazd neutronowych obserwowanych we wszystkich długościach fali w Galaktyce i Obłokach Magellana. Dla około sześćdziesięciu z nich oszacowano masę, niekiedy z dość dużą dokładnością. Przy masie porównywalnej z masą Słońca i rozmiarze kilkudziesięciu kilometrów pulsary są gwiazdami o największych wartościach gęstości i ciśnienia wsród obiektów obserwowanych we Wszechświecie. Struktura i własności materii w takich warunkach ciągle stanowią nierozwiązany problem. Gwiazdy neutronowe są unikalnym laboratorium pozwalającym na studiowanie własności gęstej materii oraz badanie teorii grawitacji.

W pracy przedstawione zostaną trzy aspekty dotyczące dynamiki i ewolucji gwiazd neutronowych.

Jeden z nich ma związek z ewolucją termiczną izolowanych oraz akreujących gwiazd neutronowych. Analiza stygnięcia gwiazd neutronowych wskazuje, że ich skorupa jest kryształem zawierającym gaz neutronowy w stanie nadciekłym. Ostatnie obserwacje chłodzenia gwiazdy neutronowej Cassiopeia A pozwoliły na określenie niektórych własności nadciekłości materii we wnętrzu gwiazdy. Okazuje się, że porównanie teoretycznych modeli ewolucji cieplnej gwiazdy neutronowej z obecnymi pomiarami ich temperatury prowadzić może do lepszego zrozumienia własności gęstej materii. Przy opisie stygnięcia gwiazdy neutronowej konieczne jest uwzględnianie takich procesów fizycznych jak emisja neutrin z wnętrza i fotonów z powierzchni, przewodnictwo cieplne, nadciekłość i nadprzewodnictwo. W pracy zajmuję się zarówno wpływem nadciekłości neutronów w skorupie na ewolucję cieplną gwiazdy, jak i prezentacją modelu zewnętrznych warstw akreującej gwiazdy neutronowej (skorupa, otoczka), który pozwala na odtworzenie obserwowanych własności relaksacji termicznej gwiazd neutronowych wkrótce po ustaniu (lub znacznym osłabieniu) procesu akrecji.

Drugim tematem pracy jest modelowanie rotacji gwiazdy neutronowej uwzględniające elastyczne własności gęstej materii. Własności te mogą być istotne w sytuacji kiedy materia przypomina kryształ; jest tak w przypadku skorupy gwiazdy neutronowej, a niektóre modele teoretyczne przewidują taki efekt również w centralnych rejonach gwiazdy neutronowej. Dotychczasowa analiza tych efektów oparta była o modele traktujące efekty elastyczności w ramach dynamiki newtonowskiej. W pracy przedstawione są równania opisujące rotację gwiazdy w oparciu o relatywistyczną teorię elastyczności w ramach ogólnej teorii względności.

W trzeciej części pracy analizowana jest ewolucja rotacji akreującej gwiazdy neutronowej. Problem ten odnosi się do własności pulsarów milisekundowych, gwiazd neutronowych rozkręconych do okresów kilku milisekund poprzez akrecję materii z gwiazdy towarzyszącej. W ramach zaproponowanego modelu akrecję rozpatruje się z uwzględnieniem oddziaływania gwiazdy z dyskiem akrecyjnym poprzez pole magnetyczne oraz bierze się pod uwagę istnienie marginalnie stabilnej orbity będącej efektem ogólnej teorii względności. Analiza obserwacji niektórych milisekundowych pulsarów pozwala na wyznaczenie ich okresu, masy i pola magnetycznego. Przedstawiony model pozwala na określenie parametrów gwiazdy neutronowej będącej prekursorem obecnie obserwowanego pulsara. Zastosowno go do trzech obiektów: dwóch pulsarów o najwyższych zmierzonych dokładnie masach i do najlżejszego obserwowanego pulsara.

Konfrontacja modeli gwiazd neutronowych z obserwacjami w aspektach przedstawionych w pracy prowadzi do lepszego zrozumienia własności materii przy bardzo dużych gęstościach.

Praca została napisana we współpracy Centrum Astronomicznego im Mikołaja Kopernika Polskiej Akademii Nauk w Warszawie oraz Laboratoire Univers et Théories w Obserwatorium Paryż-Meudon-Nançay we Francji.

Résumé

Envisagées par L. Landau en 1931 avant même la découverte du neutron par J. Chadwick l'année suivante et prédites par Baade et Zwicky en 1934, les étoiles à neutrons ne furent observées qu'en 1967 par hasard et en radio, sous forme de pulsars. Elles sont créées lors de l'explosion, appelée supernova, d'étoiles environ huit fois plus massives que notre Soleil, à la fin de leur vie. Une masse de une à deux fois celle du Soleil pour un rayon d'une dizaine de kilomètres seulement font d'elles des objets relativistes et parmi l'une des formes de matière les plus denses de notre Univers. Depuis leur première observation, environ deux mille étoiles à neutrons ont été observées dans toutes les longueurs d'onde, dans notre Galaxie et dans les nuages de Magellan et la masse d'une soixantaine d'entre elles a pu être déterminée. Néanmoins, leur structure et les propriétés de la matière en leur sein sont mal connues. Elles constituent donc des laboratoires célestes qui permettent de comprendre et de tester de nombreux domaines de la physique, parmi lesquels la physique nucléaire et la gravitation.

Le travail de cette thèse porte sur l'étude théorique de trois aspects de la dynamique et de l'évolution des étoiles à neutrons.

La premier sujet traite de l'évolution thermique des étoiles à neutrons qu'elles soient isolées ou accrétant de la matière d'une étoile compagnon. Des travaux précédents ont montré que la croûte d'une étoile à neutrons, sa partie supérieure, est cristalline et que ses neutrons sont superfluides. Récemment l'observation directe du refroidissement de l'étoile à neutrons au cœur du reste de supernova Cassiopée A a permis de mettre des contraintes sur les propriétés superfluides de la matière dans le cœur des étoiles à neutrons. Ainsi la comparaison des modèles d'évolution thermique avec les observations permet de comprendre les propriétés de la matière et contraint les modèles de physique nucléaire. La modélisation de l'évolution thermique nécessite de prendre en compte de nombreux aspects de microphysique, en particulier l'émission de neutrinos dans toute l'étoile et de photons à sa surface, la diffusivité et la possible superfluidité de la matière. D'une part, a été étudiée lors de cette thèse l'influence de la superfluidité des neutrons dans la croûte sur l'évolution thermique d'une étoile à neutrons. D'autre part, un nouveau modèle qui décrit précisément la physique de l'envelope et de l'atmosphère des étoiles à neutrons accrétantes a été mis au point. Des résultats préliminaires montrent qu'il permet pour la première fois de reproduire la relaxation thermique d'étoiles à neu-

trons, observée en X, après que l'accretion qui eut lieu pendant des périodes d'une à plusieurs dizaines d'années s'est arrêtée.

Le deuxième sujet de cette thèse porte sur la modélisation de la rotation d'étoiles à neutrons incluant les propriétés élastiques de leurs parties solides. En effet, il est admis que la croûte d'une étoile à neutrons est solide et certains travaux de physique nucléaire suggèrent qu'il en est de même pour son cœur. Jusqu'à présent l'effet de l'élasticité des parties solides sur la rotation n'a été pris en compte que dans la cadre newtonien. À partir d'un modèle relativisite qui décrit le phénomène d'élasticité, les équations qui décrivent la rotation d'une étoile à neutrons en totalité ou en partie solide ont été dérivées.

Le troisième et dernier sujet de cette thèse concerne l'évolution de la rotation et du champ magnétique d'une étoile à neutrons accrétante. En effet, certaines étoiles à neutrons, appelées pulsars millisecondes sont des objets agés dont la rotation a été accélérée à des périodes de quelques dizaines de millisecondes par l'accrétion de la matière d'une étoile compagnon. Le modèle mis au point pendant cette thèse utilise une description relativiste du disque d'accrétion magnétisé et permet de suivre à la fois l'évolution de la période de rotation et du champ magnétique de l'étoile à neutrons. La masse, la période et indirectement le champ magnétique de certains pulsars millisecondes ont été mesurés grâce à des observations en radio. Le modèle permet de mettre des contraintes sur les propriétés des étoiles à neutrons dont sont issus ces pulsars et est appliquée à trois d'entre eux : les deux plus massifs et le moins massif.

Ainsi la modélisation des étoiles à neutrons et la comparaison avec les observations permet de comprendre les propriétés de la matière dite froide à très haute densité.

Cette thèse a été réalisée en cotutelle entre le Centre d'Astronomie Nicolas Copernic de l'Académie des Sciences polonaise à Varsovie, en Pologne et le Laboratoire Univers et Théories de l'Observatoire de Paris-Meudon-Nançay, en France.

Abstract

Anticipated by L. Landau in 1931, before the discovery of the neutron by J. Chadwick one year later and predicted by Baade and Zwicky in 1934, neutron stars were observed only in 1967 by chance and in radio, as pulsars. They originate from the explosion, called supernova, at the end of the life of stars that are about eight times more massive than our Sun. With a mass one to two times the one of the Sun for a radius of few tens of kilometers, neutron stars are relativistic objects and one of the densest form of matter in our Universe. Since their first observation, around two thousand neutron stars have been observed in all wavelengths in our Galaxy and in the Magellanic Clouds and the mass of approximately sixty of them has been determined. Nevertheless, their structure and the properties of the matter inside them are still poorly known. They are therefore cosmic laboratories that enable to understand and test various fields of physics, in particular nuclear physics and gravitation.

This thesis presents the theoretical study of three aspects of the dynamics and evolution of neutron stars.

The first aspect addresses the thermal evolution of isolated and accreting neutron stars. Previous studies showed that the crust of neutron stars, their upper part, is crystalline with superfluid neutrons. Recently the direct observation of the cooling of the neutron star in Cassiopeia A supernova remnant has constrained the superfluid properties of the matter in the core of neutron stars. Therefore, the comparison between the thermal evolution models and the observations of neutron stars allows to understand the properties of matter and constrains the nuclear physics models. Many aspects of microphysics have to be taken into account in the modeling of the thermal evolution, in particular, the emission of neutrinos from the interior of the neutron star and of photons at the surface, the diffusivity and the possibility of matter superfluidity. On the one hand, the influence of the superfluidity of the neutrons in the crust on the thermal evolution of neutron stars has been studied. On the other hand, a new model based on an up-to-date description of the physics of the envelope and of the atmosphere of accreting neutron stars has been developed. Preliminary results show that it enables for the first time to reproduce the thermal relaxation observed in X-rays of neutron stars when accretion stopped after they had accreted matter for years to decades.

The second subject of this thesis deals with the modeling of the rotation of neutron stars, including the elastic properties of their solid parts. Indeed, their crust is thought to be solid and some nuclear models suggest that their core may be in the same phase. Previous works considered the effects of the elasticity of the solid parts in the framework of Newtonian dynamics. Based on a general relativistic theory of elasticity, the equations for the rotation of a neutron star with a (partly) solid interior have been derived.

The third and last part of this thesis regards the evolution of the rotation and of the magnetic field of an accreting neutron star. Indeed, a certain type of neutron stars, called millisecond pulsars, are old objects that have been spun up to periods of few tens of milliseconds by the accretion of matter from a companion star. The model that has been developed during my Ph.D. studies uses a relativistic prescription for a magnetized accretion disk and describes both the variation of the period and of the magnetic field of the neutron star. The mass, the period and indirectly the magnetic field of some millisecond pulsars can be determined thanks to radio observations. The model enables to put constraints on the properties of the progenitor neutron star of these millisecond pulsars and is applied to three of them : the two most and the less massive ones.

Thus confronting the models for the evolution and dynamics of neutron stars with observations enables to understand the properties of the so-called cold matter at very high density.

My Ph.D. studies have been carried out jointly between the Nicolaus Copernicus Astronomical Center of the Polish Academy of Sciences, in Warsaw in Poland and the Laboratory Universe and Theories at Paris-Meudon-Nançay Observatory, in France.

Acknowledgments

I want to thank first Éric & Leszek, my two thesis advisors, for giving me the opportunity to continue studying these fascinating objects that neutron stars are and to discover a new country (and its language hard to learn and to pronounce !) at the same time. I have enjoyed very much our projects, discussions and their comments and support.

Many thanks to the Neutron Star group at CAMK & the Gravitation group at LUTh : Michał, Paweł, Dorota, Phillipe, Jérôme, Micaela, Silvano, Brandon and also Agata for the warm and fruitful atmosphere in both institutions and for their help. My thanks also go to Jérôme Margueron for our many discussions and to Loïc for accepting to be my thesis godfather and for his advice.

I have to thank also all the people in charge of the administration in both countries for their efficiency, kindness and ability to deal with my complex administrative situation.

I thank also all the Ph.D. students at CAMK and at LUTh, in particular Krzysiek, Mateusz, Karolina, Tomek, Odele, Radek, Wojtek, Patrycja & Luc, Bruno, Irène, Petar, Frédéric and Cécile, for the coffee/tea/infusion/crosswords/cookie boxes/whatever breaks and for the fun that we had together .

Merci aussi à Domitille, Josep, Nadine & Gabi, Anthea et aux anciens de Stan : Séb, P-G, Laurian, Benoît et Jean pour leur amitié et les soirées ciné, resto, japonais, pizza, ...

Enfin et surtout, un énorme merci à toute ma famille, à mes parents, mes trois sœurs (et même mes beaux-frères), à Jules, Adèle, Justine, Louise, Paul, Léonie et Thèse pour leur soutien et leur amour tout au long de ces années.

This work was supported by the N. Copernicus Astronomical Center, the Ministerstwa Nauki i Szkolnictwa Wyższego grant No. N N203 512 838, the Observatoire de Paris-Meudon-Nançay, the Centre National de la Recherche Scientifique, the European Laboratory LEA Astrophysics Poland-France (Astro-PF), the Compstar program of the European Science Foundation, the Laboratoire Univers & Théories and the ANR SN2NS.

Contents

Introduction

Neutron stars are among the most exotic objects in our Universe and are stellar laboratories for both astrophysics and microphysics. Indeed, their central density is so high that atomic nuclei disappear in their core. Their magnetic field can be as large as 10^{15} G and they are very compact and rapidly rotating objects. The modeling of their evolution and dynamics requires a precise description of their relativistic and microphysical properties. They are therefore of particular interest for astrophysicists together with nuclear physicists.

The first part presents general aspects concerning neutron stars. After a short historical review, chapter 1 details the neutron star formation mechanism. Then a toy model enables to understand their basic dynamics. Chapter 2 explains why neutron stars are cosmic laboratories that enable to test and understand various field of physics such as nuclear physics and gravitation.

The second part addresses the thermal evolution of neutron stars. Chapter 3 gives a general overview of the subject, with a particular attention to the connection with the observations. After a short historical review, the different microphysics ingredients that enter the modeling of the thermal evolution are presented step by step. Chapter 4 then focuses the thermal evolution of young neutron stars and details new calculations for the specific heat of the superfluid neutrons in the crust of neutron stars and their influence of the cooling. In chapter 5, the thermal evolution of accreting neutron stars is explained and a new model for the latter with promising preliminary results is presented.

The third part deals with the rotation of neutron stars. In chapter 6, a model for rotating neutron stars with a perfect fluid interior and the constraints that can be put on the microphysical properties by the observations of rotating neutron stars are presented. Chapter 7 then shows that sudden changes in the rotation of neutron stars suggest that some parts of neutron stars are solid and therefore undergo elastic deformations that have to be taken into account in the models. Both Newtonian and relativistic formalisms for elasticity are then introduced. In chapter 8, the derivation of the relativistic equations for rotating neutron stars with a solid interior and their numerical resolution, currently in progress, are explained.

In the last and fourth part, the dynamics of neutron stars in binary systems are addressed. Chapter 9 introduces the different evolutionary scenarios in binaries that can result in the formation of millisecond pulsars, that are the most rapidly rotating neutron stars observed. They are believed to have been spun up by the accretion of the matter from a companion star in a binary. Chapter 10 presents a simple model for the evolution of the rotation and of the magnetic field of an accreting neutron star. It is then applied in chapter 11 to three millisecond pulsars and enables to assess the properties these neutron stars had before accretion started.

Part I

Context

Introduction

In this first introductory part, general aspects concerning neutron stars are presented.

In chapter 1, a short historical review (section 1.1) shows that neutron stars were first theoretically predicted objects in the 1930s before their observation almost forty years later. Section 1.2 explains that neutron stars are the remnants of massive stars after their death in supernova explosions and details their formation. A toy model for neutron stars is presented in section 1.3 and enables to understand their basic dynamics and their different types (section 1.4).

Chapter 2 shows that neutron stars are cosmic laboratories that enable to test and understand various fields of physics. The structure of neutron stars is presented and the interplay between nuclear matter theories and neutron stars global properties is explained (section 2.1). Section 2.2 details how observations of neutron stars enable to constrain dense matter models. Finally, tests of theories of gravity, in particular of General Relativity, that have been performed so far thanks to the timing of pulsars are developed in section 2.3.

Chapter 1

Neutron stars : general aspects

Contents

This first chapter aims at giving some general ideas about neutron stars. After a short historical review in section 1.1, the origin of neutron stars in supernova explosions will be explained (section 1.2). A simple toy model for pulsars is presented in section 1.3 and the different types of observed neutron stars are detailed (section 1.4).

1.1 From theoretical predictions to observations

In February 1932, James Chadwick published a paper reporting the discovery of the neutron (Chadwick, 1932). The legend says that in the evening of the announcement, Lev Landau suggested Bohr and Rosenfeld that dense stars entirely composed of neutrons might exist and a paper was published also in February 1932 (Landau, 1932). The simultaneous release of the papers was in fact a coincidence (Haensel *et al.*, 2007) ! Indeed Landau had written his paper by the end of February 1931 in which he anticipates that in the stars heavier than 1.5 $M_\odot$[1], "*the density of matter becomes so great that atomic nuclei come in close contact, forming one gigantic nucleus*".

In 1934, Baade & Zwicky, who analyzed observations of supernova explosions, proposed that "*supernovæ represent the transitions from ordinary stars to neutron stars, which in their final stages consist of extremely closely packed neutrons*".

In 1939, Tolman and Oppenheimer & Volkoff independently derived the equations of hydrostatic equilibrium for a spherically symmetric star in the framework of General Relativity. Oppenheimer & Volkoff solved the equations for a model of stellar matter composed of a gas of non-interacting, degenerate and relativistic neutrons and obtained of maximum mass of $\sim 0.7\ M_\odot$. They however suggested that repulsion in the neutron-neutron interaction may increase the maximum mass. This was indeed confirmed by Cameron (1959) who obtained a maximum mass of 2 $M_\odot$.

Subsequent works focused on the composition and superfluidity of the interior, the neutrino emission and the thermal evolution of neutron stars (Haensel *et al.*, 2007).

With the beginning of X-ray astronomy, several methods and attempts tried to observe neutron stars, however unsuccessfully. In July 1967, Antony Hewish decided, with a graduate student Jocelyn Bell, to study interplanetary scintillation and constructed a radio telescope which was sensitive to weak discrete radio sources. In August, Jocelyn Bell saw large fluctuations in signal at about the same time on successive days which did not look like scintillation. It soon appeared that the fluctuations were occurring four minutes earlier each day, as expected for signals of celestial origin. In November, a very stable pulse periodicity of 1.337s was found. The discovery was published in February 1968 (Hewish *et al.*) and the authors suggested that the source may be a white dwarf or a neutron star. The pulsating source was called the pulsar PSR B1919+21 where PSR mean "Pulsating Source of Radio" and B1919+21 refers to its position in the sky. Hewish (only) received the Nobel Prize in 1974 for the discovery of pulsars.

[1]The mass of the Sun : $M_\odot = 1.98 \times 10^{33}$ g is extensively used in the following.

In June 1968, Gold identified pulsars as neutron stars and proposed that the period should increase because they loose rotational energy by emitting electromagnetic radiation. By the end of 1968, the Vela and Crab pulsars were discovered with periods of 89 ms and 33 ms. White dwarfs could not account for such short periods, they would be destroyed by the centrifugal forces. Only a neutron star could vibrate or rotate so fast. Furthermore a rotation would slow down, not a vibration. A slowdown rate was soon identified in the period of the Crab. Finally, both the Crab and Vela pulsars are located in supernova remnants, providing the confirmation of Baade-Zwicky prediction (Lyne & Graham-Smith, 2005; Haensel *et al.*, 2007).

1.2 Birth of a neutron star

There exists two types of supernovæ which can be associated with two different phenomena : thermonuclear supernovæ and core-collapse (or gravitational) supernovæ. The word *supernova* was first used in a paper by Baade & Zwicky in 1934. They were the first to distinguish the *novæ*, which are sudden thermonuclear reactions due to the accretion of matter from a red giant onto a white dwarf in a binary system, from the so-called supernovæ. A white dwarf is composed of electron degenerate matter and is the final evolutionary stage of a star whose mass is below eight solar masses ($\sim 97\%$ of the stars in our Galaxy), after the envelope of the star has been spread into space forming a planetary nebula. A given white dwarf may become a nova many times and does not necessarily expel or burn all the material that has accumulated since the last outburst. Novæ comes from the Latin word meaning "new" and refers to the fact one may think that a new star has appeared.

Baade and Zwicky realized that, since the sources are extragalactic, the amount of released energy must be much larger for supernovæ than for novæ. They also understood that supernovæ are the transition from ordinary stars to neutron stars (Gourgoulhon, 2005).

The supernovæ are classified according to the absorption lines in their spectrum soon after the explosion. If the hydrogen line is present, the supernova is of type I, otherwise it is of type II. Type I supernovæ are also subdivided into :

- type Ia if silicon II lines are visible,
- type Ib if helium I lines are visible and not silicon II ones,
- type Ic if neither silicon II nor helium I lines are visible.

No type Ib, Ic or II supernovæ have been observed in elliptical galaxies, in which no new stars are formed and all high-mass stars have already exploded. Therefore, one can conclude that contrary to type Ib, Ic and II, type Ia supernovæ are not the result of the stellar collapse of a high-mass star into a compact object but of the collapse of white dwarf because its internal degeneracy pressure can no longer support the accretion of

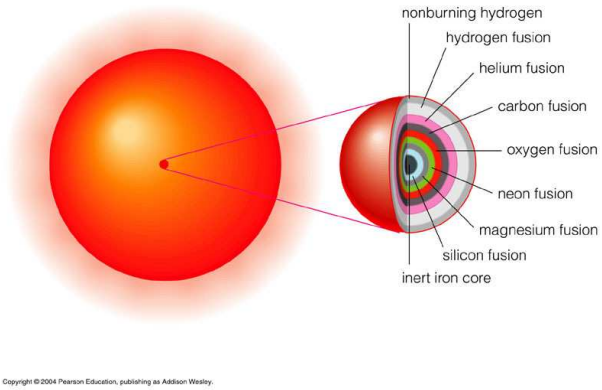

Figure 1.1: Interior of an evolved high-mass star.

matter from a companion. As the white dwarf collapses, the temperature rises and carbon fusion begins everywhere throughout the white dwarf instantaneously leading to the observation of a thermonuclear supernova. The distinctions between the other types come from the progenitors. For type Ib and Ic supernovæ, the progenitor has already lost its hydrogen envelop (for example a Wolf-Rayet star).

1.2.1 Pre-supernova evolution

The last stage of the stellar evolution of a massive star is called a pre-supernova.

1.2.1.1 High-mass stars stellar evolution

High-mass stars, with a mass $M \gtrsim 8\ \mathrm{M}_\odot$, evolve much faster than their lower-mass counterparts : their larger mass speeds up all phases of the stellar evolution. During some million years, they burn their nuclear fuel in successive nucleonsynthesis stages. A high-mass star can fuse not only hydrogen and helium, but also carbon, oxygen and heavier elements up to iron via a nucleosynthesis chain that can be schematically summarized by the reactions :

$$^{1}\mathrm{H} \rightarrow\ ^{4}\mathrm{He} \rightarrow\ ^{12}\mathrm{C} \rightarrow\ ^{16}\mathrm{O} \rightarrow\ ^{20}\mathrm{Ne} \rightarrow\ ^{28}\mathrm{Si} \rightarrow\ ^{56}\mathrm{Fe}. \tag{1.1}$$

At the end of its life, the star is observed as a red supergiant with a very large radius and a low surface temperature. Its interior resembles the layers of an onion (figure 1.1) : shells of heavier and heavier elements fuse at smaller and smaller radii and at higher and higher temperatures.

At the center of the star, a compact iron core, composed of $^{56}\mathrm{Fe}$ and neutron-rich iron-group nuclei (for example, $^{46}\mathrm{Ca}$, $^{66}\mathrm{Ni}$, $^{50}\mathrm{Ti}$ and $^{54}\mathrm{Cr}$, Bethe *et al.* (1979)) is surrounded by a shell of burning silicon, the latter fusing into iron.

1.2.1.2 The Chandrasekhar mass

Iron being the most stable element, ie. with the highest binding energy per nucleon, its fusion does not release energy. The degeneracy of electrons, at the density $\sim 10^6$ g cm^{-3}, is the source of a pressure in the iron core, which does only depend on the density and not on the temperature. The Chandrasekhar mass (1931) given by the relation (Bethe *et al.*, 1979) :

$$M_{\rm Ch} = 1.457 \left(\frac{Y_{\rm e}}{0.5}\right)^2 \ {\rm M}_\odot, \tag{1.2}$$

is the maximum mass the pressure of the degenerate electrons can support before collapsing. $Y_{\rm e}$ is the electron fraction, ie. the number of electrons per baryon (neutron and proton). In the iron core, at high densities ($\rho \simeq 10^{10}$ g cm^{-3}), electron captures on nuclei and on protons (inverse-β decay) occur :

$$(Z, A) + e^- \ \rightarrow \ (Z-1, A) + \nu_e, \tag{1.3}$$

$$p + e^- \ \rightarrow \ n + \nu_e, \tag{1.4}$$

with (A, Z) the atomic nucleus with Z protons and A nucleons, decreasing the value of $Y_{\rm e}$ below 0.5 ($Y_{\rm e} \sim 0.42$). The Chandrasekhar mass associated with the iron core is therefore slightly below 1.4 M$_\odot$, around 1.2 M$_\odot$.

1.2.2 Core-collapse supernova explosions

1.2.2.1 The implosion phase

Right after the iron core of a massive star reaches the Chandrasekhar mass, the collapse starts and the star implodes.

When the mass of the iron core becomes larger than the Chandrasekhar mass, the star internal support starts to dwindle. Gravity overwhelms the pressure of the gas and the star implodes falling on itself (upper left plot in figure 1.2). Typical initial conditions at the beginning of the collapse are (Woosley *et al.*, 2002) :

- $T_{\rm c} \sim 7 \times 10^9$ K, the central temperature,
- $M_{\rm core} \sim 1.4$ M$_\odot$, the mass of the iron core,
- $R_{\rm Fe} \sim 10^3$ km, the radius of the iron core,
- $\rho_{\rm c} \sim 8.7 \times 10^9$ g cm^{-3}, the density at the center of the star.

The increases in density and temperature due to this infall can not ignite new nuclear reactions, which could counteract the implosion, since the burning of iron does consume energy. The infall is even accelerated by two processes (Gourgoulhon, 2005; Janka *et al.*, 2007) :

- the electron captures on protons and on nuclei are strongly out of equilibrium. This leads to the neutronization of the core. The neutrinos released by this process escape freely from the core as long as the density remains under the critical density $\rho \simeq 10^{12}$ g cm^{-3}. Thus, the degeneracy pressure in the core is reduced;
- the photo-dissociation of the iron nuclei into α-particles (^{4} He) costs energy :

$$\gamma + {}^{56}\text{Fe} \rightarrow 13\alpha + 4n \tag{1.5}$$

When the density reaches the critical density, the neutrinos become trapped in the core because their diffusion time becomes larger than the collapse time (upper right plot of figure 1.2). The infall is thus quasi-adiabatic.

The collapse then proceeds homologously, meaning that it behaves as a unit, collapsing self-similarly. The infall velocity is equal to zero at the center of the core and linearly increases up to a maximum before decreasing in the outer regions. The sound velocity varies like the density, decreasing from the center to the outer layers. Thus, a point where the sound speed is equal to the infall velocity exists : it is called the sonic point. The homologous core is the region in which the sound speed is larger than the infall velocity, so different parts can communicate via pressure waves. It is the part of the iron core that collapses as unity in a subsonic way. On the contrary, the collapse in the regions situated at larger radii than the sonic point is supersonic.

1.2.2.2 The bounce phase

Ten milliseconds after the beginning of the collapse, the nuclear saturation density ($\rho_0 = 2.4 \times 10^{14}$ g cm^{-3}) is reached. At this density, the distance between the particles becomes so small that they are very close to the distance at which nuclear forces are effective. These forces are repulsive at short distances and are the source of a new pressure which abruptly opposes the collapse and rests the central part of the core. The homologous core bounces in response to the increased nuclear matter pressure and resulting pressure waves propagate at the speed of sound. In the meantime, the regions of the iron core lying outside the homologous core continue to fall inwards at a supersonic speed. At the sonic point, the pressure waves accumulate creating a shock wave, ie. a discontinuity in pressure and matter velocity (figure 1.2, middle left plot). The location and strength of the shock wave depend on the model for dense matter, which is poorly known.

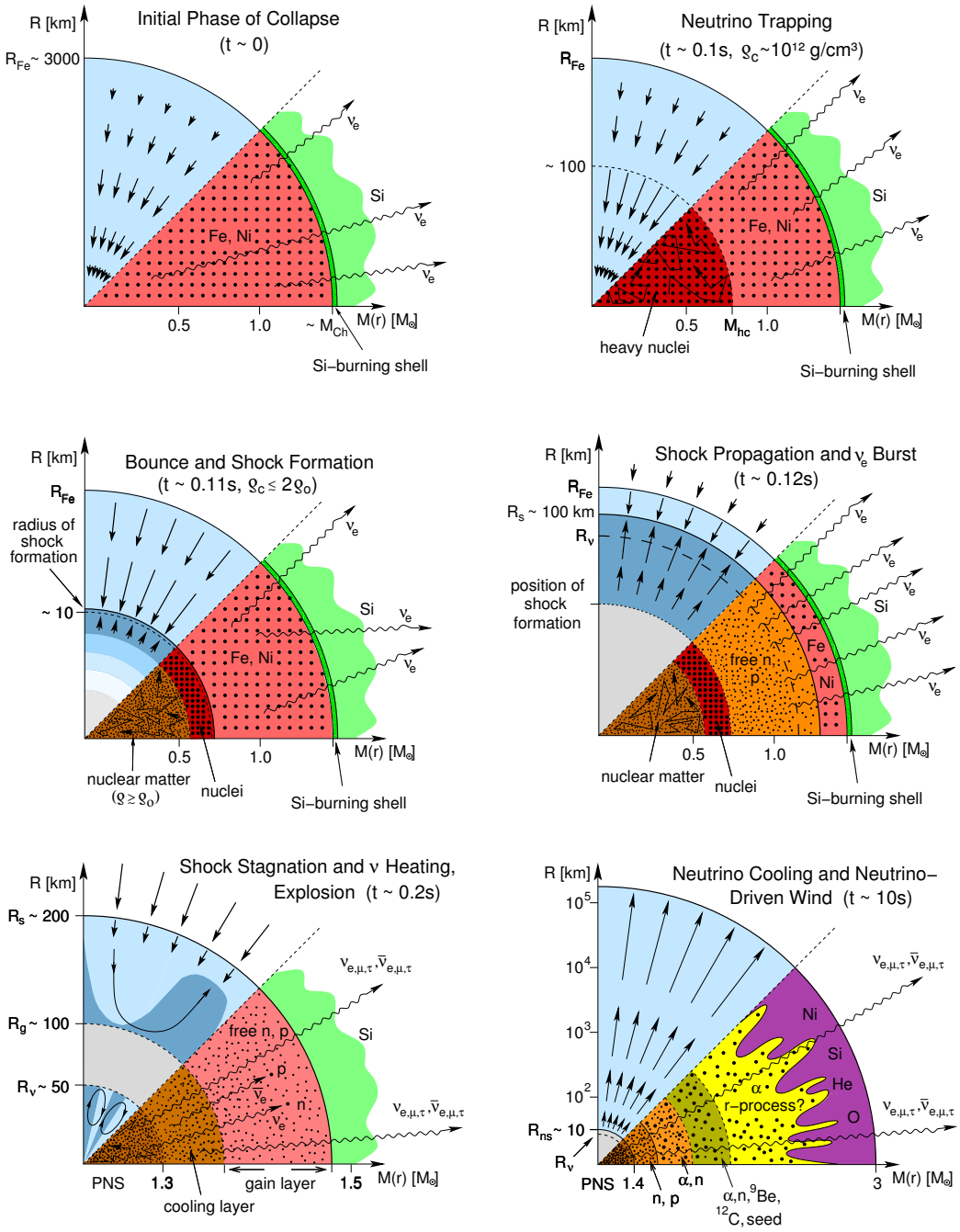

Figure 1.2: Schematic representation of the evolutionary stages of stellar core collapse. $M_{\rm Ch}$ stands for the Chandrasekhar mass, $M_{\rm hc}$ the mass of the subsonically collapsing homologous inner core, $R_{\rm Fe}$, $R_{\rm s}$, $R_{\rm ns}$, and R_ν the iron core radius, shock radius, neutron star radius, and neutrinosphere radius, respectively and ρ_0 is the nuclear saturation density. The arrows represent the velocity vectors. Figure from Janka *et al.* (2007).

1.2.2.3 The explosion phase

The shock wave at the sonic point propagates faster than the speed of sound through the rest of iron core eventually reaching the helium/hydrogen envelope. During the propagation of the wave, two different phenomena compete :

- the emission of neutrinos by the cooling proto-neutron star, formed by the compressed matter at the center of the star, can reheat the shock wave through neutrinos-nuclei interactions when the particles reach the shock-wave from behind (figure 1.2, middle right plot);
- the formation of alpha particles and of nucleons from the photo-dissociation of the iron-peaked nuclei by the shock wave leads to the loss of energy.

Naively, one can think that the shock wave will reach the envelop and blow it off. It is the prompt explosion mechanism. But sophisticated Newtonian and relativistic hydrodynamics in spherical symmetry, which take into account the description of the weak interactions, the nuclear equation of state effects and the neutrino transport have shown that the prompt bounce-shock mechanism is not the driver of supernova explosions. For stars with masses above 10 $M_\odot$, the energy available for the shock is not sufficient. Most of the shock energy is used in the outer core to dissociate heavy nuclei into nucleons. The shock stalls and turns into an accretion shock at a radius around $1-2\times10^7$ km. The compact remnant left at the center of the collapsing star begins to form and grows by the accretion of the infalling matter until the explosion restarts. In the so-called delayed explosion mechanism, the shock is revived by two phenomena (Janka *et al.*, 2007) :

- the proto-neutron star behind the shock is very hot with a central temperature of 10^{11} K and cools by emission of neutrinos. The shock gets reheated by these neutrinos after few seconds;
- in the zone between the proto-neutron star and the shock wave, convection starts in the matter heated by neutrinos. This convection allows the neutrino energy to be efficiently transferred to the shock wave.

Thus, the shock starts again and its propagation heats matter to temperatures above a billion kelvin. This leads to fusion reactions forming heavy elements such as radioactive nickel and cobalt which will latter decay into iron. When the shock wave reaches the surface, it blows off the envelop (lower plots in figure 1.2). The envelop is heated up, emitting intense electromagnetic radiation and matter is ejected into space. A type II supernova, resulting from the disruption of the star, is observed. The explosion leaves a remnant at the center, which can be of two types :

- a neutron star, ie. a tiny ultra-compressed remnant, mostly composed of neutrons,
- a black hole : the proto-neutron star can collapse into a black hole few seconds/minutes after the explosion if accretion onto its surface goes on, ie. if the velocity of parts

of the external layers is below the escape velocity. Therefore, the total mass of the remnant exceeds the neutron star maximum mass leading to the formation of a black hole.

1.2.2.4 Supernovæ simulations

The delayed neutrino-heating mechanism has been shown to lead to explosions for a progenitor $8-10\ \mathrm{M}_\odot$ star with an ONeMg core inside a very dilute He-core (Janka *et al.*, 2007).

For more massive stars, the input of multi-dimensional processes is needed to get an explosion. In fact, neutrino energy deposition behind the shock is crucial to revive it. Such effect can be triggered by the Standing Accretion Shock Instability (SASI), a generic instability of the shock to non-radial deformations, whose underlying physical mechanism is still unclear. This causes the shock to be pushed further out and increases the time matter stays in the layer heated by neutrinos, strengthening the neutrino-energy deposition and leading to an asymmetric beginning of the explosion (Janka *et al.*, 2007; Marek & Janka, 2009). So far, two-dimensional simulations of $10-11\ \mathrm{M}_\odot$ stars with a small iron core surrounded by low density shells have led to explosions.

Explosions of more massive progenitors may involve three-dimensional hydrodynamics, the rapid rotation of stars, magnetohydrodynamics or a more precise description of neutrino transport and properties and of the high-density equation of state. Marek & Janka (2009) obtained, for the first time, stellar core collapse for a $15\ \mathrm{M}_\odot$ star with a two-dimensional axisymmetric hydrodynamic simulation, confirming the importance of the SASI and of a precise description of the neutrino transport.

1.2.2.5 Energy release

The potential energy of the iron core of the pre-supernova is (Gourgoulhon, 2005) :

$$E_{\mathrm{grav}}(\mathrm{pre}-\mathrm{SN}) \sim -\frac{3}{5}\frac{\mathrm{GM_{Fe}^2}}{\mathrm{R_{Fe}}} \tag{1.6}$$

with $R_{\mathrm{Fe}} \simeq 1500$ km, M_{Fe} the mass of the core and G the gravitational constant.

The potential energy of the proto-neutron star is :

$$E_{\mathrm{grav}}(\mathrm{proto}-\mathrm{NS}) \sim -\frac{3}{5}\frac{\mathrm{GM^2}}{\mathrm{R}} \tag{1.7}$$

with $R \simeq 10$ km the radius of the neutron star and M its mass, which, under the assumption of mass conservation, is the same as the mass of the "Fe" core $M = M_{\mathrm{Fe}}$.

The energy released by a type II supernova is :

$$E_{\mathrm{SNII}} \sim E_{\mathrm{grav}}(\mathrm{pre}-\mathrm{SN}) - \mathrm{E_{grav}}(\mathrm{proto}-\mathrm{NS}) \tag{1.8}$$

$$\sim -E_{\mathrm{grav}}(\mathrm{proto}-\mathrm{NS}) \tag{1.9}$$

since $R \ll R_{\rm Fe}$. For typical values of the mass and radius ($R = 10$ km and $M = 1.4\,{\rm M}_\odot$), one gets :

$$E_{\rm SNII} \sim 3 \times 10^{53} {\rm erg}. \tag{1.10}$$

This corresponds to the total amount of energy the Sun produces when burning hydrogen during ten billion years !

The released energy is divided in the following way (Gourgoulhon, 2005) :

- the vast majority (99%) is emitted by neutrinos,
- $\sim 1\%$ is released in the kinetic energy of the matter ejected by the shock-wave,
- $\sim 0.1\% \simeq 10^{50}$ erg is emitted as electromagnetic radiation,
- less than 10^{-4} is emitted as gravitational waves.

1.2.2.6 Formation of heavy elements

Supernovæ are the furnaces in which at least half of the isotopes heavier than the iron group are formed (Woosley & Janka, 2005).

The necessary conditions for their formation : a very short time-scale ($\sim$ 1 s), a high temperature ($\sim$ 10^9 K) and a very high flux of neutrons ($\sim$ 10^{20} neutrons/cm^{-3}) can only be achieved in the explosive situations that supernovæ are. Merging neutron stars and neutron rich jets or winds from gamma-ray bursts also produce heavy elements but they are too rare to account for the observed abundances.

The heavy elements are produced by the so-called r-process, where "r" stands for rapid-neutron capture. To explain the solar abundances, this process must occur in the innermost ejecta, close to the neutron star. There, during ten seconds, a neutron-rich wind is blown by an intense flux of neutrinos from the cooling neutron star. Since the star has already blown off nearly all the stellar material, the properties of the wind reflects the one of the compact object and not of the exploding star. Therefore, the set of relative abundances in the wind will be the same for a supernova produced long ago by a star with low initial concentration of heavy elements and by a present star. This feature is consistent with the observations.

The electron neutrinos and their antiparticles blowing out from the star interact the neutron star atmosphere, composed of photons, electron-positron pairs and unbound neutrons and protons. The r-process consists in the following reactions :

$$\nu_e + n \rightarrow p + e^-, \tag{1.11}$$
$$\bar{\nu}_e + p \rightarrow n + e^+. \tag{1.12}$$

Antineutrinos are hotter because the outer layers of neutron stars are neutron-rich and they more easily pass through this layer than neutrinos. There is therefore an excess of neutrons compared with protons.

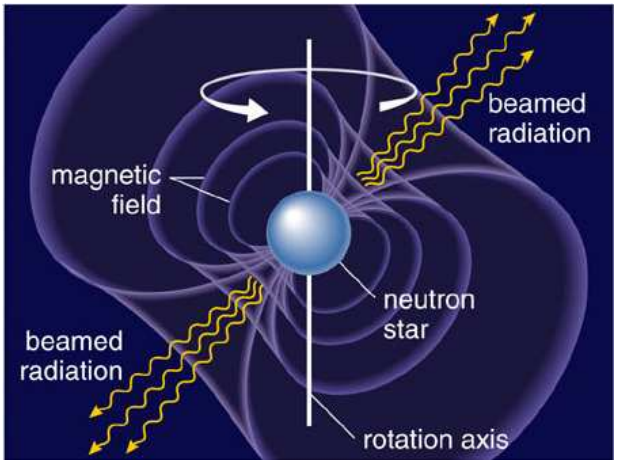

Figure 1.3: An artist view of a pulsar.

The initial temperature of 10 billion K allows two nucleons to combine to make α particles. Since there are more neutrons than protons in the wind, the latter mostly consists in α particles and free neutrons. The wind cools as it flows. At 5 billion K, some α particles assemble into heavier elements, especially the ones of the iron group. During the next seconds, when the temperature is around 1 billion K, the heavy nuclei capture many neutrons, leading to the r-process. To fully reproduce the solar abundances, one must add two major ingredients to the previous picture : magnetic field and rotation, to decrease the average density of the wind and allow more neutrino captures and energy deposition. But their role are still unclear and they are the subject of further investigation.

1.3 Neutron stars as magnetic dipoles

According to the so-called "lighthouse" model schematically plotted in figure 1.3, a pulsar is a rotating neutron star. As a neutron star spins, charged particles are accelerated along the magnetic field lines and emit electromagnetic radiation. The radiation beam that is formed sweeps the sky like a lighthouse and each time it crosses the observer's line of sight, a pulse is observed. Therefore the period of the pulses corresponds to the rotational period of the neutron star.

1.3.1 Rotational energy

Assume that a neutron star is a solid ball of mass M and radius R, rigidly rotating with an angular velocity $\Omega = 2\pi/P$, with P the rotational period.

The pulsar rotational energy is :

$$E_{\text{rot}} = \frac{1}{2} I \Omega^2 = \frac{2\pi^2 I}{P^2} \tag{1.13}$$

with I the moment of inertia.

For a solid ball, $I = \frac{2}{5}MR^2$. A simple estimate gives :

$$I = 0.8 \times 10^{45} \left(\frac{M}{M_\odot}\right) \left(\frac{R}{10^6 \text{ cm}}\right)^2 \text{ g cm}^2. \tag{1.14}$$

Thus with equation (1.3.1) the rotational energy release is :

$$\frac{\mathrm{d}E_{\text{rot}}}{\mathrm{d}t} = I\Omega\dot{\Omega} = -\frac{4\pi^2 I\dot{P}}{P^3}. \tag{1.15}$$

1.3.2 Magnetic dipole radiation

Suppose that a neutron star is a rotating magnetic dipole with α the angle between the rotation and magnetic axis and B the magnetic field strength at the magnetic equator.

Larmor formula for the power of the magnetic dipole radiation is :

$$P_{\text{rad}} = \frac{2}{3}\frac{\ddot{\mu}^2}{c^3} \tag{1.16}$$

with μ the magnetic dipole moment. For a uniform magnetized sphere, $\mu = BR^3 \sin\alpha$.

Since the dipole rotates with an angular velocity Ω around its rotation axis, $\mu = \mu_0 \exp^{-\imath\Omega t}$ so $\ddot{\mu} = \Omega^2\mu$ (Jackson, 1998).

Thus,

$$P_{\text{rad}} = \frac{2}{3}\frac{\left(BR^3 \sin\alpha\right)^2 \Omega^4}{c^3} = \frac{2}{3c^2}\left(BR^3 \sin\alpha\right)^2 \left(\frac{2\pi}{P}\right)^4. \tag{1.17}$$

1.3.3 Surface magnetic field

Assuming that the loss of rotational energy originates from the emission of electromagnetic radiation,

$$P_{\text{rad}} = -\frac{\mathrm{d}E_{\text{rot}}}{\mathrm{d}t}. \tag{1.18}$$

Finally,

$$B = \left(\frac{3c^3 I}{8\pi^2 R^6 \sin^2\alpha} P\dot{P}\right)^{1/2}. \tag{1.19}$$

Thus, the characteristic pulsar magnetic field $B_{\text{PSR}} = B\sin\alpha$ is (Haensel *et al.*, 2007) :

$$B_{\text{PSR}} = \left(\frac{3c^3 I}{8\pi^2 R^6} P\dot{P}\right)^{1/2}, \tag{1.20}$$

$$\approx 3.2 \times 10^{19} \left(\frac{I}{10^{45} \text{ g cm}^2}\right)^{1/2} \left(\frac{10^6 \text{ cm}}{R}\right)^3 \left(\frac{P}{1 \text{ s}}\right)^{1/2} \left(\frac{\dot{P}}{1 \text{ s s}^{-1}}\right)^{1/2} \text{G}. \tag{1.21}$$

1.3.4 Characteristic age

Assuming that the pulsar magnetic field does not change with time, equations (1.15) and (1.17) give :

$$P\dot{P} = \text{const.} \tag{1.22}$$

Integrating this equation from $t = 0$ to t, one gets :

$$t = \frac{P}{2\dot{P}}\left[1 - \left(\frac{P_0}{P}\right)^2\right] \tag{1.23}$$

with P and $\dot{P}$ calculated at the instant t and P_0 the initial rotational period of the pulsar.

Assuming that $P_0 \ll P(t)$, equation (1.23) gives :

$$\tau_{\text{PSR}} = \frac{P}{2\dot{P}} \tag{1.24}$$

where τ_{PSR} is the characteristic age of the pulsar.

Equation (1.24) is derived assuming that the rotational energy loss originates from the magnetic dipole radiation. A more general formula can be derived :

$$P^{n-2}\dot{P} = \text{const} \tag{1.25}$$

with n the so-called braking index. For the magnetic dipole model, $n = 3$.

Livingstone *et al.* (2006) reported that for several pulsars, the magnetic index is well below 3, suggesting that processes other than magnetic dipole radiation are at the origin of the loss of rotational energy and that the model presented here is too simple. It only gives orders of magnitude for the pulsar age and magnetic field.

1.4 A variety of neutron stars

Since the discovery of the first pulsar in 1967, neutron stars have been observed in all wavelengths from radio to γ-rays. They show a large diversity in their emission and intrinsic properties. The neutron stars for which the period P and period derivative $\dot{P}$ have been measured are plotted in the $P - \dot{P}$ diagram in figure 1.4. Are also indicated the lines of constant B_{PSR} and τ_{PSR}.

Based on observations, neutron stars can be classified into different groups, presented in the following (Haensel *et al.*, 2007; Kaspi, 2010).

Rotation-powered pulsars

Rotation-powered pulsars are neutron stars whose emission is powered by the loss of rotational energy due to magnetic braking. They are extremely regular pulsators and emit in all wavelengths. In the $P - \dot{P}$ diagram, one can distinguish two distinct populations (see also part IV) :

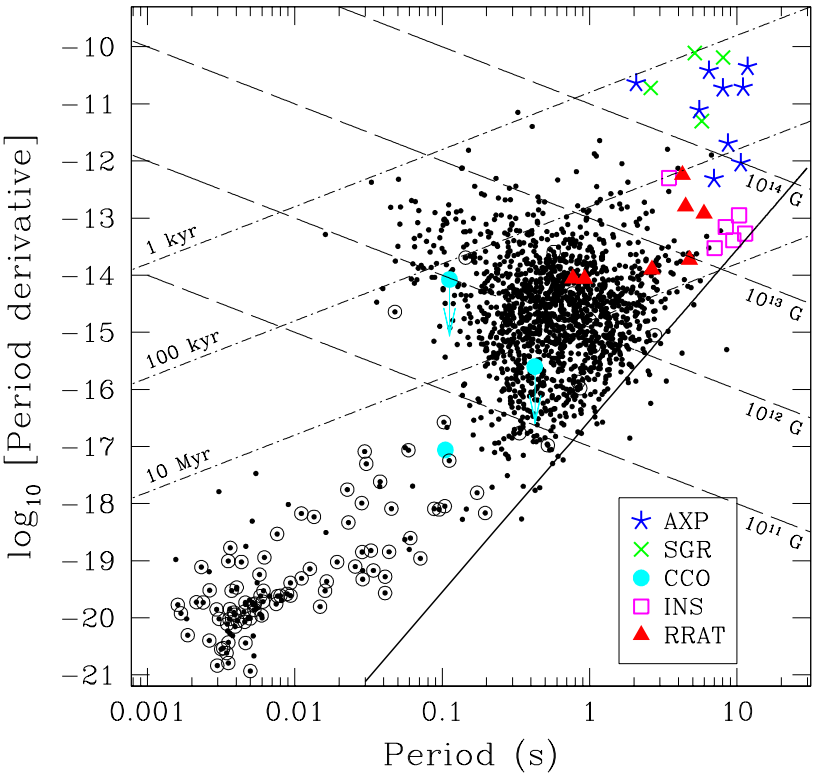

Figure 1.4: P-$\dot{P}$ diagram for 1704 objects : 1674 rotation powered pulsars (small black dots), 9 AXPs (blue crosses), 5 SGRs (green crosses), 3 central compact objects (CCO - cyan circles), 6 isolated neutron stars (ISN - magneta squares), and 7 RRATs (red triangles) for which these parameters have been measured. Lines of constant $B_{\rm PSR}$ (dashed lines) and $\tau_{\rm PSR}$ (dot-dashed lines) are plotted. The solid line is a model death-line (see text for details). From Kaspi (2010).

- the normal pulsars, with periods of the order of few seconds and $B_{\rm PSR} \sim 10^{12}$ G;
- the millisecond pulsars, in the lower left of the diagram. They have $P \lesssim 30$ milliseconds and $B_{\rm PSR} \sim 10^{8}$ G. They are old neutron stars that have been spun to millisecond periods during an accretion episode. The Fermi Space Telescope showed that some of them are bright γ-ray sources.

They exhibit both steady and pulsed X-ray emission. The former is thought to be the thermal emission from the surface of neutron stars while they cool down (see part II). The latter is non-thermal and pulsed and is due to the pulsar magnetospheric activity.

Since rotation-powered pulsars spin down, their radio emission ultimately turns off when they cross the so-called death line. This is consistent with the lack of observations

of pulsars with long periods and small period derivatives. The location of the death-line is model-dependent.

Rotating radio transients

The rotating radio transients (RRATs) do not produce periodic radio emission but exhibit short radio bursts. Whether they are a specific type of rotation-powered pulsars or a distinct population is still unclear.

Magnetars

Magnetars are believed to be young, isolated neutron stars powered by a large magnetic field $B_{\rm PSR} \sim 10^{14} - 10^{15}$ G. They have long periods $5 \lesssim P \lesssim 12$ s. Two types of magnetars exist :

- the Anomalous X-ray pulsars (AXPs) : they show a pulsed X-ray emission. Bursts were observed from some of them;
- the Soft-Gamma Repeaters (SGRs) : they exhibit highly irregular bursts in soft γ-rays and X-rays.

Observations of bursts from AXPs suggested that AXPs and SGRs belong to the same class of neutron stars.

High-B rotation-powered pulsars

Several radio pulsars have inferred magnetic fields $B \sim 4 \times 10^{13}$ G, comparable to the lowest values observed for magnetars. They are called high-B rotation-powered pulsars. The observation of a week-long X-ray burst from the young high-B rotation-powered pulsar PSR J1846-0258 (Gavriil *et al.*, 2008) suggests that they could be transient magnetars.

Isolated neutron stars

The seven isolated neutron stars (ISNs) exhibit a thermal X-ray emission with a low luminosity and are therefore close with a distance $d \lesssim 500$ pc but do not emit in radio. They have long periods $P \sim 3 - 10$ s, higher than average magnetic fields and ages : $B_{\rm PSR} \sim 10^{13}$ G and $\tau_{\rm PSR} \sim 1 - 4$ Myr. Therefore, they may be rotation-powered pulsars viewed off the radio beam. However, their luminosity is too large for their age suggesting that they undergo additional heating.

Central compact objects

Central Compact Objects (CCOs) can not basically be classified in one of the aforementioned categories. They have a bright X-ray emission and lie at the center of supernova remnants. They have very small inferred magnetic fields and large ages, much longer than the age of their supernova remnant.

Neutron stars in binaries

X-ray binaries are composed of a neutron star (or a black hole) and a companion star (neutron star, white dwarf or normal star). The former accretes matter from the latter and this phenomenon is at the origin of the observed X-ray emission. The emission can be regular or irregular, persistent or transient.

The connections between the different types of isolated neutrons are still unclear and magneto-thermal evolution models aim at accounting for their diversity.

Chapter 2

A laboratory for physics

Contents

Neutron stars are extreme objects and cosmic laboratories for various fields of physics. In particular, they are a unique probe to understand the properties of dense matter and to test the gravitation theories.

In section 2.1, the structure of a neutron star is detailed and the relativistic equations for hydrostatic equilibrium are derived. Then, section 2.2 presents the observations and the constraints derived from them that can be put on the properties of the matter inside neutron stars. Finally, it is shown that neutron stars allow to accurately test theories of gravity (section 2.3).

2.1 From microphysics to astrophysics

Neutron stars have masses $M \sim 1.4$ M$_\odot$ and radii $R \sim 10$ km. Their compactness parameter :

$$\frac{GM}{c^2 R} \sim 0.2. \tag{2.1}$$

shows that they are relativistic objects.

Their mean mass density is :

$$\bar{\rho} \simeq \frac{3M}{4\pi R^3}, \tag{2.2}$$

$$\sim 7 \times 10^{14} \text{ g cm}^{-3}, \tag{2.3}$$

$$\sim 2\rho_0, \tag{2.4}$$

where $\rho_0 = 2.8 \times 10^{14}$ g cm^{-3} is the nuclear saturation density, ie. the mass density in heavy nuclei. Neutron stars are one of the densest form of matter in the Universe.

Finally, both General Relativity and nuclear physics are necessary to describe the properties of neutron stars.

2.1.1 Structure of a neutron star

A neutron star can be divided into five different regions (Haensel *et al.*, 2007) :

Envelope

Located above the surface, the envelope is a $\sim 0.1 - 10$ cm thick layer of plasma that determines the spectrum and the properties of the neutron star emission. Theoretical models of magnetized and non-magnetized envelopes have been developed and are of great interest for the study of the thermal evolution of neutron stars (see part II).

Outer crust

The outer crust, which is few hundred meters thick, extends from a density of 10^6 g cm^{-3} to the neutron-drip density $\rho_{\text{ND}} = 4 \times 10^{11}$ g cm^{-3} and its matter consists of

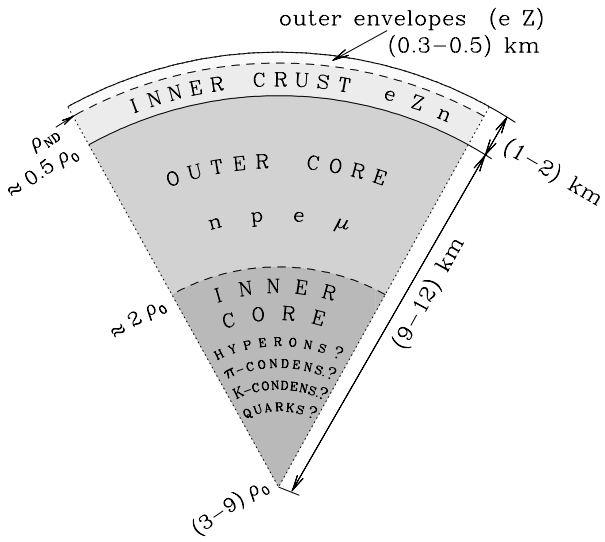

Figure 2.1: Schematic structure of a neutron star. From Haensel *et al.* (2007).

degenerate and ultrarelativistic electrons e and of ions Z that form a solid crystal. β-captures of the electrons, the so-called neutronization, make the nuclei more and more neutron-rich with increasing density. At the bottom of the outer crust, the neutrons start to drip out of the nuclei forming a neutron gas.

Inner crust

The inner crust is composed of electrons, of a lattice of neutron-rich ions and of free neutrons n, that are more and more numerous with increasing density. The free neutrons may be superfluid in the ${}^1S_0$ channel. At the bottom of the inner crust, the nuclei are believed to be so strongly deformed that they become non-spherical. They may form tubes and slabs. These are the so-called pasta phases (Ravenhall *et al.*, 1983; di Gallo *et al.*, 2011). At the boundary between the inner crust and the core, at the density $\rho = \rho_0/2$, the nuclei disappear.

Outer core

The outer core is made the so-called $npe\mu$ matter ie. of mainly neutrons together with protons p, electrons and muons μ, the two latters forming ideal Fermi gases. All species are strongly degenerate. The neutrons and protons can be superfluid. The outer core is several kilometers thick and extends up to the density $\sim 2\rho_0$. Its properties depends on the model for the many-body nucleon interaction.

Inner core

The inner core, with densities $2\rho_0 \lesssim \rho \lesssim 10\rho_0$, is present only in the center of massive neutron stars. Its composition and properties are still unknown and the subjects of

active research. Models considering the appearance of hyperons, of pion or kaon condensates and even a transition to quark matter have been proposed. So far, only matter composed of nucleons and of nucleons and hyperons can be studied in laboratories.

2.1.1.1 Equation of state

Thanks to experimental data and theoretical works, the properties and composition of the crust of neutron stars are rather well known. This is not the case for the core since its densites ($\rho \gtrsim \rho_0$) are too high to be reproduced in laboratories at the temperatures encountered in neutron stars and the modeling of many-body systems of strongly interacting particles is complex and still in progress. Therefore the so-called equation of state (EoS) is one of the many mysteries of neutron stars. It describes the dependence of the pressure with respect to the density and is model-dependent. Since the seminal works by Landau (1932) and Baade & Zwicky (1934), more and more equations of state have been developed and they are more and more accurate and complex.

2.1.2 Equations for the stellar structure

2.1.2.1 Tolman-Oppenheimer-Volkoff equations

Consider a spherically symmetric star. The effects of rotation are neglected. This is a good approximation unless it rotates as fast as millisecond pulsars. The metric for a static, spherically symmetric space-time, using the Schwarzschild coordinates $x^\alpha = (t, r, \theta, \varphi)$, is :

$$g_{\alpha\beta}\mathrm{d}x^\alpha \mathrm{d}x^\beta = -\mathrm{e}^{2\phi/c^2}c^2\mathrm{d}t^2 + \left(1 - \frac{2Gm}{rc^2}\right)^{-1}\mathrm{d}r^2 + r^2\left(\mathrm{d}\theta^2 + \sin^2\theta\mathrm{d}\varphi^2\right). \tag{2.5}$$

It can be shown that, at the Newtonian limit, $m(r)$ and $\phi(r)$ are respectively the gravitational mass enclosed in a sphere of radius r and the gravitational potential (Gourgoulhon, 2005).

According to the metric (2.5), the proper radial length $\mathrm{d}l$, the proper volume $\mathrm{d}V$ between the shells of radii r and $r + \mathrm{d}r$ and the proper time interval $\mathrm{d}\tau$ are :

$$\mathrm{d}l = \frac{\mathrm{d}r}{\sqrt{1 - 2Gm/(c^2 r)}}, \tag{2.6}$$

$$\mathrm{d}V = \frac{4\pi r^2 \mathrm{d}r}{\sqrt{1 - 2Gm/(c^2 r)}}, \tag{2.7}$$

$$\mathrm{d}\tau = \mathrm{e}^{\phi}\mathrm{d}t. \tag{2.8}$$

Considering that neutron star matter forms a perfect fluid, ie. a non-viscous medium in which all stresses are zero except for an isotropic pressure P, the stress energy tensor is :

$$T^{\alpha\beta} = \left(\rho + \frac{P}{c^2}\right)u^\alpha u^\beta + P g^{\alpha\beta} \tag{2.9}$$

with u^α the matter 4-velocity. Note that the total energy density ρ is the sum of the internal energy and the mass energy, divided by c^2.

The perfect-fluid approximation is justified under the condition that the stresses produced by elastic strains in the solid crust (see chapters 7 and 8) or by strong magnetic fields are generally negligible compared to pressure.

The Einstein equation gives (Tolman, 1939; Oppenheimer & Volkoff, 1939) :

$$\frac{\mathrm{d}m}{\mathrm{d}r} = 4\pi r^2 \rho, \tag{2.10}$$

$$\frac{\mathrm{d}\phi}{\mathrm{d}r} = \left(1 - \frac{2Gm}{rc^2}\right)^{-1} \left(\frac{Gm}{r^2} + 4\pi G r \frac{P}{c^2}\right), \tag{2.11}$$

$$\frac{\mathrm{d}P}{\mathrm{d}r} = -\left(\rho + \frac{P}{c^2}\right) \frac{\mathrm{d}\phi}{\mathrm{d}r}. \tag{2.12}$$

These are called the Tolman-Oppenheimer-Volkoff (TOV) equations. The first and third ones describe the mass balance and the hydrostatic equilibrium and the second one is the relativistic equation for the metric function ϕ.

There are four variables : $m(r), \rho(r), \phi(r)$ and $P(r)$ but only three equations. Therefore, the system has to be supplemented by an equation of state which provides the relation $P(\rho)$. The dependence of the equation of state on the neutron star temperature T is not included since few hours to few days after its birth, $k_\mathrm{B}T \ll \varepsilon_\mathrm{F}$ with ε_F the Fermi energy in the neutron star and k_B the Boltzmann constant.

The boundary conditions are :

- $m(r = 0) = 0$.
- $P(r = 0) = P_\mathrm{c}$ with P_c the central pressure;

The radius R of the neutron star is determined by the condition : $P(R) = 0$.

Outside the star, $P(R \geq 0) = 0$ and $\rho(R \geq 0) = 0$. Therefore equation (2.10) gives $m(r \geq R) = M$, where M is a constant. It is the gravitational mass of the star. Outside the star, the space-time is describes by the Schwarzschild metric. Therefore, $\mathrm{e}^{\phi(R)/c^2} = \sqrt{1 - 2GM/(c^2 R)}$.

2.1.2.2 Baryon mass

Let n_b be the baryon number density in the star measured in a local reference frame. The total baryon number A_b of the star is :

$$A_\mathrm{b} = \int_0^R n_\mathrm{b} \frac{4\pi r^2}{\sqrt{1 - 2Gm/(c^2 r)}} \mathrm{d}r. \tag{2.13}$$

A simple estimate for a $1.4\ \mathrm{M}_\odot$ neutron star is (Haensel *et al.*, 2007) :

$$A_\mathrm{b} \simeq M/m_\mathrm{n} \simeq 1.7 \times 10^{57}\ \text{baryons}, \tag{2.14}$$

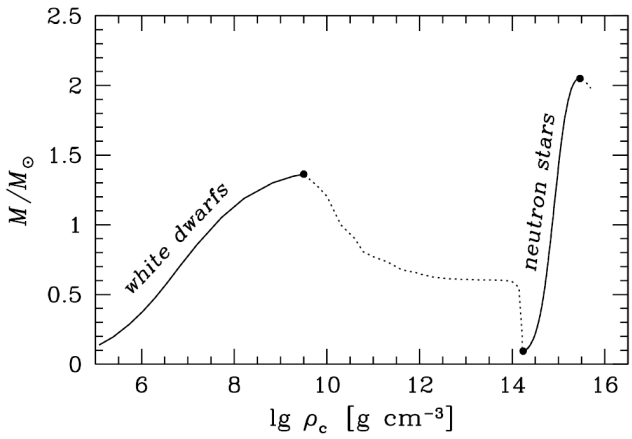

Figure 2.2: Schematic $M - \rho_c$ diagram for a cold dense matter equation of state. The solid and dotted lines indicate stable and unstable configurations respectively. The dots shows the maximum and minimum mass stars. From Haensel *et al.* (2007).

with the neutron mass : $m_n \simeq 1.67 \times 10^{-24}$ g.

With m_b the mass of one baryon, the baryon mass M_b is :

$$M_b = A_b m_b. \tag{2.15}$$

As a first approximation $m_b \approx m_n$ and thus $M_b = A_b m_n$.

Note that, during the evolution of an isolated neutron star, only A_b and M_b are constant and not M.

2.1.2.3 Minimum and maximum masses

For a given equation of state, choosing some central density ρ_c (or equivalently, by the mean of the equation of state, P_c), one can calculate $M = M(\rho_c)$ and $R = R(\rho_c)$ by solving the TOV equations (2.10-2.12).

Varying ρ_c, one can construct a $M - \rho_c$ diagram for a given equation of state. Such a diagram is schematically shown in figure 2.2 for a cold dense matter equation of state.

On figure 2.2, the static stability criterion states that configurations with :

$$\frac{dM}{d\rho_c} < 0 \tag{2.16}$$

are unstable with respect to small deformations (Harrison *et al.*, 1965) (see Haensel *et al.* (2007) for a detailed discussion).

Therefore, one can distinguish different segments : in solid lines are plotted the stable configurations and in dotted lines the unstable ones. The high-density stable segment corresponds to neutron stars and the low-density one to white dwarfs. In particular note that for neutron stars, are plotted a maximum and a minimum mass, M_{max} and M_{min} respectively.

Configurations with :

- $M > M_{\rm max}$ collapse into black holes;
- $M < M_{\rm min}$ explode.

Both the values of the minimal and maximum masses depend on the equation of state for dense matter. While $M_{\rm min}$ is well established $M_{\rm min} \simeq 0.1$ M$_\odot$ (Haensel *et al.*, 2007), $M_{\rm max}$ is not known and is in fact determined by the equation of state in the high-density regime, for $\rho \gtrsim \rho_0$, which poorly known.

However, there exists a firm upper bound on the maximum mass. By imposing that the equation of state is causal which is equivalent to the condition that the sound speed $c_{\rm s}$ is subliminal :

$$c_{\rm s}^2 = \frac{{\rm d}P}{{\rm d}\rho} < c^2, \tag{2.17}$$

one gets (Haensel *et al.*, 2007) :

$$M_{\rm max} \leq 3.0 \sqrt{\frac{5 \times 10^{14}\ {\rm g\ cm^{-3}}}{\rho_{\rm u}}}\ {\rm M}_\odot, \tag{2.18}$$

where $\rho_{\rm u} \lesssim 2\rho_0$ is the density above which the equation of state is not known. Thus,

$$M_{\rm max} \lesssim 3\ {\rm M}_\odot. \tag{2.19}$$

2.2 A laboratory for microphysics

2.2.1 Mass-radius diagram

For a given equation of state, one can construct the so-called mass-radius ($M-R$) relation by varying the central density.

Figure 2.3 plots the mass-radius relation for a set of equations of state assuming different compositions and interactions. Note that for low masses, the radius of neutron stars with pure nucleonic or nucleonic together with exotic matter decreases for increasing mass. This is the contrary for bare strange stars.

In figure 2.3, the $M-R$ relation for an equation of state is plotted up to its maximum mass. There is a large scattering in the predicted maximum masses. One can classify the equations of state according to this criterion. Soft equations of state give a low maximum mass and stiff ones a high one. Note that for a given mass, the radius of neutron star models increases with the stiffness of the equation of state. The onset of exotic matter in a neutron star model softens the equation of state.

2.2.1.1 Bounds on the mass and radius

General relativity constraint

General Relativity imposes that the radius of a neutron star is larger than the Schwarz-

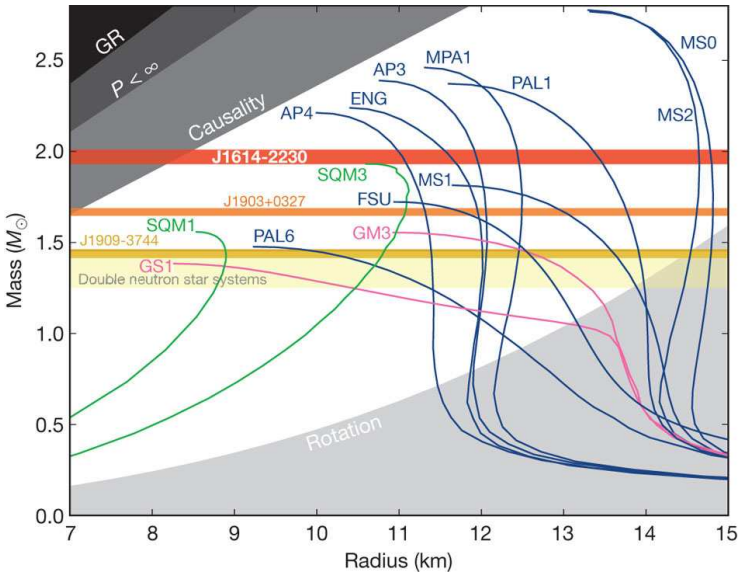

Figure 2.3: Mass-radius diagram : relation between the mass and the radius of neutron stars for different models of interior, assuming nucleonic matter (blue), nucleonic and exotic matter (pink) and strange quark matter (green). Are also plotted the different constraints and the measurements of the most massive pulsars (see text for details). From Demorest *et al.* (2010).

schild radius, ie. :

$$R > 2\frac{GM}{c^2}. \tag{2.20}$$

Finite pressure constraint

Assuming a uniform density profile inside a neutron star and finite pressure, one gets (Shapiro & Teukolsky, 1983; Glendenning, 1996) :

$$R > \frac{9}{4}\frac{GM}{c^2}. \tag{2.21}$$

Causality constraint

A lower bound on the radius of neutron stars, through the determination of the maximum value of the gravitational redshift and assuming a causal equation of state, is (Haensel *et al.*, 2007) :

$$R > 2.9\frac{GM}{c^2}. \tag{2.22}$$

Rotation limit

The fastest spinning neutron-star observed so far is PSR J1748-2446ad with a rotational frequency $f = 716$ Hz (Hessels *et al.*, 2006). This frequency constrains the masses and radii of neutron stars.

An empirical relation was derived by Lattimer & Prakash (2004), for neutron stars with masses not close to the maximum mass :

$$R_{\rm NR} < 10.4 \left(\frac{1000\ {\rm Hz}}{f}\right)^{2/3} \left(\frac{M_{\rm NR}}{{\rm M}_\odot}\right)^{1/3} \ {\rm km}, \tag{2.23}$$

with $R_{\rm NR}$ and $M_{\rm NR}$ the radius and mass of the non-rotating neutron star.

The spin frequency of PSR J1748-2446ad gives the following constraint :

$$R_{\rm NR} \leq 13.0 \left(\frac{M_{\rm NR}}{{\rm M}_\odot}\right)^{1/3} \ {\rm km}. \tag{2.24}$$

Note that the present section deals with non-rotating neutron star configurations. Discussion about the effects of rotation on the properties of neutron stars, in particular on the $M - R$ diagram, is postponed to section 6.7.

2.2.2 Observational constraints

2.2.2.1 Binary orbit

Consider a binary system composed of a pulsar and a companion star. The binary orbit can be described by the five usual Keplerian parameters (Lorimer, 2008; Haensel *et al.*, 2007) :

- the orbital period $P_{\rm b}$,
- the projected semi-major orbital axis x,
- the orbital eccentricity e,
- the longitude of periastron ω,
- the epoch of periastron passage T_0.

The parameters x and $P_{\rm b}$ enter the mass function :

$$f_{\rm mass}\left(M, M_{\rm c}\right) = \frac{4\pi^2}{G}\frac{x^3}{P_{\rm b}^2}, \tag{2.25}$$

$$= \frac{\left(M_{\rm c} \sin i\right)^3}{\left(M_{\rm c} + M\right)^2}, \tag{2.26}$$

where M and $M_{\rm c}$ are the masses of the pulsar and of the companion star, respectively, and i is the angle between the orbital plane and the plane of the sky.

If the five Keplerian parameters are measured, the only two unknowns are the neutron star and companion star masses.

For several binary systems, to describe the orbital evolution, it is necessary to take into account the relativistic effects, via the five following post-Keplerian parameters (Lorimer, 2008) :

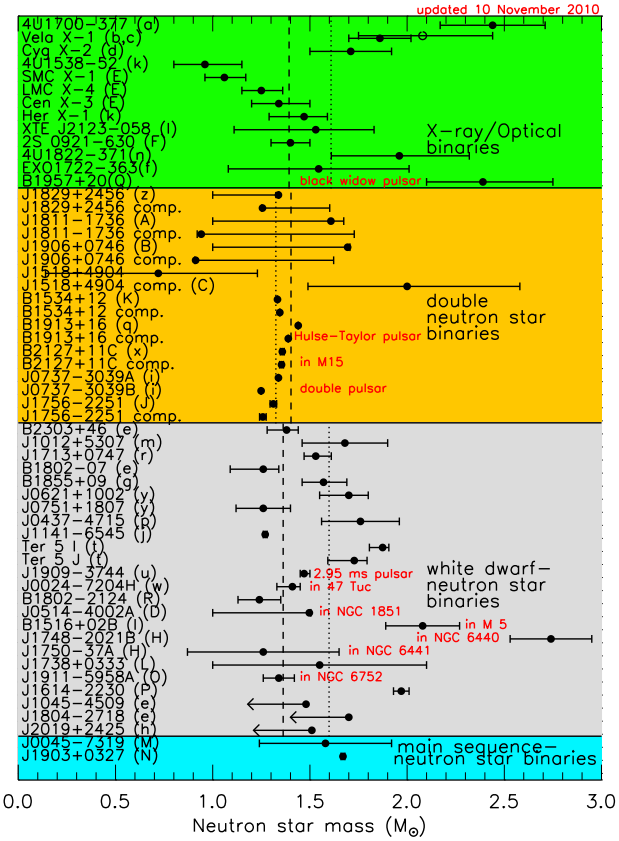

Figure 2.4: Measured neutron stars masses. From Lattimer & Prakash (2010).

- the advance of periastron $\dot{\omega}$,
- the time dilation and gravitational redshift parameter γ due to the gravitational field of the companion star,
- the rate of orbital decay due to gravitational wave radiation $\dot{P}_{\rm b}$,
- the two Shapiro delay parameters : the range r and the shape s, that describe the general relativistic delay of the pulsar signals due to the gravitational field of the companion star.

These five parameters are function of the masses of the pulsar and of the companion star and of the five Keplerian parameters. Their dependence on these variables depends on the theory of gravitation that is used. This is why measuring more than two parameters enables to the test this theory, General Relativity in particular, as shown in section 2.3.

2.2.2.2 Mass measurements

Masses of neutron stars were determined in several types of binaries as shown on figure 2.4 (Haensel *et al.*, 2007) :

- X-ray and optical binaries. The orbital period is obtained by observing the orbital variability of one of the star. The Doppler shifts of the spectral lines for optical binaries and the Doppler delay of the pulse time of arrival for X-ray binaries enable to measure the evolution of the orbital velocity on the line of sight. If the latter is determined for one of the companion, the five Keplerian parameters can be measured. Observations of the radial velocity of the other star and of eclipses in the binary then enable to calculate the masses of the stars;

- binaries composed of a radio pulsar and a degenerate (neutron star or white dwarf) or non-degenerate companion star. The very high precision of the measurement of the pulsar period enables to determine accurately the masses. The masses of the stars can be obtained through the measurements of the mass function together with two post-Keplerian parameters. Masses are most accurately measured in double neutron star binaries.

The most massive neutron star observed so far is PSR J1614-2230 reported by Demorest *et al.* in 2010 (see also section 11.2.2). The measurement of a large Shapiro delay since the system is nearly-edge on together with the standard Keplerian parameters enabled to determine the mass of the pulsar : $M = 1.97 \pm 0.04\ \mathrm{M}_\odot$. It implies that the maximum attainable mass for a given equation of state (EOS) must be higher than this highest measured mass ie. :

$$M_{\max}(\mathrm{EOS}) \geq M_{\max}^{\mathrm{obs}} \text{ with } M_{\max}^{\mathrm{obs}} = 1.97\,\mathrm{M}_\odot. \tag{2.27}$$

As shown on figure 2.3, this puts strong constraints on the equation of state, favoring stiff ones, and rules out the models for exotic or quark matter composition presented in the figure. However, recent equations of state with exotic matter compatible with PSR J1614-2230 mass measurement have been developed (eg. Bednarek *et al.* (2011)).

2.2.2.3 Radius measurements

Measurements of both the mass and radius of neutron stars can further constrain the equation of state via the mass-radius diagram (figure 2.3). Neutron star radii can be obtained by different methods (Haensel *et al.*, 2007) :

- gravitational redshift together with mass measurements;

- fitting the spectrum of the thermal emission of isolated neutron stars;

- fitting the spectrum of type I X-ray bursts or quiescent thermal emission from accreting neutron stars.

However, the radii measured from these techniques are not precise enough and/or too model-dependent to constrain the equation of state (see also part II of this thesis).

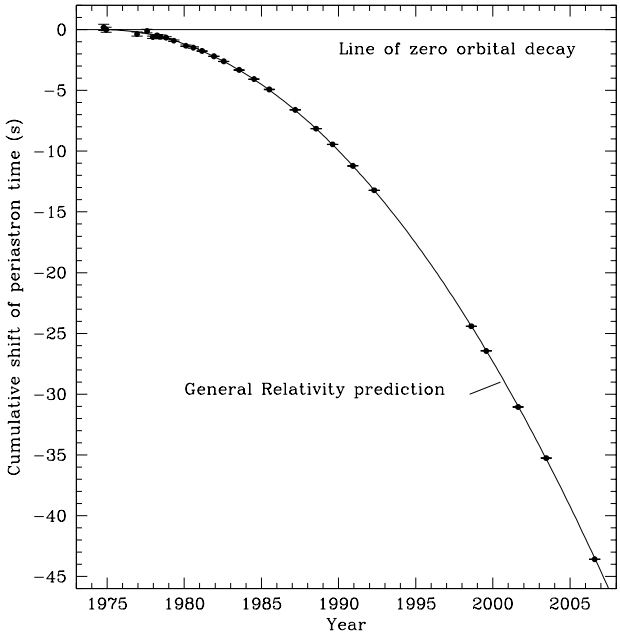

Figure 2.5: Orbital decay of PSR B1913+16. The data points correspond to the observed values, with error bars too small to be visible and the parabola to the expected ones according to General Relativity. From Weisberg *et al.* (2010).

2.2.2.4 Other constraints

Constraints on the composition and properties of the interior of neutron stars can also be obtained from the modeling the thermal evolution of isolated and accreting neutron stars, as extendedly shown in the second part of the present thesis.

Understanding the glitches, which are sudden increase in the otherwise decreasing rotational frequency of pulsars, may also to understand the properties of neutron star matter (for more details see Pizzochero (2010)).

In the near future, neutron star microphysics may be probed by the observations of gravitational waves from (Andersson *et al.*, 2011) :

- rotating neutron stars made asymmetric because of strain in the crust or in the core (see part III of this thesis) or of the magnetic field ;
- oscillations and instabilities in neutron stars;
- inspiralling binaries, which are systems of two neutron stars or a neutron star and a black hole driven to coalescence by the emission of gravitational waves.

So far, no gravitational waves have been observed but upper limits on the gravitational wave emission from the Crab and Vela pulsars and on their ellipticity were derived from LIGO and Virgo data (Abbott *et al.*, 2010; Abadie *et al.*, 2011).

2.3 A laboratory for gravitational physics

2.3.1 Gravitational wave emission

In 1974, Russel Hulse and Joseph Taylor discovered the first pulsar in a binary : PSR B1913+16. Moreover, its companion star is also a neutron star (Hulse & Taylor, 1975). Since then, regular observations have enabled to measure two post-Keplerian parameters : the advance of periastron $\dot{\omega}$ and the gravitational redshift and time-dilation parameter γ. The masses of the neutron stars were then derived : $M_1 = 1.4398 \pm 0.0002$ $M_\odot$ and $M_2 = 1.3886 \pm 0.0002$ $M_\odot$ (Weisberg *et al.*, 2010). Moreover, a third parameter has been measured : the rate of orbital decay $\dot{P}_b$. The latter originates from the emission of gravitational waves. The comparison between its observed value and the one predicted by General Relativity was made as shown on figure 2.5. The observed decrease is 99.7 ± 0.2 % the theoretical one. This is therefore an indirect evidence of the existence of gravitational waves as predicted by General Relativity. In 1993, Hulse and Taylor were awarded the Nobel Prize in Physics "*for the discovery of a new type of pulsar, a discovery that has opened up new possibilities for the study of gravitation*[1]".

2.3.2 Test of gravitation theories

Measurements of more than two post-Keplerian parameters from the observation of neutron stars allow to test the theories of gravitation in the strong-field regime.

Currently, the best system to test gravitation theories is the double neutron star system PSR J0737-3039 (Lorimer, 2008). In fact, the two neutron stars are observed as radio pulsars. The discovery of the first pulsar was reported by Burgay *et al.* (2003) and the observation of the second pulsar was published one month later by Lyne *et al.* (2004). Extended timing of the two pulsars was performed since then and the system allows to perform four independent tests of General Relativity through the measurements of the rate of orbital decay $\dot{P}_b$, the Shapiro delay parameters r and s and the gravitational redshift and time dilation parameter γ (Kramer *et al.*, 2006). The post-Keplerian parameters are function of the masses of the two pulsars. Figure 2.6 shows the constraints on the two masses derived from the measured values of the post-Keplerian parameters. The shaded regions correspond to $\sin i > 1$ and are therefore excluded. R is the ratio of the masses of the two pulsars. If General Relativity is correct, all the lines must intersect at the same point corresponding to the exact values of the neutron stars masses, as plotted in the inset. The measurements show that General Relativity is correct within an uncertainty of 0.05% (Kramer *et al.*, 2006) ! Breton *et al.* (2008) reported the measurement of the relativistic spin-orbit coupling, corresponding to the Ω_b line in figure 2.6, which is in agreement with General Relativity prediction at the 0.13 % level.

[1] Press release of 1993 Nobel Prize in Physics

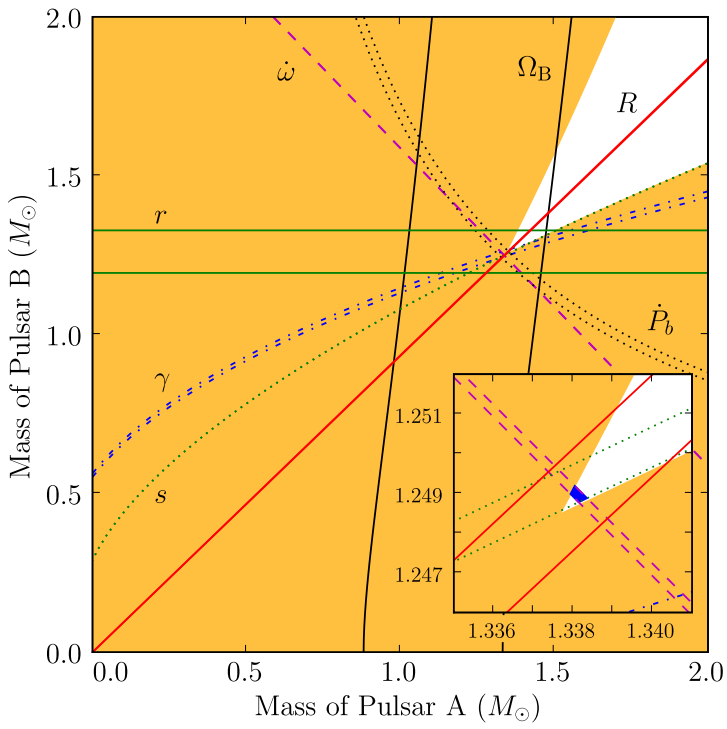

Figure 2.6: Mass-mass diagram for PSR J0737-3039 illustrating the present tests constraining general relativity in the double pulsar system. See text for details. From Breton *et al.* (2008).

In conclusion, neutron stars are cosmic laboratories whose understanding requires the involvement of various fields of physics and that enable to test in particular nuclear physics and theories of gravitation.

Part II

Thermal evolution of neutron stars

Introduction

Neutron stars are born hot in supernova explosions and the subsequent cooling is driven first by the neutrino emission from the interior and then by the emission of photons at the surface.

In chapter 3, after a short historical review in section 3.1, are introduced the relativistic heat equations and the numerical code that I used during my Ph.D. studies (section 3.2). The different microphysics ingredients that enter the equations are presented in section 3.3. This enables to construct a toy model for the cooling of isolated neutron stars and to build a scenario for their thermal history (section 3.4). In section 3.5, the effects of superfluidity in the interior and the heating processes are reviewed. Then, step by step, the influence of the different microphysics inputs on the cooling are detailed in section 3.6. After a presentation of the challenges and current status of the observations of cooling isolated neutron stars (section 3.7), their confrontation with the theoretical modeling is shown to enable to constrain the properties of the matter in the interior of neutron stars in section 3.8.

Chapter 4 focuses on the thermal evolution of young neutron stars with an age of few hundred years (section 4.1). New calculations for the specific heat of the superfluid neutrons in the inner crust are presented in section 4.2 and their influence on the cooling and the crust thermalization is detailed in section 4.3. The results were published in the paper Fortin *et al.* (2010). The theoretical and observational perspectives conclude this chapter (section 4.4).

The thermal evolution of accreting neutron stars also enable to put constraints on the properties of the matter inside neutron stars, as shown in chapter 5. The observations of accreting neutron stars allow to distinguish different accretion regimes and types of sources (section 5.1). The origin of the quiescent luminosity is explained in section 5.2 and a consistent model for the thermal evolution of accreting neutron stars is presented and confronted with the observations in section 5.4. Special focus is placed on a specific type of sources, the so-called quasi-persistent X-ray transients in the last section 5.5. They are neutron stars that accreted matter during a long period of time, from years to decades. Previous works demonstrated that the modeling of their thermal evolution just after accretion stops allows to infer information about the properties of neutron stars crust. A new model, that has been developed during my Ph.D. studies, is presented and preliminary results show promising perspectives.

I started studying the cooling of isolated neutron stars during my master's, under the supervision of Jérôme Margueron (Institute of Nuclear Physics in Orsay, France). The project about young neutron stars we started by then continued during my Ph.D. In parallel, with Leszek Zdunik and Paweł Haensel, we have focused on the thermal evolution of accreting neutron stars. I have extensively used the `NSCool` code developed by Dany Page to perform calculations. In particular, the code was modified to use the new specific heat calculations presented in Fortin *et al.* (2010) and adapted to the new model for the thermal evolution of accreting neutron stars.

Chapter 3

Cooling of isolated neutron stars

Contents

Confronting the theoretical modeling of the thermal evolution of isolated neutron stars with the available observations offers the possibility to understand the properties of dense matter. After presenting a short historical review of the field in section 3.1, the derivation of the relativistic heat equation and the `NSCool` code that is used to solve it in this thesis are presented in section 3.2. A toy model developed in section 3.3 enables to construct the cooling scenario detailed in section 3.4. Section 3.5 introduces general aspects concerning the superfluidity and the heating processes that can be encountered in neutron stars. Section 3.6 explains step by step the influence of the different microphysics inputs that enter the cooling model. Finally, the observations presented in section 3.7 are shown to enable to put constraint on the properties inside the core of neutron stars in section 3.8.

3.1 A little bit of history

The thermal evolution of neutron stars was first studied in the 1960s, before the discovery of neutron stars, when the first X-ray detectors on balloons and rockets were launched (Haensel *et al.*, 2007; Yakovlev *et al.*, 1999). Stabler (1960) and Chiu (1964) estimated that neutron stars could be observed thanks to their thermal emission. After the discovery of X-ray sources in 1963 by Bowyer *et al.*, first simplified calculations were performed by Morton (1964) and Chiu & Salpeter (1964).

The modern modeling of the cooling of neutron stars started with the seminal work by Tsuruta & Cameron (1966) that included the main elements of the theory but considered an isothermal interior (Tsuruta, 2009). Malone (1974) performed the first calculations beyond this approximation, solving the exact equations and the effects of General Relativity on the thermal evolution were included by Glen & Sutherland (1980). The subject was in fact revived in 1978 with the launch of the X-ray Einstein Observatory. The influence of the composition of the core of neutron stars, the different neutrino reactions and the modeling of the envelope, in the presence of a strong magnetic field, were studied.

Since the launch of ROSAT X-ray telescope in 1990 and XMM-Newton and Chandra X-ray observatories in 1999, active work focuses on the effects of superfluidity in neutron stars and on the late evolutionary stages of the thermal evolution.

More details on the history of neutron star cooling can be found in the nice review by Yakovlev *et al.* (1999).

3.2 Thermal evolution modeling

3.2.1 General relativistic heat equations

The general relativistic equations for the thermal evolution of a spherically symmetric star were initially derived by Thorne (1977).

3.2.1.1 Equation for energy balance

Let L be the luminosity, T the temperature and ϕ the function entering the metric (2.5).

The gradient in luminosity is a function of the change in temperature, the neutrino losses and the heat sources.

The equation for energy balance reads :

$$\boxed{\frac{\partial}{\partial r}\left(L\mathrm{e}^{2\phi}\right) = -\frac{4\pi r^2 \mathrm{e}^{\phi}}{\sqrt{1-2Gm/c^2 r}}\left(C_{\mathrm{V}}\frac{\partial T}{\partial t} + \mathrm{e}^{\phi}Q_{\nu} - \mathrm{e}^{\phi}Q_{\mathrm{h}}\right)} \tag{3.1}$$

with

- C_{V} the specific heat (in erg cm^{-3} K^{-1});
- Q_{ν} the neutrino emissivity (in erg s^{-1} cm^{-3});
- Q_{h} the rate of heat production per unit volume (in erg s^{-1} cm^{-3}).

3.2.1.2 Equation for energy transport

In neutron stars, the energy is transported by the diffusion of photons, the heat conduction and the neutrinos that freely escape.

The equation for energy transport is :

$$\boxed{\frac{\partial}{\partial r}\left(T\mathrm{e}^{\phi}\right) = -\frac{1}{\kappa}\frac{L}{4\pi r^2}\frac{\mathrm{e}^{\phi}}{\sqrt{1-2Gm/c^2 r}}}, \tag{3.2}$$

where κ is the thermal conductivity (in erg cm^{-1} s^{-1} K^{-1}).

The condition for isothermality states that the quantity $T\mathrm{e}^{\phi}$ is constant.

3.2.1.3 Boundary conditions

The system of the two equations (3.1) and (3.2) is solved to obtain the evolution of the luminosity and temperature profiles, $L(r,t)$ and $T(r,t)$ respectively, with :

- an initial profile : $L(r,t=0)$ and $T(r,t=0)$;
- at the center of the star : $L(r=0,t)=0$;
- at the surface of the star R : $L(r=R,t) = 4\pi R^2 \sigma T^4(r=R,t)$.

3.2.1.4 Heat equation

Note that the set of equations (3.1) and (3.2) can be rewritten in the form of a unique partial differential equation for the temperature T :

$$\boxed{\frac{\partial}{\partial r}\left[\sqrt{1-2Gm/c^2r}\kappa r^2 \mathrm{e}^{\phi}\frac{\partial}{\partial r}\left(T\mathrm{e}^{\phi}\right)\right] = \frac{r^2\mathrm{e}^{\phi}}{\sqrt{1-2Gm/c^2r}}\left(C_{\mathrm{V}}\frac{\partial T}{\partial t} + Q_{\nu}\mathrm{e}^{\phi} - Q_{\mathrm{h}}\mathrm{e}^{\phi}\right)}. \quad (3.3)$$

In the non-relativistic limit, $\mathrm{e}^{\phi} \simeq 1$ and $\sqrt{1-2Gm/c^2r} \simeq 1$, so the equation (3.3) becomes :

$$\frac{\partial}{\partial r}\left[\kappa r^2\frac{\partial T}{\partial r}\right] = r^2\left(C_{\mathrm{V}}\frac{\partial T}{\partial t} + Q_{\nu} - Q_{\mathrm{h}}\right), \quad (3.4)$$

that corresponds to the one-dimensional heat equation in Newtonian dynamics.

3.2.2 Modeling

The structure, composition and global properties (radius, mass, ...) are given by the solution of the Tolman-Oppenheimer-Volkoff equations (2.12) and are fixed in the subsequent cooling simulations.

To simplify the calculations, the neutron star is usually divided into two parts, following Gudmundsson *et al.* (1983) :

- the interior, where the density $\rho \geq \rho_{\mathrm{b}}$ with $\rho_{\mathrm{b}} = 10^{10} - 10^{11}$ g cm^{-3}. The heat equation is solved in this region, including all the necessary physical ingredients;

- the heat-blanketing envelope for $\rho \leq \rho_{\mathrm{b}}$. In the interior of neutron stars, the high thermal conductivity due to the degenerate electrons results in a uniform temperature profile few years after the birth. In the atmosphere, the heat transport is dominated by the photons. In between there exists a thin layer which has a low thermal conductivity since the electrons are not highly degenerate and the high density strongly prevents photon transport. This results in high temperature gradients in the envelope, that is few hundred meters thick. Therefore, a variety of models are devoted solely to the precise modeling of the envelope, in the plane-parallel and stationary approximation, including the possible presence of light elements such as hydrogen or helium resulting from the accretion of matter (Potekhin *et al.*, 1997) or the anisotropy in the thermal transport due to the magnetic field of the star (Potekhin *et al.*, 2003). More information in Page (2009).

The models of envelope provide a relation between the surface temperature T_{s} and the temperature at the inner-boundary of the envelope T_{b}. In fact, the heat equation is solved in the region that extends from the center of the star to the density ρ_{b}, as shown in the figure 3.1.

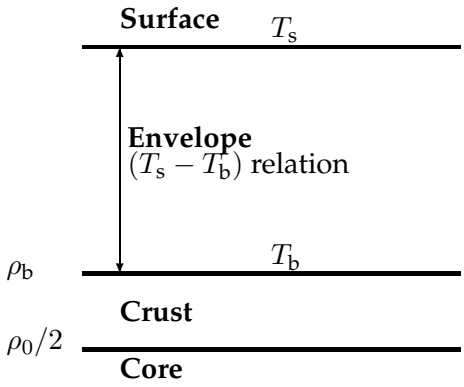

Figure 3.1: Schematic structure of a neutron star. See text for details.

Note that the temperature T_s is the temperature measured by an observer at the surface of the neutron star. However an observer at infinity will measure this temperature redshifted, ie. :

$$T_e^\infty = e^{\phi(R)} T_s. \tag{3.5}$$

The photon luminosity that is observed L_γ^∞ is also redshifted :

$$L_\gamma^\infty = e^{2\phi(R)} L_\gamma, \tag{3.6}$$

and the apparent radius of the neutron star R_∞ is given by :

$$R_\infty = e^{-\phi(R)} R. \tag{3.7}$$

3.2.3 `NSCool` code

Several groups have developed numerical codes that solve the heat equation in order to the study the thermal evolution of neutron stars. Among them is the group led by Dany Page at the National Autonomous University of Mexico (Mexico). A one-dimensional code called `NSCool` has been developed for several years now and is freely available online[1]. The results of the modeling of the thermal evolution of neutron stars that I present in this thesis have been performed with this highly-modular code.

The `NSCool` is based on an implicit scheme developed by Henyey *et al.* (1964), suitable for the study of spherically symmetric problems, that employs the Newton-Raphson method to solve the heat equation. More details can be found in the user's guide of the code, that is available on its webpage.

3.3 A toy model

The modeling of the thermal evolution of neutron stars requires a precise description of the different ingredients that enter the heat equation :

[1] http://www.astroscu.unam.mx/neutrones/NSCool/

- the thermal conductivity κ;
- the heat capacity per unit volume also called the specific heat $C_{\rm V}$;
- the neutrino emissivity Q_ν;
- the envelope model.

This section aims at giving some general though simplistic ideas about these different microphysics inputs. More details can be found in Yakovlev *et al.* (1999), Yakovlev & Pethick (2004) and Page (2009).

3.3.1 Thermal conductivity

The thermal conductivity κ measures the ability of a material to conduct heat. The higher thermal conductivity results in a faster heat transfer in the material.

Contributions to the thermal conductivity are provided (Haensel *et al.*, 2007) :

- by the photons in the atmosphere of neutron stars;
- by the electrons in the crust;
- mostly by the electrons and the neutrons in the core, for $npe\mu$ matter.

In the crust, the main contribution of the electrons to the thermal conductivity comes, for temperatures $T \gtrsim 3 \times 10^7$ K, from the electron-ion scattering and for temperatures $T \lesssim 3 \times 10^7$ K, from the electron scattering by the so-called impurities (ions that have a charge different from the one of most ions) and by the electrons.

Calculations show that the thermal conductivity in neutron star is high and therefore $\sim 10^2 - 10^3$ years after birth, the interior of neutron stars is believed to be almost isothermal. The thermal conductivity is few orders of magnitude smaller in the crust and therefore the crust remains hot during a longer time than the core.

The magnetic field influences the thermal conductivity and makes it anisotropic. In particular, the electron thermal conductivity is strongly reduced across the magnetic field but remains unchanged along the field lines. In the following, non-magnetic models of neutron stars will be considered.

3.3.2 Specific heat

The specific heat $C_{\rm V}$ is a measure of the energy that is required to increase the temperature of a given material.

The heat capacity is the sum of the contributions of :

- the electrons, the free neutrons and the atomic nuclei that form a lattice, in the crust (see section 4.2);
- the free neutrons, protons and electrons in the core, for $npe\mu$ composition.

3.3.3 Neutrino emission

Neutrinos are believed to be at the origin of the efficient cooling of neutron stars with a temperature $T \gtrsim 10^6 - 10^7$ K. In fact they are created in numerous reactions as reviewed by Yakovlev *et al.* (2001) and escape then freely, carrying away energy.

3.3.3.1 Neutrino emission from the core

The neutrino processes in the core of non-superfluid neutron stars can be divided into two groups :

- the fast ones with an emissivity of :

$$Q_\nu^{\mathrm{f}} = Q^{\mathrm{f}} T_9^6, \tag{3.8}$$

- the slow ones with an emissivity of :

$$Q_\nu^{\mathrm{s}} = Q^{\mathrm{s}} T_9^8, \tag{3.9}$$

with $T_9 = T/10^9$ K and $Q^{\mathrm{f,s}}$ slowly varying functions of the density. They will be considered as constant in the following.

Fast processes

The most powerful fast neutrino process in the so-called direct Urca (DUrca) process, which is in fact the β-decay of the neutron followed by its inverse reaction :

$$n \to p + e^- + \bar{\nu}_e \qquad \text{and} \qquad p + e^- \to n + \nu_e. \tag{3.10}$$

For this process, $Q^{\mathrm{f}} \sim 10^{27}$ erg cm^{-3} s^{-1}. However, the energy and momentum conservation imposes a density threshold to this process (Page, 2009).

The reaction (3.10) involves the degenerate particles whose energy and momentum are very close to the Fermi energy and momentum $p_{F,i}$. The number density of a species i is related to its Fermi momentum by :

$$n_i = \frac{p_{F,i}^3}{3\pi^2\hbar^3}. \tag{3.11}$$

On the one hand the energy conservation in the process (3.10) imposes, with μ_i the chemical potential of the species i, that :

$$\mu_n = \mu_p + \mu_e, \tag{3.12}$$

assuming that the neutrinos escape and have a null chemical potential. On the other hand, the conservation of the momentum in the process (3.10) requires that

$$p_{F,n} \leqslant p_{F,p} + p_{F,e}. \tag{3.13}$$

Charge neutrality imposes that $n_p = n_e$, or from the equation (3.11), $p_{F,p} = p_{F,e}$. Therefore equation (3.13) reads :

$$p_{F,n} \leqslant 2p_{F,p} \tag{3.14}$$

that gives in terms of the density

$$n_n \leqslant 8n_p. \tag{3.15}$$

Defining the proton fraction $x_p = n_p/(n_n + n_p)$, one gets :

$$x_p \geqslant 1/9 \simeq 11\%. \tag{3.16}$$

Therefore, the DUrca process is thought to operate only in the inner core of neutron stars which is present only in massive neutron stars with $M \sim 1.5$ M$_\odot$ (Lattimer *et al.*, 1991). For the DUrca process one has $Q^{\rm f} \sim 10^{27}$ erg cm^{-3} s^{-1}.

Processes similar to the DUrca one may also operate if hyperons, pions or kaon condensates or quark matter are present. The threshold on the proton fraction for this process to start is then affected. However, these processes are less efficient than the pure DUrca process (Yakovlev & Pethick, 2004).

Slow processes

There exist slow neutrino processes that may operate in particular when the DUrca process is forbidden. The analogue of the latter is the so-called modified Urca (MUrca) process :

$$n + N \to p + e^- + \bar{\nu}_e + N \qquad \text{and} \qquad p + e^- + N \to n + \nu_e + N, \tag{3.17}$$

where N is a spectator nucleon that ensures that the momentum conservation is satisfied. Nevertheless, since five degenerate fermions are involved instead of three, the efficiency is significantly reduced as compared with the DUrca process, as shown by equations (3.8-3.9). For the MUrca process, $Q^{\rm s} \sim 10^{21}$ erg cm^{-3} s^{-1}. MUrca processes involving hyperons, pions or kaon condensates or quark matter also exist if these species are present, though less efficient : $Q^{\rm s} \sim 10^{18}$ erg cm^{-3} s^{-1} .

The nucleon-nucleon bremsstrahlung is also thought to be an efficient process in the core of non-superfluid neutron stars :

$$N + N \to N + N + \nu\bar{\nu}, \tag{3.18}$$

with N a nucleon and ν, $\bar{\nu}$ an (anti)neutrino of any flavor. $Q^{\rm s} \sim 10^{19}$ erg cm^{-3} s^{-1} for this process.

Weaker neutrino reactions may also be mentioned (Yakovlev *et al.*, 2001) :

- Coulomb bremsstrahlung :

$$l + C \to l + C + \nu\bar{\nu}, \tag{3.19}$$

with l a lepton (e or μ) and C any charged fermion (e or p). $Q^{\rm s} \sim 10^{14}$ erg cm^{-3} s^{-1};

- lepton MUrca process :

$$\mu + C \rightarrow e^- + C + \nu_\mu + \bar{\nu}_e \qquad \text{and} \qquad e^- + C \rightarrow \mu + C + \nu_e + \bar{\nu}_\mu, \tag{3.20}$$

with $Q^{\rm s} \sim 10^{14}$ erg cm^{-3} s^{-1}.

3.3.3.2 Neutrino emission from the crust

The two dominant processes in the crust are (Yakovlev *et al.*, 2001) :

- the plasmon decay :

$$\Gamma \rightarrow \nu\bar{\nu}, \tag{3.21}$$

with Γ the plasmon, which is the quasiparticle associated with the plasma oscillation;

- the electron-nucleus bremsstrahlung :

$$e^- + (A, Z) \rightarrow e^- + (A, Z) + \nu + \bar{\nu}, \tag{3.22}$$

with (A, Z) the atomic nucleus.

There exist many neutrino processes in the crust. More information can be found in Yakovlev *et al.* (2001).

3.3.4 Envelope model

The first models of envelope have been obtained assuming its matter is catalyzed, ie. consists of ^{56}Fe and iron-like nuclei (Gudmundsson *et al.*, 1983; Hernquist & Applegate, 1984). However, in the early stage of the star history, lighter elements such hydrogen, helium, carbon or oxygen may have been accreted and deposited at the surface (Page, 2009). Since the electron thermal conductivity varies with the inverse of the charge number Z, the heat transport is then faster in the envelope (see eg. Potekhin *et al.* (1997)). Therefore, as shown on the figure 3.2, for a given $T_{\rm b}$ at the inner boundary of the envelope, the redshifted effective temperature $T_{\rm e}^{\infty}$ (and thus the surface temperature $T_{\rm s}$) is higher for a model of accreted envelope as compared with one for catalyzed matter.

The magnetic field makes the heat transport anisotropic (see section 3.3.1) and therefore the temperature non-uniform in the envelope, affecting the $T_{\rm s} - T_{\rm b}$ relation. Models of magnetized envelope have been developed (Potekhin & Yakovlev, 2001) for catalyzed matter in the envelope or including the effects of accreted light elements (Potekhin *et al.*, 2003). The figure 3.2 compares the envelope models for catalyzed matter when including or not the effect of the magnetic field.

3.3.5 Analytical solutions

The previous sections presented some general aspects of the microphysics input that is involved in the modeling of the thermal evolution of a neutron star. Some simple analytical results can now be obtained (Page *et al.*, 2006).

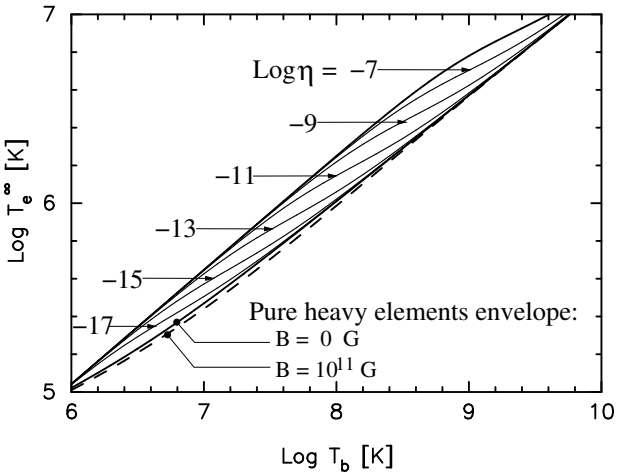

Figure 3.2: Relationships between the redshifted effective temperature $T_{\rm e}^{\infty}$ and $T_{\rm b}$ at the bottom of the envelope for different amounts of light elements parameterized by $\eta \equiv g_{\rm s\,14}^2 \Delta M_{\rm L}/M$ ($\Delta M_{\rm L}$ is the mass in light elements in the envelope, $g_{\rm s\,14}$ the surface gravity in units of 10^{14} cm s^{-2}, and M is the star mass), in the absence of magnetic field (Potekhin *et al.*, 1997). Also shown are the relationships for an envelope with catalyzed matter without and with a magnetic field with a strength of 10^{11} G following Potekhin & Yakovlev (2001). From Page *et al.* (2006).

3.3.5.1 A simple model

Approximate heat equation

Consider a neutron star in the framework of Newtonian gravity. The heat equation is therefore given by the equation (3.4). Calculations show that the thermal conductivity is high in neutron stars and therefore, as the first approximation, the interior can be considered as isothermal. Integrating the heat equation over the whole star, one gets :

$$C_{\rm V}^{\rm tot} \frac{{\rm d}T}{{\rm d}t} = -L_\nu - L_\gamma + H, \tag{3.23}$$

with $C_{\rm V}^{\rm tot}$ the total specific heat, ie. integrated over the whole star, L_ν the total neutrino luminosity, L_γ the surface photon luminosity and H the rate of energy released due to the heating processes integrated over the whole star (see also section 3.5.2). However, in the following, the heat sources are neglected : $H = 0$.

Let us assume that the initial temperature is flat ie. $T(t = 0) = T_0$.

Total specific heat

As a first approximation, one can consider that each species i in the interior of a neutron star forms a Fermi liquid with a specific heat $C_{\rm V}^i \propto T$. Therefore the total specific heat writes :

$$C_{\rm V}^{\rm tot} = C \cdot T, \tag{3.24}$$

with $C = 10^{30}$ erg K^{-2} (Page *et al.*, 2006).

Neutrino luminosity

For simplicity, only the DUrca and MUrca neutrino processes can be considered with :

$$L_\nu^{\rm f} = N^{\rm f} \cdot T^6, \tag{3.25}$$

$$L_\nu^{\rm s} = N^{\rm s} \cdot T^8, \tag{3.26}$$

respectively, where $N^{\rm f} = 10^{-9}$ erg s^{-1} K^{-6} and $N^{\rm s} = 10^{-32}$ erg s^{-1} K^{-8}.

Envelope model and photon luminosity

One consider a simple but reasonable model of envelope with a power-law dependence (cf. 3.2) :

$$T_{\rm s} \propto T^{0.5+\alpha} \tag{3.27}$$

with $\alpha \ll 1$. Therefore the photon luminosity is :

$$L_\gamma = 4\pi R^2 \sigma T_{\rm s}^4 = S T^{2+4\alpha} \tag{3.28}$$

with $S = 4 \times 10^{14}$ erg s^{-1} K$^{-2-4\alpha}$.

3.3.5.2 Different cooling stages

The neutrino cooling stage

Since the neutrino luminosity has a much stronger temperature dependence than the photon luminosity, in the first stage, one can neglect the photon luminosity L_γ.

One then finds, for $T \ll T_0$ and $\alpha \sim 0$:

- for the fast neutrino cooling :

$$T \simeq \left(\frac{C}{4N^{\rm f}}\right)^{1/4} t^{-1/4} \text{ and } T_{\rm s} \propto t^{-1/8}; \tag{3.29}$$

- for the slow neutrino cooling :

$$T \simeq \left(\frac{C}{6N^{\rm s}}\right)^{1/6} t^{-1/6} \text{ and } T_{\rm s} \propto t^{-1/12}. \tag{3.30}$$

The associated neutrino cooling time scales are :

- for the fast neutrino cooling :

$$\tau_\nu^{\rm f} \simeq \frac{C}{4N^{\rm f}T^4} \simeq 4 \text{ minutes} \cdot \left(\frac{C_{30}}{4N^{\rm f}_{-9}T_9^4}\right) \tag{3.31}$$

with $C_{30} = C/10^{30}$ erg K^{-2} and $N^{\rm f}_{-9} = N^{\rm f}/10^{-9}$ erg s^{-1} K^{-6};

- for the slow neutrino cooling :

$$\tau_\nu^{\rm s} \simeq \frac{C}{6N^{\rm s}T^6} \simeq 6 \text{ months} \cdot \left(\frac{C_{30}}{6N^{\rm s}_{-32}T_9^6}\right) \tag{3.32}$$

with $N^{\rm s}_{-32} = N^{\rm s}/10^{-32}$ erg s^{-1} K^{-8}.

These results clearly explain the fast and slow cooling terminology.

Stage transition

When the temperature has sufficiently decreased, the neutrino and photon luminosity are comparable. The neutron star keeps cooling and therefore enters the so-called photon stage, for which the neutrino luminosity can be neglected.

The transition from the neutrino stage to the photon stage occurs when the temperature of the neutron star reaches :

- for the fast neutrino cooling :

$$T^{\mathrm{f}}_{\mathrm{trans.}} \simeq \left(\frac{S}{N^{\mathrm{f}}}\right)^{1/4} \sim 10^6 \text{ K and } T_{\mathrm{s}} \sim 10^5 \text{ K}; \tag{3.33}$$

- for the slow neutrino cooling :

$$T^{\mathrm{s}}_{\mathrm{trans.}} \simeq \left(\frac{S}{N^{\mathrm{s}}}\right)^{1/6} \sim 10^8 \text{ K and } T_{\mathrm{s}} \sim 10^6 \text{ K}. \tag{3.34}$$

The photon cooling stage

In the second and last stage, the photon luminosity dominates over the neutrino one.

One gets therefore

$$t \simeq t_{\mathrm{trans.}} + \frac{C}{4\alpha S}\left(\frac{1}{T^{4\alpha}} - \frac{1}{T^{4\alpha}_{\mathrm{trans.}}}\right), \tag{3.35}$$

with $t_{\mathrm{trans.}}$ the time when $T = T_{\mathrm{trans.}}$.

When $t \gg t_{\mathrm{trans.}}$ and $T \ll T_{\mathrm{trans.}}$,

$$T \simeq \left(\frac{C}{4\alpha S}\right)^{\frac{1}{4\alpha}} t^{-\frac{1}{4\alpha}} \text{ and } T_{\mathrm{s}} \propto t^{-\frac{1}{8\alpha}}. \tag{3.36}$$

Therefore, the evolution of the temperature strongly depends on the parameters S and α and thus on the model of envelope but also on the specific heat that can be affected by the superfluidity (see section 3.5.1).

3.4 Cooling history of a neutron star

The description of the physical processes involved in the thermal evolution of a neutron star together with the estimates presented in the previous sections enable to build a simple scenario for the cooling of an isolated neutron star.

A proto-neutron star is formed in a supernova event with a high temperature $T \sim 10^{11}$ K. The proto-neutron star becomes a neutron star when it gets transparent to the neutrinos that are formed in its interior.

The neutron star enters the neutrino cooling stage. During ~ 100 years, the low thermal conductivity in the crust keeps it hot while the core cools by emission of neutrinos.

Therefore, the core and and the crust cool independently and the evolution of the surface temperature reflects the thermal state of the crust and is sensitive to its physical properties.

Then the core and the crust thermal evolutions couple. The cooling wave from the core reaches the surface and the whole neutron star cools by the emission of neutrinos, mainly from the core. The physical properties of the core are reflected in the evolution of the surface temperature.

The temperature keeps decreasing until the neutrino luminosity becomes comparable to the photon luminosity. The neutron star enters the photon cooling stage, the precise moment depending on the efficiency of the neutrino processes, and the evolution of the internal temperature is governed by the emission of photons from the surface and is sensitive to the properties of the outer parts of the star.

3.5 Towards a more realistic model

3.5.1 Superfluidity in neutron stars

It is believed that nucleons can be in a superfluid state in the interior of neutron stars. This phenomenon has a strong influence on the cooling properties of the neutron stars and therefore on the thermal evolution of neutron stars (Yakovlev *et al.*, 1999; Page *et al.*, 2006; Page, 2009).

3.5.1.1 From BCS theory to neutron star superfluidity

After the development of the BCS theory by Bardeen, Cooper & Schrieffer in 1957 to explain the electron superconductivity, Bohr *et al.* (1958) suggested that a similar phenomenon, called superfluidity may occur in systems of nucleons inside the atomic nuclei. Migdal (1959) noticed that it may also appear in the interior of neutron stars.

The main point of the theory is that, in a system of degenerate fermions, an attractive interaction between the particles near the Fermi surface results the formation of pairs of fermions, named Cooper pairs. Superfluidity of charged particles like the electrons implies superconductivity of the latter. The transition from the normal to the superfluid state is a second order phase transition that occurs when the temperature decreases below a critical temperature $T_{\rm c}$. The latter depends on the strength of the interaction between the fermions. For $T < T_{\rm c}$, the dispersion relation of the fermions has an energy gap $\Delta(T)$. The latter can be seen as the half of the binding energy of the Cooper pair. It is temperature-dependent and :

$$k_{\rm B}T_{\rm c} = 0.5669\Delta(T = 0). \tag{3.37}$$

The values of the critical temperature and of the pairing gap are also density-dependent : $T_{\rm c}(\rho), \Delta(\rho)$.

In neutron stars, the superfluidity is caused by the strong interaction between the neutrons, the protons and, if present, the hyperons. Pairing may occur in the singlet-state of the nucleon pair : the $^1S_0$ channel or in the triplet-state : the $^3P_2$ channel. Wolf (1966) showed that the neutrons are paired in the $^1S_0$ channel for $\rho < \rho_0$ and thus can be superfluid in the crust of neutron stars. Since the singlet-state neutron-neutron interaction becomes repulsive for higher densities, the neutron $^1S_0$ pairing disappears in the core. However, proton pairing in the singlet-state can occur in the core. Hoffberg *et al.* (1970) later noticed that the neutron interaction in the triplet-state is attractive when $\rho > \rho_0$ and therefore, the neutrons can be also superfluid in the core of the neutron stars.

3.5.1.2 From microphysics to astrophysics

Note that most of the seminal studies dealing with superfluidity were performed before the discovery of the pulsars in 1967. Since the neutron stars lose energy due to their electromagnetic radiation, their rotational period P is expected to decrease with time. However, the timing of radio pulsars showed that some of them exhibit sudden increases in their rotational period followed by a slow relaxation. These phenomena are called glitches and are mainly observed from young radio pulsar (see also section 7.1.2). Baym *et al.* (1969) subsequently proposed that the glitches originate from the interaction between the normal and the superfluid components of the matter inside neutron stars.

3.5.1.3 An open issue

The pairing gap of neutron star Δ is still the subject of active research and since the 1970s, nucleon critical temperatures have been calculated for different models of nuclear interaction and many-body theories and have been shown to depend a lot on the inclusion of the in-medium effects. T_c increases strongly when the attraction between the nucleons is stronger. Figure 3.3 shows for example, the variation of the pairing critical temperatures with the density for the $^1S_0$ neutron pairing in the crust and the $^3P_2$ neutron and $^1S_0$ proton pairing in the core, for various models (see also the review by Lombardo & Schulze (2001)). One can draw some general conclusions :

- $^1S_0$ neutron superfluidity can appear in the inner-crust of neutron stars and the maximum of its critical temperature ranges from $10^8 - 10^{11}$ K depending on the models of superfluidity. It is by far the most studied type of superfluidity in neutron stars;
- $^3P_2$ neutron superfluidity and $^1S_0$ proton superfluidity can be present in the core of neutron stars with a maximum critical temperature between 10^8 and 10^{10} K.

3.5.1.4 Consequences of baryon superfluidity

On the hand, when the temperature decreases below the critical temperature T_c of a given type of baryons, the appearance of an energy gap Δ in the dispersion relation of

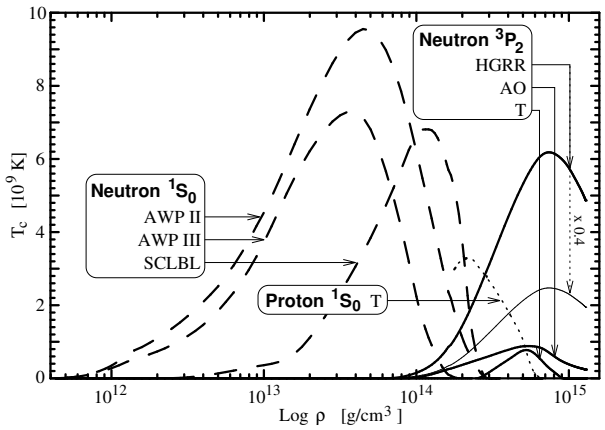

Figure 3.3: Pairing critical temperature $T_{\rm c}$ as a function of the density ρ in neutron star matter for different models of nucleon superfluidity. From Page (1998).

these baryons makes them inactive. Therefore all the physical processes : the specific heat and the neutrino emissivity involving these baryons are strongly suppressed, by a factor $\mathrm{e}^{-\Delta/k_{\rm B}T}$ if $T \ll T_{\rm c}$.

The effects of the superfluidity are included in the cooling calculations by writing :

- for the specific heat :

$$C_{\rm V}^{\rm pair}(T) = R_{\rm c}(T/T_{\rm c}) \times C_{\rm V}^{\rm norm}(T) \tag{3.38}$$

  with $C_{\rm V}^{\rm pair}$ and $C_{\rm V}^{\rm norm}$ the specific heat of the superfluid and normal baryons, respectively, and $R_{\rm c}$ a reduction factor.

- for the neutrino emissivity :

$$Q_{\nu}^{\rm pair}(T) = R_{\nu}(T/T_{\rm c}) \times Q_{\nu}^{\rm norm}(T) \tag{3.39}$$

  with $Q_{\nu}^{\rm pair}$ and $Q_{\nu}^{\rm norm}$ the neutrino emissivity of the superfluid and normal baryons, respectively, and R_{ν} a reduction factor.

When $T = T_{\rm c}$, $R_c(T/T_{\rm c}) = 1$ and $R_{\nu}(T/T_{\rm c}) = 1$ and for $T \ll T_{\rm c}$, $R_c(T/T_{\rm c}) = 0$ and $R_{\nu}(T/T_{\rm c}) = 0$. The two reduction factor are different for each neutrino process and type of superfluidity that are considered.

The neutrino emissivity of given baryons is exponentially reduced when they are superfluid. For example, the proton superfluidity in the core of a neutron star suppresses also the Urca (DUrac and MUrca) processes but do not affect the neutron-neutron bremsstrahlung.

On the other hand, the pairing of baryons initiates a new type neutrino processes called the pair breaking and formation (PBF) processes. The energy is released in the form a neutrino-antineutrino pair when a Cooper pair of baryons is formed. The figure

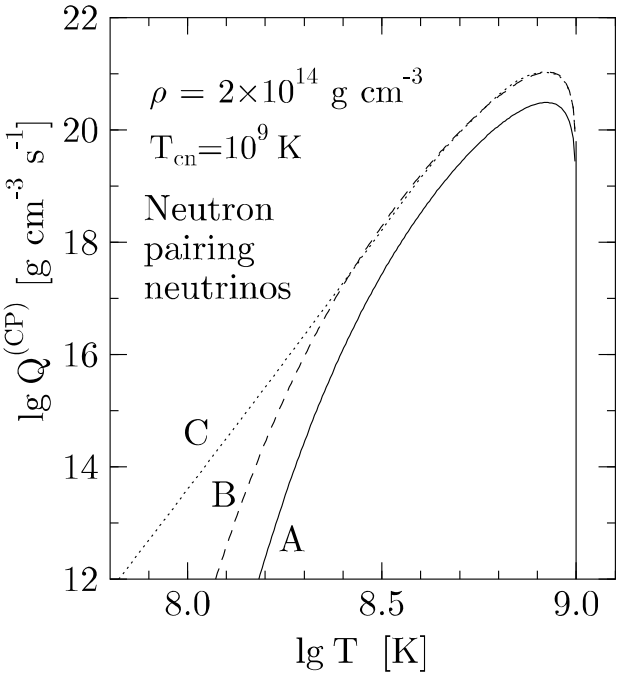

Figure 3.4: Temperature dependence of the neutrino emissivity associated with the Cooper pairing of neutrons for three models of superfluidity, at the density $\rho = 2 \times 10^{14}$ g cm^{-3} and for a maximum of the critical temperature $T_{\rm C} = 10^9$ K. From Yakovlev *et al.* (2001).

3.4 shows the variation of the neutrino emissivity due to the Cooper pairing of the superfluid neutrons for three models of superfluidity, at the density $\rho = 2 \times 10^{14}$ g cm^{-3} and for a maximum of the critical temperature $T_{\rm C} = 10^9$ K. The process starts when $T \lesssim T_{\rm C}$, is maximum when $T \sim 0.8 T_{\rm C}$ and is exponentially suppressed at $T \ll T_{\rm C}$. More information in Yakovlev *et al.* (2001).

For both $^1S_0$ and $^3P_2$ pairings, the emission of neutrinos by the PBF process can occur through two different channels : the axial and vector channel (Page *et al.*, 2009; Page, 2009). Recent calculations (Leinson & Pérez, 2006a,b) have shown that the vector part of the PBF process is in fact strongly suppressed, the axial part being then the main contributor to the PBF neutrino emissivity. As a result :

- for neutron $^1S_0$ pairing in the crust, the PBF process has a negligible effect since the contribution from the axial channel is suppressed for non-relativistic particles such as the ones in the crust;

- for proton $^1S_0$ pairing in the core, the emissivity is given by the axial part of the PBF process and is approximately :

$$Q_\nu^{p1S0} \sim 5 \times 10^{19} T_9^7 R_\nu^{p1S0}(T/T_{\rm c}); \tag{3.40}$$

- for neutron ${}^3P_2$ pairing in the core, the emissivity is slightly reduced and is of the order of

$$Q_\nu^{n3P2} \sim 4 \times 10^{21} T_9^7 R_\nu^{n3P2}(T/T_c). \tag{3.41}$$

3.5.2 Heating processes

Several heating processes that may occur in isolated neutron stars have been identified (Schaab *et al.*, 1999; Page *et al.*, 2006; Tsuruta, 2009) such as :

- Joule heating from the decaying magnetic field in neutron stars;
- crust cracking : as the neutron star slows down, it adapts its shape through a series of crust breaking. This phenomenon generates some heat in the crust;
- frictional heating : frictions between the crustal lattice that spins down with the star and the superfluid neutrons that do not can cause heating. Its efficiency depends on the strength of the pinning of the superfluid vortex in the crust;
- chemical heating : as the neutron star slows down, its density increases and the β-equilibrium is lost. The subsequent non-equilibrium reactions may be at the origin of internal heating.

These processes are believed to play an important role in the thermal evolution of neutrons older than $\sim 10^6$ years.

3.6 Influence of the microphysics input

The previous sections provide us with the description of the different ingredients that enter the modeling of the thermal evolution of isolated neutron stars. Let us now investigate separately the effects of the microphysics on the temperature evolution.

3.6.1 Non superfluid stars

Figure 3.5 shows the evolution of the redshifted surface temperature T_e^∞ for non-superfluid neutron stars of varying mass for the model described in more details in Page & Applegate (1992). Such curves are called cooling curves. The DUrca process is allowed for $M \geq 1.35$ M$_\odot$. Therefore, the MUrca process is the dominant neutrino process in neutron stars with a mass lower than this value. For neutron stars with a mass $M \geq 1.35$ M$_\odot$, the size of the region that emits neutrinos via the DUrca process increases with the mass of the star.

In the first $\sim 10 - 100$ years, all the cooling curves exhibit a plateau-like behavior. According to the cooling scenario developed in the section 3.4, at this stage, the core and crust cool independently and the evolution of the surface temperature is controled

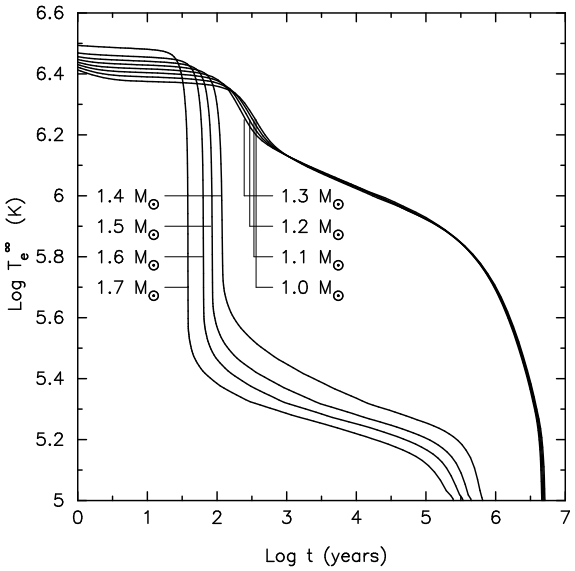

Figure 3.5: Influence of the nature of the Urca process on the cooling of stars of different masses. From Page *et al.* (2006).

by the properties of the crust, which has a low neutrino emissivity. This is at the origin of the plateau in the cooling curves.

Let us compare now the influence of the nature of the Urca process on the subsequent cooling of an isolated neutron star. The neutron stars in which DUrca process ($M > 1.35\,\mathrm{M}_\odot$) is allowed exhibit a very high neutrino emissivity that is at the origin of the sharp temperature decrease observed in the cooling curves. This decrease happens when the cooling wave from the core reaches the surface after its propagation in the crust. A more massive neutron star has a thinner crust and the propagation time of the cooling wave in the crust in thus shorter. Therefore, the temperature drops earlier in more massive stars. The temperature decrease is much less pronounced for low-mass neutron stars ($M < 1.35\,\mathrm{M}_\odot$) and the cooling curves are almost mass-independent since the microphysics properties of their interior are similar.

Then, the thermal relaxation of the neutron star is over and the whole neutron star cools by emission of neutrinos mainly from the core. The surface temperature reflects the properties of the core and a second plateau-like behavior is observed.

Finally, $\sim 10^6$ years after its birth, when the temperature is sufficiently low, the old neutron star enters the photon cooling stage and cools by emission of photons from the surface.

In conclusion, the thermal evolution of an isolated neutron star depends dramatically on the type of Urca process that occurs in its core and thus on its mass.

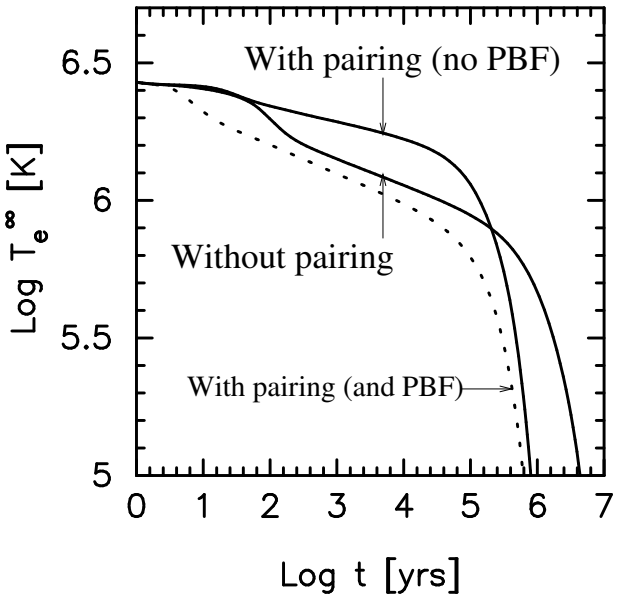

Figure 3.6: Effect of the superfluidity on the cooling of a 1.4 $M_\odot$ neutron star with and without nucleon pairing. The associated PBF process is artificially turned off or on. See text for details. From Page *et al.* (2004).

3.6.2 Superfluid stars

As presented in section 3.5.1, the effect of nucleon superfluidity is twofold. On the one hand, the specific heat and neutrino emissivity of the superfluid nucleons are significantly reduced when the temperature decreases below the critical temperature. The specific heat of nucleons which is one of the main contributor to the total specific heat for non-superfluid matter is reduced and so is the total specific heat. The neutrino emissivity due to the MUrca (and DUrca if present) process is strongly reduced. On the other hand, nucleon superfluidity triggers new efficient neutrino processes, the so-called PBF processes.

The figure 3.6 shows the influence of the superfluidity on the cooling curve of a 1.4 $M_\odot$ build for the APR equation of state (Akmal *et al.* (1998); see also section 10.4.1). The main neutrino process in the core is the MUrca process. Details on the $^1S_0$ neutron and proton and $^3P_2$ neutron pairing models can be found in Page *et al.* (2004).

Let us first consider the solid curves, when the PBF process is turned off. Both the specific heat and the neutrino emissivity are then reduced. However the decrease of the latter is smaller. Therefore during the neutrino cooling era, the star with pairing cools more slowly than the normal star. During the photon cooling era, the paired star cools faster since its specific heat is reduced, as seen in the approximate formula (3.36).

When including the PBF processes associated with nucleon superfluidity, the results are drastically different in the neutrino cooling phase. The PBF processes are so efficient that they do not only compensate the slowing down of the cooling due to the reduction

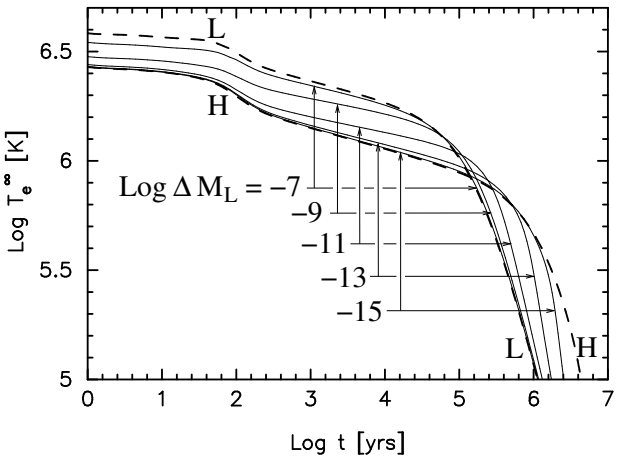

Figure 3.7: Effect of the envelope model on the cooling curve. Are plotted the cooling curves for different amounts $\Delta M_{\rm L}$ of light elements. L stands for a model with a maximum amount of light elements and H for an envelope model with catalyzed matter. From Page *et al.* (2004).

of the specific heat, but they even accelerate the cooling. The temperature decreases faster when the PBF processes are included so the transition to the photon cooling stage happens earlier. Since the thermal evolution in the photon cooling stage depends on the specific heat solely, the late cooling is similar when including or not the PBF processes.

3.6.3 Influence of the envelope model

Figure 3.7 shows the influence of the envelope model on the cooling curve of a neutron star, that is discussed in section 3.3.4. For $T \lesssim 10^4$ yr, in the neutrino cooling stage, a model with a higher amount of light elements has a higher redshifted effective temperature since the heat transport is then more efficient. Therefore it enters the photon cooling stage at earlier times and therefore, cools then faster.

3.6.4 Influence of the equation of state

The figure 3.8 illustrates the influence of the equation of state on the thermal evolution of an isolated neutron star. Cooling curves are shown with and without pairing, the pairing properties being fixed.

When no pairing is included, the different cooling curves are quasi-indistinguishable. Slight differences can be observed when the superfluid effects are included. These differences originate from the density dependence of the superfluid properties.

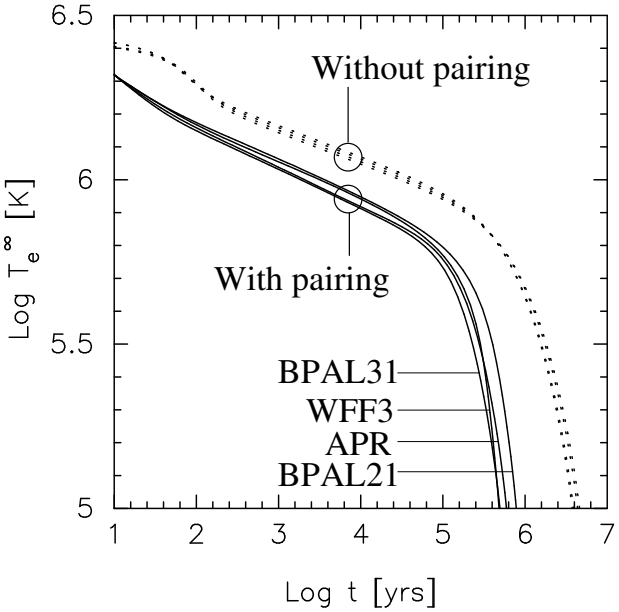

Figure 3.8: Effect of the equation of state on the cooling of 1.4 $M_\odot$ neutron star. Cases without and with pairing are considered. From Page *et al.* (2004).

3.6.5 Minimal cooling paradigm

Considering the number of parameters one can play with in the modeling of the thermal evolution of an isolated neutron star, Page *et al.* (2004) have introduced the so-called minimal cooling paradigm. Its purpose is to investigate whether observations are consistent with an enhanced cooling in some neutron stars that results from DUrca processes due to nucleonic or exotic matter.

Therefore, in the minimal cooling paradigm, no fast neutrino emission or exotic matter is allowed in the core of the neutron stars. This strongly restricts the number of equation of state that can be used. However, all the other possible ingredients entering the modeling of the thermal evolution are taken into account, in particular, the effects of the pairing on the specific heat and neutrino emissivity and of the composition of the envelope (Page, 2009). Eventually, the paradigm should also include the effects of the magnetic field.

3.7 Observations of the temperature of isolated neutron stars

Let us now discuss the observational measurements. Comparing the evolution of the surface temperature of different neutron stars whose age is known with the results of the theoretical modeling may ultimately enable to constraint the microphysics properties of the interior of neutron stars.

Neutron stars are small objects and thus their thermal radiation is weak. The modern instruments are able to detect neutron stars located only few kiloparsecs from us and with a high enough temperature $\sim 10^5 - 10^7$ K. Most of radiation is emitted in the (0.01-1 keV) range, that is the soft X-ray and hard ultraviolet range (Yakovlev *et al.*, 1999).

In 1975, a first upper limit on the surface temperature on the Crab was set by Wolff *et al.*. Then detections of or upper limits on the thermal radiation emitted by isolated neutron stars were obtained by soft X-ray telescopes on the space observatories (Einstein, EXOSAT, ROSAT, ASCA, RXTE, XMM-Newton, Chandra, ...) or by ultraviolet telescopes (eg. EUVE) (Yakovlev *et al.*, 1999).

3.7.1 An observational challenge

Determining the surface temperature and the age of a neutron star suffers from a lot of uncertainties.

On the one hand, when the spectrum from a neutron star is observed, the thermal component has to be separated from the background emission created by the supernova remnant, the non-thermal emission produced in the magnetosphere of the neutron star and the thermal emission originating from hot polar spots due to the pulsar activity. As a consequence middle-aged neutron stars are most likely to be observed since they are still hot, their supernova remnant is extended and their magnetospheric activity is reduced.

The fit of the spectrum of a neutron star depends on many parameters such as the effective temperature, the magnetic field, the chemical composition of the envelope, the temperature and size of the polar caps, the properties of the non-thermal radiation, the mass and radius of the neutron star, the distance, the column density of the interstellar medium between the source and the observer, ... The small number of detected photons makes therefore the constraints on these parameters too strong. However additional constraints can be put thanks to radio, optical, gamma-ray observations that enable to determine for example the distance to the source from parallax measurements, the column density of the interstellar gas, ... For more details, see Yakovlev *et al.* (1999).

On the other hand, the age determination is likely to be uncertain. Only if the supernova has been observed in the past can the age be well known. Otherwise, it is determined from the measurement of the expansion velocity of the supernova remnant, from the spin-down age that is likely to be approximative or by tracing back in time and space the proper motion of the source if it possible to associate it with its birth place (Ho, 2011).

3.7.2 Present status

For all the reasons presented previously, the age and surface temperature are known for only a dozen of sources. In figure 3.9 I present the available observational data on the surface temperature of isolated neutron stars. Note the large uncertainties on both

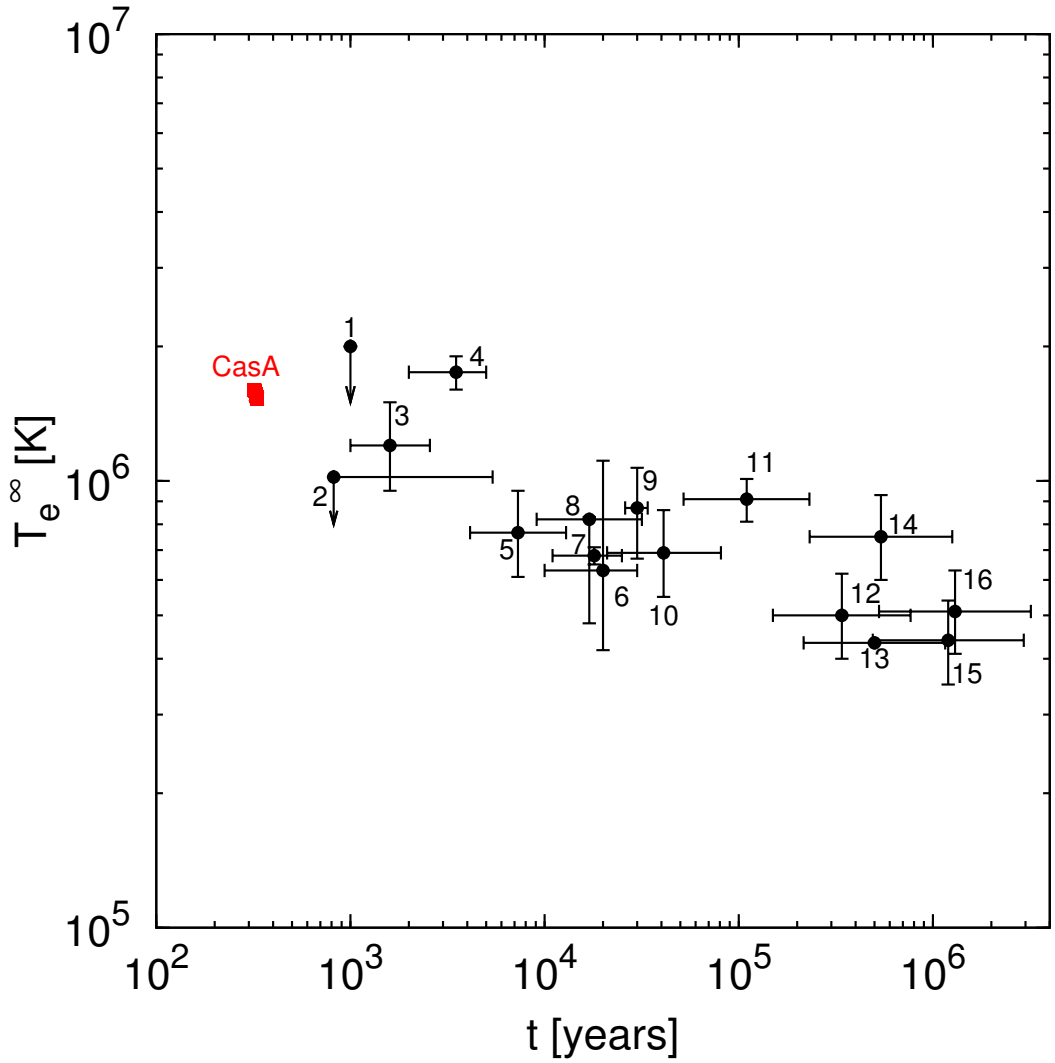

Figure 3.9: Observational limits on the redshifted surface temperature as a function of the age of isolated neutron stars. Data from the references cited in Shternin *et al.* (2011). The stars are : 1 – PSR B0531+21 (Crab), 2 – PSR J0205+6449 (in 3C 58), 3 – PSR J1119–6127, 4 – RX J0822–4300 (in Pup A), 5 – PSR J1357–6429, 6 – RX J0007.0+7303 (in CTA 1), 7 – PSR B0833–45 (Vela), 8 – PSR B1706–44, 9 – PSR J0538+2817, 10 – PSR B2334+61, 11 – PSR B0656+14, 12 – PSR B0633+1748 (Geminga), 13 – RX J1856.4–3754, 14 – PSR B1055–52, 15 – PSR J2043+2740, 16 – RX J0720.4–3125 and in red the Cassiopeia A neutron star. The measurements are uncertain so the error-bars are large.

variables. Until the observations of the neutron star in Cassiopeia A supernova remnant in 2010, the surface temperature of neutron stars was known at only one single instant in time.

Figure 3.9 shows that so far, the surface temperature was determined for neutron stars with an age ranging from ~ 300 to 10^6 years. According to the cooling scenario described in section 3.4, these neutron stars are in the neutrino cooling state and modeling their thermal evolution may enable to constraint the properties of the core.

3.7.3 Cassiopeia A neutron star

Cassiopeia A supernova remnant was discovered in radio observations in 1947 and is the brightest astronomical radio source beyond the Solar System (Ho & Heinke, 2009). The supernova was likely observed by the first Royal Astronomer John Flamsteed on August 16, 1680 (Ashworth, 1980) and has therefore an age of 331 years which is in agreement with the study of the expansion of the remnant (Fesen *et al.*, 2006). It is one of the youngest-known supernova remnants in our Galaxy. It is located at a distance of d = $3.4^{+0.3}_{-0.1}$ kpc from the Earth (Reed *et al.*, 1995). The central compact object was only identified in Chandra first-light observations in 1999 (Tananbaum).

The interpretation of the X-ray spectrum of the central compact object in Cassiopeia A was a challenging task (Pavlov *et al.*, 2004; Ho, 2011). Indeed, spectral fits with a blackbody or a model of hydrogen atmosphere give a size for the region emitting the thermal radiation of few kilometers. If the compact object is a neutron star, then the radiation is emitted by a hot spot at its surface. Thus, as the neutron star rotate, pulsations should be observed and these have never been detected in X-rays (Pavlov & Luna, 2009).

In 2009 Ho & Heinke fitted the spectrum of the compact object in Cassiopeia A supernova remnant with a model of non-magnetized atmosphere made of carbon. They obtained a size for the emitting region comparable to the typical radius of a neutron star, confirming that the central compact object is a neutron star. This study was the first determination of the composition of the atmosphere of an isolated neutron star.

In 2010, Heinke & Ho presented the results of the fit of five observations extended over nine years of the neutron star in Cassiopeia with Chandra and reported that the temperature has decreased by 4% : from 2.12×10^6 K in 2000 to 2.04×10^6 K in 2009. This work was the first direct observation of the cooling of an isolated neutron star and has opened an exciting window on the cooling of isolated neutron stars. In 2011, Shternin *et al.* (2011) reported a new determination of the surface temperature of the neutron star in Cassiopeia A supernova remnant and confirmed that the neutron star is cooling. Figure 3.10 shows the non-redshifted surface temperature of the neutron star as a function of the time of observation.

3.7.4 Future perspectives

The next generation of X-ray satellites are expected to provide more observations of cooling neutron stars, detecting fainter sources, with smaller error bars. Among them are :

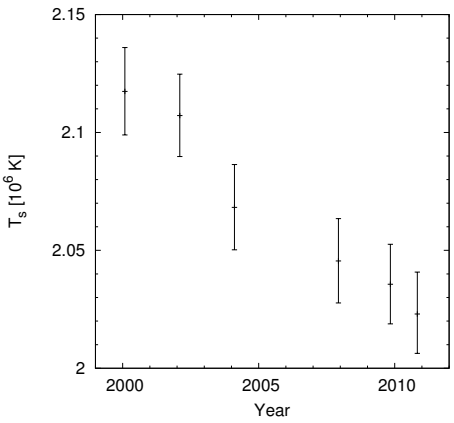

Figure 3.10: Surface temperature of Cassiopeia A neutron star as a function of the time of observation. 2σ error bars for the temperature. Between 2000 and 2011, the temperature decreased by a factor 4.5%. Data from Shternin *et al.* (2011).

- NuSTAR (USA) : an hard X-ray telescope whose launch is planned for March 12, 2012;
- ASTROSAT (India) with far UV, soft and hard X-ray telescopes, expected to be launched in 2012;
- ASTRO-H (Japan) with soft and hard X-ray telescopes, imagers and spectrometers, to be launched in 2014;
- GEMS (USA) : an X-ray telescope that will measure the polarization of emitted X-rays , expected for July 2014;
- LOFT (Europe), one of the four candidate medium-size missions on the ESA Cosmic Vision program. If selected, it will provide high-time-resolution X-ray observations of compact objects and be launched in 2022;
- ATHENA (Europe), one of the three candidate large-size missions on the ESA Cosmic Vision program. It is expected to perform high resolution X-ray imaging, timing and spectroscopy. If selected, it will also be launched in 2022.

The distance determination, which is one of the key parameter for the temperature measurements, will be more accurately calculated by parallax measurements with radio observations from VLBI or the future SKA. Better statistics on pulsars and supernova remnants age may also enable to estimate the error when using the spin-down age (Tsuruta, 2009).

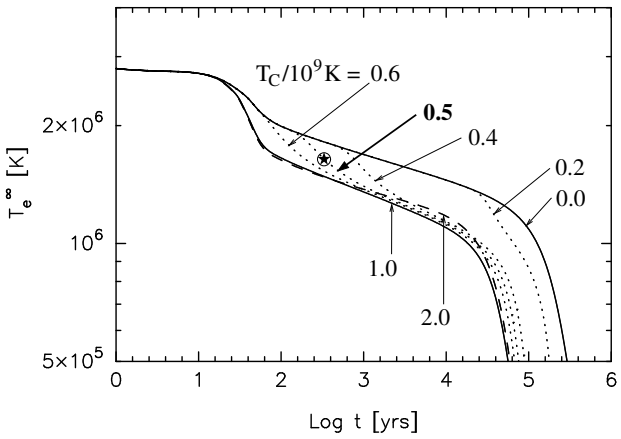

Figure 3.11: Cooling curves for various values of the maximum of the critical temperature $T_{\rm C}$ for neutron $^3P_2$ pairing. The model assumes a 1.4 $M_\odot$ neutron star with the APR equation of state and a model of carbon atmosphere consistent with the observations. Figure from Page *et al.* (2011).

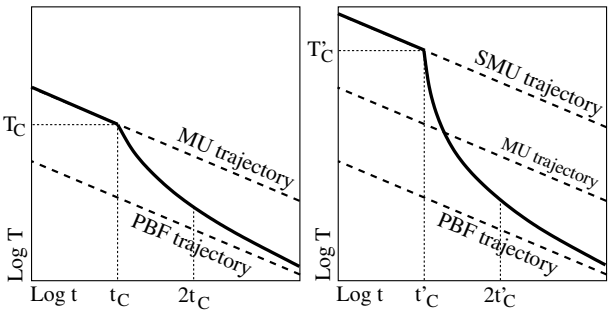

Figure 3.12: Schematic cooling curves without (left) and with (right) proton $^1S_0$ superfluidity. MU stands for MUrca and SMU for Suppressed MUrca process by the proton superfluidity. See text for details. Figure from Page *et al.* (2011).

3.8 Theoretical modeling versus observations

Finally, let us now confront the theoretical modeling with the observations presented in the previous section.

3.8.1 Modeling of the cooling of Cassiopeia A neutron star

Shternin *et al.* (2011) and Page *et al.* (2011) modeled the cooling of the neutron star in Cassiopeia A supernova remnant and independently reached similar conclusions :

- the cooling rate is too large to be triggered by the MUrca process alone;
- the temperature decrease of a neutron star undergoing DUrca process happens $\sim 30 - 100$ years after birth and is not consistent with the observations;
- the observed cooling is due to the recent onset of the neutron $^3P_2$ PBF process in the core. The maximum of the critical temperature $T_{\rm C} \simeq 5 \times 10^8$ K, as shown in the figure 3.11. The value reported by Shternin *et al.* (2011) is very close $T_{\rm C} \simeq (7 - 9) \times 10^8$ K ;
- the rapidity of the cooling of the neutron star originates from a strong proton superfluidity. Figure 3.12 schematically shows the cooling curves for different dominant neutrino processes. On the left panel, no proton superfluidity is included. The neutron star cools due to the emission of neutrinos from the MUrca process

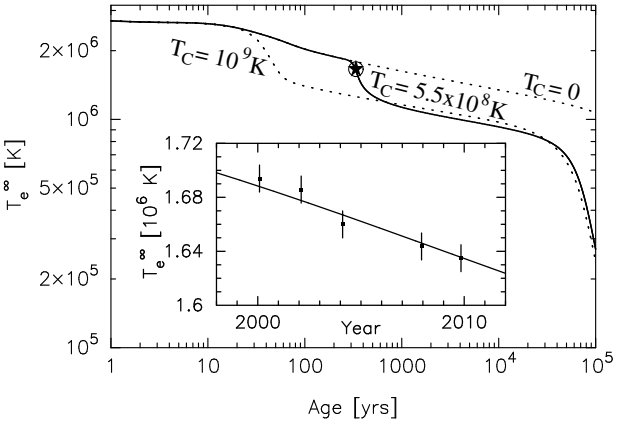

Figure 3.13: Cooling curve for a 1.4 $M_\odot$ neutron star with strong proton superfluidity in the core. Figure from Page *et al.* (2011).

until its temperature reaches T_C for the neutron $^3P_2$ pairing. The PBF process due to this superfluidity is then triggered and the neutron cools faster. On the right panel, proton superfluidity in the core strongly suppresses the MUrca process. Therefore the neutrino losses are smaller and the star is hotter. It then reaches the critical temperature for the neutron $^3P_2$ pairing and the PBF process is switched on. The slope of the cooling curve is larger when the protons are superfluid in the core. This is in agreement with the observations of the cooling of Cassiopeia A neutron star;

- these conclusions are unchanged for a large range of neutron star mass ($1.4 \lesssim M \lesssim 1.9\ M_\odot$);
- all in all, figure 3.13 shows a good fit of the observations of the cooling of the neutron star in Cassiopeia A supernova remnant.

Note that other studies simulated the cooling of the neutron star in Cassiopeia A supernova remnant. Among them Blaschke *et al.* (2011) argued that the observed cooling originates from the substantial reduction of the thermal conductivity due to medium effects.

3.8.2 Modeling of all the available data

Shternin *et al.* (2011) presented a very complete comparison between the theoretical modeling and all the available observations of isolated neutron stars. They considered a model of neutron star that is fully consistent with the observations of the Cassiopeia A neutron star. Note that this model allows for DUrca process when $M > 1.83\ M_\odot$ and has a maximum allowable mass of $1.93\ M_\odot$. Figure 3.14 shows sequences of cooling curves for neutron $^3P_2$ superfluidity with a critical temperature that has a maximum of $T_C \simeq 9 \times 10^8$ K at a density of $\rho \simeq 10^{15}$ g cm^{-3}. Low-mass neutron stars whose central

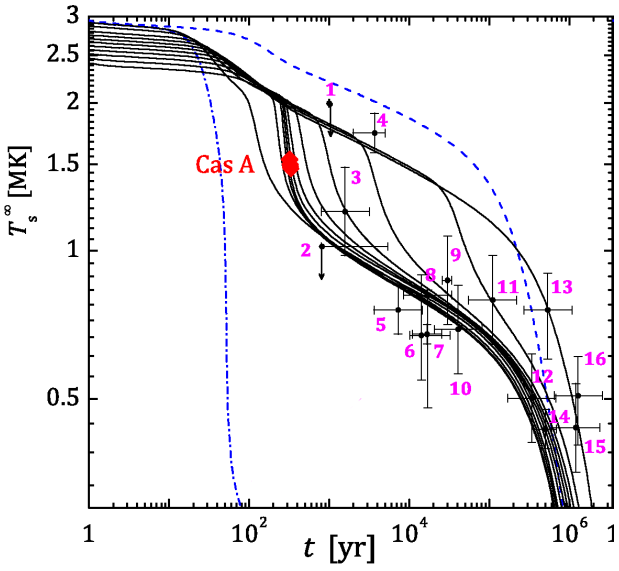

Figure 3.14: Sequences of cooling curves for neutron stars with a mass ranging from 1 $M_\odot$ to the maximum allowable mass for the APR equation of state, with strong proton superfluidity and neutron $^3P_2$ superfluidity in the core. See text for details. The dashed line is the cooling curve of the warmest possible neutron star with this model ($M = 1$ $M_\odot$ and a carbon atmosphere) and the dot-dashed for the coolest possible (maximum allowable mass and no proton superfluidity in the core). The sources are the same as in figure 3.9. Figure adapted from Shternin *et al.* (2011).

density is of the same order therefore have a moderate emissivity due to the PBF process and are therefore hotter than high-mass neutron stars. Therefore, this model enables to fit the observations of all the sources except the coolest and warmest ones.

However, on the one hand, the coolest ones can be fitted by models of high-mass neutron stars for which the DUrca process is allowed and thus not reduced by the proton superfluidity. This implies that the critical temperature of the proton superfluidity is low at the very center of massive neutron stars. On the other hand, the warmest neutron stars are consistent with low-mass ones with an atmosphere composed of light elements. As explained in section 3.3.4, a higher amount of light elements makes the redshifted effective temperature higher.

In conclusion, the modeling of the thermal evolution of isolated neutron star is a complex subject that requires the precise calculations of many properties of the interior neutron stars such the thermal conductivity, the specific heat, the neutrino emissivity or of their envelope. However, confronting the models with the observations of the cooling of the neutron star in Cassiopeia A supernova remnant has recently enabled to put constraints on the superfluid properties of the core of neutron stars. The new generation of X-ray satellites that may detect fainter sources and with better accuracy is expected to allow to further constrain the properties of dense matter.

Chapter 4

Cooling of young neutron stars

Contents

The thermal evolution of young and isolated neutron stars is driven by the properties of the matter in the crust. Therefore, their precise modeling is necessary to calculate the quickness of the crust thermalization as explained in section 4.1.

Jérôme Margueron (Institute of Nuclear Physics in Orsay, France) and I started studying the thermal evolution of young neutron stars in the fast cooling scenario, when DUrca process is triggered, during a six-months training period for my master of physics in 2008. We developed a simple cooling code with Wolfram Mathematica. Later in collaboration with Fabrizio Grill (Milan University, Italy at that time), Nicolae Sandulescu (National Institute of Physics and Nuclear Engineering, Bucharest, Romania), new calculations of the specific heat of the superfluid neutrons in the inner crust, taking into account the presence of the clusters were performed. They are detailed in section 4.2. Using the `NSCool` code developed by Dany Page (National Autonomous University of Mexico, Mexico) (section 3.2.3) I simulated the cooling of young neutron stars. The model and the results are reported in section 4.3. The results for the fast cooling scenario were published in the paper Fortin *et al.* (2010). Ultimately the model may be compared to observations of young neutron stars and may enable to understand the properties of the matter in the crust of neutron stars (section 4.4).

4.1 Thermal evolution in the early ages

As explained in section 3.4, after the neutron star interior becomes transparent to neutrinos, the core and crust cool independently during ~ 100 years. The core cools quickly by emission of neutrinos while the crust stays hot and acts like a heat-blanketing envelope. A cooling wave from the center propagates in the crust and when it reaches the surface, the effective temperature decreases, as shown on figure 3.5. One can distinguish two cooling scenarios :

- fast cooling (or enhanced cooling) due to the triggering of the very efficient DUrca process in the core of the star. The temperature drops by an order of magnitude when the cooling wave reaches the surface;
- slow cooling, if the core cools by the MUrca process. The effective temperature is then reduced by a factor ~ 2.

Brown *et al.* (1988) gave one of the first estimation of the cooling time $\tau_{\rm cool}$ that is the propagation time of the cooling wave in the crust in the case of fast cooling due to strangeness condensation in the core. Neglecting the relativistic effects and the neutrino losses in the crust, the heat equation (3.3) writes :

$$\frac{1}{r^2}\frac{\partial}{\partial r}\left[\kappa r^2 \frac{\partial T}{\partial r}\right] = C_{\rm V}\frac{\partial T}{\partial t}. \tag{4.1}$$

As a first approximation, considering that :

- the temperature T, C_V and κ are nearly constant in the crust;
- $\partial/\partial r \sim 1/l_{\rm crust}$ with $l_{\rm crust}$ the crust thickness;
- $\partial/\partial t \sim 1/\tau_{\rm cool}$,

one gets :

$$\tau_{\rm cool} \sim l^2_{\rm crust}\frac{C_{\rm V}}{\kappa}, \tag{4.2}$$

$$\sim \frac{l^2_{\rm crust}}{D_{\rm crust}} \tag{4.3}$$

with $D_{\rm crust} = \kappa/C_{\rm V}$ the thermal diffusivity in the crust. Brown *et al.* (1988) got $\tau_{\rm cool} \sim 10 - 100$ years.

Lattimer *et al.* (1994) studied the thermal evolution of young neutron stars in the fast cooling scenario with a more precise model. They showed in particular that the cooling time is insensitive to the properties of the core in particular to its neutrino emission, but depends strongly on the properties of the crust in particular its thickness.

Gnedin *et al.* (2001) used a realistic model for the thermal evolution, with a code similar to `NSCool` to study the influence of the superfluid effects in the inner crust on the cooling time. They concluded that superfluidity strongly fastens the cooling and thus reduces the cooling time.

In conclusion precise calculations of the specific heat in the inner crust of neutron stars are necessary to precisely determine the cooling time.

4.2 The specific heat in the crust

Let us detail the different calculations that are used in Fortin *et al.* (2010) for the specific heat in the crust.

4.2.1 The cluster structure of the inner crust

The structure of the inner crust was first calculated by Negele & Vautherin in 1973. The inner crust is assumed to be composed of non interacting and spherical Wigner-Seitz cells that form a periodic lattice. In each cell, a nuclear cluster is surrounded by a gas of free neutrons and relativistic electrons in equal number with the protons of the cluster. The energy minimization at β-equilibrium determines the proton and neutron fraction numbers and the size of the cells. Note that the effects of the pairing of the neutrons were not included (Hartree-Fock calculations). The properties of the cells are shown in table 4.1. In the following the pasta phases, at the interface between the inner-crust and the core, are neglected so an additional Wigner-Seitz cell calculated by Negele & Vautherin (1973) that may be in one of these phases is not included. The figure 4.1 shows the proton and neutron densities (in fm^{-3}) for a selected set of the Wigner-Seitz

cell	N	Z	$R_{\rm WS}$ [fm]	ρ [g cm^{-3}]	$\rho_{\rm n}^0$ [fm^{-3}]
10	140	40	54	4.7×10^{11}	7.4×10^{-5}
9	160	40	49	6.7×10^{11}	1.3×10^{-4}
8	210	40	46	1.0×10^{12}	2.8×10^{-4}
7	280	40	44	1.5×10^{12}	5.3×10^{-4}
6	460	40	42	2.7×10^{12}	1.15×10^{-3}
5	900	50	39	6.2×10^{12}	3.0×10^{-3}
4	1050	50	36	9.7×10^{12}	4.6×10^{-3}
3	1300	50	33	1.5×10^{13}	7.5×10^{-3}
2	1750	50	28	3.4×10^{13}	1.7×10^{-2}
1	1460	40	20	8.0×10^{13}	3.8×10^{-2}

Table 4.1: The properties of the Wigner-Seitz cells calculated by Negele & Vautherin (1973) i.e. the density ρ, the numbers of neutrons N and protons Z, the cells radius $R_{\rm WS}$ and $\rho_{\rm n}^0$ the number density of the neutron gas at zero temperature.

cells. It shows that at the center of each cell, the nucleus is surrounded by a uniform gas of unbound neutrons. With increasing density, the distance between the cells decreases and the density of the neutron gas increases.

4.2.2 Specific heat in the crust

The total specific heat (section 3.3.2) is the sum of the contributions from the different species in the crust, ie. :

- from the ultrarelativistic electrons that from a degenerate gas. Their specific heat is :

$$C_{\rm V}^{(e)} = \frac{k_{\rm B}(3\pi)^{2/3}}{3\hbar c}\left(\frac{Z}{V}\right)^{2/3} T, \tag{4.4}$$

  where $V = 4/3\pi R_{\rm WS}^3$ is the volume of the Wigner-Seitz cell and Z the number of the electrons in the cell which is equal to the number of protons;

- the lattice of nuclei. The calculations include the possible phase transition between the solid and the liquid phase and are based on the works by Slattery *et al.* (1982); Baiko *et al.* (2001); Potekhin & Chabrier (2010); Carr (1961);

- the free neutrons in the inner crust that are believed to be superfluid in the $^1S_0$ channel. The calculations of their specific heat are detailed in the following.

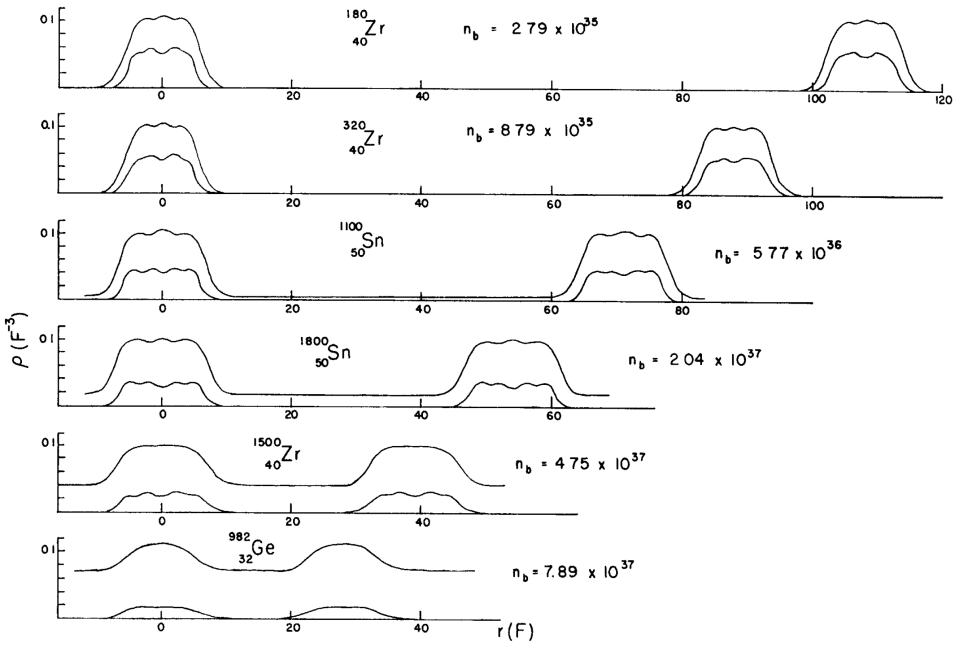

Figure 4.1: Proton (lower solid line) and neutron (upper solid line) densities (in fm^{-3}) as a function of the radius (in fm) for Wigner-Seitz cells 10, 7, 4, 2 and 1. The lower plot corresponds to the cell in the pasta phases that we do not consider here. Two nuclei are plotted in each cell. From Negele & Vautherin (1973).

4.2.3 Specific heat of the superfluid neutrons

4.2.3.1 Skyrme nuclear interaction and HFB calculations

The modeling of the nuclear interaction inside the nuclei is an unsolved and complex problem (Berger, 2009; Gulminelli, 2011). Several models for the effective nucleon-nucleon interactions have been developed. Their parameters are fixed by fitting experimental data. One can distinguish two types of effective interactions :

- the Gogny interaction that has a finite range and therefore enables to model long range interactions and pairing properties but it is complicated to use in many-body calculations;
- the Skyrme interaction that has a zero range ie. it uses a local contact force between two nucleons that is proportional to $\delta(r)$ with δ the Kronecker symbol and r the distance between the two nucleons. Its simple form makes it easy to use.

Several parameterizations for the latter have been proposed. In the following, the SLy4 (Skyrme Lyon) effective nucleon-nucleon interaction is used whose parameters have been determined to reproduce experimental constraints from neutron rich nuclei (Chabanat *et al.*, 1997). It is therefore suitable for the description of the properties of neutron star matter.

For a given nuclear interaction, the many-body problem has then to be solved. Ab initio calculations that solve exactly the Schrödinger equation exist but they are not applicable for nuclei with $A \geq 16$. The nuclear shell model that is an analog of the atomic shell model does not enable to describe the very neutron-rich nuclei that are present in the crust of a neutron star. Therefore, mean field theories were developed. The central idea is to decompose the Hamiltonian H into two parts, one corresponding to the dynamics of independent nucleons in a common nuclear potential and the other one that is called the residual interaction. The latter includes the effects of the pairing correlations, of the collective oscillations of the mean field, ... Berger (2009). The Schrödinger equation can be then be solved by different methods. Among them are Hartree-Fock (HF) calculations enables to solve the Schrödinger equations for interacting particles and the Hartree-Fock-Bogoliubov (HFB) approach that is an extension of the first one and that includes the pairing correlations and thus describes the properties of superfluid particles.

4.2.3.2 Pairing models

Since the strength of the pairing force is still unknown, two models for the pairing force of the superfluid neutrons that correspond to two pairing scenarios are used :

- strong pairing that corresponds to BCS calculations;
- weak pairing that goes beyond BCS calculations including in-medium effects, with a gap that is $\sim$ a third of the BCS gap.

These two pairing models correspond to two limiting cases and the real pairing gap is expected to be in between them.

4.2.4 Influence of the clusters on the critical temperature

The inner crust is a non-uniform system as shown on figure 4.1, where the density is very different in the center of the nuclear clusters and in the transition zone between two clusters. In particular, in the framework of HFB approach at zero temperature or at finite temperature, the presence of the nuclear clusters was shown to have an influence on the neutron pairing gap and specific heat (Sandulescu *et al.*, 2004; Sandulescu, 2004). Extending the study of Sandulescu (2004) to the low-density region in the inner crust for a temperature of 0.1 MeV[1], Monrozeau *et al.* (2007) estimated the impact of the clusters on the cooling time of the crust with a simple model of heat transport.

In Fortin *et al.* (2010) are reported new calculations of the critical temperature and specific heat of the superfluid neutrons in the framework of HFB calculations at finite temperature in the Negele & Vautherin cells. Figure 4.2 shows the variation of the critical temperature for the weak and strong pairing including or not (NC) the effects of the

[1]The megaelectron volt, MeV, is a unit of energy that is commonly used by nuclear physicists : 1 MeV $\simeq 1.16 \times 10^{10}$ K.

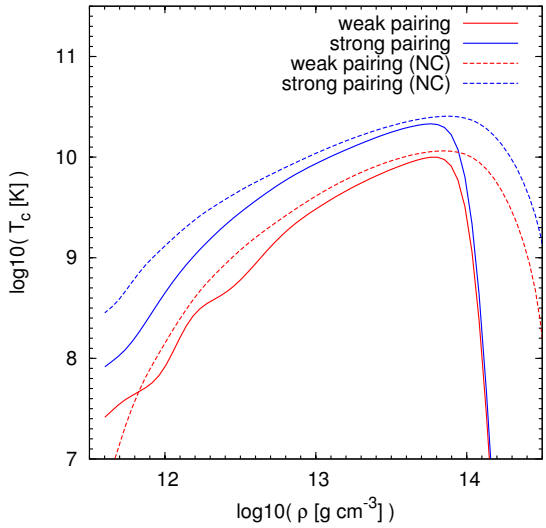

Figure 4.2: Critical temperatures for the weak (red) and strong (blue) pairings. The NC curves (dashed lines) correspond to calculations where the effects of the clusters were not taken into account.

clusters, after the interpolation of the results obtained in the different cells. The critical temperature is higher for the strong pairing than for the weak pairing since the former corresponds to BCS calculations that do not include the effects of the clusters. Except at low densities, taking into account the presence of the nuclear clusters in the calculations reduces the critical temperature.

4.2.5 Neutron specific heat in uniform matter

Levenfish & Yakovlev (1994) calculated the specific heat of superfluid neutrons in uniform neutron matter and derived an approximate formula for the reduction factor $R_{\rm c}$ that enters the equation (see also section 3.5.1.4) :

$$C_{\rm V}^{\rm pair}(T) = R_{\rm c}(T/T_{\rm c}) \times C_{\rm V}^{\rm norm}(T) \tag{4.5}$$

with $C_{\rm V}^{\rm pair}$ and $C_{\rm V}^{\rm norm}$ the specific heat of the superfluid and normal baryons, respectively.

They obtained for $T \geq T_{\rm c}$:

$$R_{\rm c}^{\rm YL}(u) = \left[0.4186 + \sqrt{1.007^2 + (0.501u)^2}\right]^{5/2} \times {\rm e}^{1.456-\sqrt{1.456^2+u^2}}, \tag{4.6}$$

$$u(x) = \sqrt{1-x}\left[1.456 - \frac{0.157}{\sqrt{x}} + \frac{1.764}{x}\right], \tag{4.7}$$

$$x = T/T_{\rm c}. \tag{4.8}$$

and for $T < T_{\rm c}$, $R_{\rm c}^{\rm YL}(u) = 1$.

In the following, the NC curves correspond to calculations for uniform matter, ie. using the prescription for the reduction factor from Levenfish & Yakovlev (1994) and the critical temperatures presented in the previous section when the effects of the clusters are not included.

4.2.6 Neutron specific heat in non-uniform matter

4.2.6.1 Results

Figures 4.3 and 4.4 show the variation of the specific heat of the free neutrons with the temperature. They have been calculated in the different Wigner-Seitz cells defined in table 4.1 in non-uniform matter, ie. when the effects of the clusters are included. The values are very different for the two pairing scenarios and the temperature dependence of the cells also varies. For strong pairing, at low density, the specific heat exhibits a transition from the superfluid to the normal phases in the cells 6-8 (it is not visible for the cells 9 and 10 though it is present). However at high density, in the cells 1-5, the specific heat is in the superfluid regime. For the weak pairing, only in the first two cells, the neutron specific heat is typical of superfluid matter. Moreover for the first cell, the transition from the quantum to the classical regime is visible at $T \simeq 0.22$ MeV. Note finally that for the cells 1-5 the specific heat increases when the density decreases. The behavior is the opposite for the cells 6-10.

4.2.6.2 Parametrization

In order to implement these new calculations for the specific heat of the superfluid neutrons in the `NSCool` code, a parametrization in terms of the temperature and density of the neutron specific heat obtained in the different cells has been derived. The transition from the quantum to the classical regimes and from the superfluid to the normal phases are taken into account.

Quantum regime

The specific heat of the non-superfluid neutrons in the quantum regime at low temperature is :

$$C_{\rm V}^{\rm q}(T,\rho_{\rm n},N,R_{WS}) = \frac{1}{6}\left(\frac{2m_{\rm n}^*}{\hbar^2}\right)^{3/2}\varepsilon_{\rm F}^{1/2}T\times\left[1-\frac{7}{40}\left(\frac{\pi T}{\varepsilon_{\rm F}}\right)^2-\frac{155}{896}\left(\frac{\pi T}{\varepsilon_{\rm F}}\right)^4\right], \qquad (4.9)$$

where $\rho_{\rm n}^0$ is the number density of the neutron gas at zero temperature given in table 4.1, $m_{\rm n}^*$ the neutron effective mass and $\varepsilon_{\rm F} = \hbar^2 k_{\rm F}^2/2m_{\rm n}^*$ the Fermi energy at zero temperature with $k_{\rm F}(\rho_{\rm n})$ the Fermi momentum. This expression is valid for $\varepsilon_{\rm F} < T$.

The effective mass $m_{\rm n}^*$ of a neutron takes into account the effects of the medium on the neutron : the more local is an interaction, the bigger is the effective mass. In the present calculations, it depends on the density according to the Skyrme SLy4 nuclear interaction.

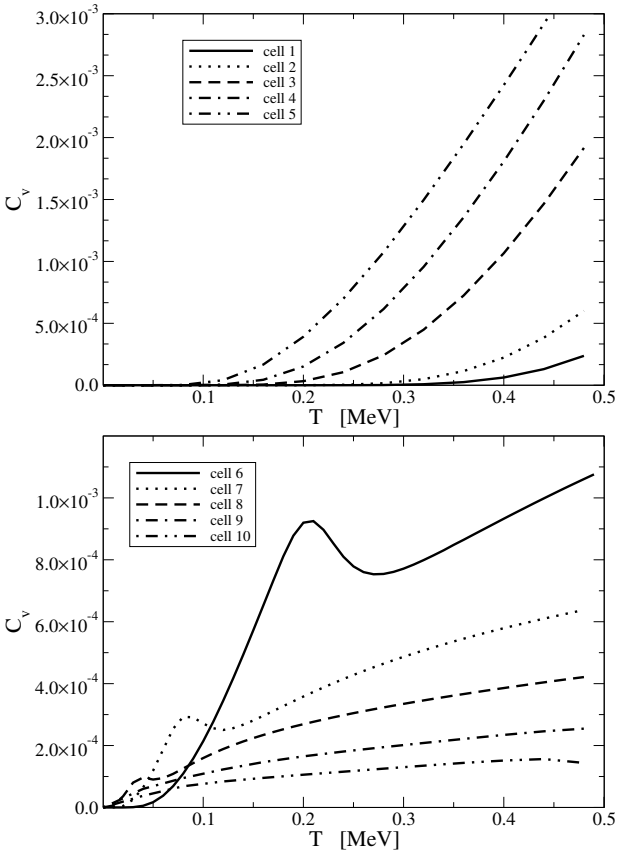

Figure 4.3: Neutron specific heats in various Wigner-Seitz cells for strong pairing. The effects of the clusters are included. The specific heat is given in units of the Boltzmann constant $k_{\rm B}$.

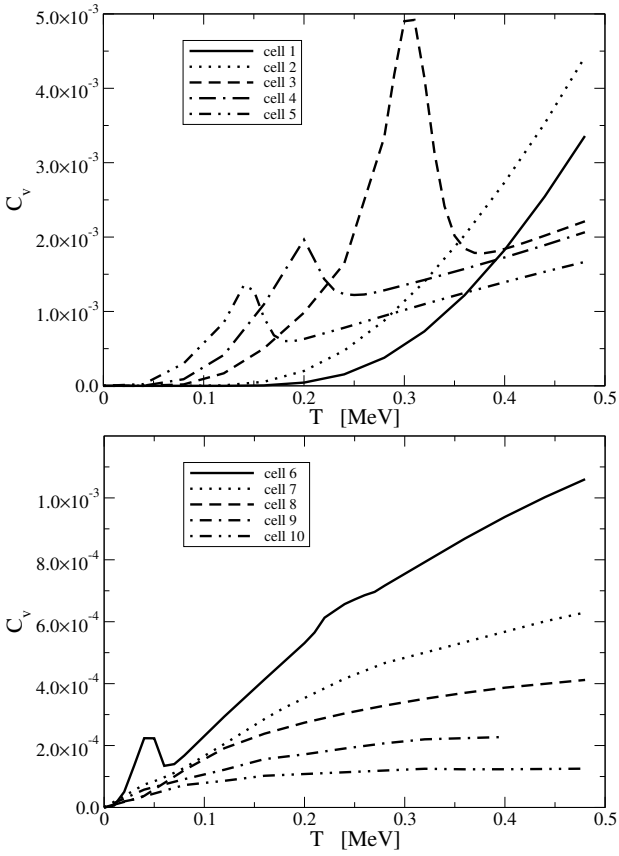

Figure 4.4: Neutron specific heats in various Wigner-Seitz cells for weak pairing. The effects of the clusters are included. The specific heat is given in units of the Boltzmann constant $k_{\rm B}$.

Superfluid phase

The reduction factor describes the reduction of the specific heat due to the superfluidity. It is parametrized by the following form :

$$R_{\rm c} = R_{\rm c}^{\rm YL}(u) f_1(T, \Delta_0, a_0, a_1, a_3)\,(1 - f_2(T, \Delta_0, a_0, a_2, a_3))\,, \tag{4.10}$$

with $R_{\rm c}^{\rm YL}$ the reduction factor derived by Levenfish & Yakovlev (1994) (see equation (4.8)) and the f_1 and f_2 functions given by :

$$f_1(T, \Delta_0, a_0, a_1, a_3) = \frac{\left(1 + e^{-a_1 a_0 \Delta_0/a_3}\right)}{\left(1 + e^{(T - a_1 a_0 \Delta_0)/a_3}\right)}, \tag{4.11}$$

$$f_2(T, \Delta_0, a_0, a_2, a_3) = \frac{\left(1 + e^{-a_2 a_0 \Delta_0/a_3}\right)}{\left(1 + e^{(T - a_2 a_0 \Delta_0)/a_3}\right)}. \tag{4.12}$$

	Weak					Strong				
cell	a_0	a_1	a_2	a_3	Δ_0 [MeV]	a_0	a_1	a_2	a_3	Δ_0 [MeV]
10	0.567	1.0	1.0	0.001	0.00	0.5	1.0	1.0	0.005	0.02
9	0.567	1.0	1.0	0.001	0.01	0.5	1.0	1.0	0.005	0.03
8	0.567	1.0	1.0	0.001	0.01	0.5	1.0	1.0	0.005	0.08
7	0.567	1.1	1.1	0.001	0.05	0.567	1.0	1.0	0.015	0.15
6	0.4	1.4	1.4	0.001	0.09	0.567	1.1	1.1	0.025	0.36
5	0.567	0.9	0.78	0.005	0.30	0.60	1.0	1.0	0.025	0.87
4	0.567	0.83	0.75	0.01	0.45	0.62	1.0	1.0	0.025	1.18
3	0.567	0.84	0.7	0.01	0.69	0.567	0.97	0.91	0.02	1.75
2	0.567	0.89	0.8	0.01	1.24	0.53	0.93	0.86	0.015	3.10
1	0.567	0.84	0.72	0.01	1.86	0.54	0.935	0.88	0.015	3.95

Table 4.2: The parameters (a_0, a_1, a_2, a_3) which define the fitting functions employed in equation (4.10) for the weak and strong pairings. In the last column are given also the neutron pairing gaps in the gas region at zero temperature.

Δ_0 is the pairing energy gap in the neutron gas at T=0 and the critical temperature is given by the equation $T_C = a_0\Delta_0$.

The parameters (a_0, a_1, a_2, a_3) are adjusted to reproduce the specific heat of neutrons determined in the framework of HFB approach at finite temperature. Their values together with the ones of Δ_0 are given in table 4.2 for the weak and strong pairing scenarios.

Classical regime

The classical regime is reached when $T \gg \varepsilon_{\rm F}$ and the specific heat is given by :

$$C_{\rm V}^{\rm cl}(T, \rho_{\rm n}, N, R_{\rm WS}) = \frac{3}{2}\rho_{\rm gas}(T, \rho_{\rm n}, N, R_{\rm WS}), \tag{4.13}$$

where $\rho_{\rm gas}$ is the number density of the neutron gas, ie. in the outer region of the cell at the temperature T. When increasing the temperature, the thermal excitations enable the neutrons to drip from the cluster to the gas. Therefore, the neutron gas number density varies with the temperature and is given by the formulas :

- for $T \leq T_{\rm gas} = 5.5$ MeV,

$$\rho_{\rm gas}(T, \rho_{\rm n}, N, R_{\rm WS}) = \rho_{\rm n}(T=0) + \frac{T}{T_{\rm gas}}\left(\rho_{\rm max}(N, R_{\rm WS}) - \rho_n(T=0)\right), \tag{4.14}$$

- for $T > T_{\rm gas}$,

$$\rho_{\rm gas}(T, \rho_{\rm n}, N, R_{\rm WS}) = \rho_{\rm max}(N, R_{\rm WS}), \tag{4.15}$$

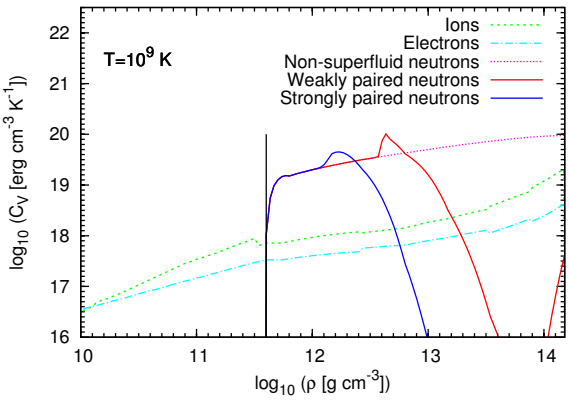

Figure 4.5: The different contributions to the total specific heat for a temperature $T = 10^9$ K in the crust. Results for different models of free neutrons when the effects of the clusters on the superfluid properties are plotted. The vertical line indicates the transition between the inner and the outer crusts.

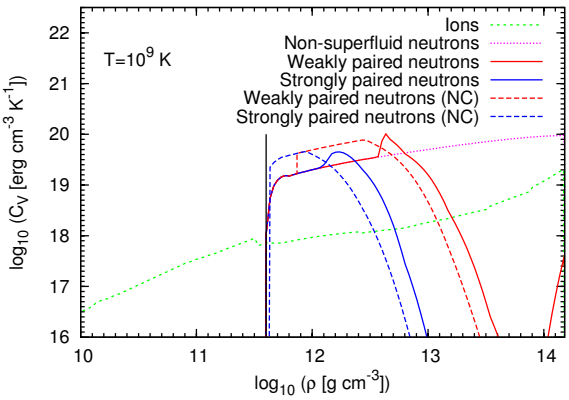

Figure 4.6: Specific heat for the five models of free neutrons for a temperature $T = 10^9$ K. For comparison, the contribution from the ions which dominates if the neutrons are paired is plotted.

Transition from the quantum to the classical regime

We describe the transition from the quantum to the classical regime by the following function :

$$x_{\rm cl} = \left(1 + e^{5(\frac{\pi T}{\varepsilon_F} - 1)}\right)^{-1}. \tag{4.16}$$

Specific heat of the free neutrons in the inner crust

Finally, the specific heat of the free neutrons in the inner crust $C_{\rm V}^{\rm n}$ is :

$$C_{\rm V}^{\rm n} = x_{\rm cl} R C_{\rm V}^{\rm q} + (1 - x_{\rm cl}) C_{\rm V}^{\rm cl}. \tag{4.17}$$

4.2.7 Total specific heat in the crust

Figure 4.5 shows the different contributions to the total specific heat for a temperature $T = 10^9$ K. In the outer crust, the specific heat of the ions dominates the one of the electrons. In the inner crust, the main contribution comes from the free neutrons if they are non-superfluid. Otherwise, in the denser parts of the crust, their contribution is so reduced because of the pairing that the contribution of the ions dominates again. Note that the reduction extends for a larger range of density for strong pairing than for the weak one.

In figure 4.6 are plotted the specific heat of the free neutrons for the different prescriptions used in the following, for $T = 10^9$ K. Note that the inclusion of the effects

of the clusters strongly affects the specific heat of the superfluid neutrons : the transition to superfluid occurs at higher density when they are included in the calculations. Therefore, one expects the thermal evolution of a young isolated neutron star to be also influenced.

4.3 Cooling simulations

4.3.1 Neutron star model

In this study, the following equations of state are used :

- for the core : the model by Douchin & Haensel (2001), (hereafter called DH) based on the SLy4 nuclear interaction (Chabanat *et al.*, 1997) for a $npe\mu$ composition;
- for the inner-crust : the calculations by Negele & Vautherin (1973) which are not based a Skyrme interaction.

The maximum mass is 2.034 $M_\odot$ and the DUrca process is opened for $M \geq 2.024\,M_\odot$.

The cooling calculations are performed for a 1.6 $M_\odot$ neutron star. Its properties are obtained by solving the TOV equations (2.12) and are :

- the total radius $R = 11.49$ km;
- the central density $\rho_c = 4.06\,\rho_0$;
- the inner crust (for $\rho_{ND} \leq \rho < \rho_0/2$) extends from the core radius $R_C = 10.72$ km to 11.19 km and has thus a thickness of 0.47 km.

4.3.2 Microphysics input

Superfluidity

In addition to the ${}^1S_0$ pairing of the neutrons in the crust described in the previous section, the superfluid properties in the core are also taken into account :

- for neutron ${}^3P_2$ pairing, the gap by Takatsuka (1973) with a maximum critical temperature $T_{cn} \sim 3 \times 10^9$ K is used;
- for proton ${}^1S_0$ pairing, the gap "a" from Page *et al.* (2004) with $T_{cp} \sim 10^9$ K is employed.

Specific heat

As shown on figure 4.7, the contributions from the superfluid neutrons and protons and from the electrons to the core specific heat are included in the calculations. They are calculated from the formula (4.10) with the reduction factor R_c calculated in uniform matter (Levenfish & Yakovlev, 1994).

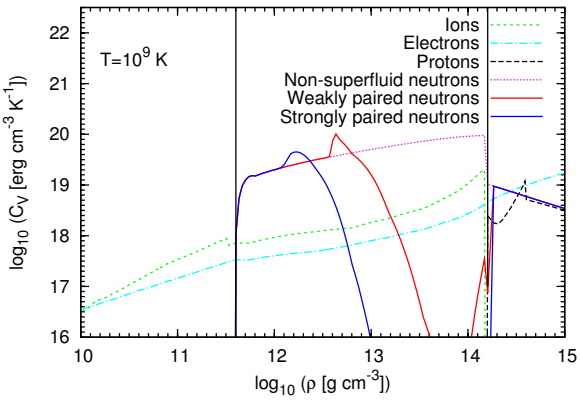

Figure 4.7: The different contributions to the total specific heat in the whole neutron star. From left to right, the vertical lines indicate the transitions from the outer crust to the inner crust and from the crust to the core.

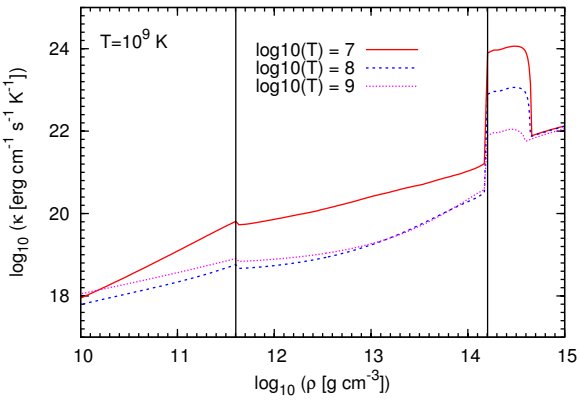

Figure 4.8: Variation of the total thermal conductivity with the density for the temperatures $T = 10^7, 10^8, 10^9$ K.

Thermal conductivity

In the crust, only the contribution of electrons to the thermal conductivity is included, with the electron-ion scattering from the reference Gnedin *et al.* (2001) and the electron-electron scattering from Shternin & Yakovlev (2006). The contribution from the electron-impurity scattering is neglected owing to its uncertainty.

In the core, the contribution from the leptons (electrons and muons) that dominates and is very sensitive to the proton superfluidity is taken from the reference Shternin & Yakovlev (2007). The contribution from the nucleons (neutrons and protons) is also included following Baiko *et al.* (2001).

The variation of the total thermal conductivity with the density is plotted in figure 4.8, for three different temperatures $T = 10^7, 10^8, 10^9$ K.

Neutrino emissivity

Figure 4.9 shows the different contributions to the total neutrino emissivity. In the core the MUrca and the bremsstrahlung processes are included. In the fast cooling scenario, the DUrca process is artificially switched on for densities $\rho \geq 5 \times 10^{14}$ g cm^{-3}. In the crust, the plasmon decay and the electron-ion, electron-electron and neutron-neutron bremsstrahlung processes are taken into account. The suppression of the neutrino emission due to the superfluidity and the PBF processes (see section 3.5.1.4) are included following Leinson & Pérez (2006b).

Envelope

The relation between the surface temperature and the temperature T_b at the density

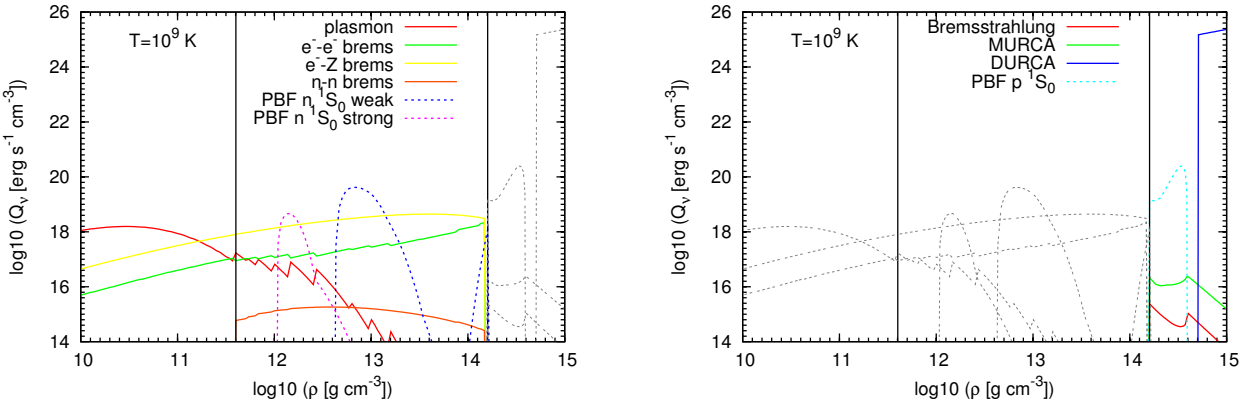

Figure 4.9: The different contributions to the total neutrino emissivity as a function of the density in the crust (left) and in the core (right) for a temperature $T = 10^9$ K.

$\rho_\mathrm{b} = 10^{10}$ g cm^{-3} is provided by the model for a nonaccreted envelope presented in the reference Potekhin *et al.* (1997).

4.3.3 Fast cooling scenario

4.3.3.1 Thermal evolution

The heat equation (3.3) is solved with the `NSCool` code for an initial constant temperature $T(r, t = 0) = T_\mathrm{i}$ with the model described previously.

In order to study the thermalization of the crust in the fast cooling scenario, the DUrca process is artificially triggered for densities $\rho \geq 5 \times 10^{14}$ g cm^{-3}.

The evolution of the effective temperature of 1.6 $\mathrm{M}_\odot$ neutron star is shown in figure 4.10, for an initial temperature $T_\mathrm{i} = 5 \times 10^9$ K. The results are similar for $T_\mathrm{i} = 3 \times 10^9$ K.

First one can notice that the evolution of the effective temperature is nearly independent of the initial temperature. As expected, since the specific heat is reduced when nucleons are paired and thus the temperature decreases faster, the superfluidity fastens the cooling. Including the clusters in the calculations has a non-trivial influence on the cooling. While there are almost no effects for the model of strong pairing, the neutron star cools faster for weak pairing.

The evolution of the redshifted temperature profiles in the crust of a 1.6 $\mathrm{M}_\odot$ neutron star for an initial temperature $T_\mathrm{i} = 5 \times 10^9$ K and for the three pairing models is displayed in the right plot of figure 4.11.

During the first year, the heat transport does not play a significant role and the thermal evolution is driven by the equation :

$$C_\mathrm{V} \frac{\partial T}{\partial t} = -Q_\nu \mathrm{e}^{\phi}. \tag{4.18}$$

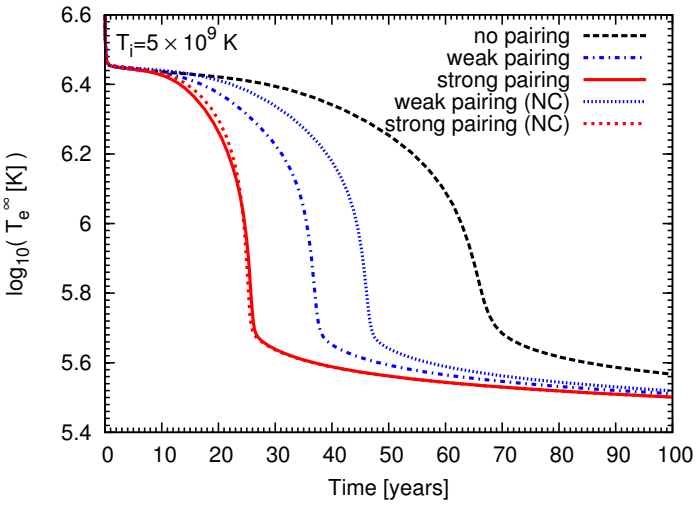

Figure 4.10: Evolution of the effective temperature of a 1.6 $M_\odot$ neutron star for the initial temperature $T_\mathrm{i} = 5 \times 10^9$ K in the fast cooling scenario. NC indicates that the effects of the clusters are not taken into account.

Therefore, $\partial T/\partial t \propto Q_\nu/C_\mathrm{V}$. The superfluidity does not affect much the neutrino emissivity in the crust since only the neutron-neutron bremsstrahlung is affected. However, the neutron specific heat is significantly reduced when the neutrons are paired in the crust. In this case, the main contribution to the specific heat is provided by the ions and the electrons but the total specific heat is smaller. Therefore, the cooling is much faster when the neutrons are paired, as can be seen in figure 4.11 for the first 0.1 years. Afterwards, the heat transport smoothes the temperature profiles and they are similar for the three pairing scenarios.

After one year, the heat transport plays an important role and the thermal evolution is driven by the equation :

$$\frac{\partial}{\partial r}\left[\sqrt{1-2Gm/c^2r}\kappa r^2 \mathrm{e}^{\phi}\frac{\partial}{\partial r}\left(T\mathrm{e}^{\phi}\right)\right] = \frac{r^2\mathrm{e}^{\phi}}{\sqrt{1-2Gm/c^2r}}C_\mathrm{V}\frac{\partial T}{\partial t} \tag{4.19}$$

Therefore, $\partial T/\partial t \propto \kappa/C_\mathrm{V}$. As a consequence, the strength of the pairing plays an important role in the thermal evolution. The cooling is faster when the pairing is stronger since the total specific heat is more reduced in agreement with Gnedin *et al.* (2001).

4.3.3.2 Cooling time

Let us now estimate the cooling time t_w. Following Lattimer *et al.* (1994), it is defined at the time when the cooling curve has the most negative slope. Figure 4.12 plots the cooling time as a function of the mass of the neutron star. For the fast cooling scenario (lower points), the cooling time decreases with the mass. In fact a more massive neutron

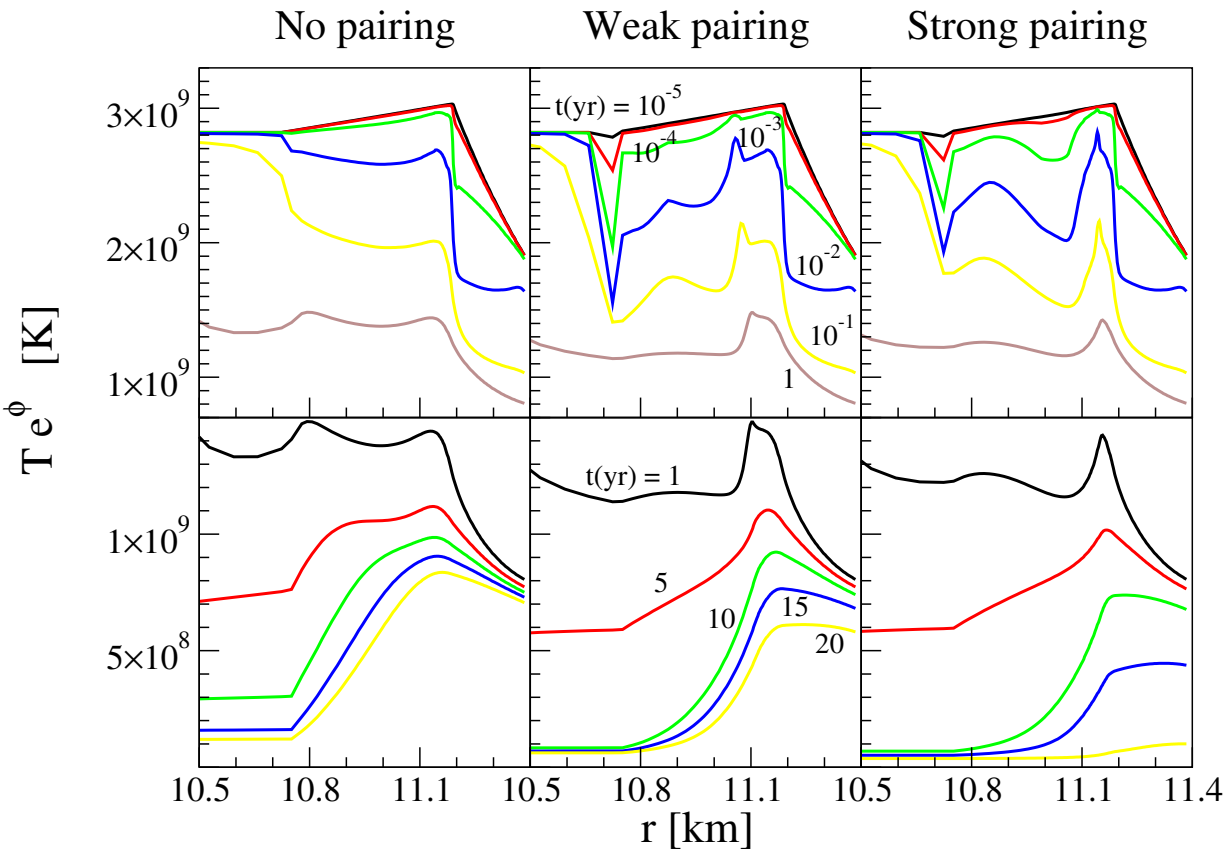

Figure 4.11: Time evolution of the redshifted temperature profiles in the crust of a 1.6 $M_\odot$ neutron star for an initial temperature $T_i = 5 \times 10^9$ K, for the three pairing models, in the fast cooling scenario. An isothermal interior correspond to a constant $e^\phi T$.

star has a thinner crust and it takes less time to the cooling wave to propagate from the core to the surface. The cooling is faster when the pairing correlations are stronger.

Lattimer *et al.* (1994) and Gnedin *et al.* (2001) noticed that t_w scales with the parameter

$$\alpha = \left(\frac{l_{\rm crust}}{1{\rm km}}\right)^2 \left(1 - \frac{2GM}{c^2 R}\right)^{-3/2} \tag{4.20}$$

that depends only on the global properties of the neutron star (mass, radius and thickness of the crust). One can also define the normalized time t_1 that depends solely on the microscopic properties of the crust :

$$t_w = \alpha t_1. \tag{4.21}$$

This scaling relation can be easily understood in the framework of the so-called independent layers model. It is based on two assumptions :

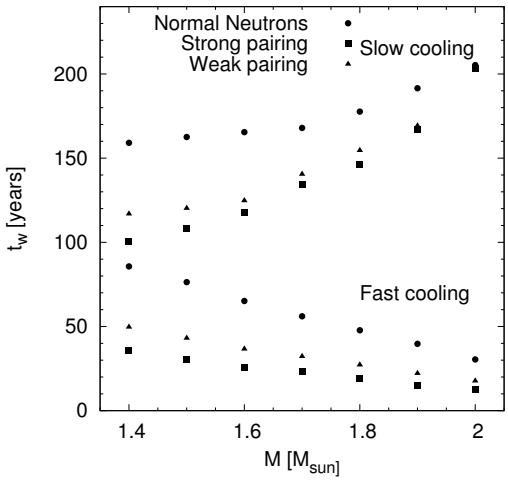

Figure 4.12: Cooling time $t_{\rm w}$ as a function of the mass of the neutron star in the fast (lower part) and slow (upper part) cooling scenarios for $T_{\rm i} = 5 \times 10^9$ K.

- since the thickness of the crust is small compared to the radius of a neutron star, one can approximate the spherical geometry by a planar one. Thus, the model consists in studying the heat diffusion through a one-dimensional crust;
- the crust is divided into N layers of thickness l_i. In each of these layers i, the density, the thermal conductivity κ^i and the specific heat $C_{\rm V}^i$ are considered to be constant.

In each layer, one considers that

$$\frac{\partial}{\partial x} \sim \frac{1}{l_i}, \tag{4.22}$$

$$\frac{\partial}{\partial t} \sim \frac{1}{\tau_i}, \tag{4.23}$$

$$\tag{4.24}$$

with τ_i the cooling time scale of the layer i.

Let us define the function

$$\Gamma(r) = \left(1 - \frac{2Gm(r)}{rc^2}\right)^{-1/2} \tag{4.25}$$

that enters equation the relativistic heat equation (3.3).

As a first approximation, in the crust,

$$\phi(r) \sim \phi(R) \tag{4.26}$$

and thus

$$\mathrm{e}^{-\phi(r)} \sim \Gamma(R). \tag{4.27}$$

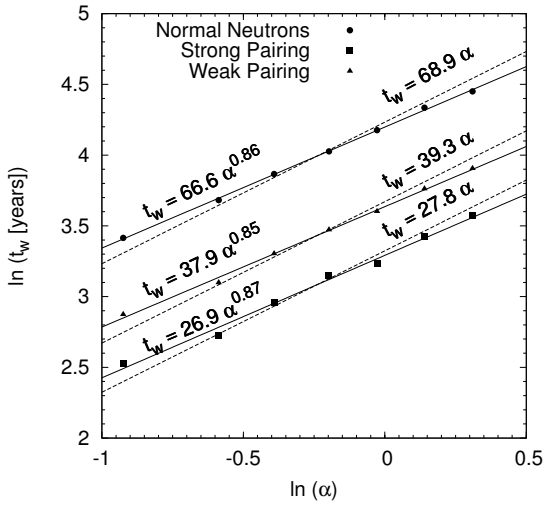

Figure 4.13: Cooling times $t_{\rm w}$ as a function of the parameter α defined in equation (4.20) for neutron star masses between 1.4 and 2.0 $M_\odot$ and $T_{\rm i} = 5 \times 10^9$ K in the fast cooling scenario. Fits with a linear scale (dashed line) and for a fractional power of α (solid line) were obtained.

Neglecting the neutrino losses in the crust, a dimensional analysis of equation (3.3) gives

$$\tau_i = \frac{\Gamma^3(R) C_{\rm V}^i l_i^2}{\kappa^i}. \tag{4.28}$$

The total cooling time scale $\tau_{\rm th}$ of a crust divided into N layers is defined by :

$$\tau_{\rm th} = \left[\sum_i^N \sqrt{\tau_i} \right]^2 . \tag{4.29}$$

The definition makes the cooling time scale independent of the number of shells in the crust contrary the mere sum of the τ_i.

Therefore, since $\sum_i^N l_i = l_{\rm crust}$, one gets

$$\begin{aligned} \tau_{\rm th} &\propto l_{\rm crust}^2 \Gamma^3(R), & (4.30)\\ &\propto l_{\rm crust}^2 (1 - 2Gm/c^2R)^{-3/2}, & (4.31)\\ &\propto \alpha. & (4.32) \end{aligned}$$

This scaling relation was checked for the three pairing scenarios : unpaired neutrons, weak and strong pairing, for neutron stars masses ranging from 1.4 to 2 $M_\odot$ and for an initial temperature $T_{\rm i} = 5 \times 10^9$ K, as shown on figure 4.13. Two fits of the cooling times $t_{\rm w}$ were derived : a linear fit and a better fit with a fractional power of α. The derived normalized times are displayed in table 4.3.

In table 4.4 are given the values of the cooling time t_w and the normalized time t_1 obtained for a $1.5\ M_\odot$ neutron star ($\alpha = 1.15$). The normalized times t_1 values are 2 to 3

Model of neutron superfluidity	t_1 (yr)
No pairing	68.9
Weak pairing	39.3
Strong pairing	22.3

Table 4.3: Normalized times t_1 for the three pairing scenarios for the neutrons in the inner crust, for the fast cooling scenario.

Model of neutron superfluidity	t_w (yr)	t_1 (yr)	$t_1^{\rm Gnedin}$ (yr)
No superfluidity	76.3	66.4	28.8
Weak pairing	43.1	37.4	12.2
Strong pairing	30.6	26.6	5.9

Table 4.4: Cooling times t_w and normalized times t_1 for a 1.5 $M_\odot$ neutron star and for three models for the neutron superfluidity in the inner crust in the fast cooling scenario. For comparison are indicated the normalized times $t_1^{\rm Gnedin}$ obtained by Gnedin *et al.* (2001).

times larger than the ones obtained by Gnedin *et al.* (2001). These differences could be explained by the effects of the nuclear clusters on the neutron specific heat, disregarded in Gnedin *et al.* (2001), and by different neutrino processes and thermal conductivities in the core matter used in the two calculations.

In a nutshell, the crust thermalization is strongly influenced by the pairing scenario and by the cluster structure of the inner crust. These results were published in the paper Fortin *et al.* (2010).

4.3.4 Slow cooling scenario

4.3.4.1 Thermal evolution

Let us now consider the thermal evolution of a neutron star in the slow cooling scenario, when the very efficient DUrca neutrino process is not triggered.

In this case, the cooling is expected to be slower since the neutrino losses are smaller than for the fast cooling scenario. This is visible when comparing figure 4.14 for the slow cooling with figure 4.10 for the fast one. The results are more sensitive to the initial temperature and contrary to the previous scenario, the inclusion of the clusters slows down the thermal evolution. The results for the different models of neutron pairing are much closer for the slow cooling.

Figure 4.15 compares the evolution of the temperature profile in an entire 1.6 $M_\odot$ neutron star with non-superfluid neutrons for the two cooling scenario. In the fast cooling scenario, the triggering of the DUrca makes the neutrino emissivity so high that the core is cooler than the crust. On the contrary, when considering slow cooling, figure 4.9 shows that neutrino emissivity is higher in the crust than in the core. Therefore, the

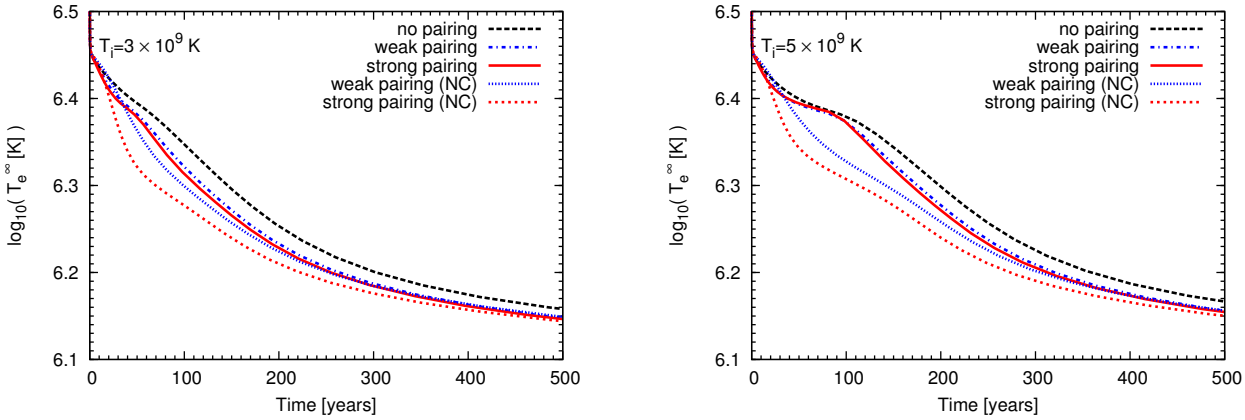

Figure 4.14: Evolution of the effective temperature of a 1.6 $M_\odot$ neutron star for the initial temperatures $T_\mathrm{i} = 3 \times 10^9$ K (left) and $T_\mathrm{i} = 5 \times 10^9$ K (right) in the slow cooling scenario. NC indicates that the effects of the clusters are not taken into account.

core stays hot while the crust temperature decreases (figure 4.15). As a consequence, the surface temperature evolution is driven by the cooling of the core.

4.3.4.2 Cooling time

The cooling time t_w was determined for neutron star with masses between 1.4 and 2.0 $M_\odot$ and for $T_\mathrm{i} = 5 \times 10^9$ K and displayed in figure 4.12 (upper part). The cooling is faster when the neutrons are more strongly paired. Contrary to the fast cooling, the cooling time increases with the mass. In fact, a more massive neutron star has thinner crust and a bigger core. Since the thermal evolution is driven by the core, a more massive star cools slower than a lighter one.

Figure 4.16 plots the cooling time as a function of the parameter α. The variation is different than for the fast cooling scenario : the cooling time decreases when the factor α increases.

For this scenario the scaling relation $t_\mathrm{w} \propto \alpha$ does not hold since the neutrino losses that enter equation (3.3) can not be neglected. The best fits are obtained for a fractional power of α indicated on figure 4.16.

4.3.4.3 Dependence on the symmetry energy

Contrary to the conclusion presented above, note that, for the slow cooling scenario, Gnedin *et al.* (2001) obtained a decrease of the cooling time with the mass of the neutron star. In their calculations, the APR equation of state (Akmal *et al.*, 1998) was used for the core.

Let us define the so-called asymmetry :

$$\delta = \frac{n_\mathrm{n} - n_\mathrm{p}}{n_\mathrm{n} + n_\mathrm{p}} \tag{4.33}$$

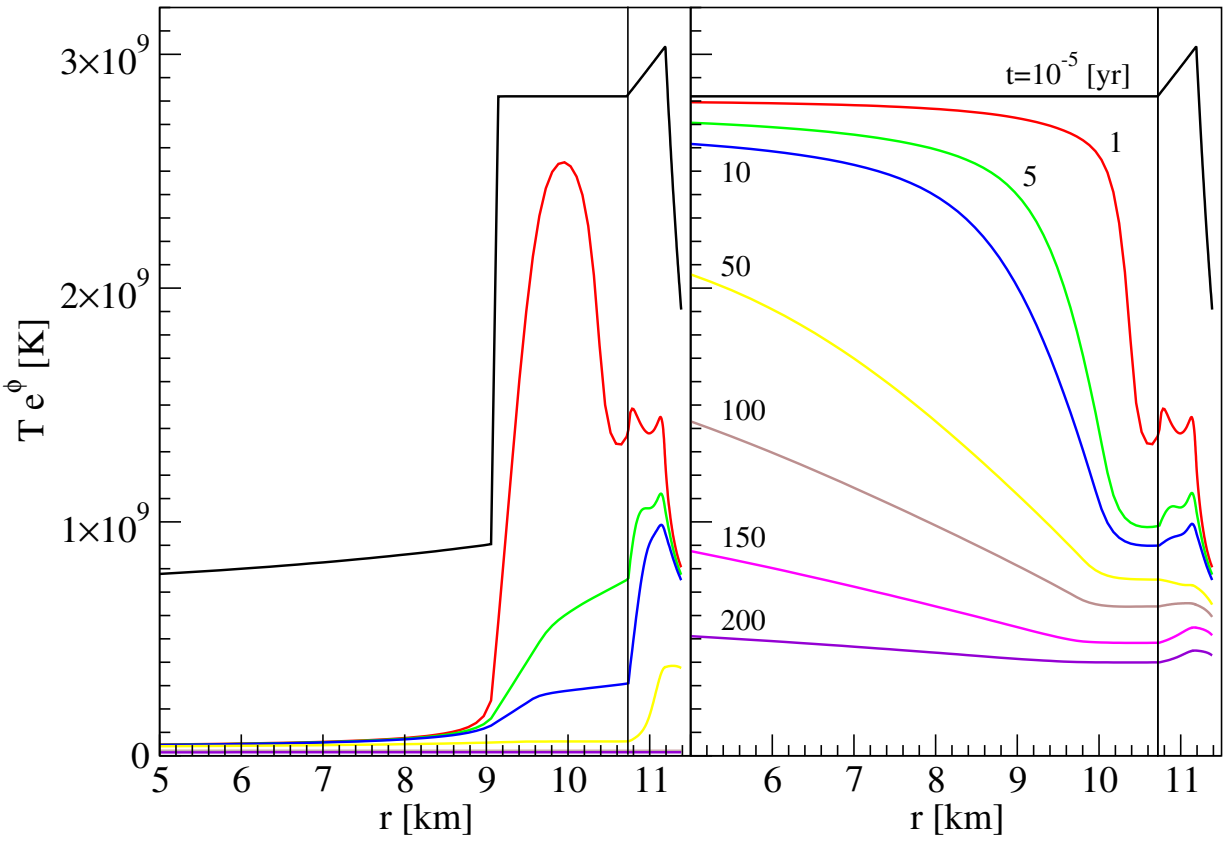

Figure 4.15: Time evolution of the redshifted temperature profiles in a 1.6 $M_\odot$ neutron star for an initial temperature $T_\mathrm{i} = 5 \times 10^9$ K, for normal neutrons models, in the fast (left) and slow (right) cooling scenarios. The vertical line indicates the location of the core-crust interface.

with $n_\mathrm{n}, n_\mathrm{p}$ the neutron and proton number densities respectively. When $\delta = 0$, the matter is symmetric ie. there is an equal number of neutrons and protons and when $\delta = 1$, the matter is exclusively composed of neutrons.

The energy per nucleon can be written as a function of the asymmetry :

$$E = E_0(\rho) + S(\rho)\delta^2 \tag{4.34}$$

with E_0 the energy of symmetric nuclear matter. S is the nuclear symmetry energy that measures the increase in the energy per nucleon due to a small change of the proton and neutron number densities, ie. of the asymmetry.

The symmetry energy can be further decomposed :

$$S(\rho) = S(\rho_0) + L\frac{\rho - \rho_0}{3\rho_0} + \frac{K_\mathrm{sym}}{2}\left(\frac{\rho - \rho_0}{3\rho_0}\right)^2, \tag{4.35}$$

with L and K_sym are the slope and curvature parameters. While the value of $S(\rho_0)$ is quite well constrained : $S(\rho_0) \sim 30 - 34$ MeV, L and K_sym are poorly known. In

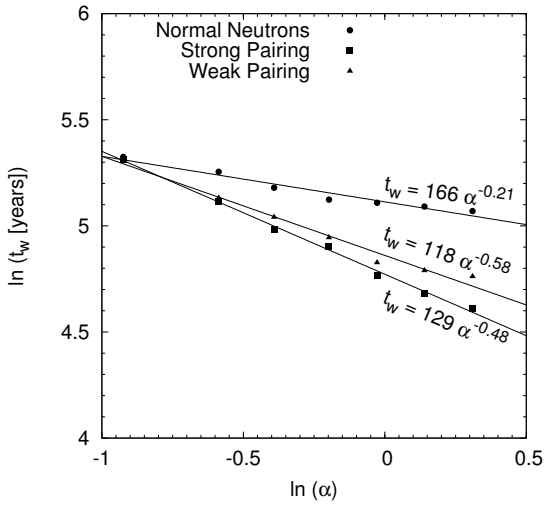

Figure 4.16: Cooling times $t_{\rm w}$ as a function of the parameter α defined in equation (4.20) for neutron star masses between 1.4 and 2.0 $M_\odot$ and $T_{\rm i} = 5 \times 10^9$ K in the slow cooling scenario. Fits with a fractional power of α were obtained.

	APR	DH
$S(\rho_0)$	32.78	32.00
L	59.63	45.94

Table 4.5: Parameters of the expansion of the symmetry energy in equation (4.35) for the APR and DH equations of state (from Akmal *et al.* (1998) and Douchin & Haensel (2001), respectively). Data from Ducoin *et al.* (2011).

particular, experimental data from heavy-ion collisions give $L = 88 \pm 25$ MeV. These parameters can be calculated for each equation of state and are shown in table 4.5 for the APR and DH equations of state. A higher value for the L parameter results in a higher proton fraction. Accordingly, for the APR equation of state, the matter is more proton-rich than for the DH one, as shown on figure 4.17.

The APR equation of state assumes $npe\mu$ composition and gives a higher proton, electron and muon fractions and a lower neutron fraction than the DH equation of state. Figure 4.18 shows, for non-superfluid matter and a temperature $T = 10^9$ K, the different contributions to the neutrino emissivity in the core from the MUrca and bremsstrahlung processes involving the neutrons and protons. The total neutrino emissivity is higher for the APR equation of state than for the DH one. Comparison with the left plot of figure 4.9 then demonstrates that the neutrino losses are larger in the core than in the crust. Therefore, the core cools faster than the crust and a more massive neutron star cools faster than a low mass one.

In conclusion, the symmetry energy alters the thermal evolution of young neutron stars since it affects the core neutrino emissivity.

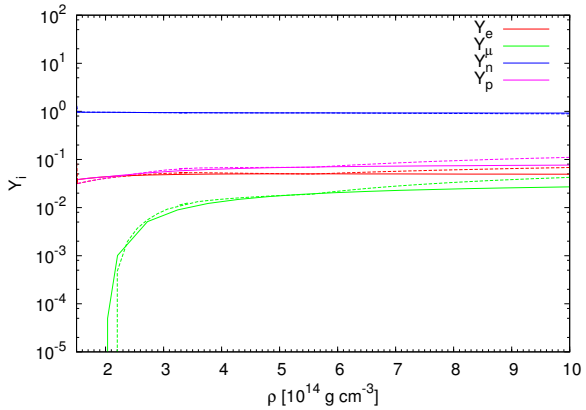

Figure 4.17: Composition of the core of neutron stars for the Douchin & Haensel (solid line) and APR (dashed line) equations of state.

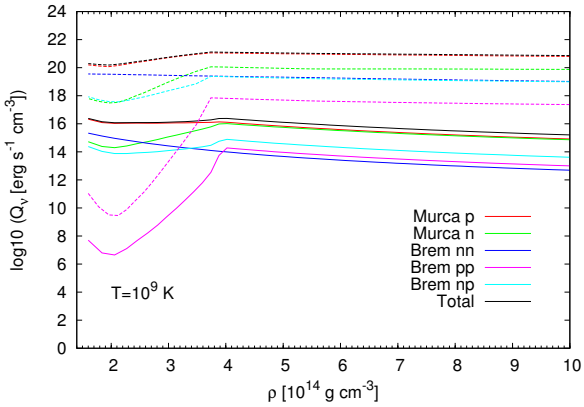

Figure 4.18: Different contributions to the neutrino emissivity in the core for the DH (solid line) and APR (dashed line) equations of state, for non-superfluid matter and $T = 10^9$ K. p and n stand for protons and neutrons, Murca and Brem for MUrca and bremsstrahlung processes.

4.4 Perspectives

4.4.1 Modeling

The model presented previously is almost entirely based on a Skyrme type nuclear interaction. Only the properties of the cells in the inner-crust from Negele & Vautherin (1973) were not calculated for such an interaction. Moreover the influence of the pairing correlations on the properties of the cells ($A, Z, R_{\rm WS}, \ldots$) was not taken into account.

However, Grill *et al.* (2011) recalculated the properties of the Wigner-Seitz in the inner crust for the Skyrme type interaction and in the framework of HFB approach, including therefore the effects of the pairing. Grill *et al.* now recalculate the specific heat of the superfluid neutrons in the inner crust and in the near future that I plan to perform new cooling calculations to study how the microphysics properties of the crust influence the thermal evolution for a model of neutron star fully based on the same nuclear interaction : the Skyrme one.

4.4.2 Observations

Eventually, the observation of a young neutron star with an age $\lesssim 100$ years, ideally a cool one, may enable to constrain the properties of the matter in the crust. However so far, none was observed.

In 1987, a type II supernova explosion, SN 1987A, in the Large Magellanic Cloud was observed, the closest since SN 1604 which occurred in the Milky Way itself. Approxi-

mately three hours before the supernova was visible on the Earth, a burst of neutrinos was observed at three separate neutrino observatories consistently with the theoretical supernova models (see section 1.2). This was the first time neutrinos from a supernova had been detected directly and it marked the beginning of neutrino astronomy. The supernova remnant has been monitored since then but so far, despite intensive observations, X-ray satellites failed to detect the flux from the central compact object (Weber *et al.*, 2007). The neutron star may be still obscured by the supernova remnant or a black hole may have been formed in the late stages of the explosion (Weisskopf *et al.*, 2007).

Chapter 5

Thermal evolution of accreting neutron stars

Contents

The modeling of the thermal evolution of neutron star can not only be confronted with the observations of isolated neutron stars. Accreting neutron stars constitute also an interesting test for the models. The different types of observed accreting neutron stars are presented in section 5.1 and the origin of the quiescent emission after accretion stops in the framework of the deep crustal heating scenario is explained in section 5.2. The equations for the heat transport that include the heat that is released by the reactions the accreted matter undergoes when sinking into the crust under the weight of the newly accreted material are derived in section 5.3. The observations of the soft X-ray transients that show short accretion episodes lasting weeks to months are then confronted with the theoretical modeling in section 5.4 and put constraints on the properties of the matter inside neutron stars. Section 5.5 details the models that are been developed to simulate the thermal relaxation of the quasi-persistent X-ray transients, that are neutron stars which accreted matter during years to decades before accretion stopped. They enable to understand the physical properties of the matter in accreting neutron stars, in particular in their crust. A new preliminary model, developed during my thesis in collaboration with Leszek Zdunik and Paweł Haensel, is presented. It enables to simulate for the first time the thermal relaxation of all quasi-persistent X-ray transients and is of particular interest since the monitoring of the relaxation of a normal transient that opens new and exciting perspectives.

5.1 Observations of accreting neutron stars

In a low-mass X-ray binary, a neutron star accretes matter from its companion star, with a mass below one solar mass, by Roche-lobe overflow (more details in section 9.1). An accretion disk is formed and the photons emitted by the accreted matter heats the inner edge of the accretion disk to temperatures $\sim 10^7$ K. This is the origin of the observed X-ray emission (Wijnands, 2004).

Among the low-mass X-ray binaries are transient sources. They are systems that have usually a low luminosity $\sim 10^{32} - 10^{34}$ erg s^{-1} but sometimes exhibit a sudden rise of their luminosity $\sim 10^{36} - 10^{38}$ erg s^{-1}. These phenomena that are called outbursts are believed to originate from an abrupt increase of the accretion rate and last for weeks to months before the accretion is strongly reduced or suppressed with a low luminosity. The systems are then said to have turned into quiescence. Figure 5.1 shows light curves obtained with RXTE for three different transients. The sources clearly exhibit a variability : only one outburst is observed for XTE J$1806-246$ and MXB $1730-335$ is a recurrent transient. Some of these systems have been observed with RXTE during the outbursts and with XMM-Newton and Chandra during the quiescence phase.

In the accretion phase, some sources exhibit so called type I X-ray bursts that are observed as a sharp rise of the luminosity followed by a slow and gradual decrease. They are thermonuclear explosions at the surface of accreting neutron stars can be observed. They are believed to originate from the explosive burning of helium that accumulates as the result of the stable burning of the accreted hydrogen.

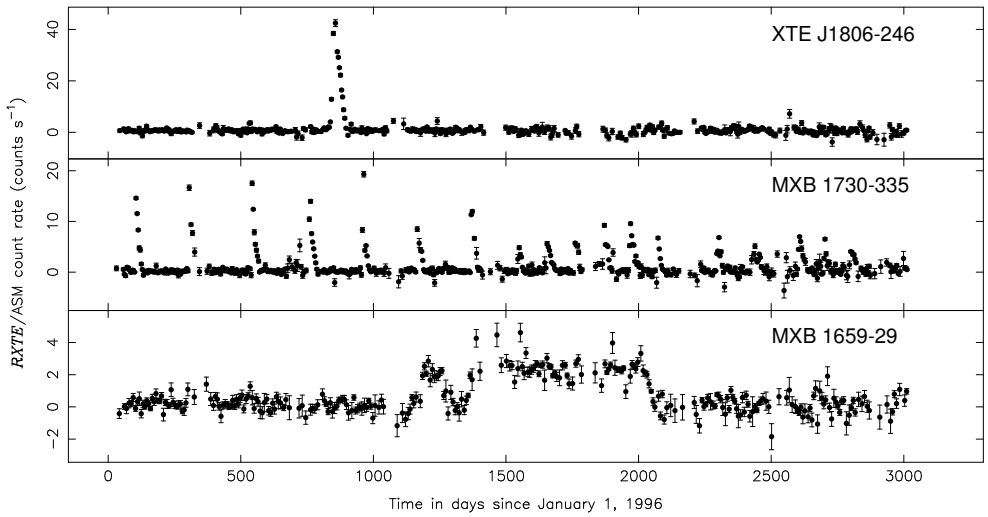

Figure 5.1: RXTE light curves for three different X-ray transients. From Wijnands (2004).

There exists a class of transient binaries, that are active not during weeks or months but during years or decade, like MXB $1659-29$ in figure 5.1. They are called the quasi-persistent X-ray transients (see section 5.5).

5.2 Quiescent state of X-ray transients

5.2.1 Nature of the quiescent emission

Several theoretical models were proposed to explain the quiescent emission of the X-ray transients such as the interaction between the pulsar wind and the surrounding matter, residual accretion or accretion stopped on the magnetosphere because of the neutron star magnetic field (Campana *et al.*, 1998).

The hypothesis that the residual emission originates from the thermal emission from the cooling neutron star was initially rejected since (Yakovlev *et al.*, 2003) :

- the fit of the quiescent spectra with a blackbody gave a size for the emitting region much smaller than the radius of a neutron star;
- the neutron star internal temperature was thought to be lower than the observed one.

5.2.2 Deep crustal heating scenario

In their seminal paper, Brown *et al.* (1998) presented the so-called deep crustal heating scenario.

If one assumes that the observed quiescent emission originates from the neutron star thermal radiation, then the derived core temperature is $\sim 10^8$ K. Thermal equilibrium between the neutrino and photon emissions from a neutron star with such temperature and the unstable burning of hydrogen and helium in the outer shells requires an accretion rate $\dot{M} \sim 10^{-11} - 10^{-9}$ M$_\odot$ yr^{-1} Hanawa & Fujimoto (1984). However, for this value of the accretion rate, the heat released by the outer shell reactions hardly diffuses inside the neutron star and heats up the core. Therefore, there must be some additional source of heating.

The catalyzed matter in the crust of an accreting neutron star is slowly compressed and sinks deeper under the weight of the accreted material. It undergoes a series of nuclear reactions that release heat proportionally to the accretion rate which propagates into the whole neutron star, particularly in the core, and heats it up. When the accretion stops, a heat wave propagates from the core up to the surface and is radiated away. This is the origin of the quiescence luminosity.

The crustal reactions triggered by the compression of matter have been in Haensel & Zdunik (1990, 2003); Gupta *et al.* (2007); Haensel & Zdunik (2008). They consist of :

- in the outer crust, electron captures in two steps :

$$(A, Z) + e^- \rightarrow (A, Z-1) + \nu_e, \tag{5.1}$$
$$(A, Z-1) + e^- \rightarrow (A, Z-2) + \nu_e + \epsilon_j, \tag{5.2}$$

  with ϵ_j the energy release (in MeV per accreted nucleon);

- in the inner crust, electron captures that trigger neutron emission :

$$(A, Z) + e^- \rightarrow (A, Z-1) + \nu_e, \tag{5.3}$$
$$(A, Z-1) + e^- \rightarrow (A-k, Z-2) + kn + \nu_e + \epsilon_j \tag{5.4}$$

  for densities below the density threshold for the pycnonuclear reactions $\rho_{\rm pyc}$. The exact value of $\rho_{\rm pyc}$ is very uncertain : $\rho_{\rm pyc} \sim 10^{12} - 10^{13}$ g cm^{-3};

- for $\rho > \rho_{\rm pyc}$, pycnonuclear fusions :

$$(A, Z-2) + (A, Z-2) \rightarrow (2A, 2Z-4) + \epsilon_{j,1}, \tag{5.5}$$
$$(2A, 2Z-4) \rightarrow (2A-k', 2Z-4) + k' + \epsilon_{j,2}, \tag{5.6}$$
$$\ldots \rightarrow \ldots + \epsilon_{j,3} \tag{5.7}$$

  where the ... are a chain of electrons captures and neutron emissions that release energy. In total the energy release is $\epsilon_j = \epsilon_{j,1} + \epsilon_{j,2} + \epsilon_{j,3}$.

As a consequence, this series of reaction also determines the composition of the matter in the crust of an accreting neutron star, ie. the crustal equation of state.

In Haensel & Zdunik (2008) are presented the series of reactions and the heat release assuming that the accreted matter that underwent burning during the X-ray bursts has

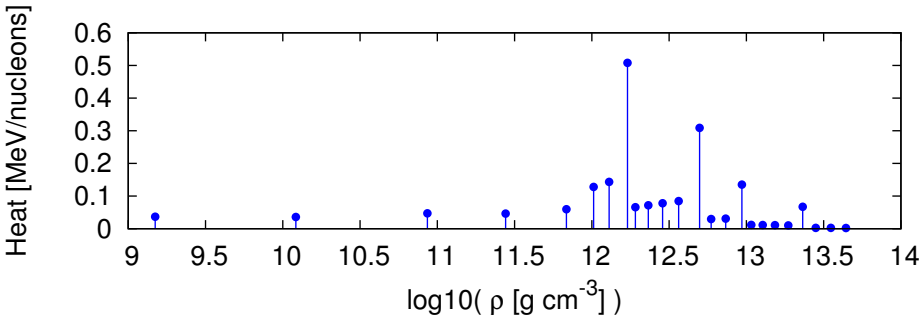

Figure 5.2: Heat sources in the crust for the model by Haensel & Zdunik (2008) for an initial ^{56}Fe composition.

two initial compositions ^{56}Fe and ^{106}Pd. Figure 5.2 illustrates the different heat sources that originates from the reactions in the crust of an accreting neutron star for an initial ^{56}Fe composition that will be adopted in the following.

Note however that the rate of pycnonuclear reactions together with the density threshold for these reactions to occur are known with large uncertainties but Haensel & Zdunik (2008) show that this does not affect the amount of total heat release which is of $\epsilon_{\rm nuc} \simeq 2$ MeV per accreted nucleon.

Brown *et al.* (1998) estimated that the averaged luminosity in quiescence due to this deep crustal heating is

$$L_{\rm q} \sim \frac{\epsilon_{\rm nuc}}{m_{\rm u}} \langle \dot{M} \rangle \tag{5.8}$$

where $\langle \dot{M} \rangle$ is the time-averaged accretion rate, $\epsilon_{\rm nuc}$ the total heat release and $m_{\rm u}$ the atomic mass unit. With $\epsilon_{\rm nuc} \sim 1.5$ MeV (Haensel & Zdunik, 1990), they got :

$$L_{\rm q} \sim 6 \times 10^{32} \frac{\langle \dot{M} \rangle}{10^{-11} {\rm M}_\odot \ {\rm yr}} \ {\rm erg \ s^{-1}}, \tag{5.9}$$

which is in fact consistent with most of the observations of quiescent transients. Moreover, this model provides a simple explanation for the slow decrease of the luminosity of Aql X-1, that originates from the thermal relaxation of the crust, followed by a steady quiescent luminosity with no short-term fluctuations (Brown *et al.* (1998) and references therein).

5.2.3 Atmosphere models

Brown *et al.* (1998) also argued that accurate models for an hydrogen atmosphere instead of blackbody models have to be used when performing the fits of the spectra. In fact, in $\sim 1 - 100$ s after the end of accretion, the heavy elements move from the envelope down to the surface of the neutron star because of the gravitational force and the star will be left with a pure hydrogen atmosphere Romani (1987). Motivated by this

idea, Rutledge *et al.* (1999, 2000) have reperformed the analysis of the X-ray emission of several transients and conclude that in fact, fits with a blackbody underestimate the size of the emitting region and overestimate the surface temperature. Fits with realistic hydrogen atmosphere models give a size for the emitting region that is comparable to the typical size of a neutron star.

However, the model of hydrogen atmosphere fails explain the hard power-law tail in the spectra of Aql X-1 and Cen X-4 that may originate from residual accretion.

5.3 Heat equation

The set of equations (3.1) and (3.2) has to be modified to include the heat release from the deep crustal heating $Q_{\rm dch}$:

$$\boxed{\frac{\mathrm{d}}{\mathrm{d}r}\left(L\mathrm{e}^{2\phi}\right) = -\frac{4\pi r^2 \mathrm{e}^{\phi}}{\sqrt{1-2Gm/c^2r}}\left(C_{\rm V}\frac{\mathrm{d}T}{\mathrm{d}t} + \mathrm{e}^{\phi}Q_{\nu} - \mathrm{e}^{\phi}Q_{\rm dch}\right)} \tag{5.10}$$

$$\boxed{\frac{\mathrm{d}}{\mathrm{d}r}\left(T\mathrm{e}^{\phi}\right) = -\frac{1}{\kappa}\frac{L}{4\pi r^2}\frac{\mathrm{e}^{\phi}}{\sqrt{1-2Gm/c^2r}}} \tag{5.11}$$

with

$$\boxed{Q_{\rm dch} = \frac{\epsilon_{\rm nuc}}{\delta V}\frac{\dot{M}}{m_{\rm u}}}. \tag{5.12}$$

For a given source, the heat is not considered to be released at a single density but instead in an infinitesimal shell with a volume δV.

5.4 Soft X-ray transients

5.4.1 Thermal evolution of a soft X-ray transient

Soft X-ray transients undergo short episodes of accretion that last few weeks or months.

Colpi *et al.* (2001) modeled the thermal evolution of accreting neutron stars. The figure 5.3 shows the evolution of the core and surface temperature as a function of the time since accretion started. They consider three heating cases :

- an initially cold neutron star that undergoes intense cycles of accretion lasting $t_{\rm out} = 30$ days every $t_{\rm rec} = 150$ days $\gg t_{\rm out}$. The total accreted mass during one episode is $\Delta M = \dot{M}t_{\rm out} = 6 \times 10^{-11}$ $\mathrm{M}_{\odot}$. The lower solid lines in figure 5.3 shows its thermal evolution;

- an initially hot neutron star that undergoes similar accretion episodes. Its thermal evolution is shown by the upper solid lines in figure 5.3;

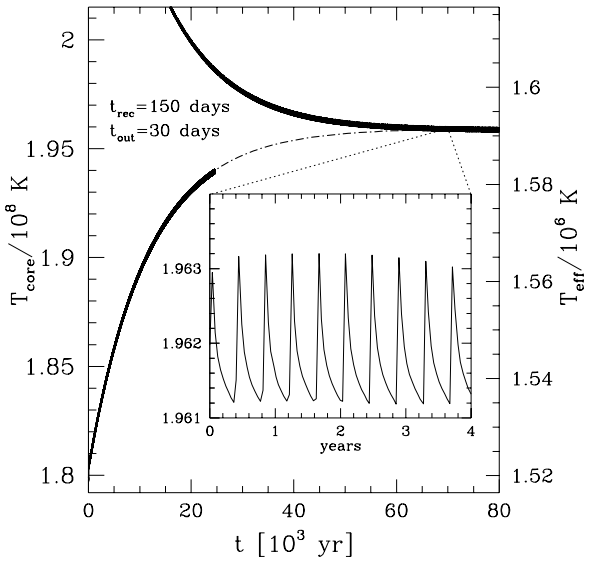

Figure 5.3: Core temperature $T_{\rm core}$ and effective surface temperature at infinity as functions of the time t since the neutron star started undergoing accretion episodes. See text for details. From Colpi *et al.* (2001).

- a cold neutron star that accretes matter at a constant rate $\langle \dot{M} \rangle = \Delta M / t_{\rm rec}$. The dot-dashed line in figure 5.3 shows the evolution of the temperature.

The three cases show that neutron stars reach thermal equilibrium $\sim 10^4$ years after accretion started. This time scale is much shorter than the time scales related to the evolution of binary systems. The steady-state is reached when the neutrino and photon losses are balanced by the deep crustal heating.

The figure also shows that the thermal equilibrium is sensitive to the time-averaged accretion rate :

$$\langle \dot{M} \rangle = \frac{\Delta M}{t_{\rm rec}} = \frac{\dot{M} t_{\rm out}}{t_{\rm rec}}, \tag{5.13}$$

and not to its transient properties.

5.4.2 A toy model

5.4.2.1 Heat equation

By analogy with Yakovlev *et al.* (2003), let us study the thermal evolution of an accreting neutron star in the steady-state approximation.

Integrating the heat equation over the whole star, one gets :

$$C_{\rm V}^{\rm tot} \frac{{\rm d}T{\rm e}^{\phi}}{{\rm d}t} = L_{\rm dch}^{\infty}(\dot{M}) - L_{\nu}^{\infty}(T{\rm e}^{\phi}) - L_{\gamma}^{\infty}(T_{\rm s}), \tag{5.14}$$

with $C_{\rm V}^{\rm tot}$ the total heat capacity of the star, L_γ^∞ the photon surface luminosity as detected by a distant observer, L_ν^∞ the redshifted neutrino luminosity, and $L_{\rm dch}^\infty$ the redshifted power of the deep crustal heating.

The temperature inside the neutron star $T{\rm e}^\phi$ is assumed to be constant and therefore in the steady state approximation equation 5.14 gives :

$$\boxed{L_{\rm dch}^\infty\left(\langle\dot{M}\rangle\right) = L_\nu^\infty(T_{\rm i}) + L_\gamma^\infty(T_{\rm s})} \tag{5.15}$$

with $T_{\rm i} = T{\rm e}^\phi$. Thus the thermal state of the neutron depends only on the time-averaged accretion rate $\langle\dot{M}\rangle$. Note that contrary to the toy-model presented in section 3.3, this model is independent of the heat capacity. The solution of this equation provides the relation $T_{\rm e}^\infty\left(\langle\dot{M}\rangle\right)$ or $L_\gamma^\infty\left(\langle\dot{M}\rangle\right)$ that defines a so-called heating curve.

Photon emission

Assuming a black-body emission from the surface, the photon surface luminosity as detected by a distant observer is :

$$L_\gamma^\infty = 4\pi\sigma T_{\rm s}^4 R^2 {\rm e}^{2\phi}, \tag{5.16}$$

$$= 4\pi\sigma\left(T_{\rm e}^\infty\right)^4\left(R^\infty\right)^2, \tag{5.17}$$

One gets :

$$L_\gamma^\infty = 4.16\times10^{32} T_{\rm s6}^4 \text{ erg s}^{-1} \tag{5.18}$$

with $T_{\rm s6}$ the surface temperature in units of 10^6 K.

Neutrino emission

The redshifted neutrino luminosity is given by :

$$L_\nu^\infty = 4\pi\int_0^R \frac{r^2 Q_\nu e^{2\phi}}{\sqrt{1-2Gm/(c^2 r)}}{\rm d}r, \tag{5.19}$$

with Q_ν the neutrino emissivity (in erg cm^{-3} s^{-1}).

Neglecting the relativistic effects and for a constant temperature, the neutrino luminosity L_ν is given :

$$L_\nu = 4\pi\int_0^R r^2 Q_\nu {\rm d}r, \tag{5.20}$$

$$= \frac{4}{3}\pi R^3 \bar{Q}_\nu. \tag{5.21}$$

Since the gravitational potential is regarded as constant in the crust, one gets :

$$L_\nu^\infty = L_\nu {\rm e}^{\phi(R)}, \tag{5.22}$$

$$= \frac{4}{3}\pi R^3 {\rm e}^{\phi(R)}\bar{Q}_\nu. \tag{5.23}$$

For the slow cooling scenario, introducing $\bar{Q}^{\rm s}_{\nu 21} = \bar{Q}^{\rm s}_{\nu}/(10^{21}$ erg s^{-1} cm$^{-3})$:

$$L^{\infty}_{\nu} = 3.20 \times 10^{39} \bar{Q}^{\rm s}_{\nu 21} T^{8}_{\rm i9} \text{ erg s}^{-1} \tag{5.24}$$

and for the fast cooling scenario, with $\bar{Q}^{\rm f}_{\nu 27} = \bar{Q}^{\rm f}_{\nu}/(10^{27}$ erg s^{-1} cm$^{-3})$:

$$L^{\infty}_{\nu} = 3.20 \times 10^{45} \bar{Q}^{\rm f}_{\nu 27} T^{6}_{\rm i6} \text{ erg s}^{-1} \tag{5.25}$$

Deep crustal heating

Similarly, the power due to the deep crustal heating is :

$$L_{\rm dch} = \epsilon_{\rm dch} \frac{\langle \dot{M} \rangle}{m_{\rm u}}, \tag{5.26}$$

and :

$$L^{\infty}_{\rm dch} = L_{\rm dch} {\rm e}^{\phi(R)}, \tag{5.27}$$

According to Haensel & Zdunik (2008), $\epsilon_{\rm dch} = 1.9$ MeV$= 3.04 \times 10^{-6}$ erg. Thus,

$$L^{\infty}_{\rm dch} = 6.74 \times 10^{33} \langle \dot{M} \rangle_{10} \text{ erg s}^{-1} \tag{5.28}$$

with $\langle \dot{M} \rangle_{10} = \langle \dot{M} \rangle / (10^{-10}$ M$_{\odot}$ yr$^{-1})$.

Envelope model

Considering the relation $T_{\rm s} - T{\rm i}$ between the surface temperature and the internal temperature derived by Potekhin *et al.* (1997) for a neutron star with a fully accreted envelope, one gets :

$$T^{4}_{\rm s6} = g_{14} \left(18.1 T_{\rm i9}\right)^{2.42} \tag{5.29}$$

with g_{14} the surface gravity in units of 10^{14} cm s^{-2}. This relation is valid for temperatures $T_{\rm i} \leq 10^{8}$ K.

5.4.2.2 Analytical solutions of the thermal steady state

Photon emission regime

When the neutron star is cold enough, the neutrino luminosity becomes negligible as compared to the photon luminosity : $L^{\infty}_{\nu} \ll L^{\infty}_{\gamma}$. The heat released by the deep crustal heating reactions propagates up to the surface and is emitted in the form of photons. Equation (5.15) becomes :

$$L^{\infty}_{\rm dch}(\langle \dot{M} \rangle) = L^{\infty}_{\gamma}(T_{\rm s}). \tag{5.30}$$

Using the previous results, one can calculate the surface temperature as a function of the mean accretion rate.

The solution is :

$$T_{\rm s6} = 2.01 \left(\langle \dot{M} \rangle_{10} \right)^{0.25} \text{ K}. \tag{5.31}$$

Using the $T_{\rm s} - T_{\rm i}$ relation of Potekhin *et al.* (1997), one gets :

$$T_{\rm i8} = 1.21 \left(\langle \dot{M} \rangle_{10}\right)^{0.41} \ {\rm K}, \tag{5.32}$$

with $T_{\rm i8} = T_{\rm i}/10^8$ K.

Neutrino emission regime

When the temperature is high enough, most of the heat released by deep crustal heating reaches the core and is emitted in the form of neutrinos. The neutrino emissivity is then dominant over the photon luminosity : $L_\gamma^\infty \ll L_\nu^\infty$ and the steady state equation (5.15) becomes :

$$L_{\rm dch}^\infty(\langle \dot{M} \rangle) = L_\nu^\infty(T_{\rm i}). \tag{5.33}$$

The dominant neutrino processes depend on the mass of the neutron star :

- In low-mass NSs, the density is not high enough to allow fast neutrino emission. Therefore, slow neutrinos processes dominate. The solution is then :

$$T_{\rm i8} = 1.95 \left(\frac{\langle \dot{M} \rangle_{10}}{Q_{\nu 21}^{\rm s}}\right)^{0.125} \ {\rm K}. \tag{5.34}$$

  The $T_{\rm s} - T_{\rm i}$ relation of Potekhin *et al.* (1997) gives:

$$T_{\rm s6} = 2.68 \left(\frac{\langle \dot{M} \rangle_{10}}{Q_{\nu 21}^{\rm s}}\right)^{0.076} \ {\rm K}. \tag{5.35}$$

  The transition from the photon emission regime to the neutrino emission regime occurs when :

$$T_{\rm s6} = 3.04/\left(Q_{\nu 21}^{\rm s}\right)^{0.52} \ {\rm K}, \tag{5.36}$$

  ie. for :

$$\boxed{\langle \dot{M} \rangle_{10} = 5.34/\left(Q_{\nu 21}^{\rm s}\right)^{0.44}}. \tag{5.37}$$

- in high-mass neutron stars, the main neutrino processes are the fast ones.

  One gets :

$$T_{\rm i8} = 0.113 \left(\frac{\langle \dot{M} \rangle_{10}}{Q_{\nu 27}^{\rm f}}\right)^{0.169} \ {\rm K}. \tag{5.38}$$

  With the $T_{\rm s} - T_{\rm i}$ relation of Potekhin *et al.* (1997) :

$$T_{\rm s6} = 0.478 \left(\frac{\langle \dot{M} \rangle_{10}}{Q_{\nu 27}^{\rm f}}\right)^{0.10} \ {\rm K}. \tag{5.39}$$

The transition from the photon emission regime to the neutrino emission stage takes place when :

$$T_{\rm s6} = 0.25/\left(Q^{\rm f}_{\nu 27}\right)^{0.169} \tag{5.40}$$

ie. for :

$$\boxed{\langle \dot{M} \rangle_{10} = 5.87 \times 10^{-5}/\left(Q^{\rm f}_{\nu 27}\right)^{0.69}}. \tag{5.41}$$

Comparing with the results for low mass neutron stars, the transition from the photon cooling stage to the neutrino cooling regime occurs for lower temperatures and for much lower values of the mean accretion rate.

5.4.3 Observations & constraints on microphysics

The heating curves for different compositions of the core of neutron stars and/or leading neutrino processes in the core can be compared with the observations of low-mass X-ray transients. L_γ^∞ is the quiescent thermal luminosity (Yakovlev *et al.*, 2003). The mean accretion rate is defined by $\langle \dot{M} \rangle = \Delta M/\Delta t$ where ΔM is the total accreted time during a "long enough" time Δt, including both the quiescent and accreting phases. The quantities $\langle \dot{M} \rangle$ and L_γ^∞ have been estimated for few sources but suffer from uncertainties.

Levenfish & Haensel (2007) confronted in particular the observations of both isolated and accreting neutron stars in soft X-ray transients with models of superfluid neutron stars. As explained in section 3.5.1, the neutrino processes are affected by the superfluid properties of the interior.

They tested the minimal cooling scenario with the observations, presented in section 3.6.5 including the effects of superfluidity on the thermal properties. They showed that it is inconsistent with the thermal state of the coolest soft X-ray transients 1H 1905+000 and SAX 1808.4-3658 as plotted in figure 5.4.

Figure 5.5 shows the results for the model of neutron stars whose thermal states reproduce all the available observational data for isolated and accreting neutron stars. This model is based on the the APR equation of state (Akmal *et al.*, 1998), allowing for DUrca process in the inner core, with strong proton superfluidity in the outer core with a maximum of the critical temperature $T_{\rm cp} \gtrsim 10^9$ K. The hotter sources correspond to slowly cooling low-mass neutron stars and the colder ones to high-mass neutron stars with different masses.

Therefore observations of both isolated neutron stars and soft X-ray transients, in particular the very cold ones 1H 1905+000 and SAX 1808.4-3658, test the same physics and enable to constrain the properties of the core of neutron stars.

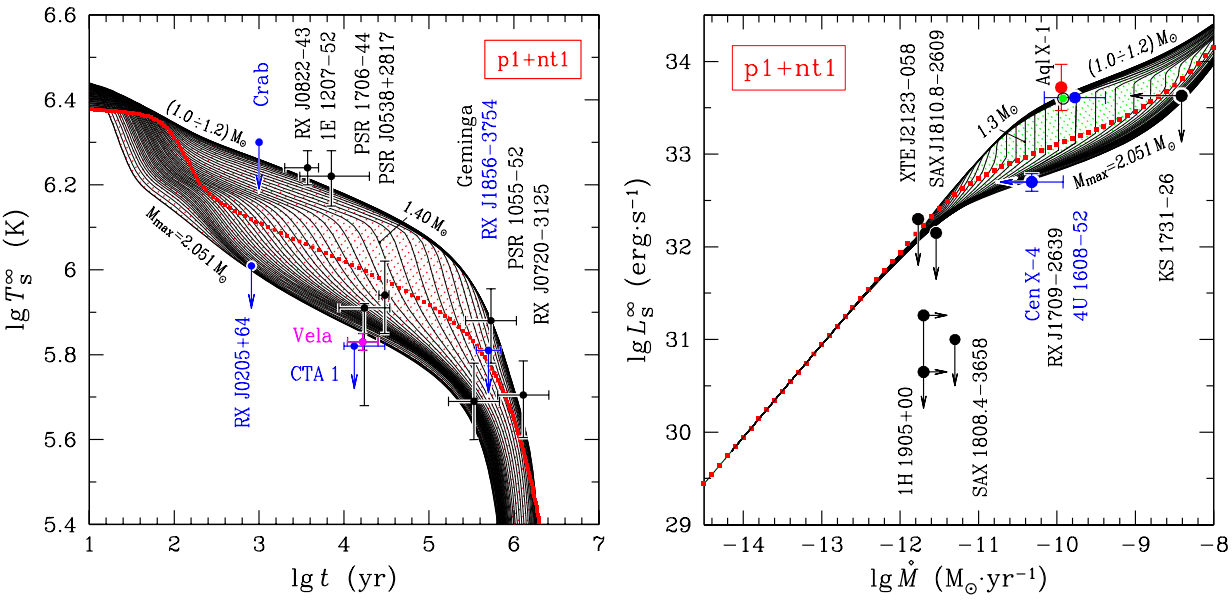

Figure 5.4: Models of superfluid neutron stars in the framework of the minimal cooling paradigm confronted with the observations of isolated neutron stars (left) and neutron stars in soft X-ray transients. The cooling and heating curves of neutron stars with masses ranging from 1 $M_\odot$ to the maximal allowable mass correspond to the hatched regions. Figure from Levenfish & Haensel (2007).

5.5 Quasi-persistent X-ray transients

The Quasi-persistent X-ray transients are X-ray transients that accreted matter during years to decades. So far, only four of them have been observed to turn to quiescence with a careful monitoring after accretion stopped.

5.5.1 Observations

5.5.1.1 KS 1731-260

KS 1731-260 is a quasi-persistent neutron star X-ray transient which was first detected in active state in August 1989 by the Kvant X-ray observatory, attached to the Mir space station. It was in retrospect seen to be already in outburst in October 1988 (Syunyaev *et al.*, 1990). The source remained active for 12.5 years until its last detection on January 21, 2001 with the Rossi X-ray Timing Explorer (RXTE). The source was first seen in quiescence with Chandra X-ray telescope on March 27, 2001 by Wijnands *et al.* (2001) and observed since then several times during $\sim$ 5 years, by the Chandra and XMM-Newton telescopes as reported by Cackett *et al.* (2006). Cackett *et al.* (2010) presented an additional Chandra observational point in May 2009 and consistently reanalyze the previous observations. The latter suggest that the source is still cooling and did not

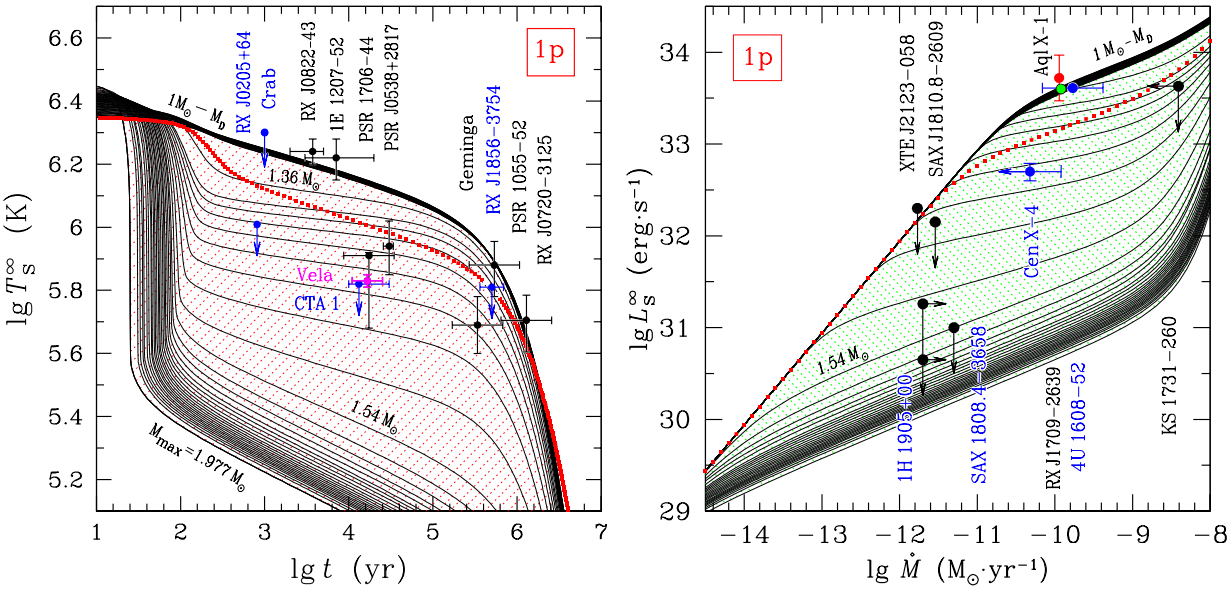

Figure 5.5: Thermal states for the model of neutron stars for confront the best with the observational data. See text for details. Figure from Levenfish & Haensel (2007).

reach thermal equilibrium in May 2009. Figure 5.6 shows the effective temperatures in quiescence of this object.

Following Cackett *et al.* (2006), t_0, the last day when the source was detected in active state is set to Modified Julian Day (MJD) $t_0 = 51930.5$ and the duration of the accretion cycle to Δt$= 12.5$ years.

5.5.1.2 MXB 1659-29

After its discovery in October 1976 by Lewin *et al.*, MXB 1659-29 was identified as an X-ray transient and observed several times between October 1976 and September 1978. The source was undetected by the Hakucho satellite in July 1979 (Cominsky *et al.*, 1983). It returned to an active state after $\sim$ 21 years in quiescence, when it was detected in outburst on April 2, 1999 by BeppoSAX (in 't Zand *et al.*, 1999). MXB 1659-29 remained active during 2.5 years, until September 2001. The final detection in outburst of the source was on September 4, 2001 and the first in quiescence on September 14, 2001. Cackett *et al.* (2006, 2008) reported several observations in quiescence since then by the Chandra and XMM-Newton telescopes spreading over $\sim$ 7 years, as shown in figure 5.6.

In agreement with Cackett *et al.* (2006), $t_0 = 52159.5$ and Δt$= 2.5$ years.

5.5.1.3 EXO 0748-676

EXO 0748-676 was discovered with EXOSAT in February 1985 and in retrospect, had already been detected by accident in May 1980 by the Einstein satellite (Parmar *et al.*,

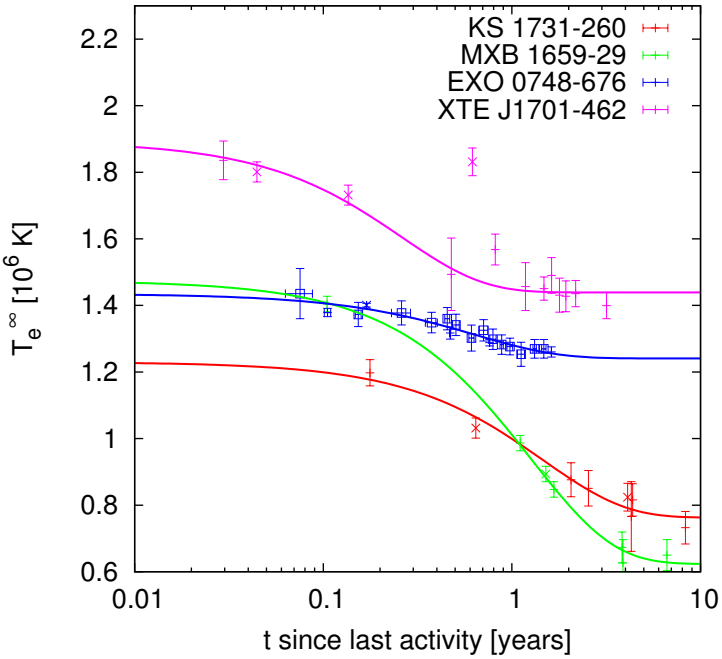

Figure 5.6: Observations of the four QPXRT with best-fit exponential decay curves $2-\sigma$ error bars.

1985; Reynolds *et al.*, 1999). After $\sim 24-26$ years of active state, RXTE and Swift X-ray telescope showed that in August-September 2008 the X-ray flux of the source was declining indicating a transition to quiescence (Wolff *et al.*, 2008). Degenaar *et al.* (2011b) reported several observations of the source in quiescence with the Chandra, Swift and XMM-Newton telescopes, as presented in figure 5.6.

Based on the joint analysis of the Eddington limit, the gravitational redshift of narrow width absorption lines and the emitting surface area from X-ray observations of EXO 0748-676, Özel (2006) claimed that the mass and radius of the source are 2.10 ± 0.28 $M_\odot$ and 13.8 ± 1.8 km respectively. However, the determination of the 552 Hz spin period of the neutron star through the analysis of oscillations in the RXTE observations of two bursts in 2007 releaved that the neutron star spins rapidly (Galloway *et al.*, 2010). This seems inconsistent with the narrow width of the absorption lines, as confirmed by Lin *et al.* (2010). Zhang *et al.* (2011) fitted an XMM-Newton observation of EXO 0748-676 in quiescence with two neutron-star atmosphere models and find a mass of 1.55 ± 0.12 $M_\odot$ and a radius of $16.0^{+0.7}_{-1.3}$ km.

In the following, the values $t_0 = 54714$ and Δt$= 26$ years, consistently with Degenaar *et al.* (2011b), are used.

5.5.1.4 XTE J1701-462

RXTE discovered XTE J1701-462 in January 2006 in outburst (Remillard *et al.*, 2006). In retrospect previous observations showed that the outburst started between 2005 December 27 and 2006 January 4 (Homan *et al.*, 2007). After ~ 1.6 years in active state with very high luminosities indicating near-Eddington accretion rates the source turned to quiescence in early August 2007. The source was then observed during ~ 800 days with Chandra and XMM-Newton (Fridriksson *et al.*, 2010). XTE J1701-462 exhibits a large increase in the temperature and luminosity in the sixth and seventh observations (see figure 5.6), inconsistent with the decreasing temperature expected from a cooling neutron star. These observations will be excluded from the subsequent analysis and may originate from a spurt of accretion.

Consistently with the observations of the source by Fridriksson *et al.* (2010), $t_0 = 54322.13$ and Δt$= 1.607$ years.

5.5.1.5 Other sources

There exists other sources that were observed to accrete during long periods of time before accretion stopped. Unfortunately, their thermal relaxation was not observed (Wijnands (2004) and references therein). Among them are :

- X 1732-304 located in the globular cluster Terzan 1. It has been observed to steadily accrete during ~ 12 years before accretion stopped in 1999. Wijnands *et al.* (2002b) performed subsequent observations with Chandra failed to detect even the quiescent emission from the source. Therefore, they suggested that the outburst duration is typical for the source and if the source is in quiescence for few decades, then enhanced neutrino emission may be required to explain the low temperature of the neutron star;

- 4U 2129+47 was repeatedly observed between 1972 and 1983, until EXOSAT failed to detect it. It was observed in quiescence with EXOSAT and Chandra. If the duration of the outburst and of the quiescent phases are typical for this source, then its low temperature may be consistent with enhanced neutrino emission in the core of the neutron star;

- XB 1905+000 was detected in the accretion phase from 1974 to the mid-1980s and was not observed since then (Jonker *et al.*, 2007).

5.5.2 Previous modelings of the thermal relaxation

5.5.2.1 KS 1731-260

Since KS 1731-260 underwent a long accretion phase of ~ 12 years, Rutledge *et al.* (2002) suggested that the crust of the neutron star was heated up by the deep crustal reactions while the temperature of the core was not affected. The crust is much hotter than the

core of the neutron star and the quiescent luminosity is dominated by the emission from the cooling crust and not from the core. So the temperature decrease after the accretion stops is due to the thermal relaxation of the crust. Rutledge *et al.* (2002) predicted that the thermal equilibrium between the core and the crust is reached in $1 - 30$ yr. Thus, monitoring the temperature evolution after the accretion stopped in quasi-persistent X-ray transients enable to put constraint on the properties of the matter in neutron stars, in particular in the crust.

Rutledge *et al.* (2002) presented different cooling scenarios for various core and crust microphysics inputs that were compared with observations of KS 1731-260 by Cackett *et al.* (2006). The latter concluded that the core undergoes enhanced neutrino emission due to DUrca processes and that the crust has a high thermal conductivity due to the absence or a low fraction of impurities. In fact, the hydrogen and helium burning in the outer layers of neutron stars produce a mixture of elements that then enters the crust. The nuclear reactions that matter undergoes while sinking into the crust then reduce the number of different elements. At a given density, a single type of elements dominates as predicted by the crustal equation of state. However, there might still be a small fraction of other elements that are called the impurities. The impurity parameter :

$$Q_{\rm imp} = \frac{\sum_i n_i \left(Z_i - \langle Z \rangle\right)^2}{\sum_i n_i} \tag{5.42}$$

with n_i and Z_i the density and charge number of the ith species and the mean ionic charge number :

$$\langle Z \rangle = \frac{\sum_i n_i Z_i}{\sum_i n_i}. \tag{5.43}$$

The impurity parameter measures the distribution of the nuclide charge numbers and therefore the presence of impurities.

Shternin *et al.* (2007) reported new and precise calculations of the thermal relaxation of KS 1731-260. They tested in particular different crustal equations of state (catalyzed or accreted), thermal conductivities and superfluidities in the crust and neutron star models (mass, equations of state, Urca processes). For a given model, they obtained the values for the surface temperature before accretion started and for the accretion rate that best reproduce the observations. Note that the accretion rate is constrained by the observations : $\dot{M} \lesssim 5 \times 10^{-9}$ M$_\odot$ yr^{-1} (Wijnands *et al.*, 2002a; Yakovlev *et al.*, 2003). The accretion rate is assumed to be constant with a value $\dot{M}$ in the active phase and to switch to a null value in the quiescent phase. Shternin *et al.* (2007) showed that the observations are best modeled for a neutron star with :

- a thin crust ie. a massive neutron star : a thicker crust implies a longer thermal relaxation;
- with crustal neutron superfluidity : since a superfluid crust has a smaller heat capacity, the thermal relaxation is fastened;

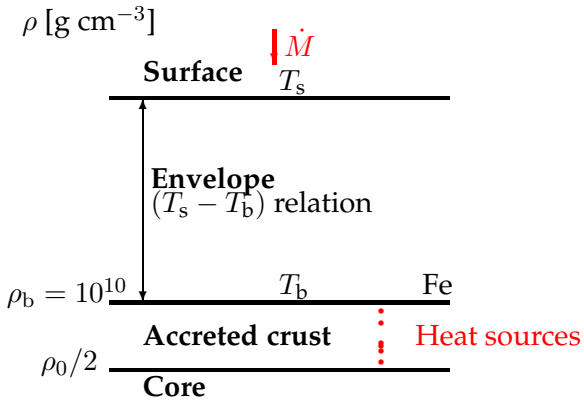

Figure 5.7: Schematic structure of an accreting neutron star for the models employed so far, for example in Shternin *et al.* (2007); Brown & Cumming (2009). See text for details.

- with a low fraction of impurities in the crust : the presence of impurities decreases the thermal conductivity and slows down the relaxation;
- with moderate neutrino emission : DUrca process makes the neutron star too cold too fast and thus requires a too high accretion rate which is not consistent with the observations.

They also predict that the thermal relaxation is not over.

Brown & Cumming (2009) reperformed cooling simulation of the thermal relaxation of KS 1731-260. Their conclusions are in agreement with the ones from Shternin *et al.* (2007). However, they find that the observations are consistent with $Q_{\rm imp} \sim 1$.

5.5.2.2 MXB 1659-29

Simulations of the thermal relaxation of MXB 1659-29 were also presented by Brown & Cumming (2009). They obtained conclusions similar to the ones for KS 1731-260 and an impurity parameter $Q_{\rm imp} \sim 5$.

5.5.2.3 Simulations with the `NSCool` code

I have also modeled the thermal relaxations of KS 1731-260 and MXB 1659-29 with the `NSCool` code. The latter was adapted to simulate accreting neutron stars.

The model that has been used is schematically represented in figure 5.7. The prescription by Potekhin *et al.* (1997) for an accreted envelope is used. Heat sources due to deep crustal heating are included following Haensel & Zdunik (2008). The equation of state for the crust is derived from the same reference and for the core from Akmal *et al.* (1998). Superfluidity is taken into account : neutron $^1S_0$ pairing from Schwenk *et al.* (2003), proton $^1S_0$ pairing from Page *et al.* (2004) (gap a) and neutron $^3P_2$ pairing from

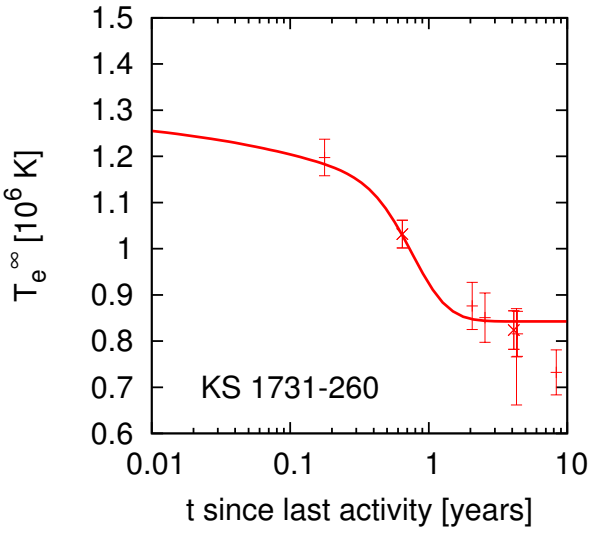

Figure 5.8: KS 1731-260 : best model for a 1.4 $M_\odot$ neutron star with $Q_{\rm imp} = 0$ and superfluidity in the crust. $\dot{M} = 2.6 \times 10^{-9}$ $M_\odot$/yr.

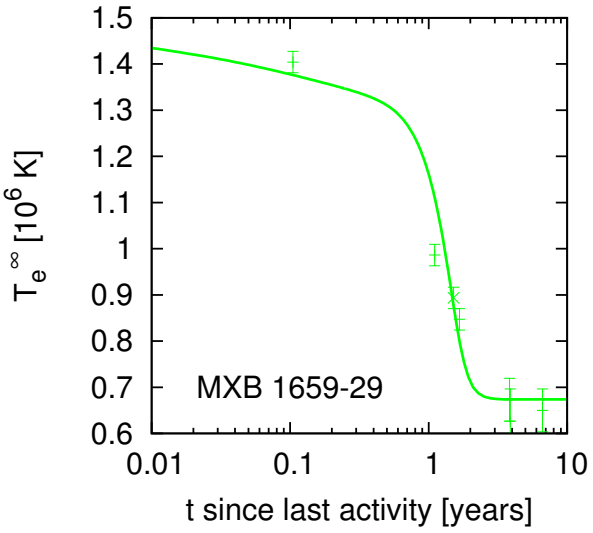

Figure 5.9: MXB 1659-29 : best model for a 1.4 $M_\odot$ neutron star with $Q_{\rm imp} = 2$ and superfluidity in the crust. $\dot{M} = 4 \times 10^{-9}$ $M_\odot$/yr.

Takatsuka (1973). All the relevant neutrino processes are included in the core and in the crust. The PBF processes are implemented following Leinson & Pérez (2006a).

Starting from an initially flat temperature profile, the neutron star undergoes accretion, described by a step-like function at a given rate $\dot{M}$ and for a given duration Δt.

The result for KS 1731-260 is presented in figure 5.8 where the temperature as seen by an observer at infinity is plotted as a function of the time since accretion stopped : $t = 0$ corresponds to the end of the accretion period and the beginning of the quiescent phase. I have got conclusions similar to the ones by Shternin *et al.* (2007); Brown & Cumming (2009) and noticed that I need not a non-zero impurity parameter to reproduce the observations.

Performing simulations for MXB 1659-29, I have observed that the thermal relaxation of a neutron star with a null impurity parameter is too fast to reproduce the observational data. Figure 5.9 shows that the relaxation is properly simulated for an impurity parameter $Q_{\rm imp} \sim 1 - 5$.

5.5.2.4 Other sources

There exists two more sources whose thermal relaxation has been observed : EXO 0748-676 and XTE J1701-462, as plotted on figure 5.6. However, their modeling is a real challenge and it has not been reported so far in the literature.

Source	$\tau_{\rm r}$ (days)
KS 1731-260	537 ± 125
MXB 1659-29	465 ± 35
EXO 0748-676	232 ± 63
XTE J1701-462	95 ± 16

Table 5.1: Thermal relaxation time scales $\tau_{\rm r}$ of the four quasi-persistent X-ray transients. For XTE J1701-462, the measurements showing a temperature increase due to residual accretion were excluded from the fit.

The solid lines in figure 5.6 are the best fits by an exponential decay of the thermal relaxation of the four quasi-persistent x-ray transients :

$$T_{\rm e}^{\infty}(t) = (T_{\rm out} - T_{\rm eq})\exp^{(-(t-t_0)/\tau_{\rm r})} + T_{\rm eq} \tag{5.44}$$

with $T_{\rm out}, T_{\rm eq}$ the temperature before accretion stopped and when thermal equilibrium between the core and the crust is reached, respectively and $\tau_{\rm r}$ the thermal relaxation time scale. Table 5.1 shows the value of this time scale for the four sources.

KS 1731-260 and MXB 1659-29 have relaxation time scales of the same order : ~ 500 days. Their thermal relaxation can be successfully modeled within the framework of the deep crustal heating scenario as presented in the previous paragraph.

The time scale of EXO 0748-676 is twice smaller and the relaxation is much faster. Therefore only a neutron star model with a very high mass (that has therefore a thin crust) can reproduce the observations. In particular, as shown on figure 5.10, I have managed to reproduce the relaxation with the `NSCool` for neutron stars with a mass $M = 1.8 - 2.0\,{\rm M}_{\odot}$. However, note that such modeling is inconsistent since the temperature measurements for EXO 0748-676 were obtained when considering a $1.4\,{\rm M}_{\odot}$ neutron star. Moreover, Zhang *et al.* (2011) obtained a mass of $1.55 \pm 0.12\,{\rm M}_{\odot}$ when fitting an XMM-Newton observation in quiescence with two neutron-star atmosphere models.

Finally, my simulations have shown that the thermal relaxation of XTE J1701-462, with a time scale of only ~ 100 days, is too fast to be modeled, even when DUrca processes are switched on.

XTE J1701-462 also exhibit a sudden increase in temperature ~ 225 days after the end of the outburst. This is believed to originate from residual accretion that is not taken into account in the calculations.

In conclusion the model presented in this section to reproduce the thermal relaxation of the quasi-persistent X-ray transients within the framework of the deep crustal heating scenario has inherent limitations that do not enable to simulate the observations.

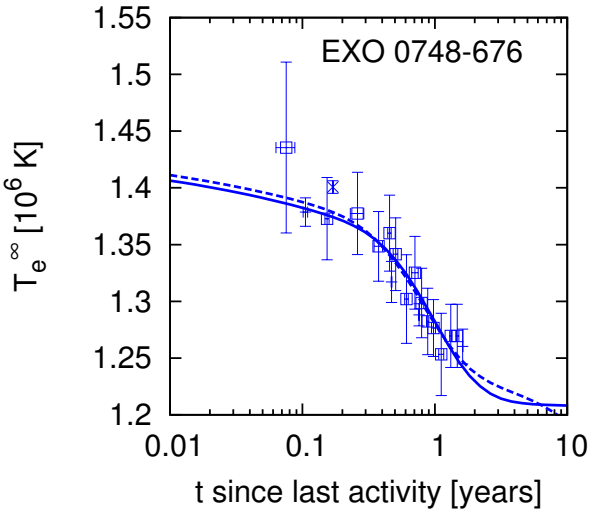

Figure 5.10: EXO 0748-676 : best models for a 1.8 $M_\odot$ neutron star for $\dot{M} = 1.7 \times 10^{-9}$ $M_\odot$/yr (solid line) and for a 2 $M_\odot$ neutron star for $\dot{M} = 1.8 \times 10^{-9}$ $M_\odot$/yr (dashed line) with $Q_{\rm imp} = 0$ and superfluidity in the crust for both models.

5.5.3 New model for an accreting neutron star

5.5.3.1 Microphysics input

The short thermal relaxation time scales of both EXO 0748-676 and XTE J1701-462 suggest that there exists heat sources at densities lower than the ones that have been considered so far. Moreover, the spurt of accretion at the origin of the temperature increase that XTE J1701-462 exhibits ~ 225 days after accretion stopped shows that residual accretion has to be taken into account in the models.

Figure 5.7 schematically shows the models that used so far (Shternin *et al.*, 2007; Brown & Cumming, 2009) to simulate the thermal relaxation. Heat sources due to deep crustal heating are included for densities ranging from $\rho_{\rm b} = 10^{10}$ to 10^{14} g cm^{-3}. The model of accreted envelope provides the relation between $T_{\rm b}$, the temperature at the density $\rho_{\rm b}$ and the surface temperature $T_{\rm s}$. However, it is not possible with such models to include heat sources at densities $\rho \leq \rho_{\rm b}$.

In collaboration with Leszek Zdunik and Paweł Haensel, I have developed a new preliminary model for accreting neutron stars as presented in figure 5.11, following the seminal works by Miralda-Escude *et al.* (1990); Zdunik *et al.* (1992). First, we consider that only one half of the accreted matter effectively enters the atmosphere and releases at the surface a photon luminosity $L_{\rm grav} = GM\dot{M}/2R$. Then, below the envelope, the accreted hydrogen burns into helium at a density of 10^5 g cm^{-3}, releasing $\epsilon_{\rm H} = 5$ MeV per accreted nucleon. At a density of 10^6 g cm^{-3}, the helium burning is unstable and occurs during bursts whose time scales are very short. Therefore, we do not include helium burning in the model. Finally a layer of iron extends up for densities between 10^6 g cm^{-3} and $\rho_{\rm b}$, at the outer boundary of the accreted crust.

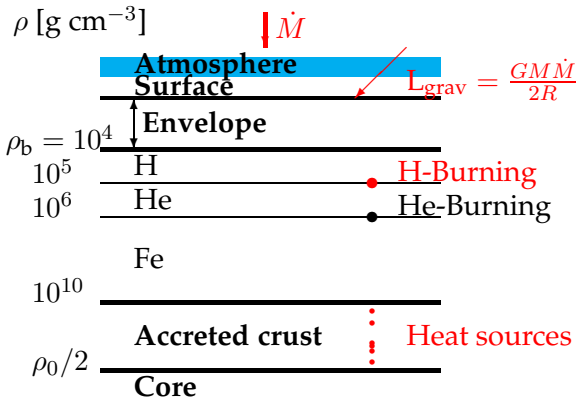

Figure 5.11: Schematic structure of an accreting neutron star for the new model. See text for details.

The analytical model of atmosphere developed by Hernquist & Applegate (1984) provides the relation between the temperature T_b at ρ_b and the surface temperature. With their equation (3.12) in the non-degenerate and non-relativistic regime, when photons dominate the heat transport, one gets :

$$T_s = 6.7 \times 10^{-5} \left(g_{14} \frac{A^3}{Z^4} \frac{T_b^{6.5}}{\rho_b^2} \right)^{1/4} \text{K}, \tag{5.45}$$

with g_{14} the surface gravity of the star, A and Z the mass and charge numbers respectively. For an hydrogen layer ($A = Z = 1$), one gets $T_s = 6.7 \times 10^{-7} \left(g_{14} T_b^{6.5} \right)^{1/4}$ K.

The microphysics properties in the layer extending for densities between 10^4 and 10^{10} g cm^{-3} that is composed of a fully ionized nonideal electron-ion plasma are accurately calculated :

- equation of state and specific heat : the code `eos10.f`[1] provides the pressure and specific heat according to Potekhin & Chabrier (2010);
- thermal conductivity : the code `condint.f`[2], based on the calculations presented in Potekhin (1999); Potekhin *et al.* (1999) is used;
- neutrino emission : according to Itoh *et al.* (1996), the neutrino emissivity at a density $\rho = 10^5$ g cm^{-3} is $Q_\nu \sim 1 - 10^{10}$ erg cm^{-3} s^{-1} $\ll Q_H$ the heat release from the hydrogen burning : $Q_H \sim 6 \times 10^{20} \dot{M}_{10}$ erg cm^{-3} s^{-1}. Therefore, the neutrino emission can be neglected.

[1] available online : `http://www.ioffe.ru/astro/EIP/index.html`
[2] available online : `http://www.ioffe.ru/astro/conduct/index.html`

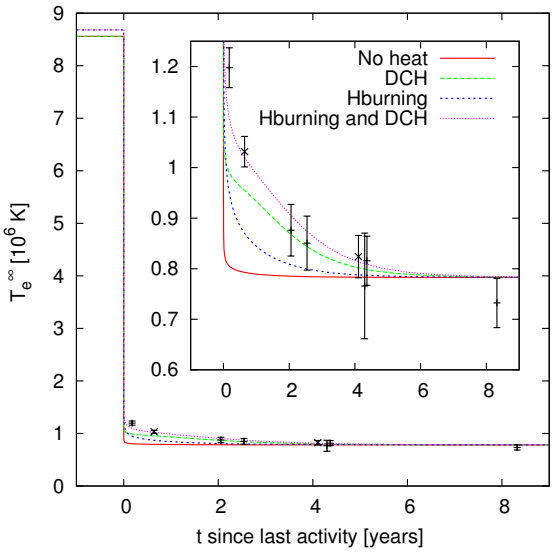

Figure 5.12: KS 1731-260 : modeling of the thermal relaxation for a 1.4 $M_\odot$ neutron star with $Q_{\rm imp} = 0$ and superfluidity in the crust for various sources of heat release : no heat source (solid line), only deep crustal heating (DCH - long dashed line), only hydrogen burning (Hburning - short dashed line) and both deep crustal heating and hydrogen burning (dotted line), for $\dot{M} = 2 \times 10^{-9}$ $M_\odot$ yr^{-1}.

5.5.3.2 Preliminary results

Influence of the inclusion of hydrogen burning

Figure 5.12 shows the influence of the model of heat release on the thermal relaxation curve for KS 1731-260. When sources are included in the crust, the photon and neutrinos losses are balanced the heat release in the crust. Therefore, the decrease in temperature after accretion stops is smoother. Hydrogen burning releases heat at a single density of 10^5 g cm^{-3} compared to deep crustal heating where the heat sources extend for densities between 10^9 and 10^{14} g cm^{-3}. Therefore, the smoothness of the curve in the case of deep crustal heating originate from the propagation of the heat from the various sources in the crust. The decrease in temperature is stiffer when considering only hydrogen burning than for deep crustal heating and as a consequence the thermal relaxation time scale is shorter. The inclusion of both hydrogen burning and deep crustal heating enables to reproduce the thermal relaxation of KS 1731-260.

Modeling of the four sources

Figures 5.13 and 5.14 compare the preliminary results of the new model with the ones of the old model for the thermal relaxation of KS 1731-260 and MXB 1659-29, respectively for a 1.4 $M_\odot$ neutron star. The main difference comes from the much higher temperature in the accretion phase for the new model. This originates from the inclusion of the gravitational luminosity $L_{\rm grav}$ at the surface of the neutron star that does *not* heats

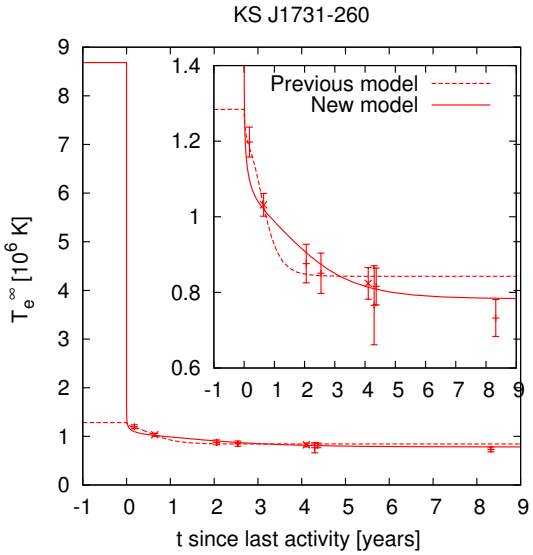

Figure 5.13: KS 1731-260 : best simulation for a 1.4 $M_\odot$ neutron star with $Q_{\rm imp} = 0$ and superfluidity in the crust. For the previous model (dashed line) : $\dot{M} = 2.6 \times 10^{-9}$ $M_\odot$ yr^{-1}. For the new one (solid line) : $\dot{M} = 2 \times 10^{-9}$ $M_\odot$ yr^{-1}.

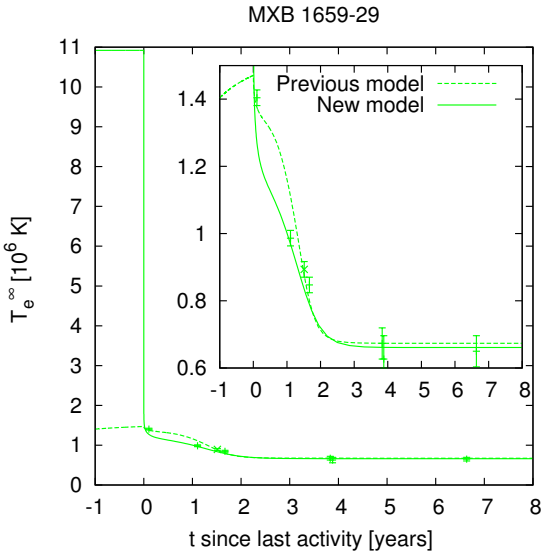

Figure 5.14: MXB 1659-29 : best simulation for a 1.4 $M_\odot$ neutron star. For the previous model (dashed line) : $\dot{M} = 4 \times 10^{-9}$ $M_\odot$ yr^{-1}, Qimp $= 2$. For the new one (solid line) : $\dot{M} = 5 \times 10^{-9}$ $M_\odot$ yr^{-1}, Qimp $= 0$.

the interior of the neutron star. The new model enables to reproduce the observations for reasonable values of the accretion rate and, in particular for MXB 1659-29, with a null impurity parameter.

The results of the modeling of the thermal relaxation of EXO 0748-676 and XTE J1701-462 for a 1.4 $M_\odot$ neutron star are presented in figures 5.15 and 5.16 respectively.

For the latter source, the observations that show a substantial temperature increase due to residual accretion (in black in the figure) are excluded. The accretion rate is modeled by two step-like functions :

- a first one with a constant accretion rate $\dot{M}_1$ that is the origin of the thermal relaxation;
- a second one with a rate $\dot{M}_2$ corresponding to the residual accretion that triggers the short temperature increase.

The new model enables to reproduce the observations of EXO 0748-676 and XTE J1701-462 for a 1.4 $M_\odot$ neutron star although they have a shorter relaxation time scale.

For the first time, the thermal relaxation of all the four quasi-persistent X-ray transients are successfully modeled.

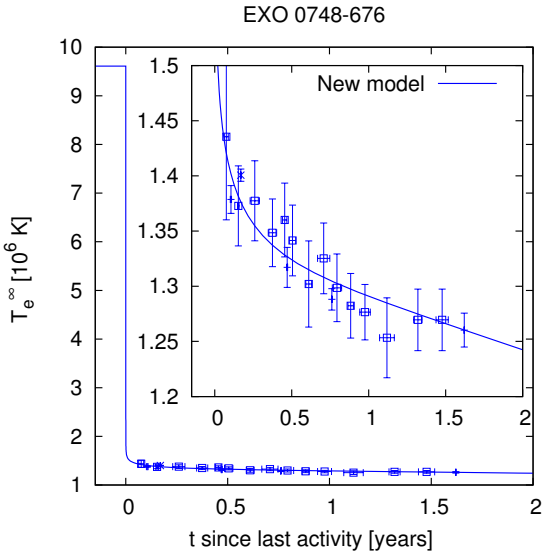

Figure 5.15: EXO 0748-676 : best simulation with the new model for a 1.4 $M_\odot$ neutron star with $Q_{\rm imp} = 0$ and superfluidity in the crust and for $\dot{M} = 3 \times 10^{-9}$ $M_\odot$ yr^{-1}.

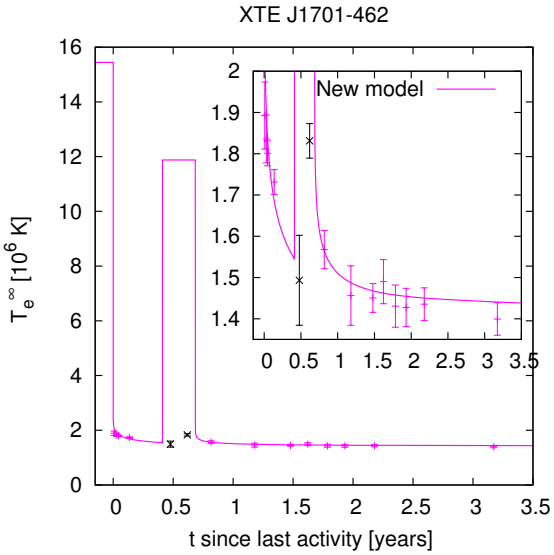

Figure 5.16: XTE J1701-462 : best simulation with the new model for a 1.4 $M_\odot$ neutron star for $\dot{M}_1 = 2 \times 10^{-8}$ $M_\odot$ yr^{-1}, $\dot{M}_2 = 7 \times 10^{-9}$ $M_\odot$ yr^{-1}. See text for details.

5.5.3.3 Perspectives

The new model for the thermal evolution of accreting neutron stars is still in progress.

In the near future, a realistic model for hydrogen and helium burnings and their stability that include the temperature and density dependences will be used. Indeed figure 5.17 shows the influence on the thermal relaxation curve of the model of hydrogen and helium burnings by varying the amount of hydrogen heat release $\epsilon_{\rm H}$ and burning densities $\rho_{\rm H}$ and $\rho_{\rm He}$ for hydrogen and helium respectively. Clearly, different models enable to reproduce the temperature evolution. It is therefore of major importance to take into account accurately the hydrogen and helium burnings in order to eventually model type I X-ray bursts and also constrain the microphysics properties of the crust of accreting neutron stars.

In collaboration with Agata Różańska (N. Copernicus Astronomical Center, Warsaw), a realistic model for the atmosphere of accreting neutron stars is being developed. Eventually, it will provides not only the relation $T_{\rm s} - T_{\rm b}$ but also the spectral properties of the emission. As a consequence, the model will be constrained not only by the temperature decrease but also by the observed spectra. Therefore, the influence of residual accretion on the thermal evolution will be assessed.

The new model presented in this thesis will describe for the first the thermal evolution in the whole neutron star, from the very center to the top of the envelope and will enable to reproduce both the thermal and spectral evolutions.

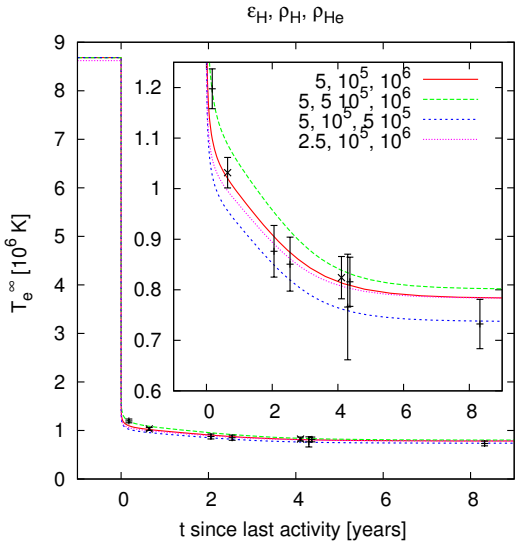

Figure 5.17: KS 1731-260 : modeling of the thermal relaxation for a 1.4 $M_\odot$ neutron star with $Q_{\rm imp} = 0$ and superfluidity in the crust for a given accretion rate : $\dot{M} = 2 \times 10^{-9}$ $M_\odot$ yr^{-1} and for various models of hydrogen and helium burning, varying the amount of heat released by the hydrogen burnings $\epsilon_{\rm H}$ and the density of the burning $\rho_{\rm H}$ and $\rho_{\rm He}$ for hydrogen and helium respectively.

5.5.3.4 An exciting new source : IGR J17480-2446

In October 2010, an X-ray activity in the globular cluster Ter 5 located 5.5 kpc from the Earth was observed by Integral (Bordas *et al.*, 2010) and subsequent observations confirmed that the source is an accreting neutron star IGR J17480 − 2446 (Strohmayer & Markwardt, 2010). It had in fact already been observed in the past with Chandra but with a low-luminosity (Heinke *et al.*, 2006). The source in fact turned on in October 2010. The timing of the X-ray pulsations showed that the neutron star orbits a $\sim 0.4 - 1.5$ $M_\odot$ companion star from which it accretes matter, in ~ 21 h (Papitto *et al.*, 2011). In December 2010, the source turned to quiescence after ~ 10 weeks of active phase and Degenaar & Wijnands (2011) reported one observation during the thermal relaxation. Moreover from past observations, the pre-accretion temperature is known and is likely to be the quiescent temperature the source will reach when its thermal relaxation ends. An additional observation is presented in Degenaar *et al.* (2011a). In agreement with the observations reported in Degenaar *et al.* (2011a), Δt= 0.17 years. Figure 5.18 shows the evolution of the surface temperature of IGR J17480-2446, compared with the four quasi persistent X-ray transients.

The thermal relaxation time scale of IGR J17480-2446 $= \tau_{\rm r}$, defined in equation (5.44) and presented in table 5.2, when fitting the observations with an exponential decay can be determined : $\tau_{\rm r} \sim 200$. It is of the same order as the time scale obtained for EXO 0748-676 and clearly shows that heat sources at densities $\rho \leq 10^{10}$ g cm^{-3} have to be

Source	τ_r (days)
KS 1731-260	537 ± 125
MXB 1659-29	465 ± 35
EXO 0748-676	232 ± 63
XTE J1701-462	95 ± 16
IGR J17480-2446	197

Table 5.2: Thermal relaxation time scales τ_r of the five sources.

included in the models. However since the source accreted during a very short period 0.17 years, the modeling of the thermal relaxation is highly sensitive to the description of the hydrogen burning and is beyond the scope of the preliminary model presented in this thesis. Therefore, a precise model for the hydrogen and helium burning has to be included.

This source is the first normal transient whose thermal relaxation has been monitored despite the short duration of the outburst. It opens a new window on the thermal evolution of accreting neutron stars. In the near future, the relaxation of other normal transients may be observed by the present or next generation of X-ray satellites and enable to constrain the properties of accreting neutron stars.

In conclusion, modeling the thermal evolution of isolated and accreting neutron stars enable to understand the properties of the matter inside them. The models that have been developed so far take into account many aspects of the microphysics inside neutron stars as described in chapter 3 : superfluidity, neutrino emission processes, specific heat, thermal conductivity, envelope composition and properties.

The cooling of young neutron stars is sensitive to the properties of the crust which have to be precisely calculated. In particular, the influence of the cluster structure of the crust on the cooling has been shown to be non-negligible and non-trivial in chapter 4.

Finally, the theoretical modeling has to be consistently confronted with the observations of both isolated and accreting neutron stars (chapter 5). The soft X-ray transients provide information on the neutrino processes in the core and the thermal relaxation after a long accretion phase exhibited by the quasi-persistent X-ray transients constrain the properties of the crust.

In the near future, the models are expected to be further contrained by the observations from the next generation of X-ray satellites.

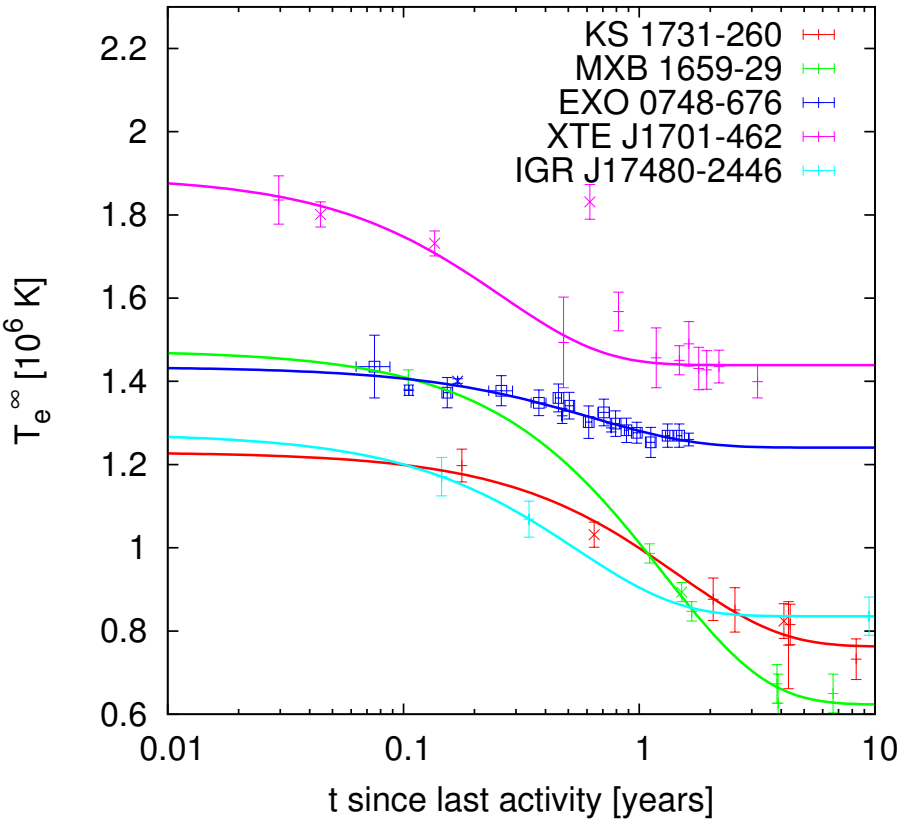

Figure 5.18: Observations of the five sources with best-fit exponential decay curves. $2-\sigma$ error bars.

Part III

Rotating elastic neutron stars

Introduction

Neutron stars rotate with periods ranging from few seconds to milliseconds and the effect of rotation on their properties has to be taken into account.

Chapter 6 presents the relativistic calculations for equilibrium configurations of rigidly rotating neutron stars, in a stationary, axisymmetric and circular spacetime, with an interior modeled by a perfect fluid. After discussing the 3+1 decomposition of spacetime and the formalism for stationary and axisymmetric configurations in section 6.1 and 6.2, section 6.3 introduces the Einstein equations for rotating stars. The latter are then derived in the special case when the interior of neutron stars is described as a perfect and rigidly rotating fluid in section 6.4. Section 6.5 presents a further slicing of spacetime, the 2+1+1 formalism and section 6.6, the `Nrotstar` code of the LORENE library that is used to compute equilibrium configurations of rotating neutron stars. Section 6.7 assesses the constraints that can be put on the microphysical properties by the observations of rotating neutron stars.

However, as explained in chapter 7, sudden changes in the rotation of neutron stars, that are called glitches have been observed and suggest that solid phases exist in neutron stars (section 7.1). These solid parts undergo elastic deformations that are not included in the perfect fluid description. After a short presentation of the Newtonian formalism for elasticity in section 7.2 and its application to the modeling of glitches, section 7.3 focuses on the relativistic formalism in particular the one developed by Carter & Quintana and its applications.

Chapter 8 presents the derivation of the relativistic equations for rotating neutron stars with a solid interior. After explaining how to describe the elastic deformations of rotating star in section 8.1, section 8.2 shows the generalization of the formalism developed in chapter 6 for a perfect fluid to a solid phase with elastic properties. The Newtonian limit is derived in section 8.3 and the numerical resolution of the relativistic equation for a solid interior that is currently in progress is presented in section 8.4 together with future perspectives in section 8.5.

This study of rotating neutron stars was performed in collaboration with Éric Gourgoulhon and Philippe Grandclément. Based on a preliminary study by E. Gourgoulhon fifteen years ago (Gourgoulhon, 1995a,b), I have derived the Einstein and equilibrium equations for a solid rotating neutron stars undergoing elastic deformations. I have created a new class called `Elastar` in the LORENE library and the numerical resolution of

the equations for equilibrium is now in progress.

In the following, Greek indices $(\alpha, \beta, \ldots)$ run in $\{0, 1, 2, 3\}$, Latin indices $(i, j, \ldots)$ in $\{1, 2, 3\}$ and indices $(a, b, \ldots)$ in $\{1, 2\}$. The Einstein summation convention on repeated indices is used. The vectors are noted $\vec{\boldsymbol{v}}$, the forms $\underline{\boldsymbol{u}}$ and the other tensors $\boldsymbol{T}$. The constants G and c that are respectively Newton gravitational constant and the speed of light are put to 1 :

$$G = 1 \qquad \text{and} \qquad c = 1.$$

Chapter 6

Rotating neutron stars

Contents

This chapter focuses on single rotating neutron stars with a fluid interior. The problem was first studied by Hartle (1967a); Hartle & Thorne (1968) for slow rotation, as a perturbation of spherically symmetric configurations. The work presented in this part is based on the formulation by Bonazzola *et al.* (1993), that first derived a system of four elliptic equations for an arbitrary rotation, and makes big use of the lecture notes of the 2010 Compstar school (Gourgoulhon, 2010) and of the review and book : Gourgoulhon (2007, 2012).

In particular are considered in the following stationary, axisymmetric and circular configurations in rigid rotation. 3+1 formalism, stationary, axisymmetric and circular spacetime and the derived Einstein equations are presented in sections 6.1, 6.2 and 6.3, respectively. The specific case of perfect fluid is developed in section 6.4. Section 6.5 introduces a further slicing of spacetime, the 2+1+1 formalism. Basics about the numerical resolution of the equations with `Nrotstar` code of the LORENE library for circular axisymmetric stationary configurations of rigidly rotating neutron stars are explained in section 6.6. Finally section 6.7 summarizes the constraints that can be put on the equation of state of dense matter from the observations of rotating neutron stars.

6.1 3+1 formalism

6.1.1 Spacetime foliation

Consider a spacetime $(\mathscr{M}, \boldsymbol{g})$ with $\mathscr{M}$ a $\mathcal{C}^\infty$ manifold of dimension 4 and $\boldsymbol{g}$ a Lorentzian metric on $\mathscr{M}$, of signature $(-,+,+,+)$. Let $\boldsymbol{\nabla}$ be the Levi-Civita connection associated with the metric $\boldsymbol{g}$.

The spacetimes generated by rotating stars have the property that they can be foliated by a family of spacelike hypersurfaces $(\Sigma_t)_{t\in\mathbb{R}}$ (they are indeed globally hyperbolic, see Gourgoulhon (2007) for a discussion), as shown on figure 6.1. An hypersurface Σ_t which is a submanifold of $\mathscr{M}$ of dimension 3 is said to be spacelike if any vector $\vec{\boldsymbol{v}}$ tangent to (Σ_t) is spacelike. The foliation is such that it covers $\mathscr{M}$ ie. :

$$\mathscr{M} = \bigcup_{t\in\mathbb{R}} \Sigma_t. \tag{6.1}$$

The parameter t labels the hypersurfaces Σ_t and is in fact some coordinate time. The vector $\vec{\boldsymbol{\nabla}} t$ associated to its gradient $\underline{\boldsymbol{\nabla}} t$ by the metric duality is normal to Σ_t.

Let $\vec{\boldsymbol{n}}$ be the unit 4-vector orthogonal to Σ_t. Since the latter is spacelike, $\vec{\boldsymbol{n}}$ is timelike. It can be future-oriented ie. oriented in the direction of increasing t. As a consequence, the two vectors $\vec{\boldsymbol{\nabla}} t$ and $\vec{\boldsymbol{n}}$ are colinear and one can write :

$$\vec{\boldsymbol{n}} = -N \vec{\boldsymbol{\nabla}} t. \tag{6.2}$$

with N the so-called the lapse function. The minus sign originates from the condition that $N \geq 0$ for increasing t.

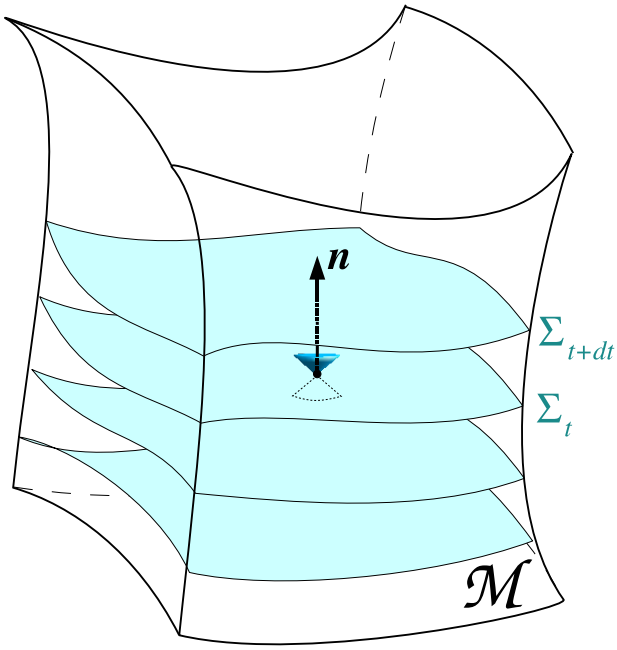

Figure 6.1: Spacetime foliation by a familly of spacelike hypersurfaces. Figure from Gourgoulhon (2007).

6.1.2 Induced metric

Let $\boldsymbol{h}$ be the 3-metric induced by $\boldsymbol{g}$ on the hypersurface Σ_t. It is in fact the restriction of $\boldsymbol{g}$ to the hypersurface and corresponds to the projection tensor onto Σ_t :

$$h_{\alpha\beta} = g_{\alpha\beta} + n_\alpha n_\beta. \tag{6.3}$$

Since Σ_t is spacelike, $\boldsymbol{h}$ is positive definite.

Let ${}^3\boldsymbol{\nabla}$ be the covariant derivative associated with the metric $\boldsymbol{h}$ on the hypersurface Σ_t. For any tensor $\boldsymbol{T}$ of type (p, q), it is given by the formula :

$${}^3\nabla_\rho T^{\alpha_1\ldots\alpha_p}{}_{\beta_1\ldots\beta_q} = h^{\alpha_1}{}_{\mu_1} \cdots h^{\alpha_p}{}_{\mu_p} h^{\nu_1}{}_{\beta_1} \cdots h^{\nu_q}{}_{\beta_q} h^\sigma{}_\rho \nabla_\sigma T^{\mu_1\ldots\mu_p}{}_{\nu_1\ldots\nu_q}. \tag{6.4}$$

6.1.3 Eulerian observer

An observer whose 4-velocity is $\vec{\boldsymbol{n}}$ is called an Eulerian observer or zero-angular momentum observer.

According to equation (6.2), the proper time τ of such an observer is given by :

$$d\tau = N dt. \tag{6.5}$$

The 4-acceleration of an Eulerian observer, which is tangent to Σ_t, is :

$$\vec{\boldsymbol{a}} = \boldsymbol{\nabla}_{\vec{n}} \vec{\boldsymbol{n}} \tag{6.6}$$

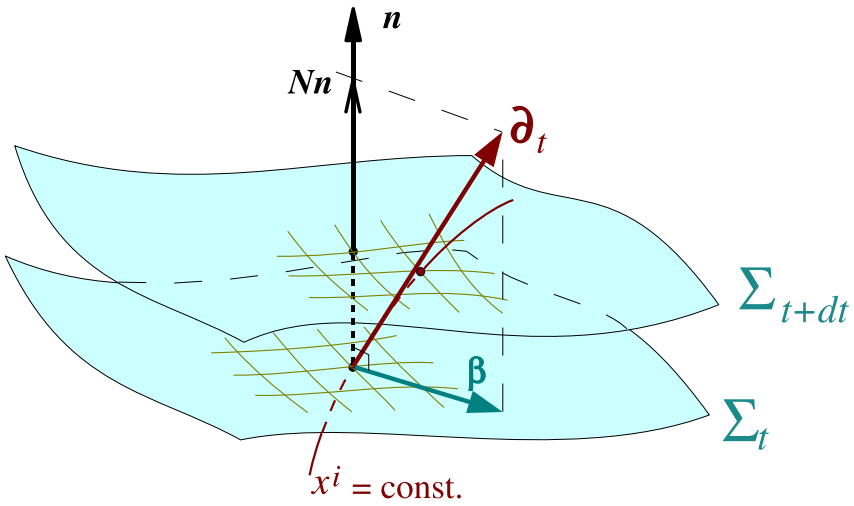

Figure 6.2: Decomposition (6.8) of time vector $\vec{\boldsymbol{\partial}}_t$. Figure from Gourgoulhon (2007).

and can be expressed as :

$$\vec{\boldsymbol{a}} = {}^3\boldsymbol{\nabla} \ln N. \tag{6.7}$$

6.1.4 Adapted coordinates

Let (x^α) be a coordinate system on $\mathscr{M}$. The system is said to be adapted to the foliation if and only if $(x^\alpha) = (t, x^1, x^2, x^3)$. Then $(x^i) = (x^1, x^2, x^3)$ constitute a coordinate system on each hypersurface Σ_t and are called the spatial coordinates.

The basis vector $\vec{\boldsymbol{\partial}}_t$ can be then decomposed into two parts : a part along $\vec{\boldsymbol{n}}$ and a part orthogonal to it, ie. tangent to Σ_t. Therefore, one can write :

$$\vec{\boldsymbol{\partial}}_t = N\vec{\boldsymbol{n}} + \vec{\boldsymbol{\beta}} \qquad \text{with} \quad \vec{\boldsymbol{n}} \cdot \vec{\boldsymbol{\beta}} = 0, \tag{6.8}$$

with $\vec{\boldsymbol{\beta}}$ a spacelike vector called the shift vector. It identifies the points with identical spatial coordinates on neighboring hypersurfaces as shown on figure 6.2. It is by definition tangent to Σ_t, so one can write $\vec{\boldsymbol{\beta}} = \beta^i \, \vec{\boldsymbol{\partial}}_i$.

Therefore, with equation (6.8) and (6.2) :

$$n^\alpha = \left(\frac{1}{N}, -\frac{\beta^1}{N}, -\frac{\beta^2}{N}, -\frac{\beta^3}{N} \right), \tag{6.9}$$

$$n_\alpha = (-N, 0, 0, 0)\,. \tag{6.10}$$

Finally, the components of the spacetime and induced metrics, $\boldsymbol{g}$ and $\boldsymbol{h}$ respectively, are related by the relation :

$$g_{\alpha\beta}\, dx^\alpha\, dx^\beta = -N^2 dt^2 + h_{ij}(dx^i + \beta^i dt)(dx^j + \beta^j dt). \tag{6.11}$$

6.1.5 Extrinsic curvature

The extrinsic curvature tensor $\boldsymbol{K}$ of the hypersurface Σ_t is :

$$\boldsymbol{K} = -\frac{1}{2}\mathcal{L}_{\vec{\boldsymbol{n}}}\,\boldsymbol{h}. \tag{6.12}$$

It is a symmetric tensor (Gourgoulhon, 2010) that is related to the variation of $\vec{\boldsymbol{n}}$ when moving on the hypersurface. In other words, it describes the embedding of the hypersurface Σ_t into the spacetime $(\mathscr{M}, \boldsymbol{g})$ (see the clear examples in Gourgoulhon (2007)).

It can be reexpressed :

$$K_{\alpha\beta} = -\nabla_\beta n_\alpha - a_\alpha n_\beta. \tag{6.13}$$

One can show that :

$$K_{\alpha\beta} = -h^\sigma_\beta \nabla_\sigma n_\alpha, \tag{6.14}$$

showing therefore that $\boldsymbol{K}$ is tangent to the hypersurface Σ_t.

The trace of the extrinsic curvature tensor $\boldsymbol{K}$ is :

$$K = -\boldsymbol{\nabla}\cdot\boldsymbol{n}. \tag{6.15}$$

6.1.6 3+1 decomposition of the stress-energy tensor

Let us define first the projector $\perp$ onto the 3-dimensional vector space $E_{\boldsymbol{u}}$ orthogonal to $\vec{\boldsymbol{u}}$:

$$\perp^\alpha{}_\beta = \delta^\alpha{}_\beta + u^\alpha u_\beta. \tag{6.16}$$

By definition $\perp^\alpha{}_\beta u^\beta = 0$.

Let $\boldsymbol{T}$ be the stress-energy tensor of the matter. The energy density E measured an observer with the 4-velocity $\vec{\boldsymbol{u}}$ is :

$$E = T_{\mu\nu}\,u^\mu u^\nu. \tag{6.17}$$

Its momentum density $\boldsymbol{p}$ is :

$$p_\alpha = -T_{\mu\nu}\,u^\nu \perp^\mu{}_\alpha \tag{6.18}$$

and its stress tensor $\boldsymbol{S}$:

$$S_{\alpha\beta} = T_{\mu\nu}\perp^\mu{}_\alpha \perp^\nu{}_\beta. \tag{6.19}$$

The energy momentum tensor $\boldsymbol{T}$ measured by an Eulerian observer can be calculated by putting $\vec{\boldsymbol{u}} = \vec{\boldsymbol{n}}$ and $\perp = \vec{\boldsymbol{h}}$ in equations (6.17-6.19). One gets :

$$\begin{aligned} E &= T_{\mu\nu}n^\mu n^\nu && (6.20)\\ p_\alpha &= -T_{\mu\nu}\,u^\nu h^\mu{}_\alpha && (6.21)\\ S_{\alpha\beta} &= T_{\mu\nu}h^\mu{}_\alpha h^\nu{}_\beta. && (6.22) \end{aligned}$$

Therefore the 3+1 decomposition of the energy-momentum tensor is :

$$T_{\alpha\beta} = E\,n_\alpha\,n_\beta + p_\alpha\,n_\beta + n_\alpha\,p_\beta + S_{\alpha\beta}. \tag{6.23}$$

The trace of $\boldsymbol{S}$ with respect to the metric $\boldsymbol{h}$ is $S = h^{ij}S_{ij}$.

6.1.7 3+1 Einstein equations

The Einstein equation is :

$$\boldsymbol{R} - \frac{1}{2} R\, \boldsymbol{g} = \frac{8\pi G}{c^4} \boldsymbol{T}, \tag{6.24}$$

with $\boldsymbol{R}$ the Ricci tensor associated with the Levi-Civita connection $\boldsymbol{\nabla}$ and its trace with respect to the metric is : $\boldsymbol{g}\ R = g^{\mu\nu} R_{\mu\nu}$.

The projection of the Einstein equation twice onto Σ_t, twice along $\vec{\boldsymbol{n}}$ and once onto Σ_t and once along $\vec{\boldsymbol{n}}$ gives (Gourgoulhon, 2012, 2010) :

$$\frac{\partial K_{ij}}{\partial t} - \mathcal{L}_{\vec{\boldsymbol{\beta}}} K_{ij} = -\,{}^3\nabla_i\, {}^3\nabla_j N + N \left\{ {}^3R_{ij} + K K_{ij} - 2K_{ik}K^k{}_j + 4\pi \left[(S-E) h_{ij} - 2S_{ij} \right] \right\} \tag{6.25}$$

$${}^3R + K^2 - K_{ij}K^{ij} = 16\pi E \tag{6.26}$$

$${}^3\nabla_j K^j{}_i - {}^3\nabla_i K = 8\pi p_i. \tag{6.27}$$

with E, p_i and S_{ij} measured by an Eulerian observer, given in equations (6.20)-(6.22).

Equations (6.26) and (6.27) are called the Hamiltonian and the momentum constraints, respectively.

$\mathcal{L}_{\vec{\boldsymbol{\beta}}} \boldsymbol{K}$, the Lie derivative of the tensor $\boldsymbol{K}$ along the vector $\vec{\boldsymbol{\beta}}$ is :

$$\mathcal{L}_{\vec{\boldsymbol{\beta}}} K_{ij} = \beta^k \frac{\partial K_{ij}}{\partial x^k} + K_{kj} \frac{\partial \beta^k}{\partial x^i} + K_{ik} \frac{\partial \beta^k}{\partial x^j}. \tag{6.28}$$

The Ricci tensor and scalar curvature of $\boldsymbol{h}$ are :

$${}^3R_{ij} = \frac{\partial\, {}^3\Gamma^k{}_{ij}}{\partial x^k} - \frac{\partial\, {}^3\Gamma^k{}_{ik}}{\partial x^j} + {}^3\Gamma^k{}_{ij}\, {}^3\Gamma^l{}_{kl} - {}^3\Gamma^l{}_{ik}\, {}^3\Gamma^k{}_{lj} \tag{6.29}$$

$${}^3R = h^{ij}\, {}^3R_{ij}. \tag{6.30}$$

The components of K are :

$$K_{ij} = -\frac{1}{2N} \left(\frac{\partial \gamma_{ij}}{\partial t} - \mathcal{L}_{\vec{\boldsymbol{\beta}}} \gamma_{ij} \right) \tag{6.31}$$

6.2 Circular, axisymmetric and stationary spacetimes

6.2.1 Stationarity and axisymmetry

In the following a spacetime $(\mathscr{M}, \boldsymbol{g})$ that is stationary, axisymmetric and asymptotically flat will be considered. Axisymmetry is relevant for a star with a fluid interior. Indeed, if it was non-axisymmetric, it would emit gravitational waves and would no longer be stationary.

For such a spacetime there exists two Killing vectors $\vec{\boldsymbol{\xi}}$ and $\vec{\boldsymbol{\chi}}$ associated with stationarity and axisymmetry, respectively. Asymptotic flatness means that, at spatial infinity,

$\vec{\boldsymbol{\xi}} \cdot \vec{\boldsymbol{\xi}} \to -1$ so that the parameter t is in fact the proper time of an inertial observer at infinity at rest with respect to the source. The Killing vector $\vec{\boldsymbol{\chi}}$ vanishes on the so-called axis of symmetry, which is a timelike 2-surface, is spacelike otherwise and has closed orbits (Gourgoulhon, 2010). At spatial infinity, $\vec{\boldsymbol{\chi}} \cdot \vec{\boldsymbol{\chi}} \to +\infty$ and $\vec{\boldsymbol{\xi}} \cdot \vec{\boldsymbol{\chi}} \to 0$.

Carter (1970) showed that the two Killing vectors commute :

$$[\vec{\boldsymbol{\xi}}, \vec{\boldsymbol{\chi}}] = 0, \tag{6.32}$$

with the commutator :

$$[\vec{\boldsymbol{\xi}}, \vec{\boldsymbol{\chi}}]^\alpha = \xi^\mu \nabla_\mu \chi^\alpha - \chi^\mu \nabla_\mu \xi^\alpha. \tag{6.33}$$

Therefore a possible choice of the two Killing vectors $\vec{\boldsymbol{\xi}}$ and $\vec{\boldsymbol{\chi}}$ is :

$$\vec{\boldsymbol{\xi}} = \vec{\boldsymbol{\partial}}_t, \tag{6.34}$$

$$\vec{\boldsymbol{\chi}} = \vec{\boldsymbol{\partial}}_\varphi. \tag{6.35}$$

The scalar function $\omega = \omega(r, \theta)$ is defined by :

$$\omega = -\frac{\vec{\boldsymbol{\xi}} \cdot \vec{\boldsymbol{\chi}}}{\vec{\boldsymbol{\chi}} \cdot \vec{\boldsymbol{\chi}}}. \tag{6.36}$$

For a rotating star, $\omega \geq 0$.

6.2.2 Circular spacetime

In addition, the stationary and axisymmetric spacetime is assumed to be circular. This is equivalent to suppose the absence of convective motion and that there is only circular motion around the axis of symmetry. This is in particular relevant for a perfect fluid interior rotating around the axis of symmetry.

One can distinguish two families of 2-surfaces (Gourgoulhon, 2010) :

- the surfaces of transitivity, each of them corresponding to fixed values of r and θ. Both Killing vectors $\vec{\boldsymbol{\xi}}$ and $\vec{\boldsymbol{\chi}}$ are everywhere tangent to them;
- the meridional surfaces, each having t and φ fixed on them.

Carter (1969) showed that for a circular space-time, the surfaces of transitivity are everywhere orthogonal to the meridional surfaces. This implies that the components g_{tr}, $g_{t\theta}$, $g_{\varphi r}$ and $g_{\varphi\theta}$ of the metric $\boldsymbol{g}$ are null.

The generalized Papapetrou theorem (Papapetrou, 1966; Carter, 1969) states that a stationary and axisymmetric spacetime ruled by the Einstein equation is circular if and only if the energy-momentum tensor $\boldsymbol{T}$ obeys to :

$$\xi^\mu T_\mu{}^{[\alpha} \xi^\beta \chi^{\gamma]} = 0 \tag{6.37}$$

$$\chi^\mu T_\mu{}^{[\alpha} \xi^\beta \chi^{\gamma]} = 0, \tag{6.38}$$

where the square brackets denote a full antisymmetrization.

Defining two vectors $\vec{\boldsymbol{V}}$ and $\vec{\boldsymbol{W}}$ by :

$$V^\alpha = \xi^\mu T_\mu{}^\alpha, \tag{6.39}$$
$$W^\alpha = \chi^\mu T_\mu{}^\alpha \tag{6.40}$$

the equations (6.37) and (6.38) are equivalent to

$$\vec{\boldsymbol{V}} \in \mathrm{Vect}(\vec{\boldsymbol{\xi}}, \vec{\boldsymbol{\chi}}) \tag{6.41}$$
$$\vec{\boldsymbol{W}} \in \mathrm{Vect}(\vec{\boldsymbol{\xi}}, \vec{\boldsymbol{\chi}}), \tag{6.42}$$

denoting that these vectors belong the vector plane generated by the two Killing vectors.

6.2.3 Metric

The adapted coordinates are chosen so that the components g_{tr}, $g_{t\theta}$, $g_{\varphi r}$ and $g_{\varphi\theta}$ of the metric $\boldsymbol{g}$ are zero and such that :

$$g_{ab}\, dx^a dx^b = A^2(r,\theta)(dr^2 + r^2 d\theta^2), \tag{6.43}$$

with $A(r,\theta)$ a scalar function.

Let the function B be defined by :

$$B^2(r,\theta) = \frac{g_{\varphi\varphi}}{r^2 \sin^2\theta}. \tag{6.44}$$

All in all, the components of the metric $\boldsymbol{g}$ for a stationary and axisymmetric and circular spacetime are :

$$g_{\alpha\beta}\, dx^\alpha\, dx^\beta = -N^2 dt^2 + A^2(dr^2 + r^2 d\theta^2) + B^2 r^2 \sin^2\theta (d\varphi - \omega dt)^2, \tag{6.45}$$

with N, A, B and ω four functions of (r,θ).

The comparison with the 3+1 form implies that :

- N is the lapse function,
- the shift vector $\vec{\boldsymbol{\beta}}$ is :

$$\beta^i = (0, 0, -\omega), \tag{6.46}$$

  and thus

$$n^\alpha = \left(\frac{1}{N}, 0, 0, \frac{\omega}{N}\right), \tag{6.47}$$
$$n_\alpha = (-N, 0, 0, 0), \tag{6.48}$$

- the induced metric $\boldsymbol{h}$ writes :

$$h_{ij}\, dx^i dx^j = A^2(dr^2 + r^2 d\theta^2) + B^2 r^2 \sin^2\theta\, d\varphi^2, \tag{6.49}$$

- equation (6.8) becomes :

$$\vec{\boldsymbol{\xi}} = N\vec{\boldsymbol{n}} - \omega\vec{\boldsymbol{\chi}}. \tag{6.50}$$

6.2.4 Maximal slicing

The components of the extrinsic curvature tensor $\boldsymbol{K}$ and its traces can then be calculated (Gourgoulhon, 2010) :

$$K_{r\varphi} = K_{\varphi r} = -\frac{B^2 r^2 \sin^2\theta}{2N}\frac{\partial \omega}{\partial r}, \tag{6.51}$$

$$K_{\theta\varphi} = K_{\varphi\theta} = -\frac{B^2 r^2 \sin^2\theta}{2N}\frac{\partial \omega}{\partial \theta}, \tag{6.52}$$

and the other components are equal to zero.

Since the trace of $\boldsymbol{K}$: $K = 0$, the foliation of the spacetime by a family of spacelike hypersurfaces $(\Sigma_t)_{t\in\mathbb{R}}$ is called a maximal slicing.

6.3 Einstein equations for rotating stars

The system of elliptic partial differential equations, with the quantities E, p_φ, ${S^r}_r$, ${S^\theta}_\theta$ and ${S^\varphi}_\varphi$ evaluated for an Eulerian observer is (Gourgoulhon, 2010) :

$$\boxed{\Delta_3 \nu = 4\pi A^2 (E+S) + \frac{B^2 r^2 \sin^2\theta}{2N^2}\,\partial\omega\partial\omega - \partial\nu\partial(\nu + \ln B)}, \tag{6.53}$$

$$\boxed{\tilde{\Delta}_3(\omega r \sin\theta) = -16\pi \frac{NA^2}{B^2}\frac{p_\varphi}{r\sin\theta} + r\sin\theta\,\partial\omega\partial(\nu - 3\ln B)}, \tag{6.54}$$

$$\boxed{\Delta_2\left[(NB-1) r\sin\theta\right] = 8\pi N A^2 B r \sin\theta ({S^r}_r + {S^\theta}_\theta)}, \tag{6.55}$$

$$\boxed{\Delta_2(\ln A + \nu) = 8\pi A^2 {S^\varphi}_\varphi + \frac{3B^2 r^2 \sin^2\theta}{4N^2}\,\partial\omega\partial\omega - \partial\nu\partial\nu}, \tag{6.56}$$

with :

$$\nu = \ln N \tag{6.57}$$

$$\Delta_2 = \frac{\partial^2}{\partial r^2} + \frac{1}{r}\frac{\partial}{\partial r} + \frac{1}{r^2}\frac{\partial^2}{\partial\theta^2} \tag{6.58}$$

$$\Delta_3 = \frac{\partial^2}{\partial r^2} + \frac{2}{r}\frac{\partial}{\partial r} + \frac{1}{r^2}\frac{\partial^2}{\partial\theta^2} + \frac{1}{r^2\tan\theta}\frac{\partial}{\partial\theta} \tag{6.59}$$

$$\tilde{\Delta}_3 = \Delta_3 - \frac{1}{r^2\sin^2\theta} \tag{6.60}$$

$$\partial u\partial v = \frac{\partial u}{\partial r}\frac{\partial v}{\partial r} + \frac{1}{r^2}\frac{\partial u}{\partial\theta}\frac{\partial v}{\partial\theta}. \tag{6.61}$$

Δ_2 is the Laplacian in a 2-dimensional flat space with the polar coordinates (r,θ) and Δ_3 the 3-dimensional axisymmetric Laplacian in a flat space.

Under the assumption of asymptotic flatness ie. that at infinity the metric $\boldsymbol{g}$ equals the Minkowski metric $\boldsymbol{\eta}$:

$$\eta_{\alpha\beta}\, dx^\alpha\, dx^\beta = -dt^2 + dr^2 + r^2 d\theta^2 + r^2 \sin^2\theta\, d\varphi^2. \tag{6.62}$$

the boundary conditions for the Einstein equations are, when $r \to +\infty$:

$$N \to 1, \tag{6.63}$$
$$A \to 1, \tag{6.64}$$
$$B \to 1, \tag{6.65}$$
$$\omega \to 0. \tag{6.66}$$

6.4 Perfect fluid

Let us consider now that the matter can be modeled by a perfect fluid. This consists in neglecting the shear stresses, the viscosity and the heat conduction.

The energy-momentum tensor of a perfect fluid with a 4-velocity $\vec{\boldsymbol{u}}$ is :

$$\boldsymbol{T} = (\varepsilon + p)\underline{\boldsymbol{u}} \otimes \underline{\boldsymbol{u}} + p\, \boldsymbol{g}, \tag{6.67}$$

with ε and p the energy density and the pressure, respectively, both in the fluid frame. For an observer comoving with the fluid :

$$E = \varepsilon, \quad p_\alpha = 0, \quad , \varphi_\alpha = 0, \quad S_{\alpha\beta} = p\, \perp_{\alpha\beta}. \tag{6.68}$$

6.4.1 Circularity

The left-hand side of the circularity conditions (6.37) and (6.38) is (Gourgoulhon, 2010) :

$$\xi^\mu T_\mu{}^{[\alpha} \xi^\beta \chi^{\gamma]} = (\varepsilon + p)\xi^\mu u_\mu\, u^{[\alpha} \xi^\beta \chi^{\gamma]}, \tag{6.69}$$
$$\chi^\mu T_\mu{}^{[\alpha} \xi^\beta \chi^{\gamma]} = (\varepsilon + p)\chi^\mu u_\mu\, u^{[\alpha} \xi^\beta \chi^{\gamma]}. \tag{6.70}$$

Since $\vec{\boldsymbol{\xi}}$ and $\vec{\boldsymbol{u}}$ being both timelike and $\xi^\mu u_\mu \neq 0$, the circularity conditions impose :

$$u^{[\alpha} \xi^\beta \chi^{\gamma]} = 0. \tag{6.71}$$

In other words,

$$\vec{\boldsymbol{u}} \in \mathrm{Vect}(\vec{\boldsymbol{\xi}}, \vec{\boldsymbol{\chi}}). \tag{6.72}$$

Therefore, one can write

$$\vec{\boldsymbol{u}} = u^t \left(\vec{\boldsymbol{\xi}} + \Omega \vec{\boldsymbol{\chi}} \right), \tag{6.73}$$

with

$$\Omega = \frac{u^\varphi}{u^t} = \frac{d\varphi}{dt}. \tag{6.74}$$

This describes a pure circular motion around the rotation axis of the star.

6.4.2 Decomposition of the fluid velocity

With equation (6.50), equation (6.73) can be rewritten :

$$\vec{\boldsymbol{u}} = (Nu^t)\left[\vec{\boldsymbol{n}} + \frac{1}{N}(\Omega - \omega)\vec{\boldsymbol{\chi}}\right], \tag{6.75}$$

$$= \Gamma\left(\vec{\boldsymbol{n}} + \vec{\boldsymbol{U}}\right) \tag{6.76}$$

with Γ the Lorentz factor of the fluid with respect to an Eulerian observer

$$\Gamma = Nu^t. \tag{6.77}$$

The fluid 3-velocity, that is a spacelike vector orthogonal to $\vec{\boldsymbol{n}}$, with respect to the same observer is :

$$\vec{\boldsymbol{U}} = \frac{1}{N}(\Omega - \omega)\vec{\boldsymbol{\chi}}. \tag{6.78}$$

Defining

$$\boxed{U = \frac{B}{N}(\Omega - \omega)r\sin\theta}, \tag{6.79}$$

since

$$\Gamma = -\vec{\boldsymbol{n}} \cdot \vec{\boldsymbol{u}}, \tag{6.80}$$

one gets the usual relation :

$$\Gamma = \left(1 - U^2\right)^{-1/2}. \tag{6.81}$$

6.4.3 Energy-momentum tensor

With equation (6.75), the quantities E, p_φ, $S^r{}_r$, $S^\theta{}_\theta$ and $S^\varphi{}_\varphi$ of the energy-momentum tensor $\boldsymbol{T}$ given in equations (6.17-6.19) can be calculated :

$$\boxed{E = \Gamma^2(\varepsilon + p) - p}, \tag{6.82}$$

$$\boxed{p_\varphi = B(E + p)Ur\sin\theta}, \tag{6.83}$$

$$\boxed{S^r{}_r = p}, \tag{6.84}$$

$$\boxed{S^\theta{}_\theta = p}, \tag{6.85}$$

$$\boxed{S^\varphi{}_\varphi = p + (E + p)U^2}, \tag{6.86}$$

$$\boxed{S = 3p + (E + p)U^2}. \tag{6.87}$$

6.4.4 Fluid equilibrium

6.4.4.1 Euler equation

Assuming a zero temperature, the equation of state can be written as :

$$\varepsilon = \varepsilon(n_{\rm b}) \tag{6.88}$$
$$p = p(n_{\rm b}), \tag{6.89}$$

with $n_{\rm b}$ the baryon number density in the fluid frame.

For a perfect fluid, a relativistic version of the Euler equation can be obtained :

$$u^\mu \nabla_\mu (h u_\alpha) + \nabla_\alpha h = 0, \tag{6.90}$$

with the enthalpy per baryon :

$$h = \frac{\varepsilon + p}{n_{\rm b}}. \tag{6.91}$$

6.4.4.2 Bernoulli theorem

Contracting the Euler equation with ξ^α, one gets the relativistic generalization of the classical Bernoulli theorem :

$$\boldsymbol{\nabla}_{\vec{\boldsymbol{u}}}(h\vec{\boldsymbol{u}} \cdot \vec{\boldsymbol{\xi}}) = 0. \tag{6.92}$$

It can be reexpressed in the form :

$$H + \nu + \ln\Gamma + \ln\left(1 + \frac{\omega}{N}\vec{\boldsymbol{\chi}} \cdot \vec{\boldsymbol{U}}\right) = \text{constant along a fluid line}, \tag{6.93}$$

where H is the log-enthalpy :

$$H = \ln\left(\frac{h}{m_{\rm b}}\right), \tag{6.94}$$

with $m_{\rm b}$ the mean baryon mass : $m_{\rm b} \simeq 1.66 \times 10^{-27}$ kg.

6.4.4.3 First integral of motion

Rewritting the fluid 4-velocity

$$\vec{\boldsymbol{u}} = u^t \vec{\boldsymbol{k}}, \tag{6.95}$$

with

$$\vec{\boldsymbol{k}} = \vec{\boldsymbol{\xi}} + \Omega\vec{\boldsymbol{\chi}}, \tag{6.96}$$

one gets :

$$\boldsymbol{\nabla} \ln(-h\vec{\boldsymbol{u}} \cdot \vec{\boldsymbol{k}}) - \frac{\vec{\boldsymbol{u}} \cdot \vec{\boldsymbol{\chi}}}{\vec{\boldsymbol{u}} \cdot \vec{\boldsymbol{k}}} \boldsymbol{\nabla}\Omega = 0. \tag{6.97}$$

In the following, rigid rotation will be considered ie. $\Omega =$ constant. Equation (6.97) then becomes :

$$\ln(-h\vec{\boldsymbol{u}} \cdot \vec{\boldsymbol{k}}) = \text{constant}. \tag{6.98}$$

which is equivalent to the first integral of motion :

$$H + \nu - \ln \Gamma = \text{constant}. \tag{6.99}$$

$H_{\rm c}$ and $\nu_{\rm c}$ being the values of H and ν at the center of the star, the previous equation becomes :

$$\boxed{H = H_{\rm c} + \nu_{\rm c} - \nu + \ln \Gamma}, \tag{6.100}$$

The surface of the star is defined by the condition :

$$p = 0. \tag{6.101}$$

6.4.5 Global properties

6.4.5.1 Total baryon number

The total number of baryons in the star is :

$$\mathcal{N} = \int_{\Sigma_t} \Gamma n_{\rm b} A^2 B r^2 \sin\theta \, dr \, d\theta \, d\varphi \tag{6.102}$$

and the total baryon mass of the star :

$$M_{\rm b} = m_{\rm b} \mathcal{N}. \tag{6.103}$$

6.4.5.2 Gravitational mass

The gravitational mass of the star can be calculated from the equation :

$$M = \int_{\Sigma_t} \left[N(E+S) + 2\omega B (E+p) U r \sin\theta \right] A^2 B r^2 \sin\theta \, dr \, d\theta \, d\varphi. \tag{6.104}$$

6.4.5.3 Angular momentum

The angular momentum for a perfect fluid rotating star is given by the following formula :

$$J = \int_{\Sigma_t} (E+p) U A^2 B^2 r^3 \sin^2\theta \, dr \, d\theta \, d\varphi. \tag{6.105}$$

For a rigidly rotating star, one defines the moment of inertia :

$$I = \frac{J}{\Omega}. \tag{6.106}$$

6.4.5.4 Radius

Let $r_{\rm eq}$ be the radius at the equator, for $\theta = \pi/2$.

One can also define the circumferential radius :

$$R_{\rm circ} = B(r_{\rm eq}, \pi/2)\, r_{\rm eq}, \tag{6.107}$$

which is independent of the coordinate system. In particular $R_{\rm circ} \geq r_{\rm eq}$.

The equatorial radius of spinning neutron stars is larger than their polar radius $r_{\rm p}$ (see figure 6.4). This reflects the expected polar flattening and the oblateness of rotating stars.

6.4.5.5 Innermost stable circular orbit

Consider a test particle of mass m orbiting the star in the equatorial plane : $\theta = \pi/2$. Its 4-momentum is :

$$p^\alpha = \left(m\frac{dt}{d\tau}, m\frac{dr}{d\tau}, 0, m\frac{d\varphi}{d\tau} \right), \tag{6.108}$$

with τ is the proper time of the test particle.

Since $\vec{\boldsymbol{\xi}}$ and $\vec{\boldsymbol{\chi}}$ are two Killing vectors, there exists two conserved quantities :

$$E = -\vec{\boldsymbol{\xi}} \cdot \vec{\boldsymbol{p}} = -p_t = \text{constant} \tag{6.109}$$

$$L = \vec{\boldsymbol{\chi}} \cdot \vec{\boldsymbol{p}} = p_\varphi = \text{constant}. \tag{6.110}$$

with E the particle energy and L its angular momentum measured both by an Eulerian observer.

The equation of the test particle is given by the equation :

$$\frac{1}{2}\left(\frac{dr}{d\tau}\right)^2 + \mathcal{V}(r, \bar{E}, \bar{L}) = 0, \tag{6.111}$$

with

$$\bar{E} = \frac{E}{m} = \text{constant}, \tag{6.112}$$

$$\bar{L} = \frac{L}{m} = \text{constant}, \tag{6.113}$$

$$\mathcal{V}(r, \bar{E}, \bar{L}) = \frac{1}{2A^2}\left[1 - \frac{1}{N^2}\left(\bar{E} - \omega\bar{L}\right)^2 + \frac{\bar{L}^2}{B^2 r^2}\right], \tag{6.114}$$

with $\mathcal{V}(r, \bar{E}, \bar{L})$ an effective potential.

A circular orbit corresponds to $r = $ constant, ie. to :

$$\frac{dr}{d\tau} = 0 \qquad \text{and} \qquad \frac{d^2 r}{d\tau^2} = 0, \tag{6.115}$$

which is equivalent to

$$\mathcal{V} = 0 \qquad \text{and} \qquad \frac{d\mathcal{V}}{dr} = 0, \tag{6.116}$$

in other words to an extremum of the potential (6.114).

A circular orbit is stable if and only if the extremum of the potential is a minimum ie. :

$$\frac{\partial^2 \mathcal{V}}{\partial r^2} > 0. \tag{6.117}$$

Such an orbit is called the innermost-stable circular orbit (ISCO), or marginally stable orbit and its location is given by the equation (Gourgoulhon, 2010) :

$$\begin{aligned} &\frac{\partial^2 \nu}{\partial r^2} - 2\left(\frac{\partial \nu}{\partial r}\right)^2 + \frac{VBr}{N}\left(\frac{\partial^2 \omega}{\partial r^2} - 4\frac{\partial \nu}{\partial r}\frac{\partial \omega}{\partial r}\right) \\ &\quad + V^2\left[-\frac{\partial^2 \beta}{\partial r^2} + \frac{4}{r}\frac{\partial \beta}{\partial r} + 2\left(\frac{\partial \beta}{\partial r}\right)^2 + \frac{3}{r^2}\right] - \frac{V^2 B^2 r^2}{N^2}\left(\frac{\partial \omega}{\partial r}\right)^2 = 0, \end{aligned} \tag{6.118}$$

with the potential evaluated in $\theta = \pi/2$ and :

$$V = \frac{\frac{Br}{N}\frac{\partial \omega}{\partial r} \pm \sqrt{\frac{B^2 r^2}{N^2}\left(\frac{\partial \omega}{\partial r}\right)^2 + 4\frac{\partial \nu}{\partial r}\left(\frac{\partial \beta}{\partial r} + \frac{1}{r}\right)}}{2\left(\frac{\partial \beta}{\partial r} + \frac{1}{r}\right)}. \tag{6.119}$$

It in fact an equation in r and its solution is the radius of the ISCO, $r_{\rm ISCO}$. One can distinguish two cases : if $r_{\rm ISCO} > r_{\rm eq}$, then the ISCO exists. Otherwise, it is located inside the star and the stable orbits extend down to its surface.

6.5 (2+1)+1 formalism

In order to study magnetized neutron stars, Gourgoulhon & Bonazzola (1993) developed a formalism for noncircular axisymmetric and stationary spacetimes, that they called (2+1)+1 formalism. It consists in further foliating the spacetime : the hypersurfaces Σ_t themselves are foliated. In the following, the study will restrict to the (2+1)+1 foliation of axisymmetric and stationary spacetimes, that are circular.

6.5.1 Foliation of the Σ_t hypersurfaces

Let $\Sigma_{t\varphi}$ be the 2-surface at the intersection between the Σ_t hypersurface and the hypersurface defined by $\varphi =$ constant : Σ_φ. In the case of circular spacetime, the $\Sigma_{t\varphi}$ surfaces are in fact the meridional surfaces and both Killing vectors $\vec{\xi}$ and $\vec{\chi}$ are orthogonal to them.

Let $\vec{\boldsymbol{m}}$ be the unit 4-vector tangent to the hypersurfaces Σ_t and orthogonal to the 2-surfaces $\Sigma_{t\varphi}$, oriented in the direction of increasing φ. It is by a construction a spacelike vector that is colinear to the Killing vector $\vec{\boldsymbol{\chi}}$ and one can write :

$$\vec{\boldsymbol{\chi}} = M\vec{\boldsymbol{m}}, \tag{6.120}$$

with M a coefficient such that $M \geq 0$.

Therefore with the metric (6.45), one gets :

$$m^\alpha = \left(0, 0, 0, \frac{1}{M}\right), \tag{6.121}$$

$$m_\alpha = (-M\omega, 0, 0, M)\,. \tag{6.122}$$

6.5.2 Induced metric

By analogy with the (3+1) decomposition, let $\boldsymbol{k}$ be the 2-metric induced by $\boldsymbol{g}$ on the 2-surface $\Sigma_{t\varphi}$. It is in fact the projector tensor onto $\Sigma_{t\varphi}$:

$$k_{\alpha\beta} = g_{\alpha\beta} + n_\alpha n_\beta - m_\alpha m_\beta, \tag{6.123}$$

$$= h_{\alpha\beta} - m_\alpha m_\beta. \tag{6.124}$$

$\boldsymbol{k}$ is positive definite.

Let ${}^2\boldsymbol{\nabla}$ be the covariant derivative associated with the metric $\boldsymbol{k}$ on the 2-surface $\Sigma_{t\varphi}$. For any tensor $\boldsymbol{T}$ of type (p, q), it is given by the formula :

$${}^2\nabla_\rho T^{\alpha_1\ldots\alpha_p}{}_{\beta_1\ldots\beta_q} = k^{\alpha_1}{}_{\mu_1} \cdots k^{\alpha_p}{}_{\mu_p}\, k^{\nu_1}{}_{\beta_1} \cdots k^{\nu_q}{}_{\beta_q}\, k^\sigma{}_\rho\, \nabla_\sigma T^{\mu_1\ldots\mu_p}{}_{\nu_1\ldots\nu_q}. \tag{6.125}$$

Note that the covariant derivatives ${}^2\boldsymbol{\nabla}$ and ${}^3\boldsymbol{\nabla}$ are related :

$${}^2\nabla_\rho T^{\alpha_1\ldots\alpha_p}{}_{\beta_1\ldots\beta_q} = k^{\alpha_1}{}_{\mu_1} \cdots k^{\alpha_p}{}_{\mu_p}\, k^{\nu_1}{}_{\beta_1} \cdots k^{\nu_q}{}_{\beta_q}\, k^\sigma{}_\rho\, {}^3\nabla_\sigma T^{\mu_1\ldots\mu_p}{}_{\nu_1\ldots\nu_q}. \tag{6.126}$$

By analogy with the definition of $\vec{\boldsymbol{a}}$ as the 4-acceleration of $\vec{\boldsymbol{n}}$, let us define $\vec{\boldsymbol{b}}$ the projection onto Σ_t of the acceleration of $\vec{\boldsymbol{m}}$:

$$b^\alpha = h^\alpha{}_\nu\, m^\sigma \boldsymbol{\nabla}_\sigma\, m^\nu, \tag{6.127}$$

$$= m^\sigma\, {}^3\boldsymbol{\nabla}_\sigma m^\alpha, \tag{6.128}$$

$$= -\,{}^2\boldsymbol{\nabla}^\alpha \ln M. \tag{6.129}$$

6.5.3 Adapted coordinates

According to equation (6.124), the components of the spacetime and induced metrics, $\boldsymbol{g}$ and $\boldsymbol{k}$ respectively are related by the relation :

$$g_{\alpha\beta}\, dx^\alpha\, dx^\beta = -N^2 dt^2 + k_{ab}\, dx^a\, dx^b + M^2(d\varphi - \omega dt)^2. \tag{6.130}$$

Comparing with the metric (6.45), one gets :

$$\begin{aligned} k_{rr} &= A^2, && (6.131)\\ k_{\theta\theta} &= A^2 r^2, && (6.132)\\ k_{\theta r} &= 0, && (6.133)\\ k_{\theta r} &= 0, && (6.134)\\ M &= Br\sin\theta, && (6.135) \end{aligned}$$

and the metric writes :

$$g_{\alpha\beta}\, dx^\alpha\, dx^\beta = -N^2 dt^2 + A^2\left(dr^2 + r^2 d\theta^2\right)\, dx^a\, dx^b + B^2 r^2 \sin^2\theta (d\varphi - \omega dt)^2. \quad (6.136)$$

6.5.4 Extrinsic curvature

By analogy with $\boldsymbol{K}$, one can define $\boldsymbol{L}$ the extrinsic curvature tensor that describes the embedding of the 2-surface $\Sigma_{t\varphi}$ into the 3-manifold Σ_t :

$$L_{\alpha\beta} = -\frac{1}{2}\, {}^3\mathcal{L}_{\vec{\boldsymbol{m}}}\, k_{\alpha\beta}, \quad (6.137)$$

with ${}^3\mathcal{L}_{\vec{\boldsymbol{m}}}$ the Lie derivative along the vector field $\vec{\boldsymbol{m}}$ in the 3-manifold Σ_t. It is a symmetric tensor.

It can reexpressed as :

$$L_{\alpha\beta} = -\,{}^3\nabla_\beta m_\alpha + b_\alpha m_\beta, \quad (6.138)$$

One can show that :

$$L_{\alpha\beta} = -k_\beta{}^\sigma\, {}^3\nabla_\sigma m_\alpha, \quad (6.139)$$

showing therefore that $\boldsymbol{L}$ is tangent to the 2-surface $\Sigma_{t\varphi}$.

The trace of $\boldsymbol{L}$ is :

$$L = -\,{}^3\boldsymbol{\nabla}\cdot\boldsymbol{m}. \quad (6.140)$$

For a circular, axisymmetric and stationary spacetime, $L_{\alpha\beta} = 0$.

The extrinsic curvature tensor of the hypersurface Σ_t, $\boldsymbol{K}$ can be decomposed for a circular spacetime :

$$K_{\alpha\beta} = m_\alpha \kappa_\beta + \kappa_\alpha m_\beta, \quad (6.141)$$

with

$$\begin{aligned} \kappa_\alpha &= k_\alpha{}^\nu K_{\nu\sigma} m^\sigma, && (6.142)\\ &= -\frac{M}{2N}\, {}^2\nabla_\alpha \frac{\omega}{M}. && (6.143) \end{aligned}$$

6.6 Numerical resolution with LORENE

Several codes have been developed over the last twenty years by different groups (Stergioulas, 2003). Among them is the `Nrotstar` code (Bonazzola *et al.*, 1993, 1998; Gourgoulhon *et al.*, 1999) which is based on the LORENE library.

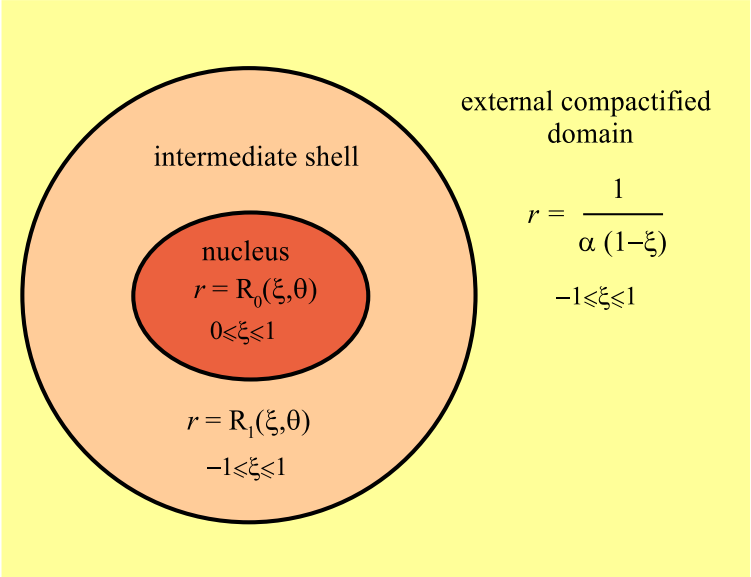

Figure 6.3: The different domains in the `nrotstar` code. From Gourgoulhon (2010).

6.6.1 Spectral methods

The equations to be solved to compute axisymmetric stationary configurations of rigidly rotating neutron stars can be divided into two groups :

- the Einstein equations (6.53)-(6.56) are Poisson-like, non-linear elliptic equations ;
- the other equations (6.82)-(6.87),(6.79) and (6.100) are algebraic.

The Einstein equations have to be solved in the whole space since their sources extend to infinity. They are solved by the mean of the multi-domain spectral methods (Bonazzola *et al.*, 1998). The all space is divided into three domains (or more), as shown in figure 6.3 :

- the non-spherical nucleus which corresponds to the interior of the star,
- an intermediate shell up to few equatorial radii, which includes the regions with a strong field,
- an external compactified domain covering the rest of the space up to infinity.

The spectral methods (Bonazzola *et al.*, 1999) consist in transforming a partial differential equation into an algebraic one. This is obtained by a series expansion of the solution on a complete basis. The choice of the basis depends on the problem and for the present study, Chebyshev polynomials in r and Legendre ones in θ (Gourgoulhon *et al.*, 1999) are used. Spectral methods reduce the number of grid points compared to finite differences and can achieve a high numeric precision.

6.6.2 LORENE library

LORENE, from the French "*Langage Objet pour la RElativité NumériquE*" (object-oriented language for numerical relativity) is a C++ library initiated by Jean-Alain Marck in 1997 at LUTh, in Meudon Observatory (France). It is a freely available software[1]. It uses a set of classes for each physical or mathematical object and makes a big use of derived classes.

6.6.3 Block diagram of the `Nrotstar` code

Figure 6.5 schematically shows the structure of the `Nrotstar` code, developed by Éric Gourgoulhon in 2010, based on the LORENE library. It is based on the so-called self-consistent-field method.

The accuracy of the `Nrotstar` calculations can be checked by evaluating two General Relativistic Virial identities : a 3-dimensional one, GRV3, presented in Gourgoulhon & Bonazzola (1994) and a 2D one, GRV2 (Bonazzola & Gourgoulhon, 1994).

6.6.4 An example

Figure 6.4 shows the results obtained with `Nrotstar` for a 1.4 $M_\odot$ neutron star rotating at the frequency $f = 716$ Hz, which is the highest observed for a pulsar (Hessels *et al.*, 2006). For the core the equation of state APR by Akmal *et al.* (1998) is used and for the crust the SL one by Douchin & Haensel (2001). The neutron star has a moderate oblateness. In particular the radius at the pole $r_{\rm p}$ is $\sim 88\%$ the one at the equator $r_{\rm eq}$.

6.7 Constraints on the equation of state for dense matter

6.7.1 Observations of millisecond pulsars

The first observed millisecond pulsar PSR B1937+214 (Backer *et al.*, 1982) was the fastest rotating neutron star ($P = 1.556$ ms, $f = 641$ Hz) until the discovery of PSR J1748-2446ad with $P = 1.396$ ms ($f = 716$ Hz) (Hessels *et al.*, 2006). Note that so far, there has been no confirmed observation of submillisecond pulsars. The optical observation of a half-millisecond pulsar in the supernova 1987A (Middleditch *et al.*, 1989) was in fact an artifact from the telescope devices. Recently, Kaaret *et al.* (2007) reported the observation of oscillations at the frequency $f = 1122$ Hz ($P = 0.89$ ms) in an X-ray burst from the X-ray transient XTE J1739-285. These may be interpreted as the rotational frequency of the neutron. However this observation was not confirmed.

[1] http://www.lorene.obspm.fr/

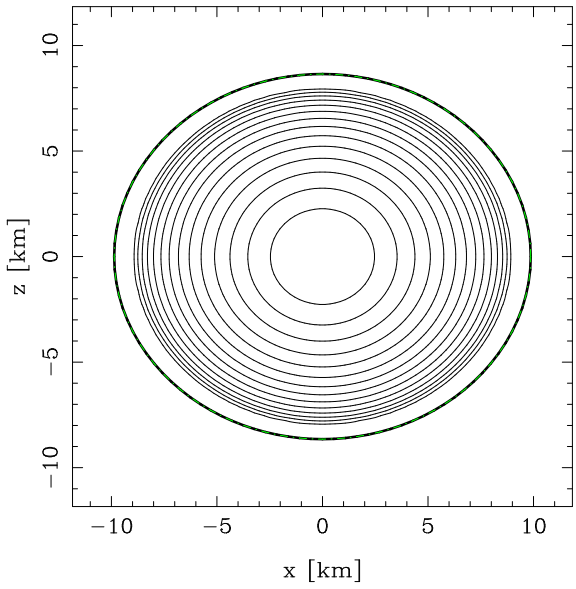

Figure 6.4: Isocontours of the proper energy density ε for a 1.4 $M_\odot$ neutron star rotating 716 Hz. The plot is made in the meridional plane $\varphi = 0$. The surface of the star corresponds to the thick line. The coordinates (x, z) are defined by $x = r \sin\theta$ and $z = r \cos\theta$. From Gourgoulhon (2010).

6.7.2 Maximum rotational frequency

The mass-shedding is an upper limit on neutron star rotational frequencies f. For a rigid sphere, one gets (Lattimer & Prakash, 2004) :

$$f_{\rm MS} = 1.83 \left(\frac{M}{\rm M_\odot}\right)^{1/2} \left(\frac{R}{10\ \rm km}\right)^{-3/2} \ \rm kHz, \tag{6.144}$$

with $f_{\rm MS}$ the mass-shedding rotational frequency and M and R the radius of the rotating neutron star.

A formula for the Keplerian frequency of neutron star was obtained for a set of equations of state (Haensel *et al.*, 2009) :

$$f_{\rm MS} \simeq 1.08 \left(\frac{M}{\rm M_\odot}\right)^{1/2} \left(\frac{R(M)}{10\ \rm km}\right)^{-3/2} \ \rm kHz, \tag{6.145}$$

with M is the gravitational mass of rotating star and $R(M)$ the circumferential radius of the non-rotating neutron star with a mass M. This is valid for masses ranging form 0.5 $M_\odot$ to 0.9 $M^{\rm NR}_{\rm max}$ with $M^{\rm NR}_{\rm max}$ the maximum mass for a non-rotating star with a given EoS.

Haensel *et al.* (1995) derived a formula for the absolute maximum value of the rotational frequency $f^{\rm max}_{\rm MS}$, obtained for a set of subluminal equations of state, with an accuracy of 5% :

$$f^{\rm max}_{\rm MS} \simeq 1.22 \left(\frac{M^{\rm NR}_{\rm max}}{\rm M_\odot}\right)^{1/2} \left(\frac{R^{\rm NR}_{\rm max}}{10\ \rm km}\right)^{-3/2} \ \rm kHz, \tag{6.146}$$

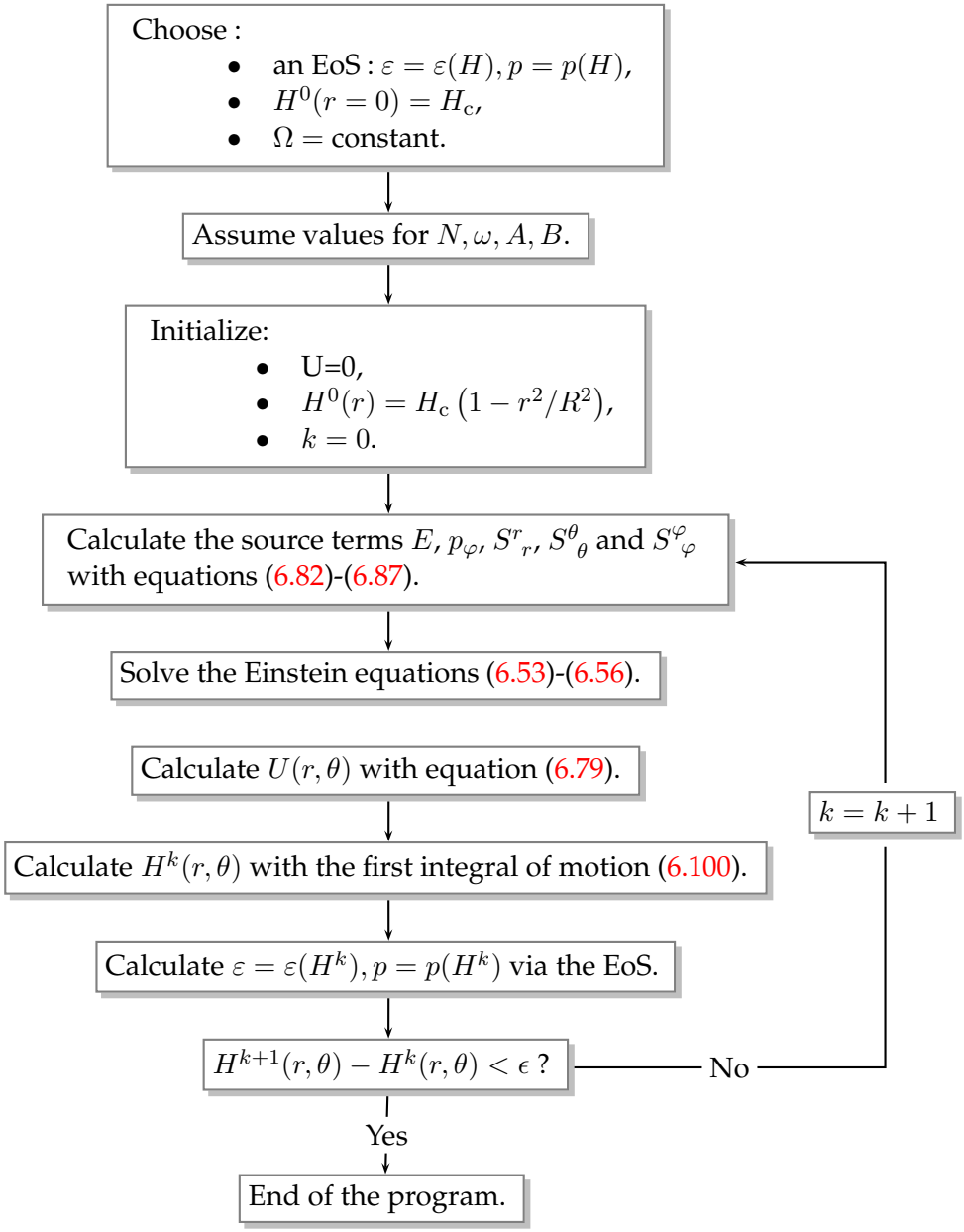

Figure 6.5: Schematic view of the `Nrotstar` code using the self-consistent field method. k is the step of the calculations, $H^k(r, \theta)$ the value of the log-enthalpy at the step k and ϵ the threshold for the convergence of the code.

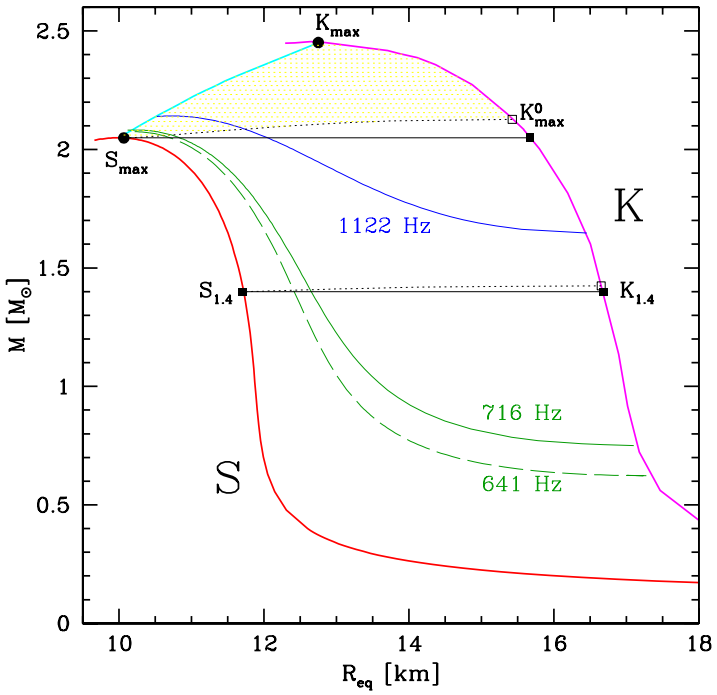

Figure 6.6: Gravitational mass M versus the equatorial radius $R_{\rm eq}$ for stable neutron stars configurations with different spin frequencies for the Douchin & Haensel (2001) equation of state. See text for details. From Haensel *et al.* (2009).

with $R_{\rm max}^{\rm NR}$ the radius of a non-rotating neutron star with the maximum attainable mass. This relation is of particular interest to assess the constraints put by the fastest rotating neutron stars on the equation of state of dense matter (see below).

By analogy with equation (2.18), one can derive an upper limit for the maximum mass of rotating neutron stars, that is reached when a neutron star rotates near the mass-shedding limit (Haensel *et al.*, 2007) :

$$M_{\rm max}^{\rm rot} \leq 3.89 \sqrt{\frac{5 \times 10^{14}\ {\rm g\ cm^{-3}}}{\rho_{\rm u}}}\ {\rm M}_\odot, \tag{6.147}$$

ie., with $\rho_{\rm u} \lesssim 2\rho_0$ the density below which the equation of state is assumed to be known,

$$M_{\rm max} \lesssim 3.89\ {\rm M}_\odot. \tag{6.148}$$

This value is 30% higher than for non-rotating configurations. This shows that the centrifugal force produced by rotation counteracts, together with the internal pressure, the gravitational pull and that therefore, higher masses are attainable for rotating neutron stars than for non-rotating ones.

6.7.3 Influence of rotation of the $M - R$ diagram

Figure 6.6 shows the $M - R_{\rm eq}$ relation with $R_{\rm eq}$ the equatorial radius for stable neutron stars configurations for the Douchin & Haensel (2001) equation of state. The relations are plotted a non-rotating neutron star (S line), stars rotating at the frequencies $f = 641, 716$ and 1122 Hz, corresponding to PSR B1937+214, PSR J1748-2446ad and XTE J1739-285 (unconfirmed), respectively. The K line corresponds to Keplerian configurations. The points $\mathrm{S_{max}}$ and $\mathrm{K_{max}}$ are the configurations with the maximum attainable mass for non-rotating and Keplerian neutron stars, respectively. As expected, the maximum mass increases with the rotational frequency. For a given mass, the equatorial radius also increases with the frequency.

The point $\mathrm{K^0_{max}}$ is the Keplerian configuration with $M_{\rm b} = M^{\rm NR}_{\rm b,max}$ the baryon mass of the maximum mass non-rotating neutron star. Neutron stars with configurations in the region located between the points $\mathrm{S_{max}}$, $\mathrm{K_{max}}$ and $\mathrm{K^0_{max}}$ are so-called supermassive and owe their existence to rotation. Note that a supermassive neutron star spinning down due to the loss of angular momentum collapses into a black hole. Finally, figure 6.7 is a $M - R$ diagram for different equations of state. The rotation frequencies of PSR B1937+214 and PSR J1748-2446ad hardly constrain the equation of state for dense matter. A very strong constraint would be given by the observation of a neutron star with at least a submillisecond period. Note that a half-millisecond period would rule out all the plotted equations of state for dense matter. This would suggest that the object is not a neutron star but a strange star (see eg. Haensel *et al.* (2007)).

This chapter focuses on rigidly rotating neutron stars, with $\Omega =$ constant. However, one may also consider differential rotation for which $\Omega = \Omega(r \sin\theta)$. This effect is expected to increase the maximum attainable mass for stable configurations. In particular, Morrison *et al.* (2004) showed that for nuclear equations of state, the maximum mass is $\sim 50\%$ higher than for non-rotating stars.

In this chapter, the Einstein equations for stationary, axisymmetric and circular configurations of rigidly rotating neutron stars with a fluid interior were considered. However, some parts of neutron stars, the crust for example, is expected to be solid and thus to undergo elastic deformations. These elastic properties are not taken into account in the fluid description presented in this chapter but further considered in the next two chapters.

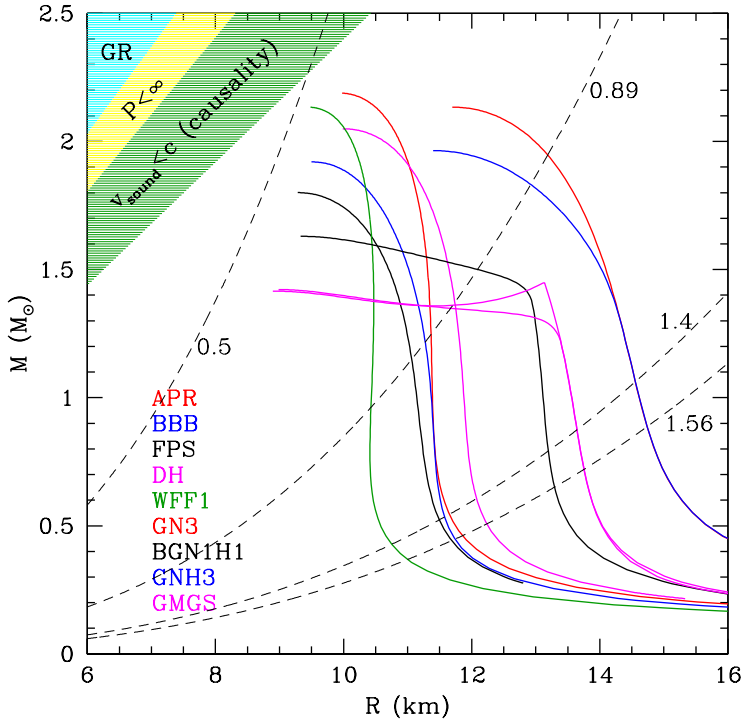

Figure 6.7: $M - R$ diagram for a set of representative equations of state for non-rotating neutron stars. The dashed lines correspond to the constraint resulting from different rotational frequency given by equation (6.146). The labels of the lines correspond to spin periods P in ms. Courtesy of J. L. Zdunik.

Chapter 7

Newtonian and relativistic elasticity

Contents

This chapter aims at presenting general aspects concerning elasticity in neutron stars. In section 7.1 are discussed the glitch phenomenon and the state of matter in neutron stars, showing that the crust is likely to be solid while the core may be liquid or solid. The solid parts of neutron stars undergo elastic deformations and the Newtonian formalism for the elasticity is presented in section 7.2, together with some simple models of (partly) solid neutron stars and of glitches. Section 7.3 reviews the different formalisms that have been developed to describe elasticity in the framework of General Relativity, with a special attention to the one by Carter & Quintana, that is extendedly used in the next chapter. The chapter concludes by a simple relativistic model for glitches.

7.1 Solid phases in neutron stars

7.1.1 Glitches

Radio pulsars are extremely stable rotators and are the most stable existing clocks in the long term compared with modern atomic clocks that are more stable in the short one. They exhibit a regular spin-down, ie. an increase of their rotational frequency f, that originates from the loss of rotational energy by the emission of electromagnetic radiation (see also section 1.3).

However, two types of irregularities have been observed in the timing of the rotation of pulsars (Lyne & Graham-Smith, 2005; Chamel & Haensel, 2008) :

- the timing noise that is observed random deviations in the pulse times of arrival. Its origin is not well understood;
- the glitches that are sudden jumps in the rotational frequency followed by an exponential recovery to the pre-glitch frequency, lasting from days to years (figure 7.1). They are rare events, occurring mostly in young pulsars.

Shortly after the discovery of radio pulsars, the first glitches were detected from the Vela and the Crab pulsars (Radhakrishnan & Manchester, 1969; Boynton *et al.*, 1969). Since then, ~ 100 glitches were observed from ~ 40 pulsars, one third of them from the Crab and Vela pulsars. The glitches of these two objects have the following properties :

- Vela pulsar (PSR B0833-45) : glitches occur every ~ 3 years with relative frequency jumps $\Delta\nu/\nu \sim 10^{-6}$;
- Crab pulsar (PSR B0531+21) : every several years, giant glitches are observed with $\Delta\nu/\nu \sim 10^{-8}$.

PSR J1806-2125 exhibited the strongest glitch ever : $\Delta\nu/\nu \sim 2 \times 10^{-5}$ (Hobbs *et al.*, 2002).

Note that glitches have been observed in X-rays in a millisecond pulsar, an accreting one and an Anomalous X-ray pulsar (Marshall *et al.*, 2004; Galloway *et al.*, 2004; Kaspi

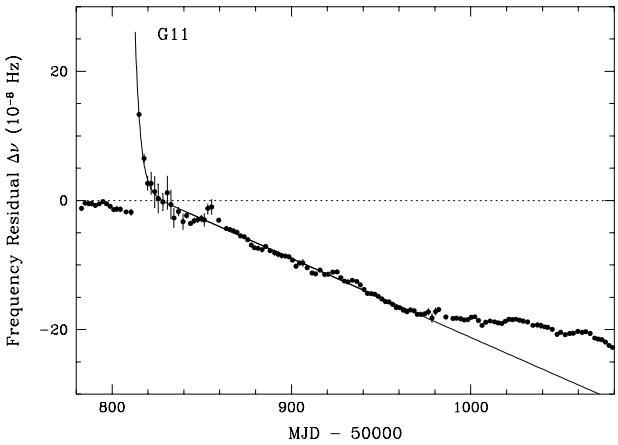

Figure 7.1: Evolution of the frequency residual $\Delta\nu = \nu - \nu_0$, with ν_0 the pre-glitch rotational frequency for a small glitch ($\Delta\nu/\nu \sim 9 \times 10^{-9}$) on December 30, 1997 from the Crab pulsar. The glitch is followed by an exponential decay with a timescale of 2.9 days. Figure from Wong *et al.* (2001).

& Gavriil, 2003).

The glitches and their exponential recovery originate from sudden adjustments of the neutron star structure during the spin-down and show neutron stars are made of two parts with at least a solid one. In fact, several models have been proposed to explain the glitch phenomenon (see also section 3.5.1 and Chamel & Haensel (2008)) :

- starquakes, that will be detailed in the following. A neutron star is made oblate by its rotation. As it slows down, its ellipticity decreases and the solid crust adjusts its structure by cracking and the neutron star becomes more spherical (Ruderman, 1969). The exponential recovery is due to the presence of superfluid matter in the interior (Baym *et al.*, 1969);

- interaction between two components. The observed exponential recovery suggests that neutron stars do not rotate as a single body but that they are made of two components which are loosely coupled : a solid crust that spins down due to magnetic braking and a superfluid component that does not and can rotate at a different rate. Only the crust slows down with the neutron star. However, the two components are coupled by superfluid vortices. When the difference in rotation is too important, a collective unpinning of superfluid vortices occurs, the coupling stops and a sudden angular momentum transfer between the two components occurs : the superfluid spins down and the crust spins up (Baym *et al.*, 1969).

Theoretical modeling is still in progress but glitches also may ultimately enable us to probe the properties of the interior of neutron stars (Chamel & Haensel, 2008).

7.1.2 Solid crust

Shortly after its birth, a neutron star cools down by emission of neutrinos to a temperature $T \sim 10^9$ K (see section 3.4). Then the influence of temperature on the composition of the crust can be neglected since $k_{\rm B}T \ll \varepsilon_{\rm F}$ with $\varepsilon_{\rm F}$ the Fermi energy. Therefore, the composition of the crust, called the ground state composition, can be calculated from the minimization of the energy : it is a body-centered cubic lattice of nuclei (A, Z) surrounded by a gas of electrons and above neutron drip also by a gas of neutrons (see section 2.1.1). Let $a = (4\pi n/3)^{-1/3}$ be the ion sphere radius with n is the ion number density and $A_{\rm cell}$ be the number of nucleons in the Wigner-Seitz cell of the lattice (see also section 4.2.1).

The temperature determines the state of matter in the crust, if it is in a solid or liquid phase (Haensel, 1997). The crystallization of matter is due to attractive forces between the different components, in the case of the crust, to Coulomb forces. The state of matter is determined by the ratio of the thermal energy and of the Coulomb energy. The importance of the Coulomb energy over the thermal one for an ion (A, Z) is determined by the so-called Coulomb coupling parameter :

$$\Gamma = \frac{Z^2 e^2}{a k_{\rm B} T}. \tag{7.1}$$

The ions form a crystal if $\Gamma > \Gamma_{\rm m}$, where $\Gamma_{\rm m} \simeq 175$ is the melting value of Γ determined by calculations (Haensel *et al.*, 2007). In other words, crystallization occurs at the melting temperature $T_{\rm m}$, at a given density ρ :

$$T_{\rm m} = \frac{Z^2 e^2}{a k_{\rm B} \Gamma_{\rm m}}, \tag{7.2}$$

$$\simeq 1.3 \times 10^5 Z^2 \left(\frac{1}{A_{\rm cell}} \frac{\rho}{10^6 \text{ g cm}^{-3}} \right)^{1/3} \frac{175}{\Gamma_{\rm m}} \text{ K}. \tag{7.3}$$

Figure 7.2 shows the melting curve ie. the variation of the melting temperature with the density for two models of crust : for the ground state and for an accreted crust (see section 5.2.2). Above the curve, for $T > T_{\rm m}$ the matter is in a liquid phase and below the curve, when $T < T_{\rm m}$, the matter solidifies. Note the significant differences between the two composition for densities $\rho \geq 10^9$ g cm^{-3}.

7.1.3 Liquid or solid core ?

A solid core may exist in neutron stars if the minimum of energy is obtained not for an homogeneous liquid but for a crystalline structure. Several models of solid neutron star cores have been proposed (Haensel, 1997; Haensel *et al.*, 2007) :

- In the 1970's the possible existence of a pure neutron solid core due to strong repulsive short range interaction was studied by eg. Canuto & Chitre (1974) but was excluded by subsequent calculations of the nuclear interaction (Takemori & Guyer, 1975; Clark & Sandler, 1975).

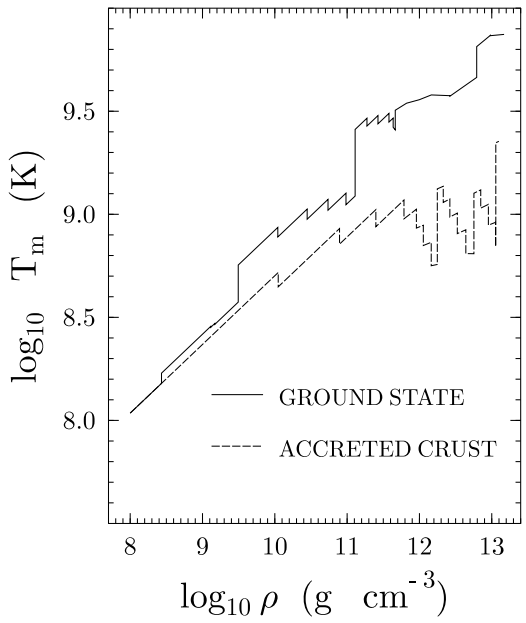

Figure 7.2: Melting temperature as a function of the density for the crust ground state composition and for accreted crust composition. See text for details. Figure from Haensel (1997).

- The appearance of solid structures in pion condensates was investigated in the mid 1970's, matter forming a three-dimensional cubic lattice of nucleons (Smith & Pandharipande, 1976) or a one-dimensional solid crystal of neutrons (Takatsuka *et al.*, 1978).
- Kutschera & Wójcik (1995) and Pérez García *et al.* (2002) suggested that protons in pure neutron matter or in hyperonic matter, respectively, could be treated as impurities in neutron matter. Their properties are determined by their interaction with the neutrons that becomes more repulsive with increasing density. This may results in a decrease of the density around the impurities where these can become localized. These localized protons could then form a crystal.
- Rajagopal & Sharma (2006) investigated the formation of crystals in color superconducting quark matter.

Note that models of solid cores are rather speculative though interesting from a theoretical point of view, the actual consensus being that the core is liquid.

7.1.4 Observational consequences

Contrary to liquid phases, solid phases can support shear and be the site of elastic strain as explained in the following.

Apart from glitches, the presence of solid phases in neutron stars could manifest themselves in different phenomena (Haensel, 1997; Haensel *et al.*, 2007; Karlovini & Samuelsson, 2003) :

- mountains : elastic strain may cause neutron stars to be deformed and non axisymmetric. Permanent mountains at the surface may be sustained by a thermal or magnetic gradient (Bildsten, 1998; Haskell *et al.*, 2006; Priymak *et al.*, 2011). Consider such a neutron star rotating at the angular frequency Ω around the z-axis and let ϵ be the oblateness parameter describing the asymmetry in the principal moments of inertia : $\epsilon = (I_{xx} - I_{yy})/I_{zz}$. This star emits gravitational waves at the frequency twice its angular frequency and the mean power is (Shapiro & Teukolsky, 1983) :
$$\dot{E}_{\rm GW} = \frac{32}{5}\frac{G}{c^5} I_{zz}^2 \epsilon^2 \Omega^6; \tag{7.4}$$
- precession : consider a rotating neutron star with a solid crust and a solid core and let $\vec{\boldsymbol{n}}_\Omega$ be the unit vector of its axis of rotation. Let $\vec{\boldsymbol{n}}_0$ be the unit vector of the symmetry axis of the non-rotating neutron star, that is deformed by the elastic stresses in the solid phase. In general the vectors $\vec{\boldsymbol{n}}_\Omega$ and $\vec{\boldsymbol{n}}_0$ will not be identical because of magnetic torques, tidal forces or crustquakes that have changed the orientation of $\vec{\boldsymbol{n}}_0$ with respect to $\vec{\boldsymbol{n}}_\Omega$. The vector $\vec{\boldsymbol{n}}_\Omega$ will rotate around $\vec{\boldsymbol{n}}_0$: this is the so-called precession. This phenomenon was observed from the pulsar B1828-11 (Stairs *et al.*, 2000), where modulations with periods of 511 and 256 days of the radio emission have been detected. Link & Epstein (2001) showed that the first periodicity originates from precession and the second one from an harmonic of the latter. This would be therefore the direct evidence of the existence of solid crust in neutron stars. According to Cutler *et al.* (2003), the observed periods are not consistent with a relaxed configuration for the crust of PSR B1828-11 : its crust is significantly stressed.
- the properties of the so-called quasi normal modes, that are associated with non-radial perturbations of neutron stars are modified by the presence of a solid crust.

Therefore, the modeling of the elastic properties of the solid phases in neutron stars may enable through the observations of the aforementioned phenomena to probe the properties of neutron stars.

7.2 Newtonian models of elastic neutron star

7.2.1 Newtonian elasticity in a nutshell

Let us now quickly summarize the basics of the theory of elasticity in the Newtonian framework (Landau & Lifshit's, 1959). The summation rule on repeated indices is adopted.

The elastic properties of matter were first studied by Robert Hooke and his work was published in 1678.

7.2.1.1 Displacement

Let A be a point with coordinates x_i of a solid body. The solid becomes deformed under the action of applied forces. Let x_i' be the coordinates the point A after the deformation. They depend on the original (unperturbed) location of the point A : $x_i'(x_i)$.

The displacement vector $\vec{\boldsymbol{\zeta}}$ describes the displacement of the point A due to the deformation of the body :

$$\zeta_i(x_i) = x_i' - x_i. \tag{7.5}$$

7.2.1.2 Strain tensor

Consider now two points A and B, infinitesimally close one to each other. The vector joining them before the deformation is $\vec{\boldsymbol{dr}}$ with the coordinates dx_i and after the deformation $\vec{\boldsymbol{dr'}}$ with the coordinates $dx_i' = dx_i + d\zeta_i$. The distance between the points is :

- before the deformation :

$$dl^2 = \sum_{i=1}^{3} (dx_i)^2 ; \tag{7.6}$$

- after the deformation :

$$dl'^2 = \sum_{i=1}^{3} (dx_i')^2 = \sum_{i=1}^{3} (dx_i + d\zeta_i)^2 . \tag{7.7}$$

Therefore, to the first order in the deformation, the change in the distance between the two points can be rewritten :

$$dl'^2 = dl^2 + 2u_{ik} dx_i dx_k \tag{7.8}$$

with u_{ik} the strain tensor :

$$u_{ik} = \frac{1}{2} \left(\frac{\partial \zeta_i}{\partial x_k} + \frac{\partial \zeta_k}{\partial x_i} \right) . \tag{7.9}$$

It is a symmetric tensor that can be therefore diagonalized at a given point and the change in the length in the direction i is

$$dl_i = dx_i' - dx_i = \sqrt{1 + 2u_{ii}} dx_i - dx_i = u_{ii} dx_i. \tag{7.10}$$

Therefore the u_{ii} are the relative changes in the distance in the direction i.

Let us consider an infinitesimal element of volume $dV = \prod_{i=1}^{3} dx_i$. After the deformation, its volume is $\mathrm{d}V' = \prod_{i=1}^{3} dx_i'$. Since $dx_i' = (1 + u_{ii}) dx_i$, to the first order, $dV' = dV(1 + \sum_{i=1}^{3} u_{ii})$. Therefore the sum of the u_{ii} gives the relative change in the volume due to the deformation.

7.2.1.3 Stress tensor

A solid body that is deformed tends to return to equilibrium because of so-called internal stresses. In a non-deformed body, the internal stresses are null. Let $\vec{\boldsymbol{F}}$ be the force per unit volume due to the internal stresses. The total force acting on a volume V in the direction i is by definition :

$$\int F_i \mathrm{d}V = \int \frac{\partial \sigma_{ik}}{\partial x_k} \mathrm{d}V = \oint \sigma_{ik} \mathrm{d}n_k \tag{7.11}$$

with σ_{ik} the stress tensor and $\mathrm{d}\vec{\boldsymbol{n}}$ the outward pointing unit vector normal to the surface enclosing the volume. The component ik of the stress tensor $\boldsymbol{\sigma}$ is the i-th component of the force per unit area perpendicular to the x^k-axis. Note that the force acting on the surface area in the direction i is $-\oint \sigma_{ik} \mathrm{d}n_k$. It can be shown that the stress tensor is symmetric (Landau & Lifshit's, 1959).

Consider a solid body undergoing static compression due to some pressure p. The latter exerts a pressure force on the body : -$p\mathrm{d}n_i$ in the direction i. In response, the internal stresses exert a force $\sigma_{ik}\mathrm{d}n_k$. The balance between them gives :

$$-p\mathrm{d}n_i = -p\delta_{ik}\mathrm{d}n_k = \sigma_{ik}\mathrm{d}n_k \tag{7.12}$$

and thus $\sigma_{ik} = -p\delta_{ik}$. The non-zero components of the stress tensor are equal to a pressure. The non-diagonal components of the stress tensor correspond to a tangential force on the surface, at the origin of shear.

7.2.1.4 Thermodynamics

Consider a small deformation of an already deformed body. This results in a small change $\delta\zeta_i$ of the displacement vector ζ_i. Let δW be the work done per unit volume by the internal stresses during this small deformation. One can show that (Landau & Lifshit's, 1959) :

$$\delta W = -\sigma_{ik}\delta u_{ik}. \tag{7.13}$$

An infinitesimal change in the internal energy $\mathrm{d}U$ of the deformed body is given by :

$$\mathrm{d}U = T\mathrm{d}S - \mathrm{d}W = T\mathrm{d}S + \sigma_{ik}\delta u_{ik}. \tag{7.14}$$

The free energy is then :

$$\mathrm{d}F = -S\mathrm{d}T + \sigma_{ik}\delta u_{ik}. \tag{7.15}$$

7.2.1.5 Hooke's law

Let us now consider an isotropic body and that both the original and deformed states are at the same temperature. Then the free energy of the deformed body can be written :

$$F = F_0 + \frac{1}{2}\lambda u_{ii}^2 + \mu u_{ik}^2, \tag{7.16}$$

with F_0 the free energy of the original state and in the following $F_0 = 0$. Note that in the previous expression and in the following, u_{ii}^2 stands for the square of the quantity u_{ii}. The coefficients λ and μ are the Lamé coefficients.

Pure shear is a deformation in which the volume of the body remains unchanged, ie. $\sum u_{ii}$=0, but its shape is changed. Hydrostatic compression corresponds to the contrary with $u_{ik} \propto \delta_{ik}$.

It can be shown that any transformation can be decomposed into the sum of a pure shear and an hydrostatic compression (Landau & Lifshit's, 1959). Then the free energy can be rewritten as :

$$F = \mu(u_{ik} - \frac{1}{3}\delta_{ik}u_{ll})^2 + \frac{1}{2}Ku_{ll}^2. \tag{7.17}$$

K is the bulk modulus or modulus of compression and μ the shear modulus or modulus of rigidity. Both coefficients are positive and one has :

$$K = \lambda + 2/3\mu. \tag{7.18}$$

With the previous coefficients, the stress tensor can be written :

$$\sigma_{ik} = Ku_{ll}\delta_{ik} + 2\mu(u_{ik} - \frac{1}{3}u_{ll}\delta_{ik}). \tag{7.19}$$

If the deformation is pure shear, then it is driven by the modulus of rigidity and if it is pure hydrostatic compression, by the bulk modulus.

Alternatively, one gets :

$$u_{ik} = \frac{1}{9K}\delta_{ik}\sigma_{ll} + \frac{1}{2\mu}\left(\sigma_{ik} - \frac{1}{3}\delta_{ik}\sigma_{ll}\right), \tag{7.20}$$

where the strain tensor that describes the deformation is a function of the stress tensor that describes the applied forces. This is the so-called Hooke's law.

7.2.2 Models of neutron stars with a (partially) solid interior

Let us now present some simple models of neutron stars with a (partially) solid interior. They provide limiting cases against which numerical simulations can be tested.

7.2.2.1 Incompressible interior

In the slow rotation approximation, considering a relaxed state spherically symmetric with zero angular velocity, Gourgoulhon (1995a) derived the flattening of an incompressible neutron star with a solid crust and liquid core, as shown figure 7.3, with constant density ρ_0 and modulus of rigidity μ. For small elastic deformations, the equations for the surface and the interface are :

$$R(\theta) = R_0\left(1 + NP_2(\cos\theta)\right), \tag{7.21}$$

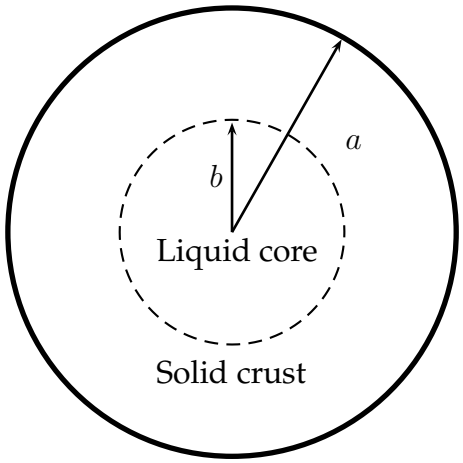

Figure 7.3: Schematic structure for the model of incompressible star.

with $R_0 = a$ at the surface and $R_0 = b$ at the interface, P_2 the second-order Legendre polynomials and N a factor depending on the model adopted for the body, as described in the following. Let us define $\kappa = b/a$ and :

$$\Xi = \frac{3\mu}{8\pi G\rho_0^2 a^2}. \tag{7.22}$$

At the surface :

$$N_{\rm inc}^{\rm surf} = -\frac{5\Omega^2}{8\pi G\rho}\frac{1}{\Delta}\left[1+\kappa+\kappa^2+\frac{8}{3}(\kappa^3+\kappa^4+\kappa^5+\kappa^6)+\frac{19}{24}(\kappa^7+\kappa^8+\kappa^9)\right] \tag{7.23}$$

with

$$\Delta = (1+19\Xi)(1+\kappa+\kappa^2)+8(\frac{1}{3}-7\Xi)(\kappa^3+\kappa^4)+8(\frac{1}{3}+7\Xi)(\kappa^5+\kappa^6)+19(\frac{1}{24}-\Xi)(\kappa^7+\kappa^8+\kappa^9). \tag{7.24}$$

At the interface between the liquid core and the crust :

$$N_{\rm inc}^{\rm inte} = -\frac{5\Omega^2}{8\pi G\rho}\frac{1}{\Delta}\left[1+\kappa+\frac{43}{64}(\kappa^2+\kappa^3+\kappa^4)+\kappa^5+\kappa^6\right]. \tag{7.25}$$

For an entirely fluid interior, when $\kappa = 1$ or $\mu = 0$, one gets :

$$N_{\rm inc}^{\rm fluid} = -\frac{5\Omega^2}{8\pi G\rho} \tag{7.26}$$

ie. the flattening of MacLaurin ellipsoid.

For an entirely solid interior, for $\kappa = 0$:

$$N_{\rm inc}^{\rm solid} = -\frac{5\Omega^2}{8\pi G\rho} N_{\rm inc}^{\rm Love}, \tag{7.27}$$

with $N_{\rm inc}^{\rm Love}$ the factor derived by A. E. H. Love in the framework of geodynamics (Love (1911, 1944)) :

$$N_{\rm inc}^{\rm Love} = \frac{1}{1 + 19\Xi}. \tag{7.28}$$

7.2.2.2 Baym & Pines model

Ruderman (1969) proposed that glitches are starquakes originating from the crack of the solid crust of slowing-down neutron stars and Baym & Pines (1971) further investigated this idea. They presented a simple one-parameter Newtonian model. The idea is that the crust of neutron stars is formed relatively oblate. As the neutron star slows down, the centrifugal forces decrease and the crust tends to a less oblate shape, that is however prevented by its rigidity. The crust is therefore stressed, up to a point when the maximum stress it can sustain is reached. The crust then cracks, reducing its oblateness and moment of inertia and increasing the rotation rate of the whole star by conservation of the angular momentum. Baym & Pines (1971) supposed that not all the stress is released during a glitch that the crust is still stressed after it and considered incompressible deformations.

Consider a slowly rotating liquid neutron star with an the angular velocity Ω. Due to rotation, its shape is deformed with respect to a non-rotating and thus spherically symmetric configuration. Let $I_{\rm c}$ be the moment of inertia of the crust of a rotating star and $I_{\rm c0}$ the one for a non-rotating star. The deviation from the spherical configuration due to the rotation can be described by the oblateness parameter ϵ defined as follow :

$$\epsilon = \frac{I_{\rm c} - I_{\rm c0}}{I_{\rm c0}}. \tag{7.29}$$

For $\epsilon \ll 1$, the energy of a rotating fluid star can be written as :

$$E = E_0 + \frac{L^2}{2I} + A\epsilon^2 \tag{7.30}$$

with E_0 the energy of the non-rotating star, L and I the total angular momentum and moment of inertia, respectively of the rotating star with $L = \Omega I$. The parameter A is model-dependent.

The value of the oblateness of the liquid star rotating with an angular velocity Ω_0 at equilibrium is determined by minimizing the energy :

$$\epsilon_0 = \frac{\Omega_0}{4A}\frac{\partial I}{\partial \epsilon}. \tag{7.31}$$

Consider now that a liquid star rotating at the angular velocity Ω_0 solidifies at least partly and has at that moment an oblateness ϵ_0. As the star slows down to a velocity Ω at rate $\dot{\Omega}$, its oblateness decreases and the solid part is strained. The strain energy of the latter is :

$$E_{\text{strain}} = B\left(\epsilon - \epsilon_0\right)^2, \tag{7.32}$$

with B a model-dependent parameter.

The total energy of the star with a solid part is then :

$$E = E_0 + \frac{L^2}{2I} + A\epsilon^2 + B\left(\epsilon - \epsilon_0\right)^2 \tag{7.33}$$

and thus the value of the oblateness at equilibrium is :

$$\epsilon = \frac{\Omega}{4(A+B)}\frac{\partial I}{\partial \epsilon} + \frac{B}{B+A}\epsilon_0. \tag{7.34}$$

The mean stress in the solid part, that is considered to be isotropic, is then defined by :

$$\sigma = \mu\left(\epsilon - \epsilon_0\right), \tag{7.35}$$

with μ the mean shear modulus of the solid part : $\mu = 2B/V_{\text{s}}$ with V_{s} the volume of the latter.

The strain increases as the neutron star slows down and the star is assumed to undergo only purely elastic quasi-stationary deformations between rigidly rotating equilibrium configurations. The star eventually reaches a critical value σ_{g} of the mean stress for the velocity Ω_{g}. The solid part then cracks and the reference oblateness ϵ_0 is changed by an amount $\Delta\epsilon_0$. The oblateness gets reduced by an amount $\Delta\epsilon_{\text{g}}$ and according to equation (7.34) :

$$\Delta\epsilon_{\text{g}} = \frac{B}{A+B}\Delta\epsilon_0. \tag{7.36}$$

The rotational frequency increases by an amount $\Delta\Omega_{\text{g}}$ given by :

$$\frac{\Delta\Omega_{\text{g}}}{\Omega_{\text{g}}} = -\Delta\epsilon_{\text{g}}. \tag{7.37}$$

This is the origin of the observed glitches. The quake releases a stress :

$$\Delta\sigma = \mu(\Delta\epsilon_0 - \Delta\epsilon_{\text{g}}) = \mu\frac{A}{B}\Delta\epsilon_{\text{g}}. \tag{7.38}$$

Considering that $\Omega_0 \sim 2\Omega_g$, the energy release in the glitch is

$$E_g \approx 4\left(\frac{I_0\Omega_g^2}{2}\right)\Delta\epsilon_g. \tag{7.39}$$

The next glitch will take place after a time :

$$t_g \approx \frac{2A^2}{B\left(\partial I/\partial\epsilon\right)_{\epsilon_g}}\frac{\Omega_g}{\dot{\Omega}^2}|\Delta\epsilon_g|. \tag{7.40}$$

Subsequent publications (Pines & Shaham, 1972; Pines *et al.*, 1972) using the model by Baym & Pines (1971) concluded that the hypothesis that the glitches of the Crab pulsar originate from the crack of its crust is consistent with the observations. Nevertheless, it is not the case for the Vela, whose time intervals between two glitches is too small compared to the model predictions assuming sole crust cracks and therefore suggesting that they are due to both the cracks of the crust and of the core, the latter being solid. Heintzmann *et al.* (1973) examined the idea of crustquakes and corequakes for the Vela pulsar and used a semi-relativistic treatment, considering relativistic effects, via the TOV equations (see section 2.1.1), on the structure of the fluid core before it gets solidified. Note that they assume perfect rigidity. They showed that the observations of the glitches of the Vela pulsars, in particular the large ones are consistent with the hypothesis of a solid core that undergoes large quakes.

Note however that several works have shown that large glitches such as the ones exhibited by the Vela pulsar, are unlikely to originate from corequakes (Alpar & Baykal, 1994; Alpar, 1995). In particular, the energy that can be released in a large glitch by a corequake exceeds its observed thermal X-ray luminosity of the Vela pulsar. However, the small glitches of the Crab pulsar can be explained by crust cracks together with vortex unpinning.

Finally, Cutler *et al.* (2003) and Zdunik *et al.* (2008) have reconsidered the model by Baym & Pines (1971) with more realistic microphysics input and for a solid crust and liquid core. In particular, they used a different definition for the oblateness parameter ϵ. Assuming that the star rotates around the z-axis, they write the moment of inertia of the whole deformed star (and not only the crust) $I_{xx} = I_{yy} = I_0(1 - \epsilon/2)$ and $I_{zz} = I_0(1 + \epsilon)$ with I_0 the moment of inertia of the relaxed non-rotating configuration. The oblateness parameter is then :

$$\epsilon = \frac{I_{zz} - I_0}{I_0}. \tag{7.41}$$

Using axisymmetric and stationary configurations of rotating neutron stars calculated by the mean of the LORENE library for different equations of state for the crust and core, Zdunik *et al.* (2008) calculated the A and B parameters and approximate formulas for these quantities.

7.3 Elasticity in General Relativity

7.3.1 Previous formulations

Attempts to develop a suitable formalism for elasticity in the framework of General Relativity started only in the 1950's. Such works aimed at describing the interaction of gravitational waves with elastic solid matter, motivated by the design of a gravitational waves detector by Weber (1960) that consisted of aluminum cylinders. The subsequent formalisms were either unsuccessful (Synge, 1959) or incomplete (Rayner, 1963; Bennoun, 1965). More details in Carter & Quintana (1972); Carter (1980).

7.3.2 Carter & Quintana formalism

The first successful theory of elasticity was formulated by Carter & Quintana (1972) and developed in series of subsequent papers : Carter & Quintana (1972), Carter (1973) and Carter & Quintana (1975b), that are the basis of the following exposure.

7.3.2.1 Material space and canonical projection

Consider a spacetime $(\mathscr{M}, \boldsymbol{g})$ with $\mathscr{M}$ a $\mathcal{C}^\infty$ manifold of dimension 4 and $\boldsymbol{g}$ a Lorentzian metric on $\mathscr{M}$ ie. of signature $(-,+,+,+)$.

Let $\mathscr{X}$ be a $\mathcal{C}^\infty$ manifold of dimension 3, the so-called material space. Its points represent the idealized matter particles of the elastic medium and the local coordinates on this manifold are (X^i) with $i = 1, 2, 3$. Tensors on $\mathscr{X}$ are called material tensors and the ones of $\mathscr{M}$, spacetime tensors.

On $\mathscr{X}$, let n_{ijk} be a totally antisymmetric pseudo-tensor representing the canonical measure of the number density of matter particles, such that

$$\mathrm{d}N = \frac{1}{3!} n_{ijk} \mathrm{d}X^i \wedge \mathrm{d}X^j \wedge \mathrm{d}X^k \tag{7.42}$$

is the number of particles in the element of volume $\mathrm{d}X^i \wedge \mathrm{d}X^j \wedge \mathrm{d}X^k$.

Let $\mathscr{P}$ be the canonical differential projection (figure 7.4) :

$$\mathscr{P} : \mathscr{M}' \to \mathscr{X} \tag{7.43}$$

with $\mathscr{M}' \subset \mathscr{M}$ an open submanifold, that projects the world lines of the particles in $\mathscr{M}'$ onto their corresponding points in $\mathscr{X}$. It defines a field of so-called unit flow vectors u^α, that are tangent to the world lines in $\mathscr{M}$ ($u^\alpha u_\alpha = -1$) and an orthogonal projection tensor :

$$\gamma_{\alpha\beta} = g_{\alpha\beta} + u_\alpha u_\beta. \tag{7.44}$$

$\boldsymbol{\gamma}$, the so-called Cauchy strain tensor, determines the distances between the particles in their rest frame and describes the local state of strain of the medium.

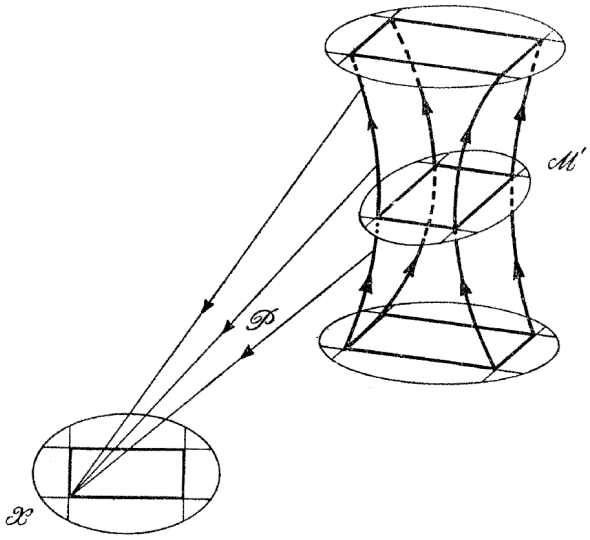

Figure 7.4: Schematic representation of the projection $\mathscr{P}$ from the spacetime manifold $\mathscr{M}$ onto the material space $\mathscr{X}$. The arrows on the world lines in $\mathscr{M}'$ indicate the direction of the flow vector u^α. Figure from Carter & Quintana (1972).

An orthogonal spacetime tensor on $\mathscr{M}$ is such that its contractions with the flow vector $\vec{\boldsymbol{u}}$ all vanish.

A materially constant orthogonal tensor $\boldsymbol{T}$ is such that, for any point $x \in \mathscr{M}$, the projection in $\mathscr{X}$ of its value $\boldsymbol{T}(x)$ at the point $X = \mathscr{P}(x)$ does not depend on the choice of x.

The projection $\mathscr{P}$ induces an isomorphism between the materially constant orthogonal tensors on $\mathscr{M}$ and the material tensors on $\mathscr{X}$.

A medium is said to have a rigid motion or equivalently to be in constant strain state if the projection tensor $\boldsymbol{\gamma}$ is materially constant, ie. if it does not depend on the point $x \in \mathscr{M}$. $\boldsymbol{\gamma}$ is then a Riemannian metric on $\mathscr{X}$.

The metric $\boldsymbol{g}$ also normalizes the antisymmetric 4-volume measure tensor $\epsilon_{\alpha\beta\gamma\delta}$ on $\mathscr{M}$ and the number density of particles of the medium per unit metric volume n_{b} is given by :

$$n_{ijk} = \mathscr{P}\left(n_{\mathrm{b}}\epsilon_{\alpha\beta\gamma\delta}u^\delta\right). \tag{7.45}$$

7.3.2.2 Perfect elasticity

A material is said to behave perfectly elasticly (or hyperelasticly) if it undergoes deformations that are reversible.

Adiabatic or frictionless gas, liquid or solid can be considered as perfectly elastic. A material is not perfectly elastic if it undergoes deformations whose characteristic length-scales are of the order of the ones determining the structure of the material or if it is subject of so high gravitational field that the inertial forces between the particles are of

the same order as the interactions that determine the properties of the material. This is not the case for our problem.

The energy-momentum tensor of a perfectly elastic material is then given by the equation :

$$T^{\alpha\beta} = \varepsilon u^{\alpha} u^{\beta} + p^{\alpha\beta} \tag{7.46}$$

where ε is the energy density and $p^{\alpha\beta}$ is the symmetric pressure tensor, the projections on $\mathscr{X}$ of both quantities being functions of the projection of $\boldsymbol{\gamma}$.

In the following perfectly elastic materials will be considered.

One defines the average mass per particle :

$$m = n_{\mathrm{b}} \varepsilon. \tag{7.47}$$

7.3.2.3 Hookean and quasi-Hookean approximations

The Hookean approximation holds if there exists a so-called unstrained state, a fully relaxed state for which the projection tensor of the material $\boldsymbol{\gamma}$ take the value $\boldsymbol{\sigma}$ such that the energy per particle m is minimum. $\boldsymbol{\sigma}$ is then called the unstrained reference tensor.

Under such conditions, one can define the relative strain tensor :

$$e_{\alpha\beta} = \frac{1}{2} \left(\gamma_{\alpha\beta} - \sigma_{\alpha\beta} \right). \tag{7.48}$$

For some materials, an unstrained state may not even exist. This is the case in particular for matter in the crust of neutron stars whose crystalline structure only exist because of high pressure.

Then, one can defined an unsheared state as being not for the absolute minimum of the energy per particle but for a minimum of m for a given constant particle number density n_{b} : $\check{m}(n_{\mathrm{b}})$. The value of the projection tensor $\boldsymbol{\gamma}$ is then labeled $\boldsymbol{\eta}(n_{\mathrm{b}})$ and of the density $\check{\rho}(n_{\mathrm{b}})$.

One can define a constant volume shear tensor for a fixed particle number n_{b} :

$$s_{\alpha\beta} = \frac{1}{2} \left(\gamma_{\alpha\beta} - \eta_{\alpha\beta} \right) \tag{7.49}$$

and by definition the shear is everywhere zero for an unsheared state.

7.3.2.4 Perfect solid

A perfect solid is such that its structure is cubically symmetric and isotropic with respect to its unsheared state.

Following Carter & Quintana (1975b), the subsequent calculations will limit to the first order in the shear tensor and therefore the perfect solid can be considered as quasi-Hookean whose properties are given by two functions that are the same in the whole material : the relaxed energy density $\varepsilon = \varepsilon(n_{\mathrm{b}})$ and rigidity $\mu = \mu(n_{\mathrm{b}})$.

The density and the pressure tensor are then :

$$\varepsilon = \check{\varepsilon}(n_{\rm b}) + O(s^2), \tag{7.50}$$
$$p_{\alpha\beta} = \check{p}(n_{\rm b})\gamma_{\alpha\beta} - 2\mu s_{\alpha\beta} + O(s^2). \tag{7.51}$$

Therefore according to equation (7.46) and with equation (7.44), the energy-momentum tensor of a solid fluid is :

$$T_{\alpha\beta} = (\varepsilon + p)u_\alpha u_\beta + p g_{\alpha\beta} - 2\mu s_{\alpha\beta}, \tag{7.52}$$

with for simplicity : $\varepsilon = \check{\varepsilon}$ and $p = \check{p}$.

Note that one recovers the fluid limit by putting $\mu = 0$, showing that this formulation enables to describe both solid and liquid media.

7.3.3 Karlovini & Samuelsson formalism

Several works have reconsidered the general relativistic elasticity formalism such as Magli & Kijowski (1992); Beig & Schmidt (2005), compared by Frauendiener & Kabobel (2007) and Brito *et al.* (2011b,a) who extended the study by Magli & Kijowski.

In particular, Karlovini & Samuelsson (2003) revisited the formalism by Carter & Quintana (1972) and applied it to the study of different types of perturbations in elastic neutron stars in a series of subsequent papers (Karlovini *et al.*, 2004; Karlovini & Samuelsson, 2004, 2007).

Following Carter & Quintana (1972), they considered the projection between the spacetime manifold and the material space but viewed in terms of push-forward and pull back. Moreover, the energy density is written as a function of the spacetime metric instead of the Cauchy strain tensor as in Carter & Quintana (1972). They derived an interesting form of the Euler equations for elastic matter and used a different formula for the shear.

7.3.4 Relativistic formulation of starquakes

Following their seminal work in 1972, Carter (1975) and Carter & Quintana (1975a) revisited the semi-Newtonian models by Baym & Pines (1971) and Heintzmann *et al.* (1973) of neutron starquakes in the framework of the theory of relativistic elasticity and accounting for finite compressibility and rigidity. The only limitation is that the model restricts to axisymmetric configurations.

A configuration is said to be relaxable if there exists a value of the angular velocity for which the equilibrium state of the rotation star is relaxed, ie. unsheared.

The key point is that the parameters in the equations describing the structure of a rotating star, whether the star is relaxable or not, can be derived by considering the slow-rotation of a relaxable structure when the unsheared state is obtained for no rotation.

Assuming that the solid matter in the neutron star is isotropic and perfectly elastic for small deformations, Carter & Quintana (1975a) considered relaxable neutron stars made of a perfect solid.

Let I_* and Z_* be the constant moment of inertia and so-called solidity constant of the non-rotating (and thus spherical) relaxed state. The total moment of inertia I of a relaxed state with an angular velocity $\check{\Omega}$ is, expanding in terms of the angular velocity $\check{\Omega}$ up to the second order, which fully determines a relaxable configuration :

$$I = I_* + \frac{1}{2} Z_* \check{\Omega}^2. \tag{7.53}$$

Thus, the total energy at equilibrium of the star with a relaxable structure and an angular velocity Ω, to the second order is (Carter & Quintana, 1975a) :

$$E = \frac{1}{8} Z_* \check{\Omega}^2 + \frac{1}{2} \left(I_* + \frac{1}{2} Z_* \check{\Omega}^2 \right) \Omega^2 + \frac{3}{8} P_* \Omega^4. \tag{7.54}$$

Following Baym & Pines (1971); Cutler *et al.* (2003); Zdunik *et al.* (2008), let us consider the oblateness parameter :

$$\epsilon = \frac{I - I_*}{I_*}. \tag{7.55}$$

Comparing equation (7.54) with equation (7.33), one gets

$$P_* = \frac{I_*}{2(A+B)} \qquad \text{and} \qquad Z_* = \frac{B I_*}{2A(A+B)}. \tag{7.56}$$

Finally, the values of the two constants P_* and Z_* can be explicitly calculated from the papers Carter & Quintana (1975b); Quintana (1976).

In conclusion, the glitch phenomenon suggests that there exist some solid parts in neutron stars, in particular the crust that becomes solid shortly after the neutron star birth. There is no clear consensus for state of the core and models with solid core have been developed since the 1970's. The starquake model provides a reasonable explanation for Crab-like glitches but not for Vela-like ones.

The relativistic formalism for elasticity by Carter & Quintana (1972) presented in this chapter will be used in the next chapter to compute neutron star configurations with a solid interior.

Chapter 8

Rotating neutron stars with a solid interior

Contents

In this chapter is presented the derivation of the equations for stationary and axisymmetric configurations of neutron stars including the elastic properties of the solid phases. For simplicity a fully solid interior is assumed but the calculations can be generalized for a partly solid one. The formalism for elasticity in the framework of General Relativity developed by Carter & Quintana (1972) and presented in the previous chapter is used. How to take into account elastic deformations of a rotating star is developed in section 8.1. In section 8.2 the formalism and the derivation of the Einstein and equilibrium equations for stationary axisymmetric and circular configurations of rigidly rotation neutron stars with a solid interior are explained. The Newtonian limit of the latter developed in section 8.3 and their numerical resolution currently in progress is presented in section 8.4. Finally, possible applications of this study are indicated in section 8.5.

8.1 Elastic deformation of rotating stars

In the following, a small elastic deformation of an homogeneous perfect solid whose unperturbed (original) state has zero shear tensor will be considered. Its relaxed energy density and rigidity are then functions of the baryon number density : $\varepsilon = \varepsilon(n_{\rm b})$ and $\mu = \mu(n_{\rm b})$. An asterisk $*$ will be used to distinguish the symbols referring to the original state from the ones of the perturbed state. The original state is also assumed to have a rigid motion that implies that the Cauchy strain tensor is constant along the worldlines.

8.1.1 Small deformations

Let $\boldsymbol{\gamma}$ be the Cauchy strain tensor.

The fixed strain reference tensor $\boldsymbol{\sigma}$ is defined such that the relative strain tensor :

$$e_{\alpha\beta} = \frac{1}{2}\left(\gamma_{\alpha\beta} - \sigma_{\alpha\beta}\right), \tag{8.1}$$

is of the same order as the shear :

$$e_{\alpha\beta} = O(s) = O(e). \tag{8.2}$$

The choice of $\boldsymbol{\sigma}$ consists in considering small perturbations to the unperturbed state.

The shear reference tensor $\boldsymbol{\eta}$ is then :

$$\eta_{\alpha\beta} = \left(\frac{n_{\rm b}}{n_{\rm b0}}\right)^{-2/3} \sigma_{\alpha\beta}, \tag{8.3}$$

with $n_{\rm b0}$ the particle number density when $\boldsymbol{\gamma} = \boldsymbol{\sigma}$.

To the first order in the relative strain (Carter & Quintana, 1975b),

$$n_{\rm b} = n_{\rm b0}(1 - e_{\alpha}{}^{\alpha}) + O(e^2), \tag{8.4}$$

and equation (8.3) becomes

$$\eta_{\alpha\beta} = \left(1 - \frac{2}{3}\frac{n_{\rm b} - n_{\rm b0}}{n_{\rm b}}\right)\sigma_{\alpha\beta} + O(e^2). \tag{8.5}$$

$$s_{\alpha\beta} = e_{\alpha\beta} - \frac{1}{3}e_{\alpha}{}^{\alpha}\gamma_{\alpha\beta} + O(e^2). \tag{8.6}$$

8.1.2 Eulerian variation

In the following the perturbed and the original states are assumed to differ by a small Eulerian variation δ. This implies in particular that there exists a coordinate system, as explained in the following, in which the points on $\mathscr{M}$ before and after the perturbation have the same coordinates.

Let us require that in the original state:

$$n^*_{\rm b0} = n^*_{\rm b}. \tag{8.7}$$

This is equivalent to the choice :

$$\sigma^*_{\alpha\beta} = \eta^*_{\alpha\beta}. \tag{8.8}$$

This condition uniquely defines the relative strain tensor $\boldsymbol{e}$ and implies that :

$$e^*_{\alpha}{}^{\alpha} = O(e^2). \tag{8.9}$$

8.1.3 Lagrangian variation

The Lagrangian variation of a field, denoted by Δ, consists in comparing the field before and after the perturbation at a given point whose coordinates are transported by the medium.

Let $\mathscr{P}^*$ be the projection from $\mathscr{M}$ to $\mathscr{X}$ in the original state, x^α be the Eulerian coordinates of a point x in $\mathscr{M}$ and $x^\alpha - \xi^\alpha$ of the point $x - \Delta x$. The Lagrangian coordinates $x^\alpha - \xi^\alpha$ of the point x are given by the requirement that :

$$\mathscr{P}^*(x - \Delta x) = \mathscr{P}(x). \tag{8.10}$$

The definition (8.7) of the original state gives :

$$n_{\rm b} - n_{\rm b0} = \Delta n_{\rm b}. \tag{8.11}$$

8.1.4 Semi-Lagrangian variation

In the following, the Lagrangian displacement $\vec{\xi}$ is not postulated to be small. It is nevertheless the related semi-Lagrangian displacement $\vec{\zeta}$ that is supposed to be small ie. $\zeta^\alpha = O(e)$.

Let us denote the semi-Lagrangian variation of a field by D. Let $x' = x - Dx$ and $x'' = x - \Delta x$ be the results of the semi-Lagrangian and Lagrangian transport of x respectively. The condition that $\vec{\zeta}$ is small is equivalent to the requirement that the points x' and x'' lie on the same surface of transitivity determined by the invariance group of the stationary and axisymmetric spacetime, in this case a fixed ring of particles.

One can then write for a given tensor $\boldsymbol{T}$ (Carter & Quintana, 1975b) :

$$D\boldsymbol{T} = \delta\boldsymbol{T} + \mathcal{L}_{\vec{\zeta}}\boldsymbol{T} + O(e^2). \tag{8.12}$$

For a scalar field, like the particle number density n :

$$Dn = \Delta n, \tag{8.13}$$
$$\Delta n = \delta n + \nabla_\alpha \zeta^\alpha + O(e^2). \tag{8.14}$$

In particular

$$\delta g_{\alpha\beta} = g_{\alpha\beta} - g^*_{\alpha\beta} \tag{8.15}$$

is the change in the metric due to the elastic perturbation.

In the case of a fluid region, the semi-Lagrangian displacement is determined by imposing that :

- $\vec{\zeta}$ is the gradient of a scalar in a fluid region,
- the normal component of $\vec{\zeta}$ is continuous at each solid-liquid interface, at the first order in e.

Therefore the elastic displacement $\vec{\zeta}$ introduced previously enables to describe consistently both elastic and fluid phases. This is therefore a generalization of the perfect fluid model.

8.2 Stationary and axisymmetric configurations of rotating stars

8.2.1 Metrics

Let us consider now that :

1. the original state, with the angular velocity Ω^*, is asymptotically flat, stationary, axisymmetric and circular,

2. the original state is relaxed : $\boldsymbol{s}^* = 0$.

3. the perturbed state, with the angular velocity Ω, is asymptotically flat, stationary, axisymmetric and circular.

Therefore, Papapetrou coordinates (t, x^1, x^2, φ) and the following metrics on $\mathscr{M}$, given by equation (6.136) can be used :

- for the original state :

$$g_{\alpha\beta}\, dx^\alpha\, dx^\beta = -N^{*2}dt^2 + k^*_{ab}\, dx^a\, dx^b + M^{*2}(d\varphi - \omega^* dt)^2; \tag{8.16}$$

- for the perturbed state

$$g_{\alpha\beta}\, dx^\alpha\, dx^\beta = -N^2dt^2 + k_{ab}\, dx^a\, dx^b + M^2(d\varphi - \omega dt)^2. \tag{8.17}$$

8.2.2 Quasi-isotropic coordinates

Since one expects the elastic deformations to be small, the axisymmetric and stationary spacetime will be consider as circular in the following (section 6.2.2).

Therefore, the isotropic coordinates (t, r, θ, φ) can be adopted and in the perturbed state the metric k_{ab} in each 2-surface $M_{t\varphi}$ writes :

$$k_{ab} = A^2(r, \theta)\left(dr^2 + r^2 d\theta^2\right) \tag{8.18}$$

and similarly for the metric k^*_{ab} in the unperturbed state.

Then the metrics (8.16) and (8.17) on $\mathscr{M}$ can be rewritten :

- for the original state :

$$g_{\alpha\beta}\, dx^\alpha\, dx^\beta = -N^{*2}dt^2 + A^{*2}\left(dr^2 + r^2 d\theta^2\right)\, dx^a\, dx^b + M^{*2}(d\varphi - \omega^* dt)^2; \tag{8.19}$$

- for the perturbed state :

$$g_{\alpha\beta}\, dx^\alpha\, dx^\beta = -N^2dt^2 + A^2\left(dr^2 + r^2 d\theta^2\right)\, dx^a\, dx^b + M^2(d\varphi - \omega dt)^2, \tag{8.20}$$

with $M = Br\sin\theta$.

8.2.3 Strain tensors

Let us introduce for convenience the comoving angle coordinate :

$$\psi = \varphi - \Omega t \tag{8.21}$$

(and its equivalent for the original state).

The projection $\mathscr{P}^*$ in the original state is :

$$\begin{aligned} \mathscr{P}^* : \mathscr{M} &\to \mathscr{X} && (8.22)\\ (t, x^1, x^2, \varphi) &\mapsto X^1 = x^1 && (8.23)\\ & \quad X^2 = x^2 && (8.24)\\ & \quad X^3 = \psi^* = \varphi - \Omega^* t. && (8.25) \end{aligned}$$

In the perturbed state, the projection $\mathscr{P}$ is :

$$\begin{aligned} \mathscr{P} : \mathscr{M} &\to \mathscr{X} && (8.26)\\ (t, x^1, x^2, \varphi) &\mapsto X^1 = x^1 - \zeta^1 && (8.27)\\ & \quad X^2 = x^2 - \zeta^2 && (8.28)\\ & \quad X^3 = \psi = \varphi - \Omega t. && (8.29) \end{aligned}$$

In fact the symmetry of the problem imposes that ζ^3 is independent of x^1 and x^2 and can be taken equal to zero (Carter & Quintana, 1975b).

According to equation (7.44), the strain tensor on $\mathscr{M}$ is :

$$\gamma_{\alpha\beta} = g_{\alpha\beta} + u_\alpha u_\beta. \tag{8.30}$$

The flow vector is given by equation (6.75) and since $\vec{\boldsymbol{\chi}} = M\vec{\boldsymbol{m}}$ (equation 6.120),

$$\vec{\boldsymbol{u}} = \Gamma \left[\vec{\boldsymbol{n}} + \frac{M}{N}(\Omega - \omega)\vec{\boldsymbol{m}} \right]. \tag{8.31}$$

Therefore, the strain tensor on $\mathscr{M}$ writes :

$$\begin{aligned} \gamma_{\alpha\beta}\, dx^\alpha\, dx^\beta &= \Gamma^2 M^2 \left(d\varphi - \Omega dt\right)^2 + k_{ab}\, dx^a\, dx^b, && (8.32)\\ &= \varpi^2 d\psi^2 + k_{ab}\, dx^a\, dx^b && (8.33) \end{aligned}$$

with $\varpi = \Gamma M$ the proper circumferential radius.

The strain tensor on $\mathscr{X}$ is :

$$\gamma_{ij}\, dX^i\, dX^j = \varpi^2 (dX^3)^2 + k_{ab}\, dX^a\, dX^b, \tag{8.34}$$

The strain reference tensor on $\mathscr{X}$ in the original state is such that $\sigma^*_{ij} = \gamma^*_{ij}$ and thus :

$$\begin{aligned} \sigma^*_{ij} &= \varpi^{*2}(X^1, X^2)(dX^3)^2 + k^*_{ab}(X^1, X^2)\, dX^a\, dX^b, && (8.35)\\ &= \sigma_{ij} && (8.36) \end{aligned}$$

By reversing the projection $\mathscr{P}$, the strain reference tensor on $\mathscr{M}$ in the perturbed state is :

$$\sigma_{\alpha\beta} = \varpi^{*2}(x^1 - \zeta^1, x^2 - \zeta^2) d\psi^2 + k^*_{ab}(x^1 - \zeta^1, x^2 - \zeta^2)\, d(x^1 - \zeta^1)\, d(x^2 - \zeta^2). \tag{8.37}$$

8.2.4 Relative strain tensor

The relative strain tensor (in the perturbed state) defined in equation (8.1) is :

$$
\begin{aligned}
e_{\alpha\beta}\, dx^\alpha\, dx^\beta &= \frac{1}{2}\left\{\left[\varpi^2(x^1,x^2) - \varpi^{*2}(x^1-\zeta^1, x^2-\zeta^2)\right](d\varphi - \Omega dt)^2 + \right. && (8.38)\\
&\quad \left.\left[k_{ab}(x^1,x^2) - k^*_{ab}(x^1-\zeta^1,x^2-\zeta^2)\right] dx^a dx^b\right\}, && (8.39)\\
&= \frac{1}{2} D\varpi^2 \left(d\varphi - \Omega dt\right)^2 + \frac{1}{2} D k_{ab} dx^a dx^b. && (8.40)
\end{aligned}
$$

One can show (sections A.2 and A.4) that :

$$
\begin{aligned}
Dk_{ab} &= \delta g_{ab} + {}^2\nabla_a \zeta_b + {}^2\nabla_b \zeta_a, && (8.41)\\
D\varpi^2 &= \delta\varpi^2 + 2\varpi^2\Gamma^2\left(-b_\alpha - U^2 a_\alpha + 2U\sigma_\alpha\right). && (8.42)
\end{aligned}
$$

The trace of the relative strain tensor is (section A.5) :

$$
e_\alpha{}^\alpha = {}^2\nabla_a \zeta^a + \frac{1}{2} k^{ab}\delta g_{ab} + \frac{1}{2}\frac{D\varpi^2}{\varpi^2} \tag{8.43}
$$

8.2.5 Shear tensor

The shear tensor defined in equation (8.6) is (section A.6) :

$$
\begin{aligned}
s_{\alpha\beta} dx^\alpha dx^\beta &= \left[{}^2\nabla_{(a}\,\zeta_{b)} - \frac{1}{3}\left({}^2\nabla_c \zeta^c\right) k_{ab} + \frac{1}{2}\left(\delta g_{ab} - \frac{1}{3} k^{cd}\delta g_{cd} k_{ab}\right)\right.\\
&\quad \left. - \frac{1}{6}\frac{D\varpi^2}{\varpi^2} k_{ab}\right] dx^a\, dx^b\\
&\quad - \frac{1}{3}\left[\varpi^2\left({}^2\nabla_c\zeta^c + \frac{1}{2} k^{cd}\delta g_{cd}\right) - D\varpi^2\right](d\varphi - \Omega dt)^2
\end{aligned} \tag{8.44}
$$

where the parentheses denotes full symmetrization.

8.2.6 Energy momentum tensor of an elastic fluid

According to equations (7.52), the energy momentum tensor of an elastic fluid can be written in the following way :

$$
T_{\alpha\beta} = T^{\rm perf}_{\alpha\beta} + T^{\rm elas}_{\alpha\beta}, \tag{8.45}
$$

with $T^{\rm perf}_{\alpha\beta}$ the usual contribution to the energy-momentum tensor from the perfect fluid and $T^{\rm elas}_{\alpha\beta}$ the one from the elastic fluid :

$$
\begin{aligned}
T^{\rm perf}_{\alpha\beta} &= (p+\varepsilon) u_\alpha u_\beta + p g_{\alpha\beta}, && (8.46)\\
T^{\rm elas}_{\alpha\beta} &= -2\mu s_{\alpha\beta}. && (8.47)
\end{aligned}
$$

8.2.7 Circularity condition

A priori the axisymmetric and stationary spacetime for an elastic medium is not circular.

In a non-circular spacetime (Gourgoulhon & Bonazzola, 1993), the Killing vectors $\vec{\boldsymbol{\xi}}$ and $\vec{\chi}$, for stationary and axisymmetry respectively, are :

$$\xi^\alpha = Nn^\alpha - N^\alpha \quad \text{with} \quad N^\alpha = (0, N^1, N^2, \omega) \tag{8.48}$$

$$\chi^\alpha = Mm^\alpha - M^\alpha \quad \text{with} \quad M^\alpha = (0, M^1, M^2, 0) \tag{8.49}$$

$$n^\alpha = \frac{1}{N}\left(1, N^1, N^2, \omega\right) \quad \text{and} \quad n_\alpha = (-N, 0, 0, 0) \tag{8.50}$$

$$m^\alpha = \frac{1}{M}\left(0, M^1, M^2, 1\right) \quad \text{and} \quad m_\alpha = (-M\omega, 0, 0, M)\,. \tag{8.51}$$

According to the Generalized Papapetrou theorem, assuming a circular spacetime is equivalent to the two following conditions on the energy-momentum tensor $\boldsymbol{T}$ (section 6.2.2) :

$$\xi^\mu T_\mu{}^{[\alpha}\xi^\beta\chi^{\gamma]} = 0 \tag{8.52}$$

$$\chi^\mu T_\mu{}^{[\alpha}\xi^\beta\chi^{\gamma]} = 0, \tag{8.53}$$

Let us write the (2+1)+1 decomposition of shear tensor $\boldsymbol{s}$ (Gourgoulhon, 1995b) :

$$s_{\alpha\beta} = \bar{\bar{s}}_{\alpha\beta} + m_\alpha\bar{\bar{s}}_\beta + m_\beta\bar{\bar{s}}_\alpha + m_\alpha m_\beta\bar{\bar{s}} + n_\alpha\bar{s}_\beta + n_\beta\bar{s}_\alpha + n_\alpha m_\beta\bar{s} + n_\beta m_\alpha\bar{s} + n_\alpha n_\beta s. \tag{8.54}$$

The left-hand side of the equations (8.52-8.53) are given in section A.7 and can not be further simplified.

However one can assume that the spacetime is circular since the elastic deformations are expected to be small.

Therefore, one can write, following section 6.4.2, :

$$\vec{\boldsymbol{u}} = \Gamma\left(\vec{\boldsymbol{n}} + \vec{\boldsymbol{U}}\right). \tag{8.55}$$

8.2.8 Einstein equations

In a circular spacetime, one can show that $\bar{s}_\alpha = 0$ and $\bar{\bar{s}}_\alpha = 0$. Therefore the shear tensor writes (Gourgoulhon, 1995b) :

$$s_{\alpha\beta} = \bar{\bar{s}}_{\alpha\beta} + m_\alpha m_\beta\bar{\bar{s}} + n_\alpha m_\beta\bar{s} + n_\beta m_\alpha\bar{s} + n_\alpha n_\beta s, \tag{8.56}$$

with

$$\bar{\bar{s}}_{\alpha\beta} = \bar{\bar{s}}_{ab}, \tag{8.57}$$

$$\bar{\bar{s}} = -\frac{1}{3}\Gamma^2 Q, \tag{8.58}$$

$$\bar{s} = -\frac{1}{3}\Gamma^2 UQ = U\bar{\bar{s}}, \tag{8.59}$$

$$s = -\frac{1}{3}\Gamma^2 U^2 Q = U^2\bar{\bar{s}}, \tag{8.60}$$

where

$$Q = {}^2\nabla_a \zeta^a + \frac{1}{2} k^{ab} \delta g_{ab} - \frac{D\varpi^2}{\varpi^2}. \tag{8.61}$$

Therefore the quantities E, p_φ, $S^r{}_r$, $S^\theta{}_\theta$ and $S^\varphi{}_\varphi$ of the energy-momentum tensor can then be decomposed into two contributions : the one from the perfect fluid part, given by equations (6.82-6.87) and the one from the elastic part, given by equations (A.31-A.37).

All in all, one gets :

$$\boxed{E = \Gamma^2(\varepsilon + p) - p - 2\mu U^2 \bar{\bar{s}}}, \tag{8.62}$$

$$\boxed{p_\varphi = B(E+p)Ur\sin\theta + 2\mu B r \sin\theta U \left(U^2 - 1\right) \bar{\bar{s}}}, \tag{8.63}$$

$$\boxed{S^r{}_r = p - 2\mu \bar{\bar{s}}^r{}_r}, \tag{8.64}$$

$$\boxed{S^\theta{}_\theta = p - 2\mu \bar{\bar{s}}^\theta{}_\theta}, \tag{8.65}$$

$$\boxed{S^\varphi{}_\varphi = p + (E+p)U^2 + 2\mu \left(U^4 - 1\right) \bar{\bar{s}}}, \tag{8.66}$$

$$\boxed{S = 3p + (E+p)U^2 - 2\mu \left[\left(1 - U^4\right) + \bar{\bar{s}}^r{}_r + \bar{\bar{s}}^\theta{}_\theta\right]}. \tag{8.67}$$

8.2.9 Equation for equilibrium

The equation (6.100) for the equilibrium of a rotating star and that is used in the `Nrotstar` code of the LORENE library (figure 6.5) has been derived for a fluid interior and thus can be not be used for an elastic one.

According to the Einstein equation and Bianchi identity, the divergence of the energy-momentum tensor is :

$$\nabla_\sigma T^\sigma_\alpha = 0. \tag{8.68}$$

In the case of elastic matter, this condition is equivalent to (Gourgoulhon, 1995b) :

$$(\varepsilon + p) u_\sigma \nabla_\sigma u - \alpha + \nabla_\alpha p - 2\mu \nabla_\sigma s_\alpha{}^\sigma - 2 s_\alpha{}^\sigma \nabla_\sigma \mu = 0, \tag{8.69}$$

since in a circular spacetime, $u^\sigma \nabla_\sigma \varepsilon = u^\sigma \nabla_\sigma p = 0$ and $\nabla_\sigma u^\sigma = 0$.

With (section A.9),

$$u^\sigma \nabla_\sigma u_\alpha = {}^3\nabla_\alpha \ln \frac{N}{\Gamma} + \Gamma^2 U m_\alpha m^\beta \, {}^3\nabla_\beta U, \tag{8.70}$$

where Γ is the Lorentz factor, one gets :

$${}^3\nabla_\alpha \left[H + \ln \frac{N}{\Gamma} \right] - \frac{2\mu}{\varepsilon + p} \nabla_\sigma s^\sigma_\alpha - \frac{2}{\varepsilon + p} s^\sigma_\alpha \nabla_\sigma \mu + \Gamma^2 U m_\alpha m^\beta \, {}^3\nabla_\beta U = 0, \tag{8.71}$$

defining the log-enthalpy H :

$$H(n) = \int_0^n \frac{p(n')}{\varepsilon(n') + p(n')} \mathrm{d}n'. \tag{8.72}$$

Since (section A.10) :

$$\nabla_\sigma s^\sigma_\alpha = {}^3\nabla_\sigma \bar{\bar{s}}^\sigma_\alpha + \bar{\bar{s}}^\sigma_\alpha a_\sigma - \frac{1}{3}\Gamma^2 Q\left(b_\alpha - 2U\kappa_\alpha + U^2 a_\alpha\right), \tag{8.73}$$

the equation for equilibrium is :

$$\begin{aligned} {}^3\nabla_\alpha\left[H + \ln\frac{N}{\Gamma}\right] \quad & -\frac{2\mu}{\varepsilon+p}\left[{}^3\nabla_\sigma \bar{\bar{s}}^\sigma_\alpha + \bar{\bar{s}}^\sigma_\alpha a_\sigma - \frac{1}{3}\Gamma^2 Q\left(b_\alpha - 2U\kappa_\alpha + U^2 a_\alpha\right)\right] & (8.74)\\ & -\frac{2}{\varepsilon+p}\bar{\bar{s}}^\sigma_\alpha \nabla_\sigma \mu + \Gamma^2 U m_\alpha m^\beta\, {}^3\nabla_\beta U = 0. & (8.75)\end{aligned}$$

Writing $\bar{\bar{s}}^\sigma_\alpha$ with equation (8.44) and calculating its divergence, one gets an equation of the form :

$${}^3\nabla_a\left[H + \ln\frac{N}{\Gamma}\right] = \lambda_a. \tag{8.76}$$

Taking the divergence of this latter expression leads to :

$$\Delta_3\left[H + \ln\frac{N}{\Gamma} - \frac{2\mu}{\varepsilon+p}(\Theta - F)\right] = \Lambda, \tag{8.77}$$

with Λ a source term given in section A.11 and

$$\begin{aligned} \Theta &= {}^2\nabla_a \zeta^a, & (8.78)\\ F &= \frac{1}{3}Q - \zeta^a b_a + \Gamma^2 U \zeta^c\, {}^2\nabla_c U + \frac{1}{2}\frac{\delta\varpi^2}{\varpi^2}. & (8.79)\end{aligned}$$

Rewritting $\Lambda = \Delta_3\Psi$, equation (8.77) gives :

$$H + \ln\frac{N}{\Gamma} = \Psi + \frac{2\mu}{\varepsilon+p}(\Theta - F). \tag{8.80}$$

One can then reformulate equation (8.76) :

$$\Delta_3\zeta_a + \frac{1}{3}\,{}^3\nabla\Theta = \mathcal{S}(\Psi, F), \tag{8.81}$$

with the source term given in section A.12.

All in all, the equilibrium equations are, with $\Lambda = \Delta_3\Psi$:

$$\boxed{\Delta_3\left[H + \ln\frac{N}{\Gamma} - \frac{2\mu}{\varepsilon+p}(\Theta - F)\right] = \Lambda}, \tag{8.82}$$

$$\boxed{\Delta_3\zeta_a + \frac{1}{3}\,{}^3\nabla_a\Theta = \mathcal{S}(\Psi, F)}. \tag{8.83}$$

8.2.10 Boundary conditions

At the surface of the star, the boundary conditions are, since the pressure is null (Landau & Lifshit's, 1959) :

$$S_{ij}N^j = 0 \tag{8.84}$$

with S_{ij} the stress tensor and N^j the normal vector to the surface.

The components of the stress tensor are :

$$S_{rr} = p - 2\mu\bar{\bar{s}}_{rr} \qquad S_{r\theta} = -2\mu\bar{\bar{s}}_{r\theta} \tag{8.85}$$

$$S_{\theta\theta} = p - 2\mu\bar{\bar{s}}_{\theta\theta} \qquad S_{\theta\varphi} = 0 \tag{8.86}$$

$$S_{\varphi\varphi} = (\varepsilon + p)\Gamma^2U^2 - 2\mu\bar{\bar{s}} \qquad S_{r\varphi} = 0, \tag{8.87}$$

with :

$$\bar{\bar{s}}_{ab} = \frac{1}{2}\delta g_{ab} + \frac{1}{2}\,{}^2\nabla_a\zeta_b + \frac{1}{2}\,{}^2\nabla_b\zeta_a\frac{1}{6}\left(3\Theta - Q + \frac{3}{2}k^{cd}\delta g_{cd}\right). \tag{8.88}$$

The surface can be parametrized by the equation $r = R_{\rm s}(\theta)$ and the components of $\vec{\boldsymbol{N}}$ are :

$$N^r = \frac{1}{A}N^\theta = -\frac{1}{A}\frac{\mathrm{d}}{\mathrm{d}\theta}\ln R_{\rm s}(\theta). \tag{8.89}$$

Therefore, the boundary conditions write :

$$r\text{-component} \quad : \quad \bar{\bar{s}}_{rr} - \frac{\mathrm{d}}{\mathrm{d}\theta}\ln R_{\rm s}(\theta)\bar{\bar{s}}_{r\theta} = 0, \tag{8.90}$$

$$\theta\text{-component} \quad : \quad \bar{\bar{s}}_{r\theta} - \frac{\mathrm{d}}{\mathrm{d}\theta}\ln R_{\rm s}(\theta)\bar{\bar{s}}_{\theta\theta} = 0 \tag{8.91}$$

and are functions of the derivatives of the displacement $\vec{\boldsymbol{\zeta}}$.

The regularity condition at the center for the displacement writes

$$\zeta^a(r = 0) = 0. \tag{8.92}$$

8.3 Newtonian limit

8.3.1 Equation for equilibrium

Let us now derive the equation for equilibrium in the framework of Newtonian gravity.

Consider stationary and axisymmetric configurations. The metric is :

$$h_{ij}dx^idx^j = dr^2 + r^2d\theta^2 + r^2\sin^2\theta d\varphi^2. \tag{8.93}$$

For an elastic medium, writing $H = H = p/\varepsilon$ the specific enthalpy, one gets :

$$\nabla_i\left[H + \Phi_g - \frac{1}{2}\Omega^2r^2\sin^2\theta\right] - \frac{1}{3\rho}\nabla_i(\mu\Theta) - \frac{\mu}{\rho}\Delta_3\zeta_i - \frac{1}{\rho}\left(\nabla_i\zeta^j + \nabla^j\zeta_i\right)\nabla_j\mu + \frac{\Theta}{\rho}\nabla_i\mu = 0 \tag{8.94}$$

with $\Theta = \nabla^i \zeta_i$ and the Poisson equation for the gravitational potential Φ_g :

$$\Delta_3 \Phi_g = 4\pi G\rho, \tag{8.95}$$

where

$$\Delta_3 = \frac{\partial^2}{\partial r^2} + \frac{2}{r}\frac{\partial}{\partial r} + \frac{1}{r^2}\frac{\partial^2}{\partial \theta^2} + \frac{1}{r^2 \tan\theta}\frac{\partial}{\partial \theta}. \tag{8.96}$$

8.3.2 Boundary conditions

At the center, regularity imposes $\zeta^i = 0$.

At the surface,

$$\sigma_{ik} N^k = 0 \tag{8.97}$$

with σ_{ik} the stress tensor and N^k the normal to the surface.

With

$$\sigma_{ik} = -2\mu s_{ik} \tag{8.98}$$

since the pressure is null at the surface, and with the shear tensor

$$s_{ik} = \frac{1}{2}\left(\nabla_i \zeta_j + \nabla_j \zeta_i\right) - \frac{1}{3} e^j_j h_{ik} \tag{8.99}$$

the condition at the surface is :

$$s_{ik} N^k = 0. \tag{8.100}$$

Since the equation of the surface is $r - R_s(\theta) = 0$ with R_s the radius of the star at a given angle θ, the vector N^k normal to the surface is given by :

$$N^k = \nabla^k \left[r - R_s\left(\theta\right)\right]. \tag{8.101}$$

8.4 Numerical resolution

8.4.1 Block diagram of the `Elastar` code in LORENE

A new class called `Elastar`, derived from the `Starrot` class and the `Nrotstar` code has been created in LORENE and is currently in progress. Figure 8.1 schematically shows how the code may proceed.

All the modifications to the perfect fluid case have been implemented. The key point of the calculation lie in the loop to solve the equations for equilibrium (8.82-8.83).

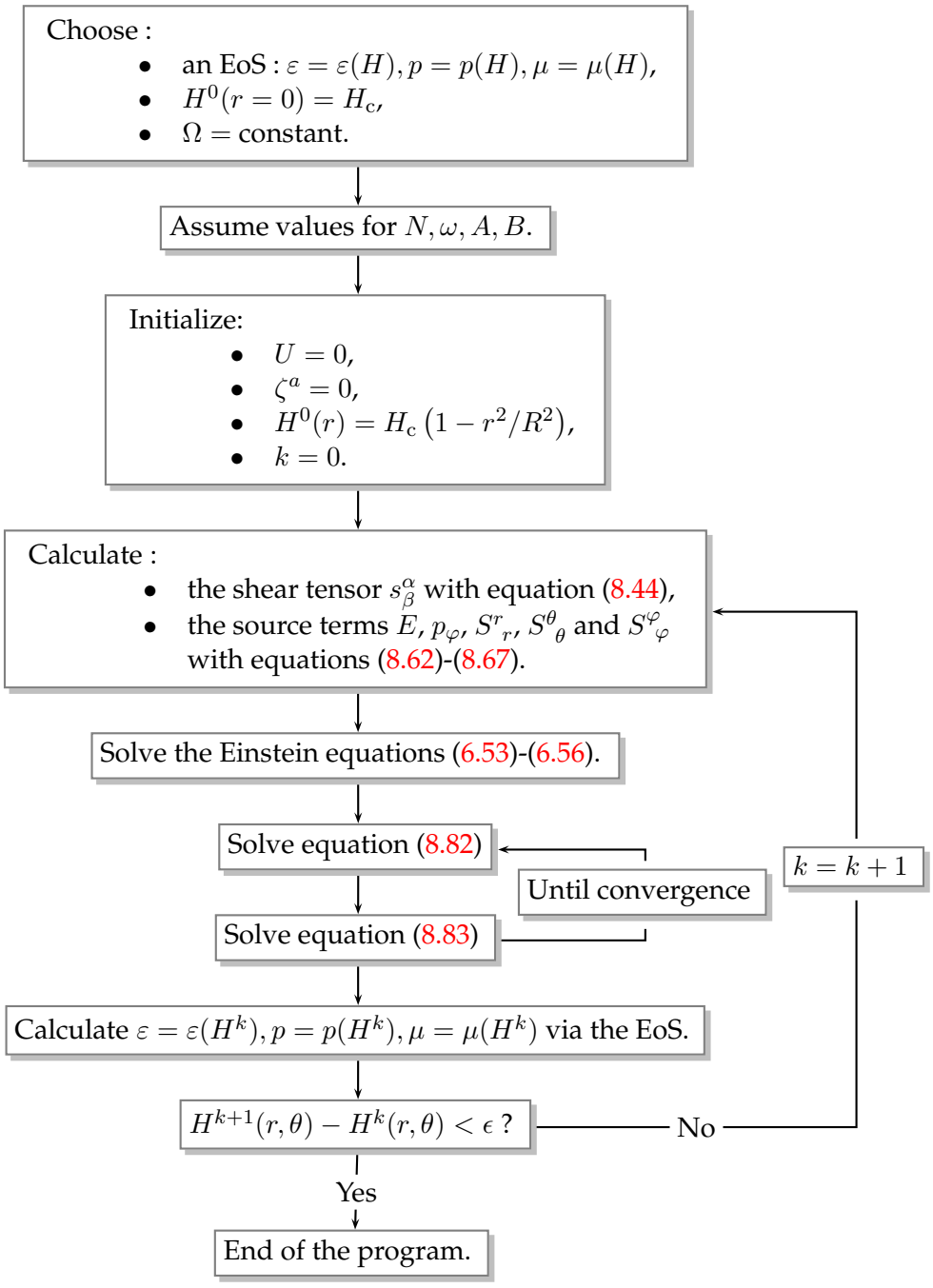

Figure 8.1: Schematic view of the `Elastar` code adapted from the `Nrotstar` one. k is the step of the calculations, $H^k(r,\theta)$ the value of the log-enthalpy at the step k and ϵ the threshold for the convergence of the code.

8.4.2 KADATH

Investigations are currently in progress to solve the vectorial Poisson equation (8.83) with KADATH, a new C++ library solving equations by the mean of spectral methods, developed by Philippe Grandclément at LUTh (Grandclément, 2010). Contrary to LORENE, KADATH is suitable for solving equations with boundary conditions such as equations (8.90-8.91) that are functions of the derivatives of the displacement.

Philippe Grandclément has adapted KADATH to solve the equations for an elastic rotating object in Newtonian gravity as presented in section 8.3 and their numerical resolution is currently in progress.

In the near future, the possibility to perform all the calculations detailed in figure 8.1 with KADATH will also be investigated.

8.5 Perspectives

In the near future, exact calculations of equilibrium configurations of rotating neutron stars with a solid crust and a liquid core and both solid crust and core will be performed. Different models of solid cores will be included. Among the applications is the study of the glitch phenomenon.

In the continuation of the study by Penner *et al.* (2011), a long term perspective is to calculate neutron star configurations with a (partly) solid interior in a binary system after generalizing the formalism for binary neutron stars to include the elastic properties of the solid phases.

One may also take into account the possible crystallization or melting in the interior and its consequences on the rotation by solving both the relativistic equations for elasticity and the heat equation (see also part II).

This chapter presented the derivation of the equations for stationary, axisymmetric and circular configurations of rigidly rotating neutron stars with a solid interior, taking into account the elastic properties of the latter. The formalism of elasticity in the framework of General Relativity introduced by Carter & Quintana (1972) and developed in subsequent papers : Carter (1973); Carter & Quintana (1975b); Quintana (1976) is used. The source terms in the Einstein equations and the equations for equilibrium have been derived. Their numerical resolution with the LORENE and KADATH libraries is currently in progress.

Part IV

Spin-up of accreting neutron stars

Introduction

The $P - \dot{P}$ diagram reveals that there exist two distinct populations of pulsars : the normal pulsars and the millisecond pulsars (see section 1.4). These millisecond pulsars have a period $P \lesssim 30$ milliseconds and a characteristic age $\tau_{\rm PSR} \gtrsim 10^9 - 10^{10}$ years whereas ordinary pulsars have $\tau_{\rm PSR} \lesssim 10^7$ years. Since they have a period derivative $\dot{P} \lesssim 10^{-18}$ s s^{-1}, their magnetic field is $B_{\rm PSR} \sim 10^8$ G, four orders of magnitude smaller than for the normal pulsars and they can be observed as radio pulsars during a longer time than normal pulsars.

According to the standard theory of neutron star evolution, millisecond pulsars are rejuvenated neutron stars. A normal pulsar is born in a supernova explosion, spins down from a period of few tens of milliseconds to few seconds and becomes radio-quiet or undetectable. A millisecond pulsar is a radio-dead pulsar that was spun-up to millisecond periods by the accretion of matter from its companion star during $\sim 10^9$ years (Alpar *et al.*, 1982; Radhakrishnan & Srinivasan, 1982).

Chapter 9 introduces general aspects concerning the accretion process (section 9.1) and the different evolutionary scenarios that lead to the formation of millisecond pulsars in neutron star binaries (section 9.2).

In chapter 10, a simple model for the rotational evolution of an accreting neutron star is presented (section 10.1). The influence of the magnetic field of the neutron star on the accretion process is included (section 10.2) together with the accretion-induced magnetic field decay as explained in section 10.3. The model considers configurations of rotating neutron stars, for different equations of state, with an increasing mass as a result of the accretion process and a varying rotational frequency (section 10.4).

Applications of the model to the recycling scenario are developed in chapter 11. In particular, are studied the spin-up of the puzzling pulsar J1903+0327 in section 11.1 and of the less and most massive millisecond pulsars observed in a binary, J0751+1807 and J1614-2230, respectively (section 11.2).

This project concerning the rotational evolution of accreting neutron stars is a collaboration with Michał Bejger, Paweł Haensel and Leszek Zdunik. I have been involved in the development of the `Evol` code, with a particular attention to the models of accretion-induced magnetic field decay. I have looked for interesting millisecond pulsars that could be studied with our model. I have performed calculations for the

various pulsars addressed in the chapter 11 that enable to constrain the properties of the progenitor neutron stars.

Chapter 9

Formation of millisecond pulsars

Contents

A millisecond pulsar is thought to be an old neutron star that has been recycled when undergoing accretion from its companion in a binary system (Alpar *et al.*, 1982; Radhakrishnan & Srinivasan, 1982). The system is observed as an X-ray binary during the recycling phase and by the end of it, the pulsar becomes an X-ray millisecond pulsar (Wijnands & van der Klis, 1998). When accretion stops, the X-ray pulsar becomes a radio millisecond pulsar. This scenario is in agreement with the radio pulsar statistics and is a very efficient mechanism in globular clusters due to the interactions and exchanges between the neutron stars and the other stars.

The chapters aim to give some general ideas about the evolution of neutron stars in binaries and the formation of millisecond pulsars. However the binary evolution in a globular cluster is complex and it will not be considered in the following. For more information see the review by Verbunt & Lewin (2004).

Section 9.1 explains how a neutron star can accrete matter from its companion star. General aspects concerning the Robe lobe overflow of the companion, the formation of an accretion disk around the neutron star and the spin-up of the latter are addressed. In section 9.2, the different types of neutron star X-ray binaries and the end product of their evolution are presented.

9.1 Accretion in binary systems

9.1.1 Roche-lobe overflow

Consider a binary system consisting of two stars of mass and radius (M_1, R_1) and (M_2, R_2) respectively, separated by a distance a (Frank *et al.*, 2002). This problem was addressed by the French mathematician Édouard Roche (1820-1883) in the context of planetary sciences. It studies the orbit of a test particle in the gravitational potential of a binary system. It is assumed that $R_{1,2} \ll a$ and that the orbits of the two stars are circular. The latter assumption is reasonable in binaries since the tidal forces between the stars circularize the orbit and synchronize the rotation of the stars.

The binary separation a between the two stars is given by Kepler law :

$$4\pi^2 a^3 = G(M_1 + M_2)P_{\rm b}^2 \tag{9.1}$$

with $P_{\rm b}$ the binary period and the system orbits its center of mass with an angular velocity :

$$\Omega = \sqrt{\frac{G\left(M_1 + M_2\right)}{a^3}}. \tag{9.2}$$

In the frame of reference rotating with the binary system, the Euler equation for a gas flow between the two stars, with a density ρ, pressure P and velocity $\vec{\boldsymbol{v}}$ is :

$$\frac{\partial \vec{\boldsymbol{v}}}{\partial t} + \left(\vec{\boldsymbol{v}}.\vec{\boldsymbol{\nabla}}\right)\vec{\boldsymbol{v}} = -\vec{\boldsymbol{\nabla}}\Phi_{\rm R} - 2\vec{\boldsymbol{\Omega}} \times \vec{\boldsymbol{v}} - \frac{1}{\rho}\vec{\boldsymbol{\nabla}}P, \tag{9.3}$$

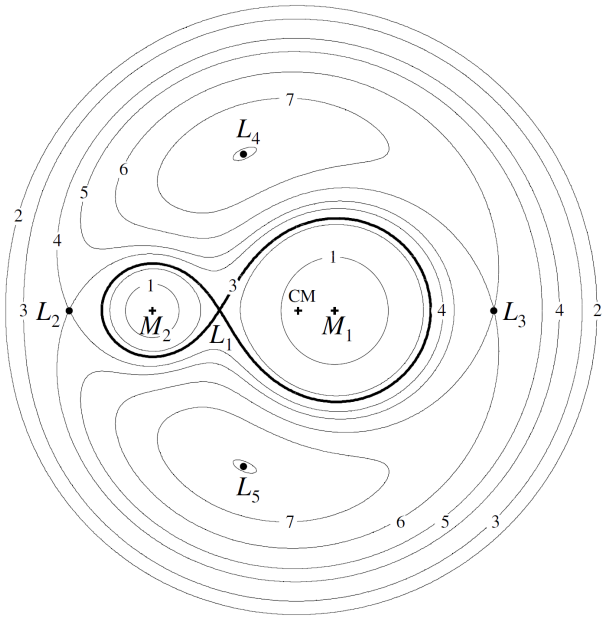

Figure 9.1: Cross-sections in the orbital plane of the Roche potential for $q = 0.25$. The numbers 1-7 correspond to increasing values of the Roche potential. Are shown the center of mass (CM) of the binary system and the Lagrange points $L_1 - L_5$. See text for details. From Frank *et al.* (2002).

where $\vec{\mathbf{\Omega}} = \Omega\vec{\boldsymbol{e}}$ with $\vec{\boldsymbol{e}}$ a unit vector normal to the orbital plane and $\Phi_{\rm R}$ the so-called Roche potential :

$$\Phi_{\rm R}(\vec{\boldsymbol{r}}) = -\frac{GM_1}{|\vec{\boldsymbol{r}} - \vec{\boldsymbol{r_1}}|} - \frac{GM_2}{|\vec{\boldsymbol{r}} - \vec{\boldsymbol{r_2}}|} - \frac{1}{2}\left(\vec{\mathbf{\Omega}} \times \vec{\boldsymbol{r}}\right)^2. \tag{9.4}$$

The shape of the equipotentials of the Roche potential is governed by the mass ratio $q = M_2/M_1$ and the scale is given by the binary separation a. Figure 9.1 shows sections in the orbital plane of the Roche equipotentials. The potential has two valleys centered on each star that are called the Roche lobes. In a given lobe, the dynamics is dominated by the gravitational attraction of the star at its center. When moving from the bottom of the valley to its top, the equipotentials are less circular and have with a tear-drop shape. The Roche lobes join at the inner Lagrange point L_1.

A Roche lobe is not spherical and one defines an average radius $R^L_{1,2}$ for a given Roche lobe so that a sphere of radius $R^L_{1,2}$ has the same volume as the lobe, as shown on figure 9.2. An approximate analytic formula derived by Eggleton (1983) is :

$$\frac{R^L_2}{a} = \frac{0.49q^{2/3}}{0.6q^{2/3} + \ln\left(1 + q^{1/3}\right)} \tag{9.5}$$

and R^L_1 is given by replacing q by q^{-1} in the previous formula.

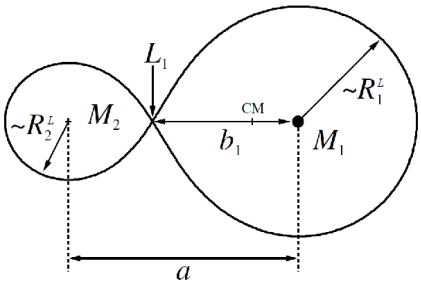

Figure 9.2: Schematic representation of the Roche lobes. See text for details. From Frank *et al.* (2002).

Paczyński (1971) derived a simpler form for $0.1 \lesssim q \lesssim 0.8$:

$$\frac{R_2^L}{a} = \frac{2}{3^{4/3}} \left(\frac{q}{1+q} \right)^{1/3} = 0.462 \left(\frac{M_2}{M_1 + M_2} \right)^{1/3}. \tag{9.6}$$

9.1.2 Mass transfer dynamics

Consider now the surface of one of the stars of the binary. By definition $\vec{v} = 0$ and $P = 0$ so that according to equation (9.3), the star has an almost spherical shape given by the Roche potential (9.4). In a given lobe the gravitational pull of the star at the center dominates and there is no tendency for the matter of one star to be accreted by the other. The binary system is said to be detached. Accretion can proceed only if matter is ejected from a star by a stellar wind and captured by the second star.

Suppose that, as a result of stellar evolution, the star 2 extends and fills its Roche lobe. In this case, according to equation (9.3), its surface is not spherical but has a tear-drop shape. The matter of the star 2 lies near the inner Lagrange point. If perturbed, by pressure forces for example, the matter passes by the L_1 point, reaches the Roche lobe of the star 1 and is captured by the latter. The system is said to be semi-detached and an efficient mass transfer between star 2 and star 1 settles as long as the star 2 fills its Roche lobe. The phenomenom is called a Roche-lobe overflow.

Since the star 2 losses matter, its mass decreases and the mass ratio q changes. Therefore, mass transfer affects the dynamics of the system (Frank *et al.*, 2002).

The orbital angular momentum J is given by :

$$J = \left(M_1 a_1^2 + M_2 a_2^2 \right) \Omega \tag{9.7}$$

with the distances from the center of mass to the center of the stars :

$$a_1 = \left(\frac{M_2}{M_1 + M_2} \right) a \qquad \text{and} \qquad a_2 = \left(\frac{M_1}{M_1 + M_2} \right) a. \tag{9.8}$$

From (9.1), one gets :

$$J = M_1 M_2 \left(\frac{Ga}{M_1 + M_2} \right)^{1/2} . \tag{9.9}$$

Assuming that the mass lost by the star 2 is accreted by the star 1, $\dot{M}_1 + \dot{M}_2 = 0$. Since the star 2 losses matter, $\dot{M}_2 < 0$.

Differentiating equation (9.9), one gets :

$$\frac{\dot{a}}{a} = \frac{2\dot{J}}{J} - \frac{2\dot{M}_2}{M_2} \left(1 - \frac{M_2}{M_1} \right) . \tag{9.10}$$

If one supposes that the mass and the angular momentum of the binary is conserved, ie. for a conservative mass transfer, then $\dot{J} = 0$. Therefore, equation (9.10) gives :

$$\frac{\dot{a}}{a} = \frac{2\left(-\dot{M}_2\right)}{M_2} \left(1 - \frac{M_2}{M_1} \right) . \tag{9.11}$$

If the more massive star accretes from the less massive star, $\dot{a} > 0$ and the binary extends. Physically, there is more mass near the center of mass of the system, so that the lighter star moves to a wider orbit to conserve the system angular momentum. If accretion proceeds from the more massive to the less massive, the binary separation decreases.

Differentiating equation (9.6) gives :

$$\frac{\dot{R}_2^L}{R_2^L} = \frac{\dot{a}}{a} + \frac{\dot{M}_2}{3M_2}, \tag{9.12}$$

and with equation (9.10),

$$\frac{\dot{R}_2^L}{R_2^L} = \frac{2\dot{J}}{J} + \frac{2\left(-\dot{M}_2\right)}{M_2} \left(\frac{5}{6} - \frac{M_2}{M_1} \right) . \tag{9.13}$$

For $q < 5/6$, the Roche lobe expands for a conservative mass transfer and the mass transfer may continue if angular momentum is lost by wind for example or if the star expands, for giant or subgiant stars for example.

Therefore, the stability of the overflow depends on the complex evolution of the radius of the donor star and of the Roche lobe radius. More information can be found in Tauris & van den Heuvel (2006).

9.1.3 Disk formation

Consider now a particle of the flow that passes through the L_1 point. It has a high specific angular momentum and thus cannot be accreted directly by the mass-capturing

star. In particular, in a non-rotating frame, the component of the flow velocity perpendicular to the lines joining the center of the two stars is $v_\perp \sim b_1\Omega$ with b_1 the distance between the center of accreting star and the L_1 point. However, the velocity component parallel to the line of centers is $v_\parallel \lesssim c_\mathrm{s} \ll v_\perp$ with c_s the sound speed in the envelope of the mass-losing star (Frank *et al.*, 2002). As a consequence, the stream of matter is supersonic when crossing the L_1 point and is even more accelerated by the gravitational potential of the accreting star.

A test particle of the flow released from the L_1 point and falling in the gravitational potential of the mass-gaining star has an elliptic orbit in the plane of the binary and its trajectory slowly precesses due to the influence of the second star. Thus, since matter continuously passes the L_1 point, a particle of the flow undergoes shocks which dissipate its energy. Since the angular momentum of the particle is conserved, it moves to the orbit of lowest energy for a given angular momentum, that is a circular orbit. In conclusion, the matter that passes through L_1 orbits the accreting star in the binary plane with a radius R_circ such that the angular momentum that it had at the L_1 is conserved :

$$R_\mathrm{circ} v_\perp \left(R_\mathrm{circ}\right) = b_1^2\Omega \tag{9.14}$$

with

$$v_\perp \left(R_\mathrm{circ}\right) = \left(\frac{GM_1}{R_\mathrm{circ}}\right)^{1/2}, \tag{9.15}$$

ie.,

$$\frac{R_\mathrm{circ}}{a} = (1+q)\left(\frac{b_1}{a}\right)^4. \tag{9.16}$$

Plavec & Kratochvil (1964) fitted to a good accuracy the distance b_1 from the L_1 point to the center of the star 1 by the equation :

$$\frac{b_1}{a} = 0.500 - 0.227\log q, \tag{9.17}$$

so that equation (9.16) writes :

$$\frac{R_\mathrm{circ}}{a} = (1+q)\left(0.500 - 0.227\log q\right)^4. \tag{9.18}$$

R_circ is called the circularization radius. It is always smaller than the Roche lobe radius R^L. The inflowing matter orbits the star inside the Roche lobe unless the radius of the star is larger than the circularization radius which is never the case when the accreting object is a compact object such as a neutron star.

Therefore, the flow of matter forms a ring of radius at the radius $r = R_\mathrm{circ}$ to the center of the accreting star. However, because of dissipative processes such as collisions, shocks, viscosity, ..., the matter in the flow is heated and radiates energy. It loses energy and therefore moves to an orbit closer to the star. All in all, the infalling matter spirals inwards the accreting star in the orbital plane and this results in the formation of an accretion disc.

If the accreting star is a compact object, the radius of the marginally stable orbit (see section 6.4.5.5) may be larger than the radius of the star. In this case, the accretion disk does not extend up to the surface of the star but up to the radius of the marginally stable orbit. The magnetic field of the accreting object, which is very strong for neutron stars in particular, has also an influence on the location of the innermost radius of the accretion disk.

The details of the dynamics in the accretion disk is far beyond the scope of this thesis (for more details see eg. Frank *et al.* (2002); Balbus (2007)).

9.1.4 Neutron star recycling

Consider a binary star system with at least one high-mass star ($M > 10$ M$_\odot$). The initially more massive star, star 1, forms a neutron star after a supernova explosion at the end of its life (cf section 1.2). On the one hand, if the binary disrupts due to the asymmetry of the explosion and/or the neutron star kick velocity received ($\sim$ 100-1000 km s^{-1}) at birth, it produces a neutron star with a large velocity and a runway star. On the other hand, if the binary system survives the explosion, the eccentricity is likely to be large. During $\sim 10^7 - 10^8$ years, the neutron star spins down and may be observed as a radio pulsar. When the energy is low enough, the radio emission stops. Meanwhile, the companion star, star 2, evolves and eventually overflows its Roche lobe. An accretion disk is formed and the neutron star accretes matter from its companion. An accreted particle from the disk transfers its angular momentum to the mass-gaining star, ie. to a neutron star. Therefore, the latter gains not only mass but is also spun-up. This process is believed to recycle the radio-dead pulsars to millisecond pulsars.

9.2 Evolution of neutron star binaries

9.2.1 The population of millisecond pulsars

About 200 of the known millisecond radio pulsars are in a binary with a companion star. The figure 9.3 shows the nature of their companion. One can roughly distinguish four different populations (Tauris, 2011) :

- the fully recycled millisecond pulsars : they have a period $P \lesssim 10$ ms and are in a binary mainly with helium white dwarf companions or ultra light companions such as brown dwarfs;
- the mildly recycled millisecond pulsars, with 10 ms $\lesssim P \lesssim 100$ ms and with carbon-oyxgen white dwarf or neutron star companions;
- the millisecond pulsars in globular clusters : the interactions and exchanges between the neutron stars and the other stars are believed efficiently produce millisecond pulsars;

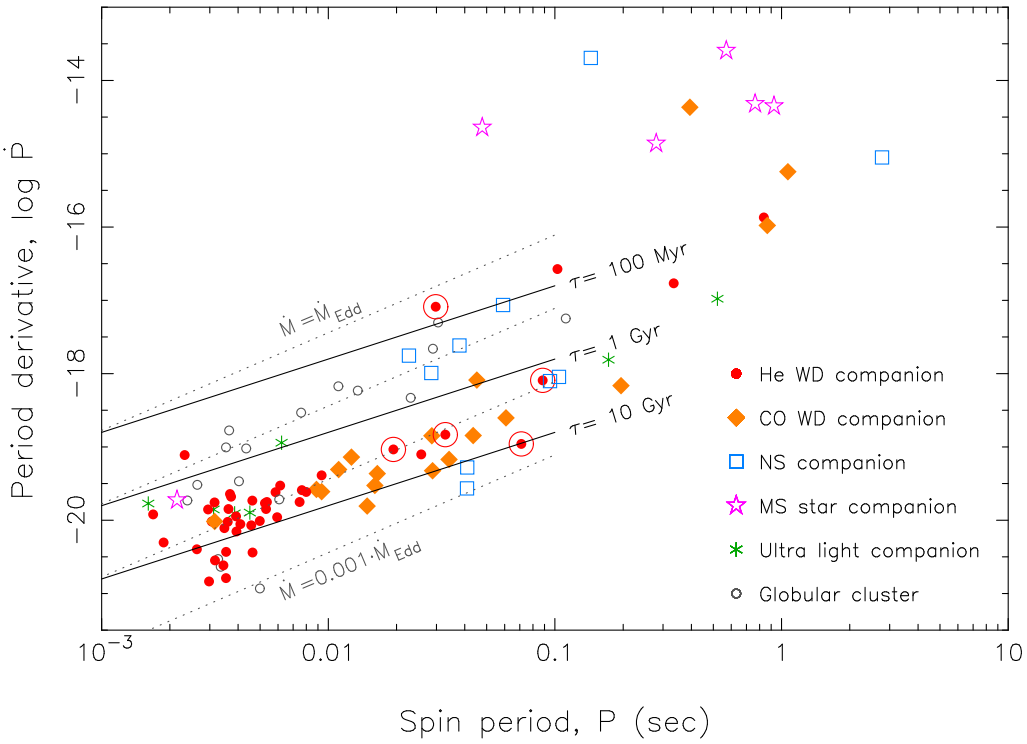

Figure 9.3: $P - \dot{P}$ of the $\sim$ 100 binary radio pulsars and the nature of the companion star. He and CO WD stand for Helium and Carbon-Oxygen White Dwarf and MS star for Main-Sequence star. Figure from Tauris (2011) based on the *ATNF Pulsar Catalogue* (Manchester *et al.*, 2005, http://www.atnf.csiro.au/research/pulsar/psrcat).

- the pulsars in a binary with a main-sequence star. They have large spin periods and are not recycled.

Note that there also exists isolated millisecond pulsars.

Figure 9.4 shows the orbital period $P_{\rm orb}$ of the binary as a function of the mass of the companion star M_2. Depending on the location in the $P_{\rm orb} - M_2$ plan, one can distinguish classes of binaries that will be explained in the following. These correspond to different evolutionary processes in binary systems that lead to the formation of millisecond pulsars.

9.2.2 The different cases of Roche lobe overflows

Figure 9.5 shows the evolution of the radius of a 5 $M_\odot$ star during its different evolutionary stages :

i. in the long-lasting main sequence stage (point 1 to 2), hydrogen burns in the core of the star;

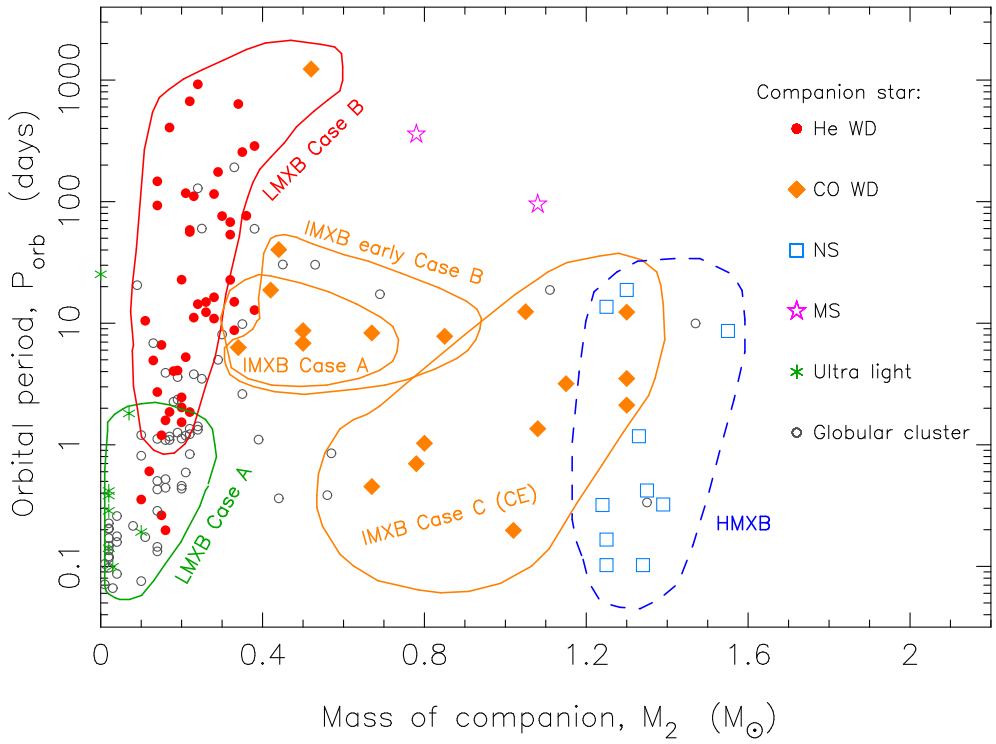

Figure 9.4: Orbital period $P_{\rm orb}$ as a function of the companion mass M_2 for ~ 200 binary radio pulsars. The boundaries between the different classes are schematic. Figure from Tauris (2011).

ii. in the red giant branch (RGB), there is no more hydrogen at the center (point 3) and the hydrogen burning proceeds in a shell around the helium core. Then the helium core ignites (point 4);

iii. when the star exhausts the helium in its core, the helium burns in a shell around a carbon core and the star enters the asymptotic giant branch (AGB).

Following Tauris (2011), one can define three classes of Roche lobe overflow depending on the onset of the mass transfer. If the distance between the accretor and the donor is such that overflow starts in the phase (i), (ii) or (iii) then it is called a case A, B or C Roche lobe overflow, respectively. The cases B and C cover a large range of radii and thus orbital periods according to figure (9.5). Once the mass transfer has started it continues until the mass-donor star no longer fills its Roche lobe.

The endpoint of the evolution of a binary system depends on the initial mass of the donor star and on the onset and nature of mass-transfer, as explained in the following.

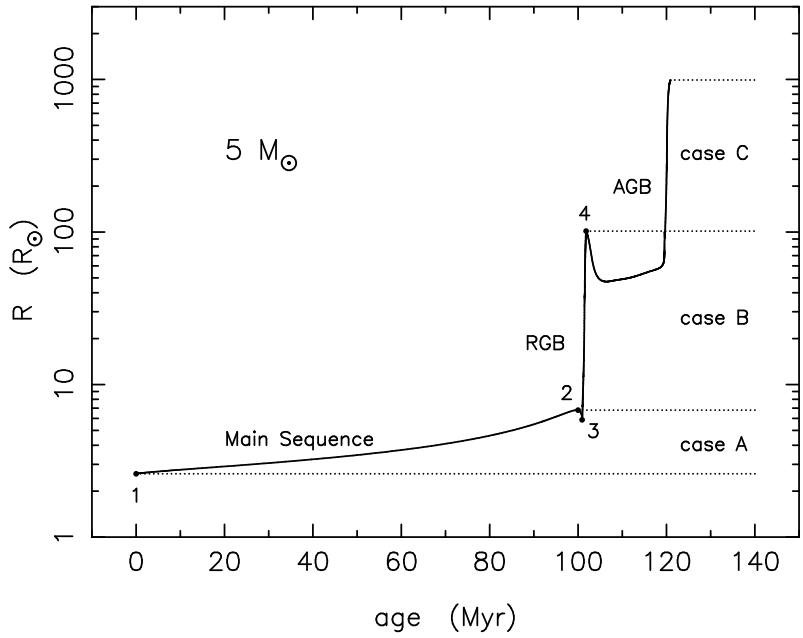

Figure 9.5: Evolution of the radius of a 5 $M_\odot$ star. The different cases of Roche lobe overflow are indicated. From Tauris & van den Heuvel (2006).

9.2.3 Neutron star X-ray binaries & millisecond pulsars

9.2.3.1 The different neutron star X-ray binaries

There are observational evidence that the X-ray binaries harbor not only neutron stars but also black holes. However, only neutron stars binaries will be considered in the following.

One can define three types of X-ray binaries depending on the mass of the companion star M_2.

- High-Mass X-ray Binaries (HMXB) : $M_2 > 10$ $M_\odot$. The companion star is an evolved (sub)giant star that is massive enough to have a strong stellar wind ($\dot{M} \sim 10^{-6}$ $M_\odot$ yr^{-1}) or to undergo atmospheric Roche-lobe overflow (figure 9.6). The outgoing matter is accreted by the neutron star and powers a bright X-ray emission for $10^5 - 10^6$ years. Ultimately, the companion star is massive enough to also explode in a supernova and to form a second neutron star. If the binary survives the second explosion, then a double neutron star system is formed with a partly recycled millisecond pulsar. Nine such systems are known so far (Lorimer, 2008; Kiziltan *et al.*, 2010);

- Low-Mass X-ray Binaries (LMXB) : $M_2 \lesssim 1 - 2$ $M_\odot$. The neutron star accretes matter ($\dot{M} \sim 10^{-10} - 10^{-8}$ $M_\odot$ yr^{-1}) via the accretion disk that originates from the companion star overflowing its Roche lobe, during $\sim 10^8 - 10^9$ years (figure 9.6).

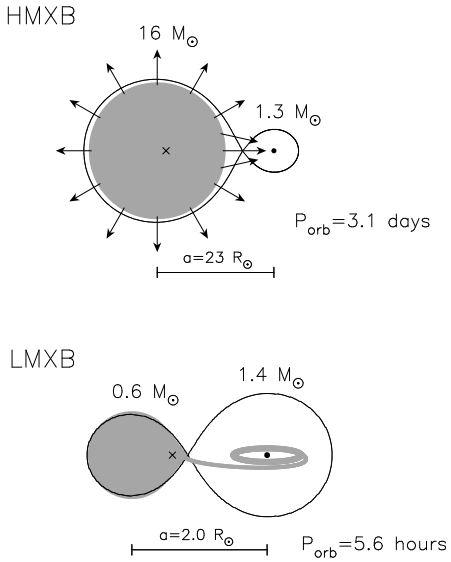

Figure 9.6: Schematic representation of a HMXB and a LMXB. From Tauris & van den Heuvel (2006).

At the end of the accretion phase, the companion becomes a white dwarf orbiting a millisecond neutron star;

- Intermediate-Mass X-ray Binaries (IMXB) : $1 - 2 \lesssim M_2 < 10$ $M_\odot$. The companion star in these systems is not massive enough to produce efficient wind that can trigger strong X-ray emission. Therefore, the mass transfer originates from the companion Roche lobe overflow. However, since the companion star is more massive than in a LMXB, the overflow lasts only ~ 1000 years with an accretion rate $\sim 10^{-4}$ $M_\odot$ yr^{-1}. For such high accretion rate, the X-ray emission is likely to be absorbed by the surrounding gas. Therefore, IMXBs are not easily observable.

9.2.3.2 The evolution of the Low-Mass X-ray Binaries

In a LMXB, the companion star of the neutron star has a mass $\lesssim 1 - 2$ $M_\odot$. The subsequent evolution and the endpoint depend on the orbital period of the binary :

- for $P_{\rm orb} \leqslant 1$ day, ie. for a close binary, the Roche lobe overflow starts while the companion is still on the main-sequence. It is thus a case A overflow. A low-mass helium white dwarf is then formed and the neutron star is spun-up to millisecond periods. However the white dwarf may evaporate under the irradiation from first the X-ray emission of the accreting neutron star and then the pulsar wind. This leads either to the formation of a single millisecond pulsar, for example the Black Widow pulsar B1937+21 (Fruchter *et al.*, 1988), or to a system with ultra light, substellar companions, such as planets as observed around the pulsar B1257+12

(Wolszczan & Frail, 1992). If the binary survives, it has a short orbital period $\lesssim 1$ day;

- for $P_{\rm orb} \geqslant 1$ day, the system is a wide binary and therefore, the onset of the overflow requires a large increase of the radius of the companion. The star fills its Roche lobe when it has evolved reaching the red giant branch. This a case B overflow and the result is a binary system composed of an helium white dwarf with a mass $0.2 \leqslant M_2 \leqslant 0.46$ M$_\odot$ and a fully recycled neutron star, with a large range of possible orbital periods $\sim 1 - 1000$ days.

These two scenarios are consistent with the figure 9.4 where millisecond pulsar binary systems originating from Low-Max X-ray Binaries are indicated, for the case A and B Roche lobe overflows.

9.2.3.3 The evolution of the Intermediate-Mass X-ray Binaries

The companion star in a IMXB has a mass $1 - 2 \leq M_2 \leq 10$ M$_\odot$. The three cases of Roche lobe overflow are encountered in the IMXBs, which correspond to the three groups indicated on the figure 9.4 :

- for $P_{\rm orb} \leqslant 2.5$ day, a stable mass transfer is initiated by a case A overflow and lasts $\sim 10^7$ years. The neutron star is therefore fully recycled and a Carbon-Oxygen white dwarf, or an helium white dwarf if the system is very close, is formed. The resulting binary system has an orbital period of $3 - 20$ days;

- for $2.5 \leqslant P_{\rm orb} \leqslant 10$ days, for a companion star which has just left the main sequence, ie. for a case B overflow, most of the matter accreted by the neutron star is ejected in a jet. This stabilizes the mass transfer but moderately spins up the neutron star. This results in the formation a system with a carbon-oxygen white dwarf and a partially recycled pulsar with $1 \leqslant P_{\rm orb} \leqslant 50$ days;

- for $P_{\rm orb} = 100 - 1000$ days, ie. a wide system, a case C overflow starts when the companion is on the asymptotic giant branch. This results in a short common envelope phase where the companion stellar envelope engulfs the neutron star. During this phase, the orbital period may be strongly reduced. The envelope is then ejected and the neutron star is later recycled either by the wind or by a case B overflow from the companion star. The result is a carbon-oxygen white dwarf orbiting a partially recycled neutron star with a short orbital period ($3 - 20$ days).

In conclusion, the end product of the evolution of a binary and the recycling of a neutron star to millisecond periods depend on the mass of the companion star and on the orbital period before the overflow starts. One should note however that modeling the evolution of an X-ray binary is complex since many factors concerning the evolution of the companion star, the mass-transfer process and its stability, the accretion of matter onto the neutron star, ... have to be taken into account all together.

A model for the spin evolution of an accreting magnetized neutron star is presented in chapter 10 and is applied to the study of the spin-up of neutron stars to millisecond periods in chapter 11.

Chapter 10

Model of accreting magnetized neutron stars

Contents

Consider a binary system consisting of a young radio pulsar and a low-mass main-sequence companion. As explained in the previous chapter, the neutron star evolves independently of its companion at first and spins down by magnetic dipole braking down to the period of a few seconds in few million years. Finally, it crosses the radio pulsar death line and disappears as a pulsar (see also chapter 1.4).

In the recycling scenario, after several billion years, the low-mass companion enters the red giant phase and fills its Roche lobe. An accretion disk is then formed and accretion onto the neutron star starts. The binary system becomes a Low Mass X-ray Binary (LMXB). During $\sim 10^8 - 10^9$ yrs, the accretion process increases the mass of the neutron star, accelerate its rotation and induces its magnetic field decay.

The spin-up of an accreting neutron star can be modeled by a sequence of stellar configurations with increasing mass and rotational frequency. This study may ultimately enable to determine the mass that the neutron star has accreted to reach its current observed millisecond period, within a reasonable time interval. Constraints may also be put on the accretion rate and on the progenitor neutron star properties (mass, magnetic field, equation of state, ...)

The spin-up of an accreting neutron star was first modeled by Kluźniak & Wagoner (1985) considering slowly rotating neutron stars configurations, based on the work by Hartle (1967b). Cook *et al.* (1994) extended the model to stationary rigidly rotating neutron stars. The influence of the magnetic field was first included by Burderi *et al.* (1999) in a semi-analytical model based on the results by Cook *et al.* (1994).

Zdunik *et al.* (2002) studied the recycling of strange stars to millisecond period and considered accretion from the innermost stable circular orbit (see also section 6.4.5.5). They used stationary axisymmetric rigidly rotating neutron star configurations calculated by the mean of the `Rotstar` class in LORENE (for details, see section 6.6). They did not include the influence of the magnetic field and of the accretion disk.

The last part of this thesis is in the continuation of Zdunik *et al.* (2002). This chapter aims to provide a description of the model and formulas that are originally presented in Bejger *et al.* (2011). The location of the inner boundary of the accretion disk, from which accretion takes place, is calculated for a model of thin magnetized accretion disk as described in section 10.2. Indeed, the accretion radius is moved from the radius of the innermost stable orbit to a larger one by the neutron magnetic field. Moreover, the accretion-induced magnetic field decay is modeled by an observationally-motivated though simplistic prescription, detailed in section 10.3. The properties of the stationary rotating configurations of neutron stars are summarized in section 10.4. Finally, section 10.5 presents a schematic view of the `Evol` code that is used to model the spin-evolution of an accreting neutron stars.

10.1 Spin-up modeling

Consider a neutron star of mass M, radius R, rotational period P, spin frequency $f = 1/P$, rotation frequency $\omega_{\rm s} = 2\pi f$ and surface magnetic field B. It has a total baryon mass $M_{\rm b}$.

10.1.1 Mass increase and accretion rate

Let $t_{\rm i}$ be the instant when accretion starts. The increase of baryon mass $\Delta M_{\rm b}(t)$ at a given time t is :

$$\Delta M_{\rm b}(t) = \int_{t_{\rm i}}^{t} \dot{M}_{\rm b}(t'){\rm d}t'. \tag{10.1}$$

where $\dot{M}_{\rm b}(t)$ is the accretion rate at the time t as measured by a distant observer.

Since the evolution of the accretion rate is unknown, as a first approximation, $\dot{M}_{\rm b}$ can be considered as constant, so that $\Delta M_{\rm b}(t) \approx \dot{M}_{\rm b}(t - t_{\rm i})$.

Observations do not provide a measurement of $M_{\rm b}$ but of the gravitational mass M (see also section 2.2.2.2). By definition the increase of the latter is :

$$\Delta M(t) = \int_{t_{\rm i}}^{t} \dot{M}(t'){\rm d}t'. \tag{10.2}$$

The two quantities ΔM and $\Delta M_{\rm b}$ are related by the equation (see e.g., Friedman *et al.* 1988) :

$${\rm d}M = \Omega {\rm d}J + u^t {\rm d}M_{\rm b}, \tag{10.3}$$

where J is the total angular momentum and u^t the time component of fluid 4-velocity as measured by a distant observer.

10.1.2 Angular momentum evolution

Assuming that the increase of the angular momentum of the star J is related to the accreted mass, one can write :

$${\rm d}J = x_l l_{\rm tot} {\rm d}M_{\rm b}. \tag{10.4}$$

Zdunik *et al.* (2002) considered accretion from the marginally stable orbit (the so-called ISCO, section 6.4.5.5) and thus write :

$$l_{\rm tot} = l_{\rm ms}, \tag{10.5}$$

where $l_{\rm ms}$ is the specific angular momentum of a particle at the ISCO. In the new model presented here, the radius r_0 at which accretion takes place is calculated precisely for a model of magnetized accretion disk based on the paper by Kluźniak & Rappaport (2007), that includes both the angular momentum transfered to the star by the infalling

matter $l(r_0)$ and the effect of the interaction between the magnetic field of the neutron star and the accretion disk, $l_{\rm mag}$. Therefore, one writes $l_{\rm tot} = l_{\rm tot}(M_{\rm b}, f, B)$ ie.

$$\boxed{l_{\rm tot} = l(r_0) + l_{\rm mag}}. \tag{10.6}$$

The parameter x_l ($0 \leq x_l \leq 1$) is the fraction of $l_{\rm tot}$ that is effectively transfered to the star. In the following, we consider that $x_l \simeq 1$, in accordance with recent numerical simulations (Beckwith *et al.*, 2008).

Therefore, for a star accreting at the rate $\dot{M}_{\rm b}$, the time evolution of the total angular momentum J equation is :

$$\frac{{\rm d}J}{{\rm d}M_{\rm b}} = l_{\rm tot} \tag{10.7}$$

Finally, the equation for the evolution of the accretion rate $\Delta M(t)$ is :

$$\Delta M(t) = \int_{t_{\rm i}}^{t} \dot{M}_{\rm b}(u^t + l_{\rm tot}\Omega){\rm d}t'. \tag{10.8}$$

10.2 Accretion disk model

In the following the spin-up by accretion from a thin magnetized accretion disk is modeled using the magnetic-torque disk-pulsar coupling presented in Kluźniak & Rappaport (2007) in Newtonian gravity. However this formulation is modified to include the existence of the marginally stable orbit in General Relativity.

10.2.1 Magneto-hydrodynamic equation

Consider a steady thin axisymmetric magnetized disk around a neutron star having a dipole moment aligned with its rotation axis. In the following, the index i ranges from 1 to 3 and we use the cylindrical coordinates $(x^1 = r, x^2 = \varphi, x^3 = z)$ and the Einstein summation convention on repeated indices. We assume that the accretion disk is thin, ie. $H\left(r\right)/r \ll 1$ with $H(r)$ the height of the disk at a distance r of the neutron star.

10.2.1.1 Mass conservation

The steady-state mass conservation equation reads :

$$\partial_i \left(\rho v^i\right) = 0 \tag{10.9}$$

with ρ is the density and the fluid velocity components $v^i = (v^r, v^\varphi, v^z)$. Neglecting a vertical outflow from the axisymmetric disc, one gets

$$\frac{1}{r}\frac{\partial}{\partial r}\left(r\rho v^r\right) = 0 \tag{10.10}$$

and integrating over the thickness of the disk :

$$\frac{1}{r}\frac{\partial}{\partial r}\left(r\Sigma v^r\right) = 0 \tag{10.11}$$

with $\Sigma(t,r) = \int_{-H}^{H} \rho(r,t)\,\mathrm{d}z$. Therefore $r\Sigma v^r$ is conserved and there is a constant inflow of mass through each point of the disk. The accretion rate corresponding to this inflow is :

$$\dot{M}(r,t) = -2\pi r\Sigma(r,t)v^r(r), \tag{10.12}$$

since $v^r < 0$.

10.2.1.2 Angular momentum transport

The steady-state Navier-Stokes equation is :

$$\rho v^i \partial_i v^j = -\partial^j P - \rho\partial^j\Phi + \partial_i t^{ij} \tag{10.13}$$

with P the thermal pressure, φ the gravitational potential and t^{ij} the stress tensor. The latter can be decomposed into two contributions :

$$t^{ij} = t^{ij}_{\mathrm{vis}} + t^{ij}_{\mathrm{Max}} \tag{10.14}$$

with the t^{ij}_{vis} the viscous stress-energy tensor and t^{ij}_{Max} the Maxwell stress tensor :

$$t^{ij}_{\mathrm{Max}} = \frac{1}{4\pi}\left(E^iE^j + B^iB^j - \frac{1}{2}(E^2+B^2)\delta^{ij}\right) \tag{10.15}$$

with B and E the magnetic and electric fields respectively and δ^{ij} the Kronecker symbol. In the non-relativistic part of the flow, $E \sim v/cB \ll B$ and can therefore be neglected.

The φ-component of equation (10.13) reads (Tessema & Torkelsson, 2010) :

$$\rho\frac{v^r}{r}\frac{\partial}{\partial r}\left(rv^\varphi\right) = \frac{1}{r}\frac{\partial}{\partial r}\left(rt^{r\varphi}_{\mathrm{Max}}\right) + \frac{\partial}{\partial z}\left(t^{z\varphi}_{\mathrm{Max}}\right) + \frac{1}{r}\frac{\partial}{\partial r}\left(rt^{r\varphi}_{\mathrm{vis}}\right). \tag{10.16}$$

From equation (10.15),

$$\frac{1}{r}\frac{\partial}{\partial r}\left(rt^{r\varphi}_{\mathrm{Max}}\right) = \frac{1}{4\pi}\frac{1}{r}\frac{\partial}{\partial r}\left(rB^rB^\varphi\right), \tag{10.17}$$

$$\frac{\partial}{\partial z}\left(t^{z\varphi}_{\mathrm{Max}}\right) = \frac{1}{4\pi}\frac{\partial}{\partial z}\left(B^zB^\varphi\right). \tag{10.18}$$

The ratio of the $r\varphi$-component of the magnetic stress tensor over its $z\varphi$-component is $\sim \left|\frac{B^r}{B^z}\right|\left(\frac{H}{r}\right) \ll 1$ if $|B^r/B^z| \ll r/H$ which is valid for the small disk conductivities that are encountered in this problem. Therefore the $r\varphi$-component of the magnetic stress tensor can be neglected.

Integrating equation (10.16) over the thickness of the disc and multiplying by r, one gets :

$$\Sigma v^r \frac{\partial}{\partial r}\left(r v^\varphi\right) = \frac{r}{4\pi} B^z B^\varphi + \frac{\partial}{\partial r}\left(r T^{r\varphi}_{\rm vis}\right) \tag{10.19}$$

where the magnetic field is evaluated at $z = H$ and $T^{ij}_{\rm vis}$ the height-integrated viscous tensor.

Since $v^\varphi = r\Omega$, with Ω the local orbital frequency of the disk material, the height-averaged angular momentum equation is :

$$-\frac{\dot{M}}{4\pi H r}\frac{\partial}{\partial r}\left(r\Omega^2\right) = \Gamma_{\rm vis} + \Gamma_{\rm B}, \tag{10.20}$$

with

$$\Gamma_{\rm vis} = \frac{1}{2H}\frac{\partial}{\partial r}\left(r T^{r\varphi}_{vis}\right), \tag{10.21}$$

$$\Gamma_{\rm B} = \frac{r}{4\pi H} B^z B^\varphi. \tag{10.22}$$

10.2.1.3 Prescription for the azimuthal component of the magnetic field

Following Kluźniak & Rappaport (2007), a simple analytical model for the azimuthal component of the magnetic field B_φ at $z = H$ is used :

$$B^\varphi \simeq B^z \left(1 - \frac{\Omega}{\omega_{\rm s}}\right) \tag{10.23}$$

with $B^z > 0$. This prescription assumes that the magnetic field penetrates the accretion for a large range of radii. The magnetic torque then vanishes when $\Omega = \omega_{\rm s}$. For large distances, $B^\varphi \sim B^z$, which ensures the stability and equilibrium of the field above the disk plane (Rappaport *et al.*, 2004).

10.2.1.4 Height-averaged momentum transport equation

Since the magnetic dipole is assumed to be aligned with the rotation axis, $B^z = \mu/r^3$.

Therefore, with the equations (10.23) and (10.20) and since $l = r\Omega^2$, one gets the height-averaged momentum transport equation :

$$-\frac{\dot{M}}{4\pi H r}\frac{\partial}{\partial r}\left(r\Omega^2\right) = \frac{1}{2H}\frac{\partial}{\partial r}\left(r T^{r\varphi}_{\rm vis}\right) + \frac{1}{4\pi H}\frac{\mu^2}{r^5}\left(1 - \frac{\Omega}{\omega_{\rm s}}\right). \tag{10.24}$$

10.2.2 Inner radius of the accretion disk

Kluźniak & Rappaport (2007) assume that the viscous torque vanishes at a certain radius r_0 and that the disk is Keplerian for $r \geq r_0$. At the radius r_0, the angular momentum is

removed by the high magnetic stresses at the rate needed to sustain the accretion rate. Since the magnetic stresses increase inward for $r < r_0$, the viscous torque also vanishes in this region.

Therefore the equation for r_0, the inner radius of the accretion rate, reads :

$$\frac{\mathrm{d}l}{\mathrm{d}r} = -\frac{\mu^2}{\dot{M}r^4}\left(1-\omega^{-1}\right), \tag{10.25}$$

where l is the specific angular momentum of a particle of the accretion disk and $\omega = \omega_\mathrm{s}/\Omega_\mathrm{K}(r_0)$ is the fastness parameter with the Keplerian angular frequency

$$\Omega_\mathrm{K}(r) = (GM/r^3)^{1/2}. \tag{10.26}$$

Defining the corotation radius r_c as the radius where the Keplerian angular frequency is equal to the rotation frequency of the central star, one can write :

$$\boxed{r_\mathrm{c} = \left(\frac{GM}{\omega_\mathrm{s}^2}\right)^{1/3}}. \tag{10.27}$$

In particular,

$$\boxed{\omega = (r_0/r_\mathrm{c})^{3/2}}. \tag{10.28}$$

10.2.3 Relativistic specific angular momentum

The calculations by Kluźniak & Rappaport (2007) are restricted to the non-relativistic limit and, in particular, do not include the existence of the marginally stable orbit of radius r_ms. The model is valid for $r_0 \gg r_\mathrm{ms}$.

Since the relativistic effects can be important for rotating neutron stars, in particular near the mass-shedding limit and for massive stars, the original formalism needs to be modified. Therefore a relativistic formula for the specific angular momentum $l(r_0)$ transfered by a particle accreted at r_0 is used.

Bejger *et al.* (2010) reported a simple analytical formula approximating the specific angular momentum for a particle in circular orbit around a neutron star. It is checked for several equations of state and for rigidly rotating axisymmetric and stationary configurations of neutron stars in General Relativity and describes exact results with a high accruracy. By this method, the existence of the marginally stable orbit is included. They got :

$$\boxed{l(r) = r\frac{v}{\sqrt{1-v^2/c^2}}} \tag{10.29}$$

with

$$v = \frac{r}{\sqrt{1-2GM/(rc^2)}}\left(\sqrt{\frac{GM}{r^3}} - \frac{2GJ}{r^3c^2}\right). \tag{10.30}$$

One defines a non-dimensional function $f_{\rm ms}$ by :

$$f_{\rm ms}(r) = \frac{2}{\Omega r}\frac{{\rm d}l}{{\rm d}r}. \tag{10.31}$$

In the Newtonian framework as described in Kluźniak & Rappaport (2007), $f_{\rm ms} = 1$.

Equations (10.29) and (10.30) give :

$$\boxed{f_{\rm ms}(r_0) = \frac{1-\alpha/\bar{r}^{3/2}}{(1-v^2/c^2)^{3/2}\sqrt{1-1/\bar{r}}}\left(\frac{\bar{r}-2}{\bar{r}-1} - 2\frac{v^2}{c^2} + \frac{3\alpha}{\bar{r}^{3/2}-\alpha}\right)}, \tag{10.32}$$

with $\alpha = Jc/(\sqrt{2}GM^2)$, $\beta = r_{\rm c}/r_{\rm s}$ and $\bar{r} = r_0/r_{\rm s} = \beta\omega^{2/3}$ with $r_{\rm s} = 2GM/c^2$ the Schwarzschild radius. The radius of the marginally stable orbit $r_{\rm ms}$ corresponds to

$$\left.\frac{{\rm d}l}{{\rm d}r}\right|_{r=r_{\rm ms}} = 0 \text{ ie. } f_{\rm ms}(r_{\rm ms}) = 0. \tag{10.33}$$

Finally, the radius of the inner boundary of the accretion disk r_0 is given by :

$$\frac{1}{2}f_{\rm ms}(r_0) = \left(\frac{r_{\rm m}}{r_0}\right)^{7/2}\left(\sqrt{\frac{r_{\rm c}^3}{r_0^3}-1}\right), \tag{10.34}$$

or

$$\boxed{\frac{1}{2}f_{\rm ms}(r_0) = \frac{\xi^{7/2}}{\omega^{10/3}}\left(1-\omega^{-1}\right)} \tag{10.35}$$

with the magnetospheric radius, for which the magnetic pressure balances the pressure of the matter accreted at the rate $\dot{M}_{\rm b}$ (Elsner & Lamb, 1977) :

$$\boxed{r_{\rm m} = (GM)^{-1/7}\,\dot{M}_{\rm b}^{-2/7}\mu^{4/7}} \tag{10.36}$$

and

$$\boxed{\xi = \frac{r_{\rm m}}{r_{\rm c}}}. \tag{10.37}$$

Note that in the seminal model for magnetized accretion disk by Ghosh & Lamb (1979), ξ has a fixed value.

10.2.4 Magnetic torque

According to equation (10.24), the total magnetic torque acting on the star is :

$$\tau_{\rm B} = -\int_{r_0}^{\infty}\frac{\mu^2}{r^4}\left(1-\omega^{-1}\right){\rm d}r \tag{10.38}$$

$$= -\frac{\mu^2}{9r_0^3}\left(3-2\sqrt{\frac{r_{\rm c}^3}{r_0^3}}\right). \tag{10.39}$$

10.2.5 Total angular momentum equation

The right-hand side of equation (10.6) reads :

$$l_{\rm tot}(M_{\rm b}, f, B) = l_0 + \frac{\tau_{\rm B}}{\dot{M}_{\rm b}} \tag{10.40}$$

where $l_0 = l(r_0)$ describes the transfer of specific angular momentum by the accreted matter, calculated from equation (10.29) and $\tau_{\rm B}$ the magnetic torque given in equation (10.39). So

$$\boxed{l_{\rm mag} = -\frac{\mu^2}{\dot{M}_{\rm b} 9 r_0^3}\left(3 - 2\sqrt{\frac{r_{\rm c}^3}{r_0^3}}\right)}. \tag{10.41}$$

Finally, the equation for the evolution of the total angular momentum is :

$$\boxed{\frac{{\rm d}J}{{\rm d}M_{\rm b}} = l_0 - \frac{\mu^2}{9 r_0^3 \dot{M}_{\rm b}}\left(3 - 2\sqrt{\frac{r_{\rm c}^3}{r_0^3}}\right)} \tag{10.42}$$

with $\mu = B^z R^3$. In the following, $B^z = B_{\rm p}$ the polar surface magnetic field, ie. :

$$\boxed{\mu = B_{\rm p} R^3}. \tag{10.43}$$

According to equation (10.42), the spin evolution of the neutron star results from the interplay between the spin-up resulting from the accreted matter and the spin-down caused by the magnetic field torque.

An additional equation for the evolution of the magnetic field of the star under the influence of the accreted matter is needed.

10.2.6 Degeneracy parameter

Note that the set of equations (10.34) and (10.42) depends only on the quantity :

$$\kappa = B^2/\dot{M}, \tag{10.44}$$

via the magnetospheric radius in equation (10.36) and not on B and $\dot{M}$ separately. Therefore, the model is degenerate with respect to the constant κ.

This property is extensively used in the numerical simulations presented in the next chapter.

10.3 Magnetic field evolution of accreting neutron stars

The $P - \dot{P}$ diagram (cf chapter 1.4) clearly shows that there exists two distinct populations of neutron stars : the "normal" ones with $B \sim 10^{11} - 10^{13}$ G and the millisecond with a magnetic field about four times weaker : $B \sim 10^8$ G.

Bhattacharya *et al.* (1992) reported that the observations of "normal" pulsars are consistent with no magnetic field decay or decay over the time scale higher than the one needed for a neutron star to stop being a pulsar, ie. $\sim 10^8$ yr.

10.3.1 Accretion-induced magnetic field decay

While the normal pulsars are isolated objects, most of the millisecond pulsars are in binary systems with a degenerate companion and thus interacted with their companion star in the past.

Different models propose to explain the magnetic field decay at the origin of the low field in millisecond pulsars (Colpi *et al.*, 2001) :

- decay of the crustal magnetic field :
  the Ohmic decay of the magnetic field is due to both the heating of crust, resulting from the accretion, that reduces the conductivity and to the transport of matter and currents deeper into the crust toward the core. The core may either expel the crust magnetic field (Geppert & Urpin, 1994) or assimilate and retain it (Konar & Bhattacharya, 1997);

- screening of the magnetic field by accreted matter :
  Bisnovatyi-Kogan & Komberg (1974) originally suggested that the magnetic field decays since it is buried and screened by the accreted matter. The screening may happen either within the neutron star, the field being buried under a mountain of accreted plasma channelled onto the magnetic poles (Payne & Melatos, 2004) or within the magnetosphere due to the electric current of the infalling plasma (Lovelace *et al.*, 2005; Wette *et al.*, 2010);

- spin-driven scenario :
  the neutron superfluid vortices migrate in the outer crust during the spin-down and drag the proton magnetic flux tubes because of the strong interpinning that exists between them (Srinivasan *et al.*, 1990; Konar & Bhattacharya, 1999). This results in the expulsion of the magnetic flux from the superconducting core and in the decay of the magnetic field due to the ohmic dissipation in the crust.

The evolution of the magnetic field in accreting neutron stars is the subject of active research but, so far, no scenario with precise microphysics and magneto-hydrodynamic modeling has emerged.

Therefore, in the following, simple phenomenological and observationally-motivated models will be adopted.

10.3.2 Model of magnetic field decay

Taam & van den Heuvel (1986) noticed a possible inverse correlation between the polar surface magnetic field $B_{\rm p}$ and the estimated amount of accreted material for a set of LMXBs of different age, later confirmed by van den Heuvel & Bitzaraki (1995).

Shibazaki *et al.* (1989) proposed the following *ad-hoc* formula for the evolution of the magnetic field :

$$\boxed{B_{\rm p}(\Delta M_{\rm b}) = \frac{B_{\rm i}}{1 + \Delta M_{\rm b}/m_{\rm B}}}, \tag{10.45}$$

where $B_{\rm i}$ is initial (ie. pre-accretion) magnetic field, $B_{\rm p}(\Delta M_{\rm b})$ the magnetic field after the neutron star accreted $\Delta M_{\rm b} = \dot{M}_{\rm b} t$ and $m_{\rm B}$ a constant. The value $m_{\rm B} \sim 10^{-4}$ M$_\odot$ is consistent with the observed or estimated P, B and ΔM of binary and isolated millisecond radio pulsars and the prescription (10.45) reproduces the inverse correlation noted by Taam & van den Heuvel (1986).

The equation (10.45) is stated for a subset of accreting neutron stars and is obviously too simplistic to describe the magnetic-field decay in all of them. Wijers (1997) showed in particular that a decay law $B_{\rm p} \propto 1/\Delta M_{\rm b}$ is inconsistent with a broader set of available data on accreting neutron stars in both X-ray binaries and recycled millisecond pulsars and suggests an additional dependence on the accretion rate.

Wijers (1997) proposed another observationally-motivated formula :

$$B_{\rm p}(\Delta M_{\rm b}) = \frac{B_{\rm i}}{(1 + \Delta M_{\rm b}/m_{\rm B})^2}, \tag{10.46}$$

but with a lower value of $m_{\rm B} \sim 10^{-2}$ M$_\odot$.

Kiel *et al.* (2008) and Osłowski *et al.* (2011) used an exponential decay for $B_{\rm p}$ in their population synthesis codes :

$$B_{\rm p} = (B_{\rm i} - B_{\rm min}) \exp(-\Delta M_{\rm b}/m_{\rm B}) + B_{\rm min}, \tag{10.47}$$

with $B_{\rm min}$ the assumed minimal residual magnetic field. Osłowski *et al.* (2011) found that the values $B_{\rm min} = 10^8$ G and $m_{\rm B} = 0.05$ M$_\odot$ are consistent with the observed $P - \dot{P}$ distribution.

Figure 10.1 compares the evolution of the magnetic field with the amount of accreted matter $\Delta M_{\rm b}$ for the three magnetic field prescriptions : equation (10.45) from Shibazaki *et al.* (1989), equation (10.46) from Wijers (1997) and equation (10.47) from Osłowski *et al.* (2011). The accretion-induced decay is more pronounced for the Shibazaki *et al.* (1989) prescription, but asymptotically, for a large accreted mass, the three prescriptions give the same value of the magnetic field. In fact the parameters of each of the formulas have been chosen so that the final value for the magnetic field after accretion of few tens of solar masses equals the typical observed magnetic field for millisecond pulsars : 10^8 G.

Despite its limitations, the prescription (10.45) proposed by Shibazaki *et al.* (1989) will be adopted in the following. Nevertheless, the results with the prescriptions (10.46) and (10.47) will be compared to assess the dependence of the results on the model of accretion-induced magnetic field decay.

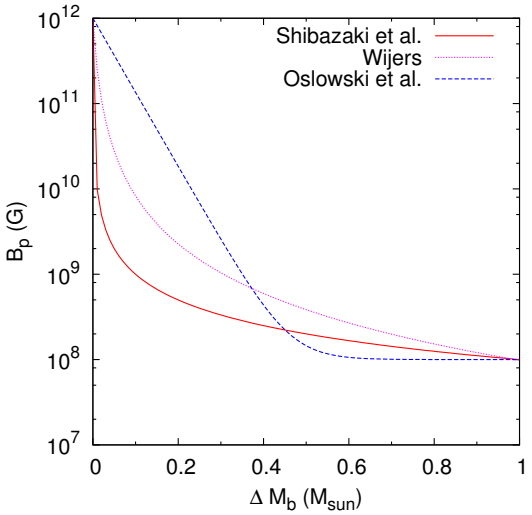

Figure 10.1: Variation of the magnetic field $B_{\rm p}$ with the amount of accreted matter $\Delta M_{\rm b}$ for the three different magnetic field prescriptions. See text for details.

10.4 Models of neutron stars

The detailed modeling of the spin-up of an accreting neutron stars requires the knowledge of the structure of the neutron star. The latter is determined by the equation of state (EoS) (see also section 2.1.1.1). Moreover, the effect of rotation on this structure should be taken into account (cf. section 6.7).

10.4.1 Equations of state

Three equations of state based on different microphysical models are used. For the two first ones, the matter is assumed to be only composed neutrons, protons, electrons, and muons in β-equilibrium :

- non-relativistic equation of state by Douchin & Haensel (2001) - DH in the following. It is based on the SLy4 nuclear interaction and offers a unified description of the core and the crust. It has a maximum mass $M_{\rm max} = 2.05\,{\rm M}_\odot$.

- model $A18 + \delta v + {\rm UIX}^*$ by Akmal *et al.* (1998) - APR in the following. Some relativistic corrections are included in this non-relativistic model. The maximum mass is $M_{\rm max} = 2.21\,{\rm M}_\odot$.

- relativistic equation of state from Bednarek *et al.* (2011), with minor changes - BM in the following. It includes a high-density softening due to the appearance of hyperons. The maximum mass $M_{\rm max}$ is $2.03\,{\rm M}_\odot$.

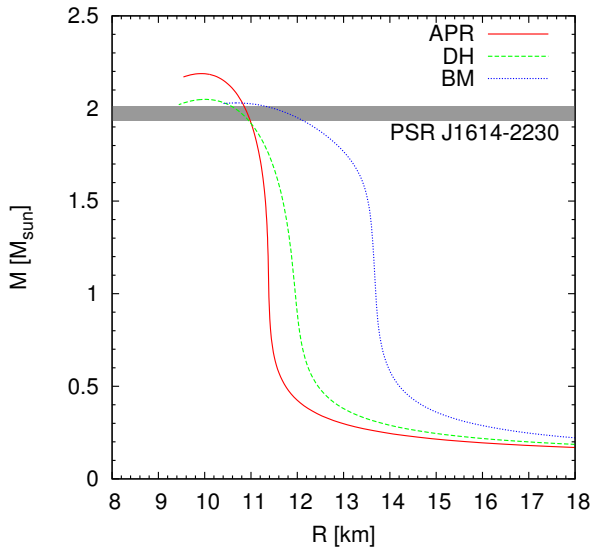

Figure 10.2: Mass-radius diagram for the three equations of the state considered in this model together with PSR J1614-2230 mass constraint.

Figure 10.2 shows the mass-radius diagram for the equations of state. All the three of them are consistent by the recent mass measurement of PSR J1614-2230 by Demorest *et al.* (2010) $M = 1.97 \pm 0.04$ M$_\odot$ (cf section 11.2.2).

10.4.2 Rotating neutron star configurations

The spin evolution of an accreting neutron star is described by a sequence of stationary rotating configurations of neutron stars with increasing baryon mass, resulting from the accretion of matter, and varying spin frequency, depending of the torque acting on the neutron star and on the angular momentum transfer of the infalling matter.

In order to take into account the effects of rotation on the structure of neutron stars, the models of rotating neutron stars are computed with the `Nrotstar` code based on the LORENE library (see also section 6.6). For a given central enthalpy h_c, the baryon mass M_B, gravitational mass M, equatorial radius R_{equ}, total stellar angular momentum J of neutron stars with increasing rotational frequency are computed, up to the mass-shedding limit with the frequency f_K. The evolution of the accreting star, ie. the changes of the angular momentum J and of the baryon mass M_b are calculated using the equation 10.42.

10.5 Block diagram of the `Evol` code

The figure 10.3 schematically shows the structure of the `Evol` code, developed in collaboration with Michał Bejger, Paweł Haensel and Leszek Zdunik.

For a given equation of state and magnetic field prescription, the code determines the parameters, including the magnetic field, of a neutron star rotating at a given $f_{\max}$.

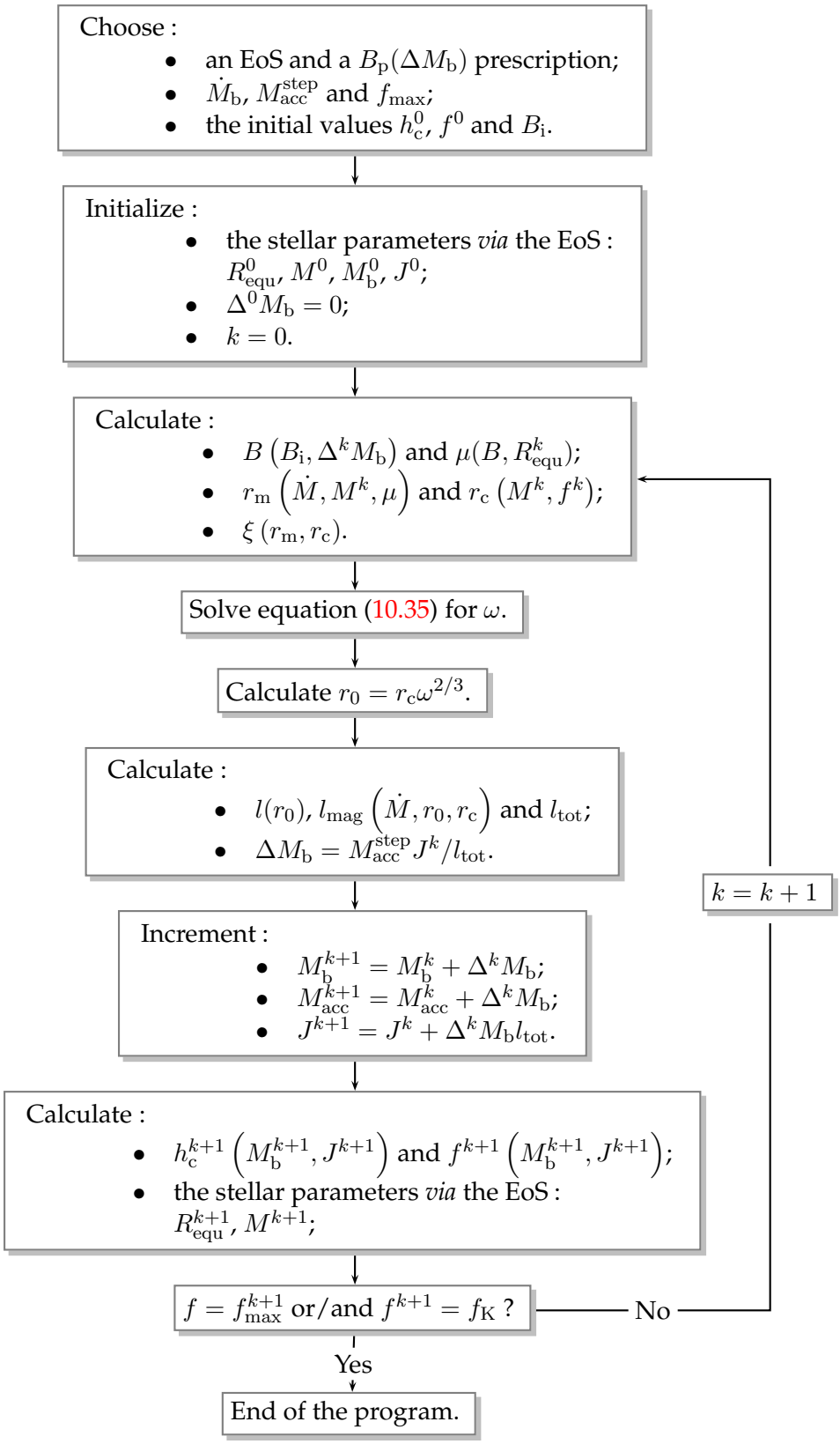

Figure 10.3: Schematic view of the Evol code. $M_{\rm acc}^{\rm step}$ and $f_{\rm max}$ are respectively the given step in the accreted mass and the given maximum rotational frequency of the accreting star. k is the step in the calculation.

Chapter 11

Application to the spin-up of neutron stars

Contents

The model for the evolution of the rotational frequency of accreting neutron stars presented in the previous chapter enables to study in details the recycling process that currently observed millisecond pulsars underwent. Constraints on the progenitor neutron star and on the accretion rate are derived for the pulsar J1903+0327 which has an unusually high eccentricity (section 11.1) and for the lowest and highest millisecond pulsars in a binary in the section 11.2. Further application to the formation of submillisecond pulsars is presented in section 11.3.

11.1 PSR J1903+0327

This section aims to show the direct application of the model presented in the previous chapter to the pulsar J1903+0327. At the beginning of my Ph.D. studies in 2009, it was the most massive observed Galatic millisecond pulsar with an accurately measured mass of $M = 1.667 \pm 0.021$ M$_\odot$. However, the pulsar J1614-2230 has been reported with a higher mass : $M = 1.97 \pm 0.04$ M$_\odot$ in 2010 (Demorest *et al.*, 2010).

The mass of the pulsar J1903+0327 and its magnetic field, *via* its period and period derivative (equation 1.21), are known. Constraints on the progenitor neutron star and on the average accretion mass can be put. The model, approach and results are published in Bejger *et al.* (2011).

11.1.1 An eccentric millisecond pulsar

The pulsar J1903+0327 was discovered with a 2.15 ms period while performing a pulsar survey of the Galactic plane with Arecibo radiotelscope in October 2005 (Champion *et al.*, 2008). The highly eccentric binary orbit of the pulsar was later noticed in follow-up observations with Arecibo, Green Bank and Westerbrook Telescopes. Measurements of the advance in periastron and the detection of the Shapiro delay in the $\sim$ 1.5 years timing of the pulsar constrained the mass of the pulsar $M_1 = 1.74 \pm 0.04$ M$_\odot$ and of its companion $M_2 = 1.051$ M$_\odot$. Nevertheless, the short span of the timing did not enable to take into account the proper motion of the pulsar in these measurements, though it may affect them.

The mass of the companion suggests that it may be a neutron star, a white dwarf or a main-sequence star. No pulsations from the companion were detected in Arecibo observations. A main-sequence star, a possible companion of the pulsar, was identified with the optical and ground-accessible infrared Gemini North telescope in 2007. No eclipse of the pulsar by the stellar wind of the main-sequence or strong irradiation of the companion by the pulsar relativistic wind were detected in multifrequency observations. Champion *et al.* (2008) suggested a triple system scenario : a non-observed white dwarf may be in a close binary with the neutron star, the main-sequence star being in a much wider orbit around this inner binary.

Freire *et al.* (2011) presented new observations of the binary. The optical observations with the Very Large Telescope confirmed that the companion of the pulsar is the main-

Parameter	Value
Distance d (kpc)	6.4 ± 1.0
Spin period P (ms)	2.15
Spin frequency f (Hz)	465
Spin period derivative $\dot{P}$ (s s^{-1})	1.88×10^{-20}
Dipolar magnetic field B (G)	2.0×10^{8}
Orbital eccentricity e	0.44
Orbital inclination angle	$78(2)^{\circ}$
Orbital period P_b (days)	95.17
Pulsar mass $M_{\rm PSR}$ ($M_\odot$)	1.667(21)
Companion star	Main-sequence star
Companion mass $M_{\rm C}$ ($M_\odot$)	1.029(8)

Table 11.1: Parameters of PSR J1903+0327 with $1-\sigma$ uncertainties from Freire *et al.* (2011). The mass measurements are given with 99.7% confidence limits. $B_{\rm surf}$ is calculated with the formula (1.21) for a neutron star with $R = 10$ km and $I = 10^{45}$ g cm^{-2}.

sequence star, with an age $\sim 4-7$ Gyr. This rules out the triple system scenario. The new and longer ($\sim$ 4-years) radio timing of the pulsar with Arecibo and Green Bank radiotelescopes gave more precise measurements of the binary properties, as presented in table 11.1. In fact the advance in periastron together with a very clear Shapiro delay were detected. In particular, the mass of the pulsar is 1.67 $M_\odot$. Stellar winds or tidal forces acting on the companion are negligible.

On the one hand, PSR J1903+0327 has period and period derivative that are typical of a millisecond pulsar. On the other hand, the large orbital eccentricity and the main-sequence companion of this pulsar located in the Galactic plane are not consistent with the conventional binary evolution scenarios presented in the chapter 9 making PSR J1903+0327 a puzzling pulsar.

11.1.2 Formation scenarios

Four different scenarios were presented so far to explain the origin of PSR J1903+0327 system with a millisecond spin period but a large orbital eccentricity and a main-sequence companion.

11.1.2.1 Rapid rotation at birth

Champion *et al.* (2008) proposed that the neutron star was not recycled. It was born spinning rapidly in a core-collapse supernova in a binary system in the Galactic disk, with a main-sequence companion.

According to Liu & Li (2009), the supernova kick made the orbit strongly eccentric. The new-born neutron star underwent hyperaccretion from the fallback disk with

a mean rate of $\sim 10^{-4}$ $M_\odot$ yr^{-1} during the supernova. This spun up the pulsar to a frequency of 465 Hz and resulted in the decay of the magnetic field to its current value $\sim 10^8$ G. The accretion then stopped and the radio emission started.

Nevertheless, as noted by Champion *et al.* (2008); Freire *et al.* (2011); Portegies Zwart *et al.* (2011), this scenario is really unlikely. In fact, the spin period of the pulsar, its low magnetic field, its wide orbit and its high mass are typical of a millisecond pulsar, which are thought to originate from a normal neutron star that accreted matter from a companion. No pulsar with these properties was observed in the ~ 50 young supernova remnants.

11.1.2.2 Formation in a globular cluster and ejection

In globular clusters, the interactions between the neutron stars and the other stars efficiently produce millisecond pulsars and, for a fraction of them, in eccentric binaries. Therefore, Champion *et al.* (2008) proposed that the pulsar was spun-up in a globular cluster. The star that spun-up the neutron star was exchanged with a main sequence star with an eccentric orbit by the stellar interactions in the cluster. But there is no known globular cluster in the vicinity of the pulsar and no new globular cluster was detected. Therefore the same interaction that exchanged the companion must have ejected the binary system from the globular cluster into the Galactic plane.

This scenario is also unlikely. Freire *et al.* (2011) simulated the present and past trajectory of the binary in the Galaxy and concluded that the binary always lay near the Galactic plane although most of the globular clusters reside outside of this plane.

11.1.2.3 Hierarchical triple system

As suggested by Champion *et al.* (2008), the pulsar may be in a hierarchical triple system. The inner binary evolves independently of the third star : the pulsar was spun up by its companion leaving a recycled pulsar and a white dwarf in a wide orbit, which was not detected. The third star in the outer binary is the main sequence star that is observed. The Kozai resonance (Kozai, 1962) between the inner and outer binaries caused the high orbital eccentricity of the pulsar.

Freire *et al.* (2011) ruled out this scenario. In fact, optical observations confirmed that the main sequence star is the companion of the pulsar, consistently with the radio timing of the pulsar. This exclude the existence of an inner binary composed of the pulsar and a white dwarf. Kozai resonance in a hierarchical triple system leads to a exponential growth of the eccentricity (Gopakumar *et al.*, 2009), which is also not consistent with the radio timing in Freire *et al.* (2011) which shows that the eccentricity is time-independent.

11.1.2.4 Tertiary system with two main-sequence stars

This scenario was recently proposed by Freire *et al.* (2011); Portegies Zwart *et al.* (2011). Consider a tertiary system composed of a massive star and two main-sequence stars of

different masses. The massive star collapses and gives birth to a pulsar but the tertiary system is left bound. The initially more massive main sequence star evolves and spins up the pulsar to millisecond periods in a Low Mass X-Ray binary. This star is then removed to the system. This may originate from :

- the ablation of the star by the neutron star radiation. Such a phenomena is observed in the Black Widow PSR B1957+20 binary, where the neutron star radiation reduced the companion mass to 0.025 $\mathrm{M}_\odot$ (Fruchter *et al.*, 1988; Kluzniak *et al.*, 1988). Nevertheless, the time scale for this ablation can be longer than the Hubble time (Levinson & Eichler, 1991).

- the ejection of the donor star from the system because of chaotic 3-body interactions (Freire *et al.*, 2011). The observed 1.03 $\mathrm{M}_\odot$ main-sequence star is then the third member of the tertiary system. Portegies Zwart *et al.* (2011) studied the evolution and dynamics of a tertiary system in this scenario. The triple system may become eventually dynamically unstable due to the mass transfer from the donor star to the neutron star. This results in either a single millisecond pulsar, if the latter is ejected or in a binary system such as J1903+0327. The observation of a low-mass main-sequence star orbiting a low-mass X-ray binary would strengthen this scenario.

Only the last of the aforementioned scenarios is not ruled out by the observations and properties of PSR J1903+0327 binary, but it lacks solid quantitative basis. Nevertheless, PSR J1903+0327 has been clearly recycled to millisecond period after accreting from a companion star. This spinning-up phase is studied in the following section.

11.1.3 Results

In the following, the model that is presented in chapter 10 is applied to the study of the spin-up due to accretion of the progenitor neutron star of PSR J1903+0327.

If not stated otherwise, the figures show the results obtained for the equation of state by Douchin & Haensel (2001) -DH. In what follows, the magnetic field B_p is denoted by B and the spin frequency by f.

After discussing the spin evolution of an accretion neutron star, the importance of the relativistic effects and the dependence of the model on the magnetic field prescription are assessed. Then by imposing step by step the final spin frequency, mass and magnetic field to be equal to the ones of PSR J1903+0327, evolutionary tracks are calculated and the properties of the progenitor neutron star of the pulsar are determined together with constraints on the average accretion rate and the equation of state.

11.1.3.1 Spin evolution during accretion

The figure 11.1 shows, for a constant accretion rate $\dot{M} = 10^{-9}$ $\mathrm{M}_\odot/\mathrm{yr}$, the evolution of the rotational frequency of the pulsar as a function of the accretion time or equivalently

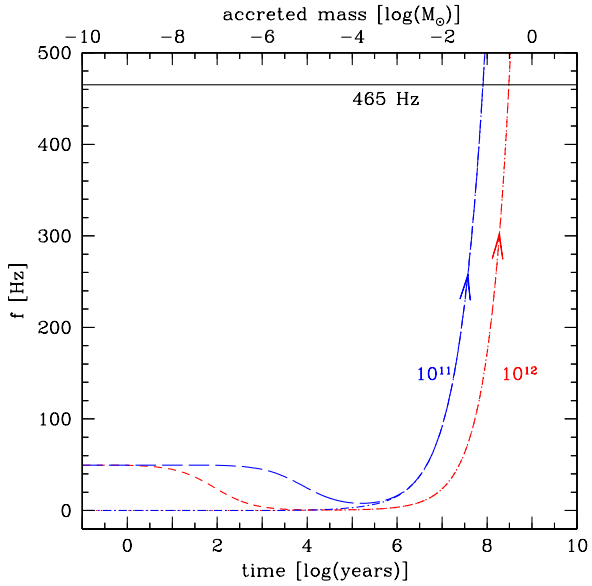

Figure 11.1: Spin frequency evolution for initial spin frequencies $f = 0$ and 50 Hz and for initial magnetic fields $B_\mathrm{i} = 10^{11}$ G and 10^{12} G as a function of the accreted mass (upper axis) or time (lower axis) calculated for constant accretion rate $\dot{M} = 10^{-9}\,\mathrm{M}_\odot/\mathrm{yr}$. Note the logarithmic scale on the x-axis.

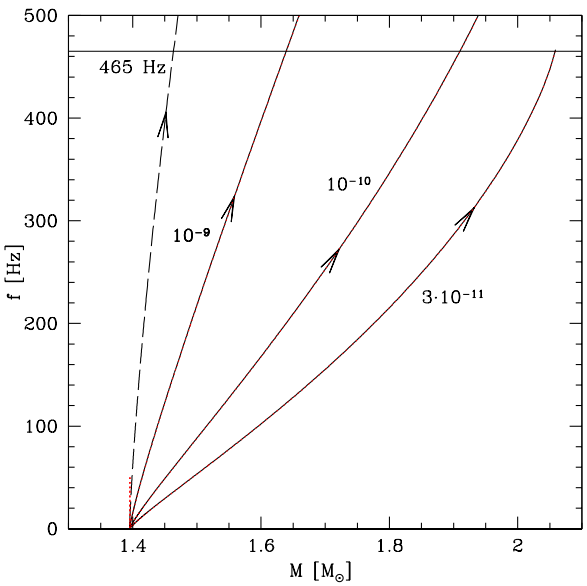

Figure 11.2: Spin frequency evolution for initial frequencies $f = 0$ and 50 Hz as a function of stellar mass of the accreting neutron star. Three different values of the accretion rate (in $\mathrm{M}_\odot/\mathrm{yr}$) for the initial magnetic fields $B_\mathrm{i} = 10^{12}$ G (solid line), 10^{11} G (dashed line) are shown.

of the accreted mass. The initial mass is $M = 1.4\,\mathrm{M}_\odot$ and the initial frequency is set to $f_\mathrm{i} = 0$ Hz and 50 Hz which corresponds to a typical frequency expected for newly-born pulsars (Faucher-Giguère & Kaspi, 2006) and the initial magnetic field to $B_\mathrm{i} = 10^{12}$ G and 10^{11} G.

The configurations with non-zero initial frequencies undergo spin-down before spin-up. In fact, when accretion starts, the magnetic torque dominates over the material torque resulting from accretion because of the high value of the magnetic field. Therefore the neutron star spins down as shown in equation (10.42). Then, the accretion-induced decay of the magnetic field reduces the magnetic torque and the star undergoes a spin-up phase. The minimal value of the spin frequency corresponds to the exact balance between the angular momentum $l_0(r_0)$ at the accretion disk edge r_0 and the magnetic torque.

For $B_\mathrm{i} \sim 10^{12}$ G, the spin-down dominates the rotational evolution for $\sim 10^3$ yrs before the spin-up starts. Since, according to equation (10.42), the magnetic torque varies with B^2, the braking time scale is two orders of magnitude smaller for $B_\mathrm{i} = 10^{11}$ G. After the braking phase, for a given value of the initial magnetic field, the spin evolution does not depend on the initial frequency. The amount of accreted material varies strongly

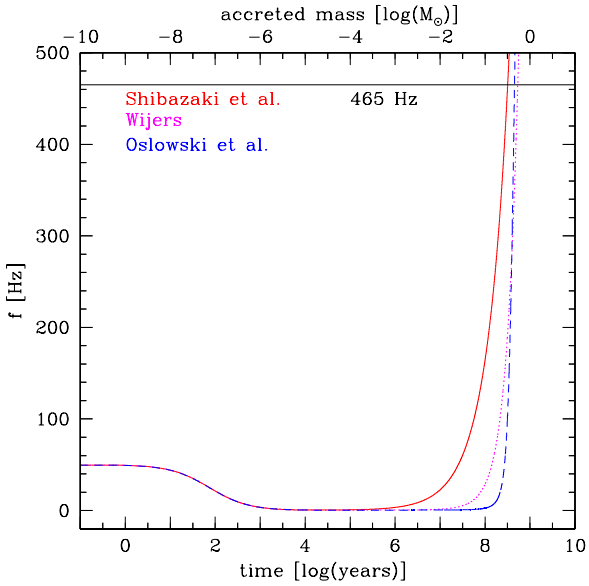

Figure 11.3: Spin frequency evolution for the three prescriptions for the accretion-induced decay of the magnetic field, with $B_{\rm i} = 10^{12}$ G and $\dot{M} = 10^{-9}$ M$_\odot$/yr.

with the strength of the initial magnetic field. Comparing two initial magnetic field configurations, a neutron star with a lower magnetic field is spun-down for a longer time but it undergoes a faster spin-up since its magnetic torque becomes smaller faster.

In the figure 11.2 is plotted the rotational frequency as a function of the mass of the accreting neutron star for two initial frequency $f_{\rm i} = 0$ and 50 Hz, three different accretion rates : $\dot{M} = 10^{-9}, 10^{-10}$ and 3×10^{-11} M$_\odot$/yr and two initial values for the magnetic field $B_{\rm i} = 10^{11}$ and 10^{12} G.

Since, as figure 11.1 shows, the spin-up time scale is by many order of magnitude longer than the braking time scale, evolutionary tracks with different initial frequencies are indistinguishable. For $B_{\rm i} = 10^{12}$ G, for accretion rates lower than $\dot{M} = 3 \times 10^{-11}$ M$_\odot$/yr, the instability with respect to axisymmetric perturbations is reached before the neutron star is spun-up to 465 Hz.

For a given initial magnetic field, a neutron star with a lower accretion rate needs to accrete more mass to reach the rotational frequency of 465 Hz. In agreement with the previous figure, the accretion rates being equal, configurations with a lower magnetic field accrete less mass to reach a given rotational frequency and therefore are recycled faster.

11.1.3.2 Effect of the magnetic field prescription

Figure 11.3 shows the spin evolution for the three different magnetic field decay prescriptions presented in section 10.3, for $B_{\rm i} = 10^{12}$ G and $\dot{M} = 10^{-9}$ M$_\odot$/yr.

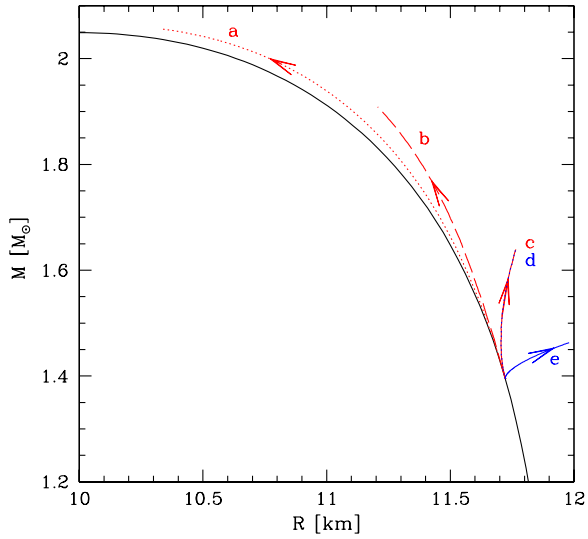

Figure 11.4: Mass-radius relation for accreting stars with $M_{\rm i} = 1.4$ M$_\odot$ spun-up to the frequency of 465 Hz. The solid black curve denotes static configurations. Evolutionary tracks (arrows mark the direction of evolution) correspond to the following initial parameters ($B_{\rm i}$ [G], $\dot{M}$ [M$_\odot$/yr]) : **a**: (10^{12}, 3×10^{-11}), **b**: (10^{12}, 10^{-10}), **c**: (10^{12}, 10^{-9}), **d**: (10^{11}, 10^{-11}), **e**: (10^{11}, 10^{-9}).

The accreted mass and the time needed to spin-up the neutron star to $f = 465$ Hz appears to be almost independent of the magnetic field prescription. The spin-up phase starts earlier for the Shibazaki *et al.* (1989) prescription, in agreement with the figure 10.1 that shows that the accretion-induced decay is more pronounced for the latter. However, since the value of the magnetic field for a large accreted matter is chosen to be the same for the three prescriptions, the differences between them become negligible as more and more mass is accreted. Therefore, the results of the model presented hereafter are expected to be similar for the three models of magnetic field accretion-induced decay.

11.1.3.3 Final frequency f = 465 Hz

The figure 11.4 shows the mass-radius relation of an accreting neutron star for different values of the accretion rate $\dot{M}$ and of the initial magnetic field $B_{\rm i}$. The initial mass is fixed to $M_{\rm i} = 1.4$ M$_\odot$ and each curve ends at the final frequency, $f = 465$ Hz.

In agreement with the figures 11.2 and 11.1, the neutron star accretes more matter to reach to final frequency $f = 465$ Hz when the accretion rate is smaller, for a given magnetic field.

Since the model is degenerate with respect to the quantity $\kappa = B^2/\dot{M}$, introduced in section 10.2.6, the tracks **c** and **d** coincide since $\kappa_{\rm c} = \kappa_{\rm d}$.

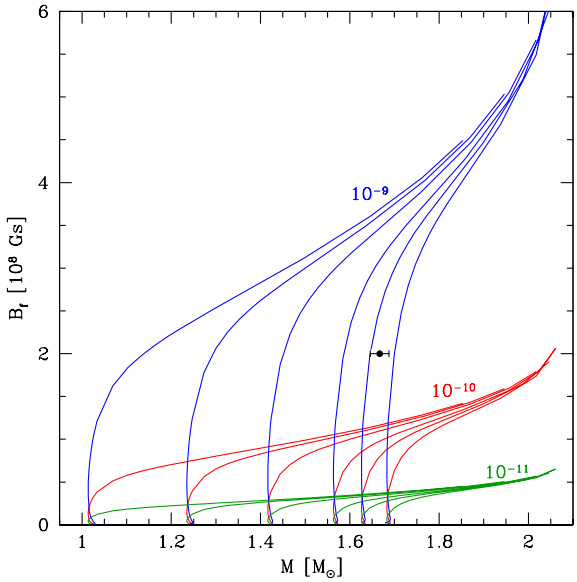

Figure 11.5: Final magnetic field B_f as a function of the gravitational mass M for configurations rotating at $f = 465$ Hz with DH equation of state for different accretion rates.

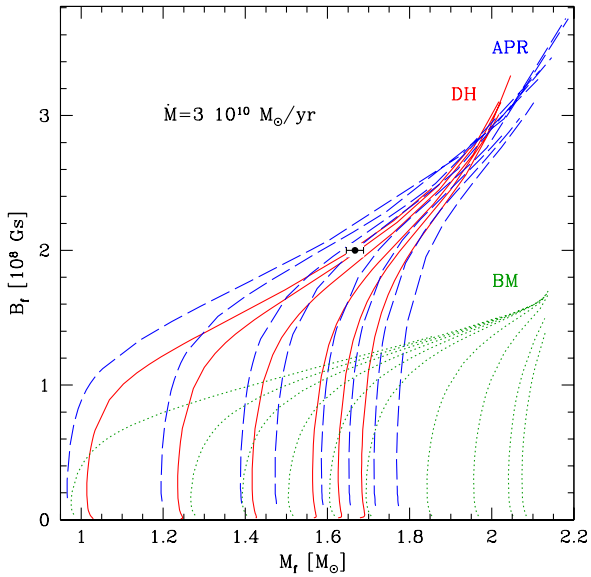

Figure 11.6: Final magnetic field B_f versus gravitational mass M for a star rotating at $f = 465$ Hz, with an accretion rate of $\dot{M} = 3 \times 10^{-10}$ $M_\odot$/yr for the different equations of state.

The figure 11.5 shows the variation of the final magnetic field with the mass of the neutron star for a final frequency of 465 Hz and for different accretion rates. Each curve corresponds to a given initial mass (or initial central density) and along it the magnetic field increases upward. The black error-bar shows the the $3-\sigma$ measurement of the mass of PSR J1903+0327 : $M = 1.667 \pm 0.021$ $M_\odot$.

With the equation (10.44), one can estimate the maximum value of a lower bound on the accretion to reach the final value $B_f = 2 \times 10^8$ G and $M_f = 1.67$ $M_\odot$. According to figure 11.5, for DH equation of state, for $\dot{M} = 10^{-10}$ $M_\odot$/yr and $M = 1.67$ $M_\odot$, $B_{\max} = 1.16 \times 10^8$ G. Therefore, from equation (10.44) :

$$B_{\max}(\dot{M}) = B_{\max}\left(10^{-10}\ M_\odot/\mathrm{yr}\right)\left(\frac{\dot{M}}{10^{-10} M_\odot/\mathrm{yr}}\right)^{1/2}. \tag{11.1}$$

Since $B_f < B_{\max}$, one gets :

$$\dot{M} > \left(\frac{B_f}{B_{\max}\left(10^{-10}\ M_\odot/\mathrm{yr}\right)}\right)^2 \left(\frac{\dot{M}}{10^{-10} M_\odot/\mathrm{yr}}\right) = 3 \times 10^{-10}\ M_\odot/\mathrm{yr}. \tag{11.2}$$

For this lower limit on the accretion rate : $\dot{M} = 3 \times 10^{-10}$ $M_\odot$/yr, figure 11.6 shows the dependence of final magnetic field as a function of the mass of the neutron star

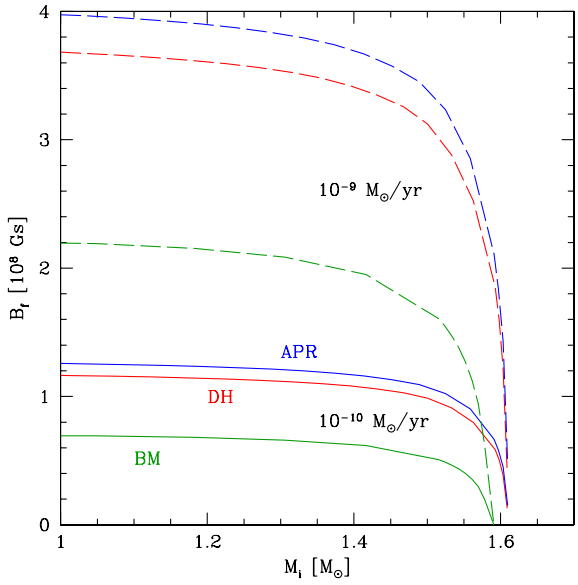

Figure 11.7: Final magnetic field B_f as a function of the initial gravitational mass $M_{\rm i}$ for a star with final parameters $M_f = 1.67$ M$_\odot$ and $f = 465$ Hz, for the three equations of state and for the accretion rates $\dot{M} = 10^{-10}$ and $\dot{M} = 10^{-9}$ M$_\odot$/yr.

on the three different equations of state : DH from Douchin & Haensel (2001), APR from Akmal *et al.* (1998) and BM from Bednarek & Manka (2009). By construction, the results for the DH equation of state are marginally consistent with the requirements that $M_f = 1.67$ M$_\odot$ and $B_f = 2 \times 10^8$ G. The differences between the APR and DH equations of state are small, but the BM one gives significantly lower values for the final magnetic field thus requires a higher accretion rate to have $B_f = 2 \times 10^8$ G. In fact, for a given mass, the stellar moment of inertia $I(M)$ is 25% higher for the BM equation of state than for the DH and APR ones, since BM is stiffer. Therefore, to reach to same final frequency, a larger angular momentum is necessary and thus a larger accreted mass. Nevertheless, the latter induces a larger decay of the magnetic field. Therefore, configurations with the BM equation of state have a smaller B_f compared to the ones obtained for APR and DH equations, for a given final frequency.

11.1.3.4 Final f $= 465$ Hz and M $= 1.67$ M$_\odot$

The figure 11.7 shows the variation of the final magnetic field B_f with the initial gravitational mass $M_{\rm i}$ for configurations with a final frequency $f = 465$ Hz and $M_f = 1.67$ M$_\odot$. Results are shown for accretion rates of $\dot{M} = 10^{-9}$ and 10^{-10} M$_\odot$/yr and for the three equations of state.

Neutron star model	B ($\times 10^8$ G)
Simple model	2.0
DH	1.72
APR	1.83
BM	1.25

Table 11.2: Values of the surface magnetic field B of PSR J1903+0327 calculated with equation (1.21) for the three equations of state considered in this study. The "simple model" considers that $R = 10$ km and $I = 10^{45}$ g cm^{-2}.

According to equation (10.44) :

$$B_f\left(10^{-9}\mathrm{M}_\odot/\mathrm{yr}\right) = B_f\left(10^{-10}\mathrm{M}_\odot/\mathrm{yr}\right)\left(\frac{10^{-9}}{10^{-10}}\right)^{1/2}, \tag{11.3}$$

$$= \frac{1}{\sqrt{10}} B_f\left(10^{-10}\mathrm{M}_\odot/\mathrm{yr}\right). \tag{11.4}$$

This scaling is effectively observed in the figure 11.7.

In agreement with the figure 11.6, the values of the final magnetic field B_f for the BM equation of state are smaller compared with the two other equations of state, for a given mass.

11.1.3.5 From a progenitor NS to PSR J1903+0327 : f = 465 Hz, M = 1.67 $\mathrm{M}_\odot$ and B = 2 × 10^8 G

The final values of the frequency, mass and magnetic field are now all fixed to the values that are been obtained from radio observations for the pulsar J1903+0327. This approach enables to constrain the parameters of the progenitor neutron star and the accretion rate.

The value of magnetic field B presented in the table 11.1 is calculated with the formula (1.21) with the approximation that the neutron star has a radius $R = 10$ km and a moment of inertia $I = 10^{45}$ g cm^{-2}. However, for consistency, the exact value of B has to be accurately calculated for each equation of state for a 1.67 $\mathrm{M}_\odot$ neutron star. The results are presented in the table 11.2.

The figure 11.8 shows spin-up tracks leading to PSR J1903+0327 configuration for the DH equation of state with a final magnetic field value consistently calculated : $B = 1.72 \times 10^8$ G, for selected sets of mean accretion rate $\dot{M}$ and initial magnetic field M_i. The dotted line shows the tracks when the effects of the magnetic field on accretion is neglected as in Zdunik *et al.* (2002), ie. when accretion takes place from the marginally stable orbit.

For the non-magnetic model, only $\simeq 0.1$ $\mathrm{M}_\odot$ is needed to reach the observed frequency of 465 Hz and the progenitor neutron star has a high mass of 1.58 $\mathrm{M}_\odot$. The spin-up when the magnetic field is neglected is more efficient than when it is taken into

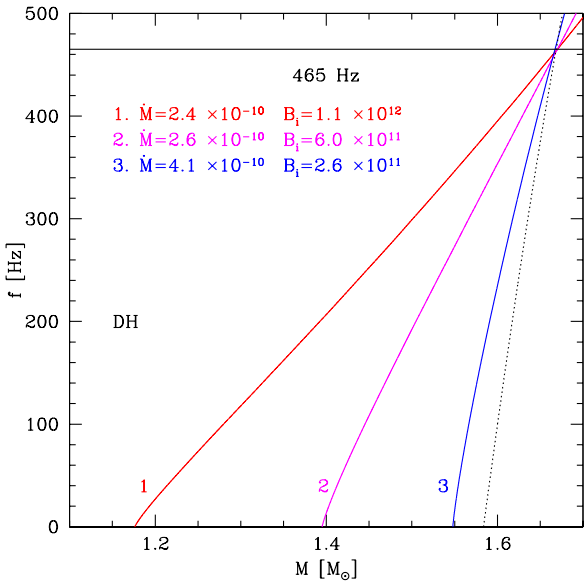

Figure 11.8: Spin-up tracks of an accreting neutron star with the final parameters $f = 465$ Hz, $M = 1.67\ \mathrm{M}_\odot$ and $B = 1.72 \times 10^8$ G, for the DH equation of state. Curves are labeled by the average accretion rate (in $\mathrm{M}_\odot/\mathrm{yr}$) and the initial value of the magnetic field (in G). For comparison, the spin-up for $B = 0$ (dotted line) ie. for accretion from marginally stable orbit, is shown.

account. In fact, in the latter case, the progenitor mass is $\sim 1.3\ \mathrm{M}_\odot$ and the accretion of more mass is needed to reach the final configuration.

In the model presented in the previous chapter, the accretion efficiency parameter x_l is maximum ie., $x_l = 1$. Nevertheless, if the latter were smaller, more accreted mass would be needed to spin up the star in the non-magnetic configuration (Zdunik *et al.*, 2002).

The figures 11.9 and 11.10 show the variation of the accretion rate $\dot{M}$ with the initial mass M_i to reach the final configurations for the three equations of state and for the three magnetic field prescriptions, respectively. The values of the final magnetic field are consistently calculated for the three equations of state and are given by the table 11.2.

The lower limit on the accretion rate depends, as expected, on the equation of state : $\sim 2.1 \times 10^{-10}\ \mathrm{M}_\odot/\mathrm{yr}$ for DH and APR and $\sim 3.25\ \times 10^{-10}\ \mathrm{M}_\odot/\mathrm{yr}$ for BM. On the one hand, if the neutron star accretes more than $0.2\ \mathrm{M}_\odot$, the accretion rate required to reach the final configuration depends weakly on the initial mass. On the other hand, there is a strong dependence of the accretion rate on the initial mass if the neutron star accretes less than $0.2\ \mathrm{M}_\odot$.

The results depend less on the magnetic field prescription than on the equation of state as shown in figure 11.10. The variation of the accretion rate with the initial mass

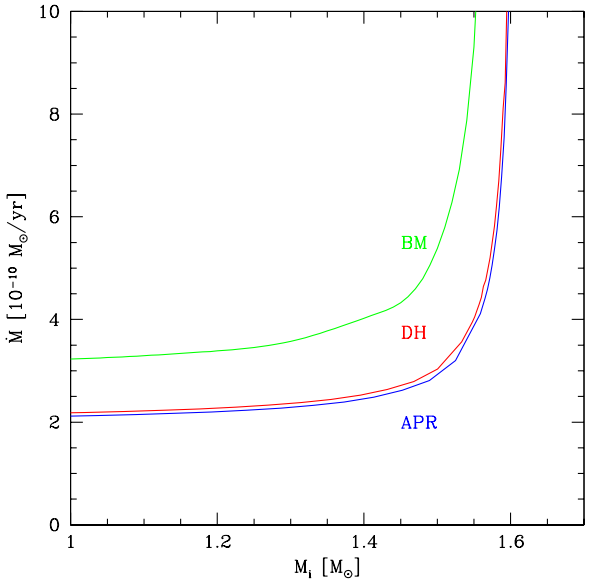

Figure 11.9: Average accretion rate $\dot{M}$ as a function of the initial mass $M_{\rm i}$ for PSR J1903+0327 final configuration for the three equations of state.

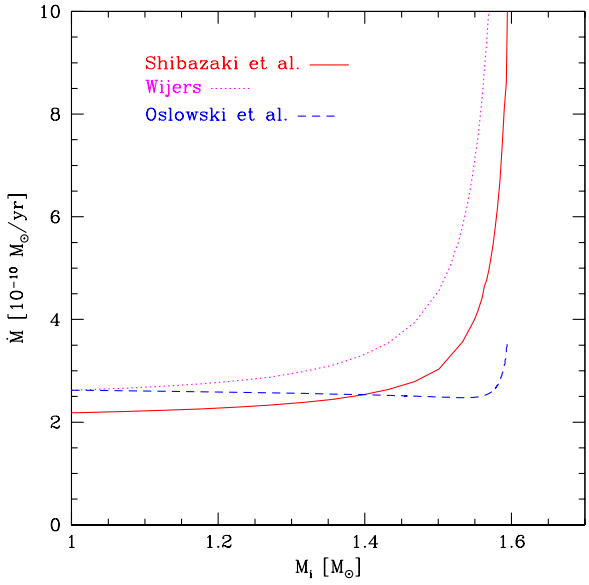

Figure 11.10: Average accretion rate $\dot{M}$ as a function of the initial mass $M_{\rm i}$ for PSR J1903+0327 final configuration for the three magnetic field prescriptions, for the DH equation of state.

is qualitatively similar for the three prescriptions, though the needed accretion rate is quantitatively higher for the Wijers (1997) prescription. The lower limit of the accretion rate is $\sim 2.1 - 2.6 \times 10^{-10}$ M$_\odot$/yr. The accretion rate hardly depends on the initial mass for the Osłowski *et al.* (2011) model. For the latter, it is possible to reach the final configuration for a high initial mass $M \sim 1.55$ M$_\odot$ and a moderate accretion rate $\dot{M} \sim 2.05 \times 10^{-10}$ M$_\odot$/yr.

Since $\Delta M_{\rm b} = \dot{M}_{\rm b} t$, one can calculate the time needed to spin up the star to its presently observed frequency. The results are presented in figure 11.11 for the three equations of state and in figure 11.12 for the different magnetic field prescriptions.

A progenitor neutron star with a mass close to the final mass requires to accrete a small amount of matter to reach the final configuration, as shown in figure 11.9 and thus its spin-up time is short. This corresponds to the left part of figures 11.11 and 11.12. On average, a neutron star with the BM equation of state or for the Wijers (1997) prescription accretes more matter in less time, ie. has a larger accretion rate, than for DH or APR equation of state or the two others magnetic field models.

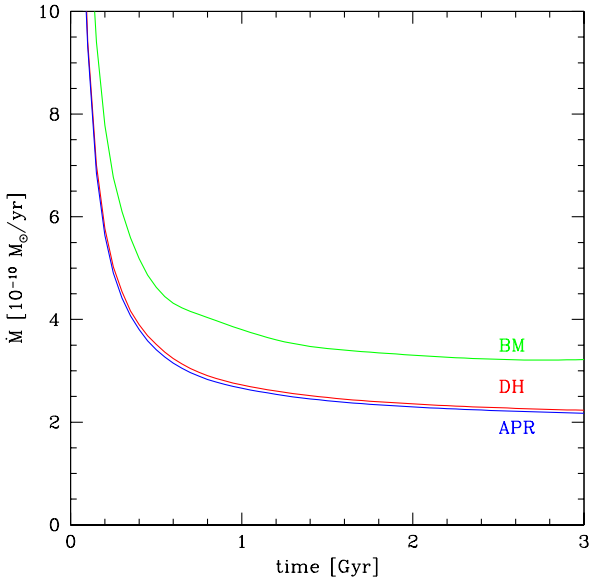

Figure 11.11: Accretion rate versus time of accretion needed to reach PSR J1903+0327 final configuration for the three different equations of state.

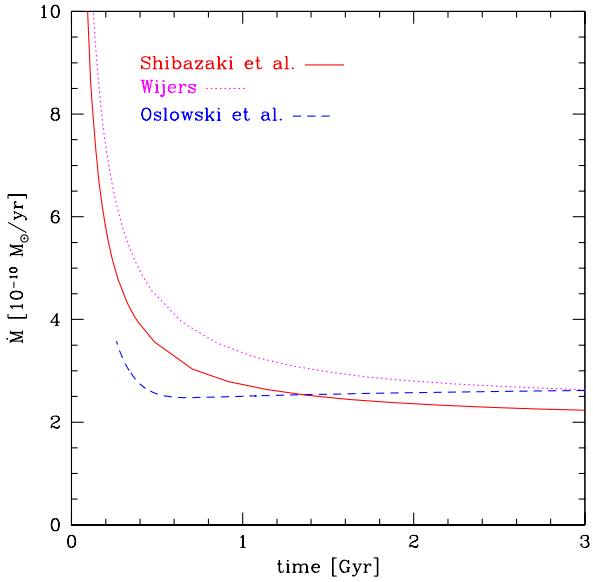

Figure 11.12: Accretion rate versus time of accretion needed to reach PSR J1903+0327 final configuration for the three different magnetic field prescription, for the DH equation of state.

11.1.3.6 Relativistic effects in the recycling process

The original model by Kluźniak & Rappaport (2007) is derived in Newtonian dynamics and therefore does not include relativistic aspects such as the existence of the marginally stable orbit. That is why the $f_{\rm ms}$ function has been introduced in the equation (10.32).

The figure 11.13 shows three characteristic radii of the problem : the inner radius of the accretion disk r_0, the stellar radius R and the radius of the marginally stable orbit $r_{\rm ms}$, calculated along a spin-up evolutionary track. For the final configuration ($f = 465$ Hz, $M = 1.67$ M$_\odot$, $B = 2 \times 10^8$ G), when r_0 reaches its minimum value, $r_0/r_{\rm ms} \simeq 2$. Comparing the value of r_0 when the relativistic effects are included and in the original model ($f_{\rm ms} = 1$), the difference in the values of r_0 are ~ 200 m, i.e., 0.7%. Therefore in the case of PSR J1903+0327, taking into account the existence of the marginally stable orbit is not necessary. Nevertheless, for very massive and/or fastly rotating configurations relativistic effects can be important as shown in the next sections.

11.1.4 Conclusions

Finally, the model presented in chapter 10 enables to estimate the parameters of the progenitor neutron star of PSR J1903+0327 that underwent accretion and was spun-up to millisecond periods. The results depend to some extent on the equation of state

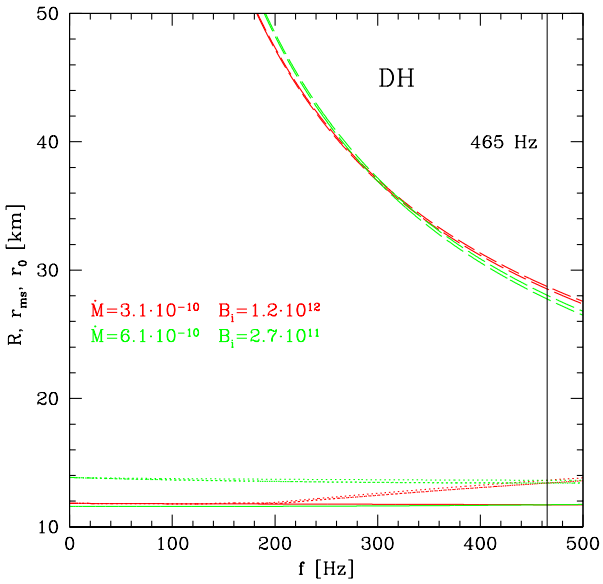

Figure 11.13: Spin-up tracks of an accreting neutron star leading to presently observed PSR J1903+0327 parameters on radius-spin frequency plane. Are plotted the characteristic radii relevant for the considered problem : stellar radius (solid curves), radius of a marginally stable orbit (dotted curves), and radius of the inner boundary of accretion disk (dashed curves).

of dense matter. In particular, the mean accretion rate $\dot{M}$ required to reach the final configuration is constrained to be larger than $(2.1-3.25)\times 10^{-10}\,\mathrm{M}_\odot/\mathrm{yr}$ with the highest value for the stiffest EOS.

The results hardly depend on the magnetic field prescription and the relativistic effects are negligible.

For neutron stars with a low initial mass of $M_\mathrm{i} = 1.0-1.4\,\mathrm{M}_\odot$, the required accretion is independent of the initial mass. Therefore, contrary to the non-magnetic model presented in Zdunik *et al.* (2002), no constraint can be put on the progenitor mass. Simulations neglecting the influence of the magnetic field give a high value for the lower bound of the progenitor mass : $M > 1.55\,\mathrm{M}_\odot$ for the BM equation of state and $M > 1.58\,\mathrm{M}_\odot$ for the DH and APR. In fact, the magnetic field torque limits the efficiency of the angular momentum transfer and therefore decreases the spin-up rate.

Thus, taking into account the magnetic field is crucial and has a non-trivial influence on the evolution of the spin of a neutron star in the recycling scenario.

11.2 The extreme-mass millisecond pulsars

11.2.1 The less massive millisecond pulsar : PSR J0751+1807

Parameter	Value	Reference
Distance d (kpc)	2.0 ± 0.4	Lundgren *et al.* (1995)
Spin period P (ms)	3.48	Nice *et al.* (2005)
Spin frequency f (Hz)	287	Nice *et al.* (2005)
Spin period derivative $\dot{P}$ (s s^{-1})	7.79×10^{-21}	Nice *et al.* (2005)
Dipolar magnetic field B (G)	1.67×10^{8}	Nice *et al.* (2005)
Orbital eccentricity e	7.1×10^{-7}	Nice *et al.* (2005)
Orbital period P_b	0.26 days = 6.32 hrs	Nice *et al.* (2005)
Pulsar mass $M_{\rm PSR}$ ($M_\odot$)	1.26 ± 0.14	Nice *et al.* (2008)
Companion star	Helium White dwarf	Lundgren *et al.* (1995); Bassa *et al.* (2006)
Companion mass $M_{\rm WD}$ ($M_\odot$)	0.12 ± 0.02	Nice *et al.* (2008)

Table 11.3: Parameters of PSR J0751+1807. $1-\sigma$ error bars. $B_{\rm surf}$ is calculated with the formula (1.21) for a neutron star with $R = 10$ km and $I = 10^{45}$ g cm^{-2}.

Lundgren *et al.* (1995) discovered the binary millisecond pulsar J0751+1807 in their their search for radio pulsars with Arecibo radiotelescope among the 12 unidentified γ-ray sources in Egret all-sky survey in 1991-1992. The estimated rotational energy of the source is not high enough to power the γ-ray emission observed by EGRET. Follow-up γ-ray observations failed to detect the source again. Therefore, the millisecond pulsar was discovered by chance in the error box of a marginal EGRET source ! It has a short orbital period P_b and a small eccentricity e as a consequence of a Low-Mass X-ray binary phase (section 9.2.3.2). The mass function, the low eccentricity, the absence of eclipses or orbital variability are consistent with a low-mass helium white dwarf companion (Lundgren *et al.*, 1995).

Nice *et al.* (2005) reported 11 years (1993-2004) of high precision timing observations of the pulsar with Arecibo and Effelsberg radiotelescopes. The measurements of three post-Keplerian parameters : the rate of change of in orbital period $\dot{P}_b$ and the shape s and range r of the Shapiro delay, implied a pulsar mass $M = 2.1 \pm 0.2\, M_\odot$ and made it the most massive pulsar observed by then. Nevertheless, 2-months Arecibo observations in 2006 led to a significant refinement of $\dot{P}_b$ which is consistent with a pulsar mass $M = 1.26 \pm 0.14\ M_\odot$ (Nice *et al.*, 2008). The discrepancy originates from the too short time baseline that did not enable to detect properly $\dot{P}_b$.

Bassa *et al.* (2006) presented optical and near-infrared observations of the binary at the Keck observatory. The color of the companion is consistent with a white dwarf with a pure helium atmosphere or an helium atmosphere with mixed hydrogen, with a very low temperature $\sim 3500 - 4300$ K. This composition is a puzzle since it is not consistent with the evolutionary models that predict an atmosphere made of hydrogen. Future deeper observations in infrared could enable to determine whether hydrogen is present or not in the atmosphere.

Table 11.2.1 summarizes the properties of PSR J0751+1807 binary.

Parameter	Value
Distance d (kpc)	1.2
Spin period P (ms)	3.15
Spin frequency f (Hz)	317
Spin period derivative $\dot{P}$ (s s^{-1})	9.62×10^{-21}
Dipolar magnetic field B (G)	1.8×10^{8}
Orbital eccentricity e	1.3×10^{-6}
Orbital inclination angle	89.17°
Orbital period P_b (days)	8.69
Pulsar mass $M_{\rm PSR}$ ($M_\odot$)	1.97 ± 0.04
Companion star	Helium-carbon-oxygen white-dwarf
Companion mass $M_{\rm WD}$ ($M_\odot$)	0.500 ± 0.006

Table 11.4: Parameters of PSR J1614-2230 from Demorest *et al.* (2010). $1-\sigma$ error bars. $B_{\rm surf}$ is calculated with the formula (1.21) for a neutron star with $R = 10$ km and $I = 10^{45}$ g cm^{-2}.

PSR J0751+1807 is a millisecond pulsar and has therefore undergone accretion from its companion in the past that increased its mass. Its properties are consistent with a formation scenario in a Low-Mass X-ray binary. However, its very low mass (see also section 2.2.2.2) is therefore a puzzle.

11.2.2 The most massive pulsar : PSR J1614-2230

PSR J1614-2230 was discovered in 2002 when pulsations were searched from 56 unidentified mid-latitude EGRET γ-ray sources, using Parkes radiotelescope. It has a 3.15 ms spin-period and is in a binary system with a short (8.7 days) orbital period and a high-mass companion (> 0.4 $M_\odot$), which is unusual for fully-recycled pulsars (section 9.2.3.2) (Hessels *et al.*, 2005; Crawford *et al.*, 2006). The companion star may be a CNO white dwarf or a low-mass denegerate dwarf. Pulsations from PSR J1614-2230 were successfully searched in the 2008-2009 Fermi Large Area Telescope data using rotation ephemerides from the radio observations (Abdo & et al., 2009).

Demorest *et al.* (2010) reported dense observations of the pulsar with the Green Bank radiotelescope, through one complete orbital orbit. They observed a strong Shapiro delay and measured a high mass (0.5 $M_\odot$) for the pulsar companion, consistent with an helium-carbon-oxygen white dwarf. The system is nearly edge-on and is the most inclined one observed so far. The combination of the Shapiro delay and the standard Keplerian parameters enabled to determine the mass of the pulsar : $M = 1.97 \pm 0.04$ $M_\odot$ which the highest mass measured at present.

Table 11.2.2 summarizes some of the properties of PSR J1614-2230 binary system.

The high mass of PSR J1614-2230 raises the question of whether the progenitor neutron star was born massive. The nature of its companion suggests that the pulsar binary

Neutron star model	J0751+1807	J1614-2230
Simple model	1.67	1.80
DH	1.08	1.98
APR	1.19	1.96
BM	0.80	1.57

Table 11.5: Values of the surface magnetic field B in units of 10^8 G for the two pulsars PSR J0751+1807 and J1614-2230 calculated with equation (1.21) for the three equations of state considered in this study. The "simple model" considers that $R = 10$ km and $I = 10^{45}$ g cm^{-2}.

originates from an Intermediate-Mass X-ray Binary (section 9.2.3.2).

Some evolutionary formation scenarios of the PSR J1614-2230 binary : high-mass pulsar and 0.50 M$_\odot$ CO white dwarf, have been recently studied by Tauris *et al.* (2011) and Lin *et al.* (2011). The pulsar is thought to originate from an Intermediate-Mass X-ray binary composed of a massive (> 1.6 M$_\odot$) neutron star and a ~ 4 M$_\odot$ donor star. The pulsar accreted at a near-Eddington rate for 5-10 Myrs, when the companion star became a red giant, overflowing its Roche lobe. The companion then formed a carbon-oxygen white-dwarf with an helium envelope. The recycling time scale was therefore much shorter than for standard Low-Mass X-ray binary systems for which it lasts few Gyrs.

Bhalerao & Kulkarni (2011) reported optical observations of the companion white dwarf of PSR J1614-2230 and concluded that its magnitude and mass are consistent with the cooling of a 2.2 Gyr helium-carbon-oxygen white dwarf.

The evolutionary scenarios studied by Tauris *et al.* (2011) put a strong constraint on the duration of the accretion phase $\mathbf{t}_{\rm acc} < 100$ Myr that will be considered in the following.

11.2.3 Modeling

The spin-up by accretion of the millisecond pulsars J0751+1807 and J1614-2230 has been modeled and a paper is currently is preparation. The magnetic field values are consistently calculated and given in table 11.5.

11.2.3.1 PSR J0751+1807

Let us first present results for the millisecond pulsar with the lowest mass. Figure 11.14 plots the accretion time needed to spin-up a neutron star to the observed properties of the pulsar PSR J0751+1807 as a function of the accreted mass, for the three equations of state. Note that, in agreement with the results of the previous section, the APR and DH equations give similar results. As expected, it takes longer time to accrete more matter.

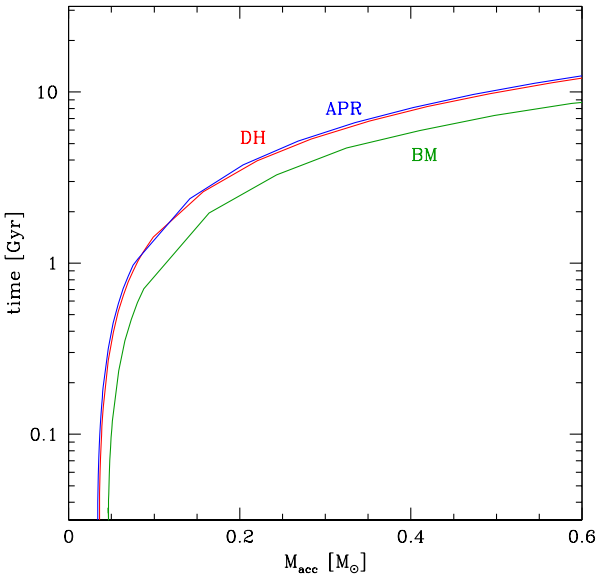

Figure 11.14: Time needed to spin-up the progenitor neutron star to the observed properties of the pulsar PSR J0751+1807 as a function of the accretion mass, for the three equations of state.

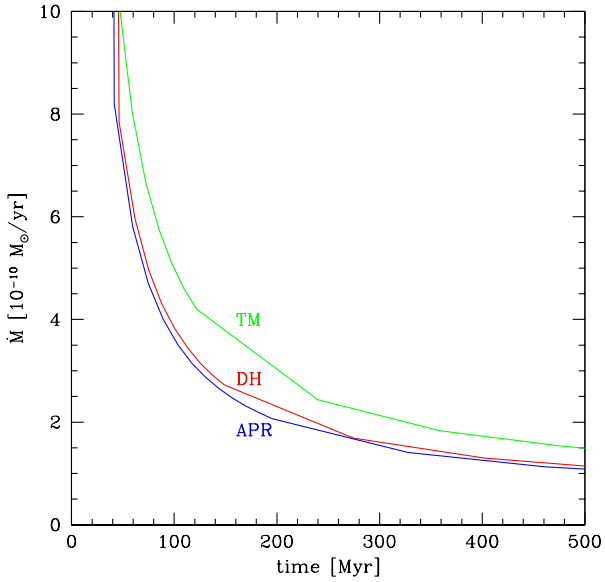

Figure 11.15: Accretion rate versus time of accretion needed to reach PSR J0751+1807 final configuration for the three equations of state.

Figure 11.15 shows the average accretion rate as a function of the accretion time needed to spin-up the progenitor neutron star. For a given total accreted mass, since the average accretion rate is higher for the BM equation of state, the accretion time is shorter than for the two others.

Four spin-up tracks for the BM equation of state for different initial magnetic fields and average accretion rates are plotted in figure 11.16. The accretion times τ are also indicated. A very-low mass progenitor neutron star ($M \lesssim 1\ M_\odot$) needs to accrete more matter than the low-mass one and thus the accretion rate and time are larger. The accretion-induced magnetic field decay implies then that its initial magnetic field is higher.

11.2.3.2 PSR J1614-2230

Figures 11.17, 11.18 and 11.19 are the analogs for the most massive millisecond pulsar PSR J1614-2230 of figures 11.14-11.16 and lead to similar conclusions. The first two figures shows results for the DH and BM equations of state only since conclusions are similar for the APR and DH ones. For the BM equation of state the calculations have been performed for three values of the final mass of the millisecond pulsar corresponding to the error bar in the mass determination : M=1.93, 1.97 and 2.01 $M_\odot$. The results hardly depends on the final mass.

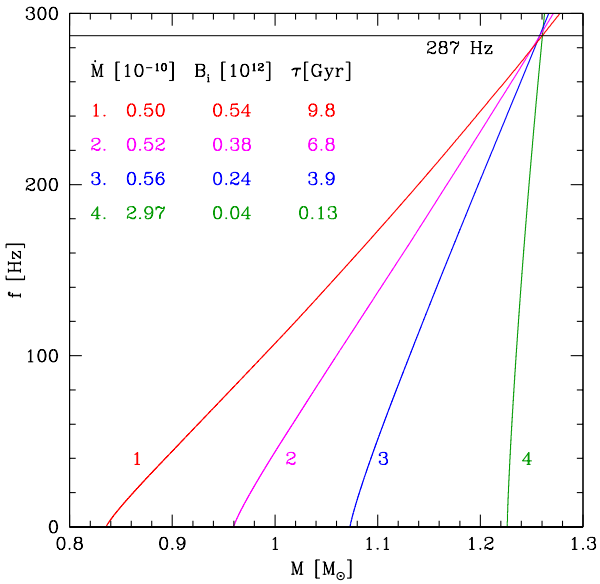

Figure 11.16: Spin-up tracks of an accreting neutron star with the final parameters of PSR J0751+1807 for the BM equation of state. Curves are labeled by the average accretion rate (in $\mathrm{M}_\odot/\mathrm{yr}$), the initial value of the magnetic field (in G) and the duration of accretion phase (in Gyr).

Note that the accretion times in figures 11.14 and 11.17 are similar for the less and most massive millisecond pulsars, in particular for low values of the accreted mass.

An interesting constraint is put by the evolutionary model developed by Tauris *et al.* (2011) : the accretion phase lasted less than 100 Myr. Figure 11.17 then shows that the progenitor neutron star accreted a mass :

$$M_{\mathrm{acc}} \leq 0.05\ \mathrm{M}_\odot \tag{11.5}$$

therefore indicating that the neutron star was born very massive. This is of particular interest for supernova simulations for which such a high value for the mass of a newly born neutron star has never been obtained and therefore constrain the supernova mechanism.

According to figures 11.18, one can then derive a lower limit on the average accretion rate experienced by the progenitor neutron star :

$$\dot{M} \geq 5 \times 10^{-10}\ \mathrm{M}_\odot\ \mathrm{yr}^{-1}. \tag{11.6}$$

Finally figure 11.19 shows spin-up tracks for PSR J1614-2230 for BM equation of state and different initial models of neutron star.

Therefore, these two pulsars that are the less and most massive ones observed so far indicate that neutron stars are born with very different initial mass that have to obtained in supernova simulations.

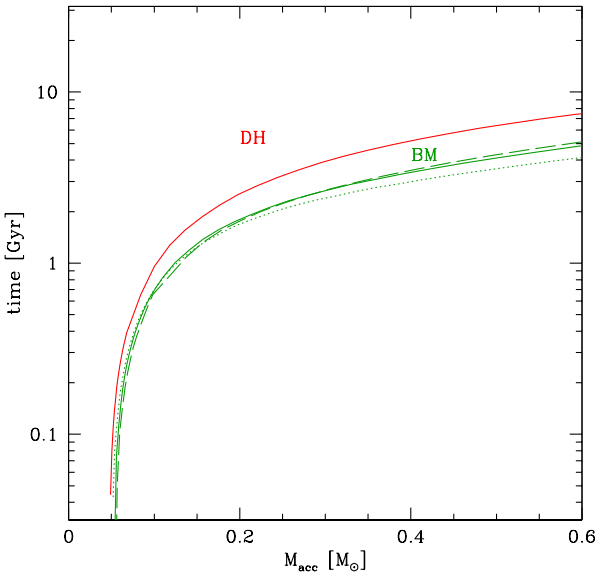

Figure 11.17: Time needed to spin-up the progenitor star to the observed properties of the pulsar PSR J1614-2230 as a function of the accretion mass, for the DH and BM equations of state. For the latter are plotted results for a final mass $M = 1.97$ M$_\odot$ (solid line) and for the lower and upper values of the mass error bar : $M = 1.93$ M$_\odot$ (dotted line), $M = 2.01$ M$_\odot$ (dashed line).

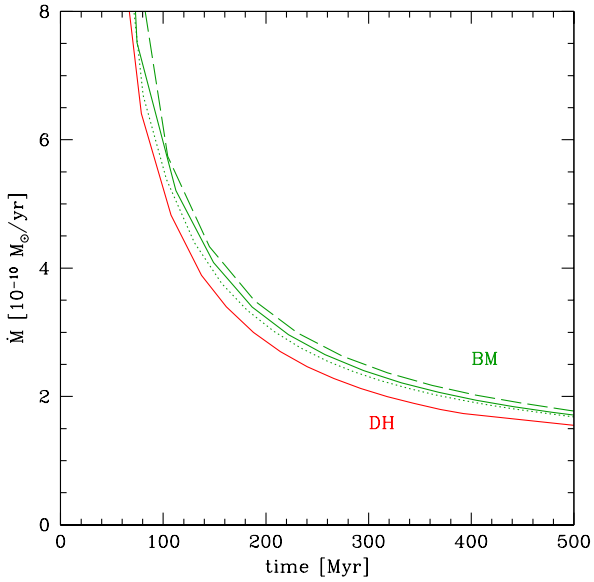

Figure 11.18: Accretion rate versus time of accretion needed to reach PSR J1614-2230 final configuration for the DH and BM equations of state.

11.3 Perspective : sub-millisecond pulsars

A natural continuation, that is currently in progress, of the modeling of the spin-up of accreting neutron stars deals with sub-millisecond pulsars with a period, as their name indicates, less than one millisecond. So far, none of them have been detected. Therefore, there *might* exist a mechanism that prevents sub-millisecond to be formed in binary systems.

White & Zhang (1997) suggested that the equilibrium period of accreting neutron stars which determined by the balance between the magnetic and the accretion torques is higher than one millisecond. Bildsten (1998) proposed that the emission of gravitational waves by accreting neutron stars inhibits their spin-up to high frequencies. In the

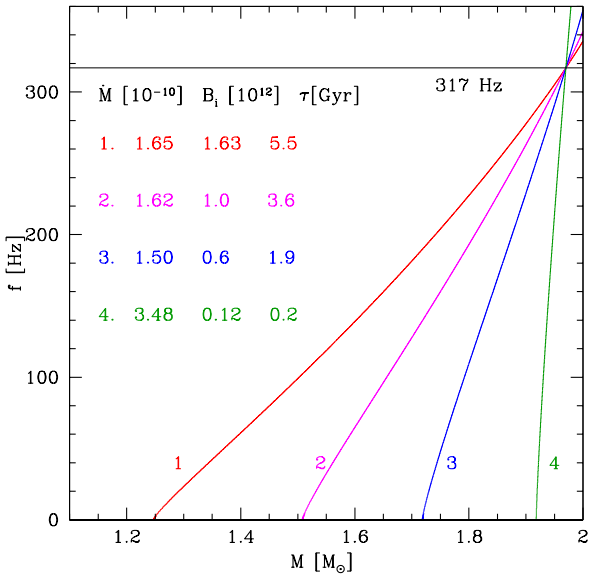

Figure 11.19: Spin-up tracks of an accreting neutron star with the parameters of PSR J1614-2230 for the BM equation of state. Curves are labeled by the average accretion rate (in $\mathrm{M}_\odot/\mathrm{yr}$), the initial value of the magnetic field (in G) and the duration of accretion phase.

continuation of the work by Burderi *et al.* (1999), the model for the spin-up of accreting neutron stars presented in this thesis enables to test such scenarios.

In conclusion, the model for the rotational evolution of an accreting magnetized neutron star presented in chapter 10 enables to study various aspects of the recycling process that is thought to be at the origin of millisecond pulsars. Constraints can be put on the progenitor neutron star properties of currently observed millisecond pulsars, as presented in sections 11.1 and 11.2. The spin-up of neutron stars to sub-millisecond pulsars, that is currently in progress, can be also be assessed (section 11.3).

Conclusion and perspectives

During my Ph.D. studies I investigated different aspects of the dynamics and evolution of neutron stars, with a particular attention to the influence of the microphysics on the macrophysical properties.

I modeled the thermal evolution of both isolated and accreting neutron stars. Specifically, I studied the influence of the superfluid properties of the neutrons in the inner-crust on the evolution of the temperature of slow and fast cooling neutron stars. I showed that precise calculations of the specific heat of the neutrons are necessary to describe the cooling of young neutron stars. I also developed a new model for the evolution of the temperature of neutron stars that accreted matter during long periods of time and whose interior therefore underwent substantially heating. Preliminary results are encouraging and the precise description of the hydrogen and helium burnings and of the atmosphere will be included in the model in the very near future. Confronting the models for the thermal evolution with the observations has already enabled to put constraints on the properties of matter in the interior of neutron stars. The current and the next generation of X-ray satellites are expected to provide more measurements of the temperature of neutron stars and offers exciting perspectives.

Glitches suggest that the crust of neutron stars is most likely to be solid and models of solid core have also been developed. So far, the relativistic models of rotating neutron stars used a perfect fluid description for their interior and therefore did not include the elastic properties of the solid parts. I derived the equations for stationary, axisymmetric and rigidly rotating neutron star configurations with a relativistic description of the elasticity in the (partly) solid interior. The numerical resolution by the mean of spectral methods is currently in progress and the model will enable to investigate the glitch phenomenon. In the longer term, I would like to perform calculations of binary neutron star systems, including the effects of the elasticity in the solid parts and to investigate the elasto-thermal evolution of neutron stars, in order to take into account the possible melting or crystallization of the interior and the effects on the rotation.

I studied the evolution of the rotation and of the magnetic field of an accreting neutron star. This is of particular interest to model the rotational evolution of old neutron stars that are spun-up by accretion of matter from a companion in a binary and become millisecond pulsars. A relativistic description for a magnetized thin accretion disk that includes the magnetic-torque disk-pulsar coupling and the existence of the marginally stable orbit is used together with a prescription for the accretion-induced decay of the neutron star magnetic field. Calculations were performed for three different millisecond pulsars : the two most massive and lest massive ones and enabled to constrain the properties of their progenitor neutron star. The modeling shows in particular that the mass of newly-born neutron stars is not uniquely determined and that both heavy and light neutron stars are formed in supernovæ constraining their simulations. The model is currently applied to assess whether accreting neutron stars can be spun-up to submil-

lisecond periods.

In the future, I plan to continue investigating how the properties of the matter inside neutron stars influence their evolution and dynamics and to focus in particular on the emission of gravitational waves and neutrinos from isolated or binary neutron stars.

Appendix

Appendix A

Equations for elastic rotating neutron stars

Contents

A.1 Expression of $\nabla_\alpha \zeta_\beta$

One can show in a circular spacetime that (Gourgoulhon, 2007) :

$$\nabla_\beta n_\alpha = -\kappa_\alpha m_\beta - \kappa_\beta m_\alpha - a_\alpha n_\beta, \tag{A.1}$$
$$\nabla_\beta m_\alpha = -b_\alpha m_\beta - n_\beta m_\alpha n^\sigma \nabla_\sigma - n_\alpha \kappa_\beta. \tag{A.2}$$

Writing

$$^2\nabla_\alpha \zeta_\beta = k_\alpha{}^\mu k_\beta{}^\nu \nabla_\mu \zeta_\nu, \tag{A.3}$$

one gets,

$$\nabla_\alpha \zeta_\beta = {}^2\nabla_\alpha \zeta_\beta - \zeta^\sigma \left[a_\sigma n_\alpha n_\beta + \kappa_\sigma \left(n_\alpha m_\beta + n_\beta m_\alpha \right) + b_\sigma m_\alpha m_\beta \right]. \tag{A.4}$$

Thus,

$$\nabla_a \zeta_b = {}^2\nabla_a \zeta_b \tag{A.5}$$

A.2 Expression of Dk_{ab}

With equation (8.12),

$$Dk_{ab} = Dg_{ab} \tag{A.6}$$
$$= \delta g_{ab} + \nabla_a \zeta_b + \nabla_b \zeta_a \tag{A.7}$$
$$= \delta g_{ab} + {}^2\nabla_a \zeta_b + {}^2\nabla_b \zeta_a. \tag{A.8}$$

A.3 Expression of $^2\nabla_\alpha U$

Since $U = \frac{M}{N}(\Omega - \omega)$,

$$^2\nabla_\alpha U = -U a_\alpha - U b_\alpha + 2\kappa_\alpha \tag{A.9}$$

with $\vec{a}, \vec{b}$ and $\vec{\kappa}$ defined in equations (6.7,6.129,6.143).

A.4 Expression of $D\varpi^2$

According to equation (8.12),

$$D\varpi^2 = \delta\varpi^2 + \zeta^\alpha \nabla_\alpha \varpi^2, \tag{A.10}$$
$$= \delta\varpi^2 + \zeta^\alpha \, {}^2\nabla_\alpha \varpi^2. \tag{A.11}$$

With $\varpi = \Gamma M$ and $\nabla_\alpha \Gamma = \Gamma U \nabla_\alpha U$, one gets :

$$^2\nabla_\alpha \varpi^2 = 2\varpi^2 \left({}^2\nabla_\alpha \ln M + \Gamma^2 U \, {}^2\nabla_\alpha U \right), \tag{A.12}$$
$$= 2\varpi^2 \Gamma^2 \left(-b_\alpha - U^2 a_\alpha + 2U\kappa_\alpha \right) \tag{A.13}$$

Thus

$$D\varpi^2 = \delta\varpi^2 + 2\varpi^2\Gamma^2 \left(-b_\alpha - U^2 a_\alpha + 2U\kappa_\alpha \right) \tag{A.14}$$

A.5 Trace of the relative strain tensor

The trace of the relative strain tensor given in equation (8.40) is :

$$e_{\alpha}^{\ \alpha} = \frac{1}{2}\left[k^{ab}Dk_{ab} + \frac{D\varpi^2}{\varpi^2}\right], \tag{A.15}$$

$$= {}^2\nabla_a\zeta^a + \frac{1}{2}k^{ab}\delta g_{ab} + \frac{1}{2}\frac{D\varpi^2}{\varpi^2} \tag{A.16}$$

A.6 Shear tensor

According to equation (8.6) and (8.40),

$$s_{\alpha\beta}\,dx^\alpha\,dx^\beta = e_{\alpha\beta}\,dx^\alpha\,dx^\beta - \frac{1}{3}e_{\alpha}^{\ \alpha}\gamma_{\alpha\beta}\,dx^\alpha\,dx^\beta, \tag{A.17}$$

$$= \left(\frac{1}{2}Dk_{ab}dx^a dx^b - \frac{1}{3}e_{\alpha}^{\ \alpha}k_{ab}\right)dx^a\,dx^b \tag{A.18}$$

$$+\left(\frac{1}{2}D\varpi^2 - \frac{1}{3}\varpi^2 e_{\alpha}^{\ \alpha}\right)(d\varphi - \Omega dt)^2 \tag{A.19}$$

With equations (A.8), (A.16) and (A.14), one gets :

$$s_{\alpha\beta}dx^\alpha dx^\beta = \left[{}^2\nabla_{(a}\zeta_{b)} - \frac{1}{3}\left({}^2\nabla_c\zeta^c\right)k_{ab} + \frac{1}{2}\left(\delta g_{ab} - \frac{1}{3}k^{cd}\delta g_{cd}k_{ab}\right)\right. \tag{A.20}$$

$$\left. -\frac{1}{6}\frac{D\varpi^2}{\varpi^2}k_{ab}\right]dx^a\,dx^b \tag{A.21}$$

$$-\frac{1}{3}\left[\varpi^2\left({}^2\nabla_c\zeta^c + \frac{1}{2}k^{cd}\delta g_{cd}\right) - D\varpi^2\right](d\varphi - \Omega dt)^2 \tag{A.22}$$

A.7 Circularity condition

The energy-momentum tensor $\boldsymbol{T}$ for an elastic medium writes :

$$T_{\alpha\beta} = T^{\rm perf}_{\alpha\beta} + T^{\rm elas}_{\alpha\beta} \tag{A.23}$$

with

$$T^{\rm elas}_{\alpha\beta} = -2\mu s_{\alpha\beta}. \tag{A.24}$$

The fluid contribution $\boldsymbol{T}^{\rm fluid}$ to the energy-momentum tensor is, according to equation (6.4.1) :

$$\xi^\nu T^{\rm fluid}_{\ \nu}\ {}^{[\alpha}\xi^\beta\chi^{\gamma]} = (\varepsilon + p)\xi^\nu u_\nu\, u^{[\alpha}\xi^\beta\chi^{\gamma]}, \tag{A.25}$$

$$\chi^\nu T^{\rm fluid}_{\ \nu}\ {}^{[\alpha}\xi^\beta\chi^{\gamma]} = (\varepsilon + p)\chi^\nu u_\nu\, u^{[\alpha}\xi^\beta\chi^{\gamma]}. \tag{A.26}$$

The elastic contribution $\boldsymbol{T}^{\rm elas}$ to the energy-momentum tensor gives

$$\begin{aligned}
\xi^\nu T^{\rm elas}_{\ \ \nu}{}^{[\alpha}\xi^\beta\chi^{\gamma]} &= -2\mu\left(\bar{s}\frac{M\omega-N}{N}+s\right)N^{[\alpha}\xi^\beta\chi^{\gamma]} \\
&\quad +2\mu\left(\frac{2}{M}N^\beta\bar{\bar{s}}_\beta+\bar{\bar{s}}\omega\right)M^{[\alpha}\xi^\beta\chi^{\gamma]} \qquad \text{(A.27)}\\
\chi^\nu T^{\rm elas}_{\ \ \nu}{}^{[\alpha}\xi^\beta\chi^{\gamma]} &= -2\mu\bar{s}\frac{M-1}{N}N^{[\alpha}\xi^\beta\chi^{\gamma]}-2\mu\bar{\bar{s}}\frac{M-1}{M}M^{[\alpha}\xi^\beta\chi^{\gamma]}. \qquad \text{(A.28)}
\end{aligned}$$

Thus the circularity conditions write :

$$\begin{aligned}
\xi^\nu T_{\ \nu}^{[\alpha}\xi^\beta\chi^{\gamma]} &= (\varepsilon+p)\xi^\nu u_\nu\, u^{[\alpha}\xi^\beta\chi^{\gamma]}-2\mu\left(\bar{s}\frac{M\omega-N}{N}+s\right)N^{[\alpha}\xi^\beta\chi^{\gamma]} \\
&\quad +2\mu\left(\frac{2}{M}N^\beta\bar{\bar{s}}_\beta+\bar{\bar{s}}\omega\right)M^{[\alpha}\xi^\beta\chi^{\gamma]} \qquad \text{(A.29)}\\
\chi^\nu T_{\ \nu}^{[\alpha}\xi^\beta\chi^{\gamma]} &= (\varepsilon+p)\chi^\nu u_\nu\, u^{[\alpha}\xi^\beta\chi^{\gamma]}-2\mu\bar{s}\frac{M-1}{N}N^{[\alpha}\xi^\beta\chi^{\gamma]} \\
&\quad -2\mu\bar{\bar{s}}\frac{M-1}{M}M^{[\alpha}\xi^\beta\chi^{\gamma]}. \qquad \text{(A.30)}
\end{aligned}$$

A.8 Energy-momentum tensor from an elastic fluid

With the equation (8.56), the contribution from the elastic fluid to the quantities E, p_φ, $S^r{}_r$, $S^\theta{}_\theta$ and $S^\varphi{}_\varphi$ is :

$$\begin{aligned}
E^{\rm elas} &= T^{\rm elas}_{\alpha\beta}n^\alpha n^\beta = -2\mu s n_\alpha n_\beta n^\alpha n^\beta \\
&= -2\mu s; \qquad \text{(A.31)}
\end{aligned}$$

$$\begin{aligned}
p^{\rm elas}_\varphi &= -T^{\rm elas}_{\alpha\beta}n^\alpha h^\beta{}_\varphi = \bar{s}m_\alpha n^\alpha m_\nu h^\nu_\alpha \\
&= -\bar{s}M; \qquad \text{(A.32)}
\end{aligned}$$

$$\begin{aligned}
S^{\rm elas}_\beta{}^\alpha &= -T^{\rm elas}_{\gamma\delta}h^{\gamma\alpha}h^\delta{}_\beta = -2\mu\bar{\bar{s}}_{\gamma\delta}h^{\gamma\alpha}h^\delta{}_\beta-2\mu\bar{\bar{s}}m_\gamma h^{\gamma\alpha}m_\delta h^\delta{}_\beta \\
&= -2\mu\bar{\bar{s}}\ \beta^\alpha+-2\mu\bar{\bar{s}}m^\alpha m_\beta, \qquad \text{(A.33)}
\end{aligned}$$

$$\begin{aligned}
S^{\rm elas}_r{}^r &= -2\mu\bar{\bar{s}}^r{}_r, \qquad \text{(A.34)}\\
S^{\rm elas}_\theta{}^\theta &= -2\mu\bar{\bar{s}}^\theta{}_\theta, \qquad \text{(A.35)}\\
S^{\rm elas}_\varphi{}^\varphi &= -2\mu\bar{\bar{s}}; \qquad \text{(A.36)}
\end{aligned}$$

$$\begin{aligned}
S^{\rm elas} &= S^{r\rm elas}_r+S^{\theta\rm elas}_\theta+S^{\varphi\rm elas}_\varphi \\
&= -2\mu\left(\bar{\bar{s}}+\bar{\bar{s}}^r{}_r+\bar{\bar{s}}^\theta{}_\theta\right). \qquad \text{(A.37)}
\end{aligned}$$

A.9 Equation for $u^\sigma \nabla_\sigma u_\alpha$

With equations (8.55) and (Gourgoulhon, 2007) :

$$\begin{aligned} m^\beta \nabla_\beta m_\alpha &= b_\alpha && \text{(A.38)} \\ m^\beta \nabla_\beta n_\alpha &= -\kappa_\alpha && \text{(A.39)} \\ n^\beta \nabla_\beta m_\alpha &= \kappa_\alpha && \text{(A.40)} \\ n^\beta \nabla_\beta n_\alpha &= a_\alpha && \text{(A.41)} \\ & && \text{(A.42)} \end{aligned}$$

one gets :

$$u^\sigma \nabla_\sigma u_\alpha = \Gamma^2 \left(a_\alpha + U^2 b_\alpha - 2U\kappa_\alpha \right). \tag{A.43}$$

Then writing ${}^3\nabla_\alpha \ln \Gamma$, one gets :

$$u^\sigma \nabla_\sigma u_\alpha = {}^3\nabla_\alpha \ln \frac{N}{\Gamma} + \Gamma^2 U m_\alpha m^\beta \, {}^3\nabla_\beta U. \tag{A.44}$$

A.10 Calculation of $\nabla_\sigma s^\sigma_\alpha$

With equations (8.56) and (A.38-A.41), one can write :

$$\nabla_\sigma s^\sigma_\alpha = \nabla_\sigma \bar{\bar{s}}^\sigma_\alpha - \frac{1}{3}\Gamma^2 Q \left(b_\alpha - 2U\kappa_\alpha + U^2 a_\alpha \right). \tag{A.45}$$

Writing ${}^3\nabla_\sigma \bar{\bar{s}}^\sigma_\alpha$ with equation (A.1), this latter expression can be rewritten :

$$\nabla_\sigma s^\sigma_\alpha = {}^3\nabla_\sigma \bar{\bar{s}}^\sigma_\alpha + \bar{\bar{s}}^\sigma_\alpha a_\sigma - \frac{1}{3}\Gamma^2 Q \left(b_\alpha - 2U\kappa_\alpha + U^2 a_\alpha \right). \tag{A.46}$$

A.11 Source term Λ

$$\begin{aligned} \Lambda = \quad & \frac{2\mu}{\varepsilon + p} \left[\frac{1}{2} {}^3\nabla^a {}^3\nabla^c \delta g_{ac} + \frac{1}{2} a_b \left({}^3\nabla^b \Theta + \Delta_3 \zeta^b \right) + {}^3\nabla_{(a}\zeta^{b)} \, {}^3\nabla^a a_b + \frac{1}{2} {}^3\nabla^a \left(a^c \delta g_{ac} \right) \right. \\ & \left. - {}^3\nabla \left(F a_a \right) - \frac{1}{3} {}^3\nabla^a \left(\Gamma^2 Q \left[b_a - 2U\kappa_a + U^2 a_a \right] \right) \right] \\ & + {}^3\nabla \left(\frac{2\mu}{\varepsilon + p} \right) \left[\frac{1}{2} {}^3\nabla_a \Theta + \frac{1}{2} \Delta_3 \zeta_a + \frac{1}{2} {}^3\nabla^c \delta g_{ac} - {}^3\nabla_a F + a_b \, {}^3\nabla_{(a}\zeta^{b)} \right. \\ & \left. + \frac{1}{2} a^c \delta g_{ac} - F a_a - \frac{1}{3}\Gamma^2 Q \left[b_a - 2U\kappa_a + U^2 a_a \right] - 2 \left({}^3\nabla_a \Theta - {}^3\nabla_a F \right) \right] \\ & + 2 \, {}^3\nabla_a \left(\frac{{}^3\nabla^b \mu}{\varepsilon + p} \right) \left[{}^3\nabla_{(a}\zeta^{b)} + \frac{1}{2} k^{bc} \delta g_{ac} - F k_a{}^b \right] \\ & + \frac{2}{\varepsilon + p} \, {}^3\nabla_b \mu \left[\frac{1}{2} {}^3\nabla^b \Theta + \frac{1}{2} \Delta_3 \zeta^b + \frac{1}{2} {}^3\nabla^a \left(k^{bc} \delta g_{ac} \right) - {}^3\nabla^b F \right]. \end{aligned} \tag{A.47}$$

A.12 Source term $\mathcal{S}$

$$\begin{aligned}\mathcal{S} = \quad & \frac{\varepsilon+p}{\mu}\,{}^3\nabla_a\left[\Psi+\frac{2\mu}{\varepsilon+p}\left(\Theta-F\right)\right] \\ & -2\left[\frac{1}{2}\,{}^3\nabla^c\delta g_{ac}-\,{}^3\nabla_a I+a_b\,{}^3\nabla_{(c}\zeta^{b)}+\frac{1}{2}a^c\delta g_{ac}\right. \\ & \qquad\left.-a_a\left(\frac{1}{3}\Theta+I\right)-\frac{1}{3}\Gamma^2 Q\left[b_a-2U\kappa_a+U^2a_a\right]\right] \\ & -2\,{}^3\nabla_b\ln\mu\left[\,{}^3\nabla_{(a}\zeta^{b)}+\frac{1}{2}k^{bc}\delta g_{ac}-Fk_a{}^b\right], \end{aligned} \tag{A.48}$$

with

$$F=\frac{1}{3}\Theta+I. \tag{A.49}$$

Bibliography

ABADIE, J., ABBOTT, B.P., ABBOTT, R., ABERNATHY, M., ACCADIA, T., ACERNESE, F., ADAMS, C., ADHIKARI, R., AFFELDT, C., ALLEN, B. & ET AL. (2011). Beating the Spin-down Limit on Gravitational Wave Emission from the Vela Pulsar. *ApJ*, **737**, 93.

ABBOTT, B.P., ABBOTT, R., ACERNESE, F., ADHIKARI, R., AJITH, P., ALLEN, B., ALLEN, G., ALSHOURBAGY, M., AMIN, R.S., ANDERSON, S.B. & ET AL. (2010). Searches for Gravitational Waves from Known Pulsars with Science Run 5 LIGO Data. *ApJ*, **713**, 671–685.

ABDO, A.A. & ET AL. (2009). Detection of 16 Gamma-Ray Pulsars Through Blind Frequency Searches Using the Fermi LAT. *Science*, **325**, 840–.

AKMAL, A., PANDHARIPANDE, V.R. & RAVENHALL, D.G. (1998). Equation of state of nucleon matter and neutron star structure. *Phys. Rev. C*, **58**, 1804–1828.

ALPAR, M.A. (1995). Models for Pulsar Glitches. In M. A. Alpar, U. Kiziloglu, & J. van Paradijs, ed., *The Lives of the Neutron Stars*, 185.

ALPAR, M.A. & BAYKAL, A. (1994). Expectancy of Large Pulsar Glitches - a Comparison of Models with the Observed Glitch Sample. *MNRAS*, **269**, 849.

ALPAR, M.A., CHENG, A.F., RUDERMAN, M.A. & SHAHAM, J. (1982). A new class of radio pulsars. *Nature*, **300**, 728–730.

ANDERSSON, N., FERRARI, V., JONES, D.I., KOKKOTAS, K.D., KRISHNAN, B., READ, J.S., REZZOLLA, L. & ZINK, B. (2011). Gravitational waves from neutron stars: promises and challenges. *General Relativity and Gravitation*, **43**, 409–436.

ASHWORTH, W.B., JR. (1980). A Probable Flamsteed Observations of the Cassiopeia-A Supernova. *Journal for the History of Astronomy*, **11**, 1.

BAADE, W. & ZWICKY, F. (1934). Supernovae and cosmic rays. *Physical Review*, **45**, 138.

BACKER, D.C., KULKARNI, S.R., HEILES, C., DAVIS, M.M. & GOSS, W.M. (1982). A millisecond pulsar. *Nature*, **300**, 615–618.

BAIKO, D.A., HAENSEL, P. & YAKOVLEV, D.G. (2001). Thermal conductivity of neutrons in neutron star cores. *A&A*, **374**, 151–163.

BAIKO, D.A., POTEKHIN, A.Y. & YAKOVLEV, D.G. (2001). Thermodynamic functions of harmonic coulomb crystals. *Phys. Rev. E*, **64**, 057402.

BALBUS, S.A. (2007). "Astrophysical Gasdynamics", cours du Magistère Interuniversitaire de Physique (ENS Paris).

BARDEEN, J., COOPER, L.N. & SCHRIEFFER, J.R. (1957). Theory of Superconductivity. *Physical Review*, **108**, 1175–1204.

BASSA, C.G., VAN KERKWIJK, M.H. & KULKARNI, S.R. (2006). The ultra-cool white dwarf companion of PSR J0751+1807. *A&A*, **450**, 295–303.

BAYM, G. & PINES, D. (1971). Neutron starquakes and pulsar speedup. *Annals of Physics*, **66**, 816–835.

BAYM, G., PETHICK, C. & PINES, D. (1969). Superfluidity in Neutron Stars. *Nature*, **224**, 673–674.

BECKWITH, K., HAWLEY, J.F. & KROLIK, J.H. (2008). The Influence of Magnetic Field Geometry on the Evolution of Black Hole Accretion Flows: Similar Disks, Drastically Different Jets. *ApJ*, **678**, 1180–1199.

BEDNAREK, I. & MANKA, R. (2009). The role of nonlinear vector meson interactions in hyperon stars. *Journal of Physics G Nuclear Physics*, **36**, 095201–+.

BEDNAREK, I., HAENSEL, P., ZDUNIK, J.L., BEJGER, M. & MAŃKA, R. (2011). Hyperons in neutron-star cores and two-solar-mass pulsar. *ArXiv e-prints 1111.6942*.

BEIG, R. & SCHMIDT, B.G. (2005). Relativistic elastostatics: I. Bodies in rigid rotation. *Classical and Quantum Gravity*, **22**, 2249–2268.

BEJGER, M., ZDUNIK, J.L. & HAENSEL, P. (2010). Approximate analytic expressions for circular orbits around rapidly rotating compact stars. *A&A*, **520**, A16+.

BEJGER, M., FORTIN, M., HAENSEL, P. & ZDUNIK, J.L. (2011). Implications of the measured parameters of PSR J1903+0327 for its progenitor neutron star. *A&A*, **536**, A87.

BENNOUN, J.F. (1965). étude des milieux continus élastiques et thermodynamiques en relativité générale. *Annales de l'Institut Henri Poincaré, A Phys. Théor.*, **3**, 41–.

BERGER, J.F. (2009). "Structure nucléaire théroique", cours du master 2 Noyaux, Particules, Astroparticules et Cosmologie.

BETHE, H.A., BROWN, G.E., APPLEGATE, J. & LATTIMER, J.M. (1979). Equation of state in the gravitational collapse of stars. *Nuclear Physics A*, **324**, 487–533.

BHALERAO, V.B. & KULKARNI, S.R. (2011). The White Dwarf Companion of a 2 Msun Neutron Star. *ApJ*, **737**, L1+.

BHATTACHARYA, D., WIJERS, R.A.M.J., HARTMAN, J.W. & VERBUNT, F. (1992). On the decay of the magnetic fields of single radio pulsars. *A&A*, **254**, 198–212.

BILDSTEN, L. (1998). Gravitational Radiation and Rotation of Accreting Neutron Stars. *ApJ*, **501**, L89.

BISNOVATYI-KOGAN, G.S. & KOMBERG, B.V. (1974). Pulsars and close binary systems. *Soviet Ast.*, **18**, 217–+.

BLASCHKE, D., GRIGORIAN, H., VOSKRESENSKY, D.N. & WEBER, F. (2011). On the Cooling of the Neutron Star in Cassiopeia A. *ArXiv e-prints 1108.4125*.

BOHR, A., MOTTELSON, B.R. & PINES, D. (1958). Possible Analogy between the Excitation Spectra of Nuclei and Those of the Superconducting Metallic State. *Physical Review*, **110**, 936–938.

BONAZZOLA, S. & GOURGOULHON, E. (1994). A virial identity applied to relativistic stellar models. *Classical and Quantum Gravity*, **11**, 1775–1784.

BONAZZOLA, S., GOURGOULHON, E., SALGADO, M. & MARCK, J.A. (1993). Axisymmetric rotating relativistic bodies: A new numerical approach for 'exact' solutions. *A&A*, **278**, 421–443.

BONAZZOLA, S., GOURGOULHON, E. & MARCK, J.A. (1998). Numerical approach for high precision 3D relativistic star models. *Phys. Rev. D*, **58**, 104020.

BONAZZOLA, S., GOURGOULHON, E. & MARCK, J.A. (1999). Spectral methods in general relativistic astrophysics. *Journal of Computational and Applied Mathematics*, **109**, 433–473.

BORDAS, P., KUULKERS, E., ALFONSO-GARZÓN, J., BECKMANN, V., BIRD, T., CHENEVEZ, S.B.J., COURVOISIER, T., DEL SANTO, M., DOMINGO, A., EBISAWA, K., FERRIGNO, C., JONKER, P., KRETSCHMAR, P., MARKWARDT, C., OOSTERBROEK, T., PAIZIS, A., POTTSCHMIDT, K., SÁNCHEZ-FERNÁNDEZ, C. & WIJNANDS, R. (2010). A hard X-ray transient in the direction of Terzan 5 detected by INTEGRAL. *The Astronomer's Telegram*, **2919**, 1.

BOWYER, S., BYRAM, E.T., CHUBB, T.A. & FRIEDMAN, H. (1964). X-ray Sources in the Galaxy. *Nature*, **201**, 1307–1308.

BOYNTON, P.E., GROTH, E.J., III, PARTRIDGE, R.B. & WILKINSON, D.T. (1969). Precision Measurement of the Frequency Decay of the Crab Nebula Pulsar, NP 0532. *ApJ*, **157**, L197.

BRETON, R.P., KASPI, V.M., KRAMER, M., MCLAUGHLIN, M.A., LYUTIKOV, M., RANSOM, S.M., STAIRS, I.H., FERDMAN, R.D., CAMILO, F. & POSSENTI, A. (2008). Relativistic Spin Precession in the Double Pulsar. *Science*, **321**, 104–.

BRITO, I., CAROT, J. & VAZ, E.G.L.R. (2011a). Erratum to: General spherically symmetric elastic stars in relativity. *General Relativity and Gravitation*, 334.

BRITO, I., CAROT, J. & VAZ, E.G.L.R. (2011b). The Einstein field equations for cylindrically symmetric elastic configurations. *Journal of Physics Conference Series*, **314**, 012028.

BROWN, E.F. & CUMMING, A. (2009). Mapping Crustal Heating with the Cooling Light Curves of Quasi-Persistent Transients. *ApJ*, **698**, 1020–1032.

BROWN, E.F., BILDSTEN, L. & RUTLEDGE, R.E. (1998). Crustal Heating and Quiescent Emission from Transiently Accreting Neutron Stars. *ApJ*, **504**, L95.

BROWN, G.E., KUBODERA, K., PAGE, D. & PIZZOCHERO, P. (1988). Strangeness condensation and cooling of neutron stars. *Phys. Rev. D*, **37**, 2042–2046.

BURDERI, L., POSSENTI, A., COLPI, M., DI SALVO, T. & D'AMICO, N. (1999). Neutron Stars with Submillisecond Periods: A Population of High-Mass Objects? *ApJ*, **519**, 285–290.

BURGAY, M., D'AMICO, N., POSSENTI, A., MANCHESTER, R.N., LYNE, A.G., JOSHI, B.C., MCLAUGHLIN, M.A., KRAMER, M., SARKISSIAN, J.M., CAMILO, F., KALOGERA, V., KIM, C. & LORIMER, D.R. (2003). An increased estimate of the merger rate of double neutron stars from observations of a highly relativistic system. *Nature*, **426**, 531–533.

CACKETT, E.M., WIJNANDS, R., LINARES, M., MILLER, J.M., HOMAN, J. & LEWIN, W.H.G. (2006). Cooling of the quasi-persistent neutron star X-ray transients KS 1731-260 and MXB 1659-29. *MNRAS*, **372**, 479–488.

CACKETT, E.M., WIJNANDS, R., MILLER, J.M., BROWN, E.F. & DEGENAAR, N. (2008). Cooling of the Crust in the Neutron Star Low-Mass X-Ray Binary MXB 1659-29. *ApJ*, **687**, L87–L90.

CACKETT, E.M., BROWN, E.F., CUMMING, A., DEGENAAR, N., MILLER, J.M. & WIJNANDS, R. (2010). Continued Cooling of the Crust in the Neutron Star Low-mass X-ray Binary KS 1731-260. *ApJ*, **722**, L137–L141.

CAMERON, A.G. (1959). Neutron Star Models. *ApJ*, **130**, 884.

CAMPANA, S., COLPI, M., MEREGHETTI, S., STELLA, L. & TAVANI, M. (1998). The neutron stars of Soft X-ray Transients. *A&A Rev.*, **8**, 279–316.

CANUTO, V. & CHITRE, S.M. (1974). Crystallization of dense neutron matter. *Phys. Rev. D*, **9**, 1587–1613.

CARR, W.J. (1961). Energy, specific heat, and magnetic properties of the low-density electron gas. *Phys. Rev.*, **122**, 1437–1446.

CARTER, B. (1969). Killing Horizons and Orthogonally Transitive Groups in Space-Time. *Journal of Mathematical Physics*, **10**, 70–81.

CARTER, B. (1970). The commutation property of a stationary, axisymmetric system. *Communications in Mathematical Physics*, **17**, 233–238.

CARTER, B. (1973). Elastic perturbation theory in General Relativity and a variation principle for a rotating solid star. *Communications in Mathematical Physics*, **30**, 261–286.

CARTER, B. (1975). Application of continuous variation formulas and discrete invariance principles to black holes and neutron star models. *Annals of Physics*, **95**, 53–73.

CARTER, B. (1980). Rheometric Structure Theory, Convective Differentiation and Continuum Electrodynamics. *Royal Society of London Proceedings Series A*, **372**, 169–200.

CARTER, B. & QUINTANA, H. (1972). Foundations of General Relativistic High-Pressure Elasticity Theory. *Royal Society of London Proceedings Series A*, **331**, 57–83.

CARTER, B. & QUINTANA, H. (1975a). Relativistic formulation of the neutron starquake theory of pulsar glitches. *Annals of Physics*, **95**, 74–89.

CARTER, B. & QUINTANA, H. (1975b). Stationary elastic rotational deformation of a relativistic neutron star model. *ApJ*, **202**, 511–522.

CHABANAT, E., BONCHE, P., HAENSEL, P., MEYER, J. & SCHAEFFER, R. (1997). A skyrme parametrization from subnuclear to neutron star densities. *Nuclear Physics A*, **627**, 710 – 746.

CHADWICK, J. (1932). Possible Existence of a Neutron. *Nature*, **129**, 312.

CHAMEL, N. & HAENSEL, P. (2008). Physics of neutron star crusts. *Living Reviews in Relativity*, **11**.

CHAMPION, D.J., RANSOM, S.M., LAZARUS, P., CAMILO, F., BASSA, C., KASPI, V.M., NICE, D.J., FREIRE, P.C.C., STAIRS, I.H., VAN LEEUWEN, J., STAPPERS, B.W., CORDES, J.M., HESSELS, J.W.T., LORIMER, D.R., ARZOUMANIAN, Z., BACKER, D.C., BHAT, N.D.R., CHATTERJEE, S., COGNARD, I., DENEVA, J.S., FAUCHER-GIGUÈRE, C.A., GAENSLER, B.M., HAN, J., JENET, F.A., KASIAN, L., KONDRATIEV, V.I., KRAMER, M., LAZIO, J., MCLAUGHLIN, M.A., VENKATARAMAN, A. & VLEMMINGS, W. (2008). An Eccentric Binary Millisecond Pulsar in the Galactic Plane. *Science*, **320**, 1309–.

CHIU, H.Y. (1964). Supernovae, neutrinos, and neutron stars. *Annals of Physics*, **26**, 364–410.

CHIU, H.Y. & SALPETER, E.E. (1964). Surface X-Ray Emission from Neutron Stars. *Physical Review Letters*, **12**, 413–415.

CLARK, J.W. & SANDLER, D.G. (1975). Evidence against solidification of a model neutron system. *Phys. Rev. D*, **11**, 3365–3369.

COLPI, M., POSSENTI, A., POPOV, S. & PIZZOLATO, F. (2001). Spin and Magnetism in Old Neutron Stars. In D. Blaschke, N. K. Glendenning, & A. Sedrakian, ed., *Physics of Neutron Star Interiors*, vol. 578 of *Lecture Notes in Physics, Berlin Springer Verlag*, 440–+.

COMINSKY, L., OSSMANN, W. & LEWIN, W.H.G. (1983). Irregular X-ray variability in the transient X-ray burst source MXB 1659-29. *ApJ*, **270**, 226–232.

COOK, G.B., SHAPIRO, S.L. & TEUKOLSKY, S.A. (1994). Recycling Pulsars to Millisecond Periods in General Relativity. *ApJ*, **423**, L117+.

CRAWFORD, F., ROBERTS, M.S.E., HESSELS, J.W.T., RANSOM, S.M., LIVINGSTONE, M., TAM, C.R. & KASPI, V.M. (2006). A Survey of 56 Midlatitude EGRET Error Boxes for Radio Pulsars. *ApJ*, **652**, 1499–1507.

CUTLER, C., USHOMIRSKY, G. & LINK, B. (2003). The Crustal Rigidity of a Neutron Star and Implications for PSR B1828-11 and Other Precession Candidates. *ApJ*, **588**, 975–991.

DEGENAAR, N. & WIJNANDS, R. (2011). The accretion-heated crust of the transiently accreting 11-Hz X-ray pulsar in the globular cluster Terzan 5. *MNRAS*, **414**, L50–L54.

DEGENAAR, N., BROWN, E.F. & WIJNANDS, R. (2011a). Evidence for crust cooling in the transiently accreting 11-Hz X-ray pulsar in the globular cluster Terzan 5. *MNRAS*, **418**, L152–L156.

DEGENAAR, N., WOLFF, M.T., RAY, P.S., WOOD, K.S., HOMAN, J., LEWIN, W.H.G., JONKER, P.G., CACKETT, E.M., MILLER, J.M., BROWN, E.F. & WIJNANDS, R. (2011b). Further X-ray observations of EXO 0748-676 in quiescence: evidence for a cooling neutron star crust. *MNRAS*, **412**, 1409–1418.

DEMOREST, P.B., PENNUCCI, T., RANSOM, S.M., ROBERTS, M.S.E. & HESSELS, J.W.T. (2010). A two-solar-mass neutron star measured using Shapiro delay. *Nature*, **467**, 1081–1083.

DI GALLO, L., OERTEL, M. & URBAN, M. (2011). Collective excitations in the neutron star inner crust. *Phys. Rev. C*, **84**, 045801.

DOUCHIN, F. & HAENSEL, P. (2001). A unified equation of state of dense matter and neutron star structure. *A&A*, **380**, 151–167.

DUCOIN, C., MARGUERON, J., PROVIDÊNCIA, C. & VIDAÑA, I. (2011). Core-crust transition in neutron stars: Predictivity of density developments. *Phys. Rev. C*, **83**, 045810.

EGGLETON, P.P. (1983). Approximations to the radii of Roche lobes. *ApJ*, **268**, 368.

ELSNER, R.F. & LAMB, F.K. (1977). Accretion by magnetic neutron stars. I - Magnetospheric structure and stability. *ApJ*, **215**, 897–913.

FAUCHER-GIGUÈRE, C.A. & KASPI, V.M. (2006). Birth and Evolution of Isolated Radio Pulsars. *ApJ*, **643**, 332–355.

FESEN, R.A., HAMMELL, M.C., MORSE, J., CHEVALIER, R.A., BORKOWSKI, K.J., DOPITA, M.A., GERARDY, C.L., LAWRENCE, S.S., RAYMOND, J.C. & VAN DEN BERGH, S. (2006). The Expansion Asymmetry and Age of the Cassiopeia A Supernova Remnant. *ApJ*, **645**, 283–292.

FORTIN, M., GRILL, F., MARGUERON, J., PAGE, D. & SANDULESCU, N. (2010). Thermalization time and specific heat of the neutron stars crust. *Phys. Rev. C*, **82**, 065804–+.

FRANK, J., KING, A. & RAINE, D.J. (2002). *Accretion Power in Astrophysics: Third Edition*. Cambridge University Press.

FRAUENDIENER, J. & KABOBEL, A. (2007). The static spherically symmetric body in relativistic elasticity. *Classical and Quantum Gravity*, **24**, 4817–4837.

FREIRE, P.C.C., BASSA, C.G., WEX, N., STAIRS, I.H., CHAMPION, D.J., RANSOM, S.M., LAZARUS, P., KASPI, V.M., HESSELS, J.W.T., KRAMER, M., CORDES, J.M., VERBIEST, J.P.W., PODSIADLOWSKI, P., NICE, D.J., DENEVA, J.S., LORIMER, D.R., STAPPERS, B.W., MCLAUGHLIN, M.A. & CAMILO, F. (2011). On the nature and evolution of the unique binary pulsar J1903+0327. *MNRAS*, **412**, 2763–2780.

FRIDRIKSSON, J.K., HOMAN, J., WIJNANDS, R., MÉNDEZ, M., ALTAMIRANO, D., CACKETT, E.M., BROWN, E.F., BELLONI, T.M., DEGENAAR, N. & LEWIN, W.H.G. (2010). Rapid Cooling of the Neutron Star in the Quiescent Super-Eddington Transient XTE J1701-462. *ApJ*, **714**, 270–286.

FRIEDMAN, J.L., IPSER, J.R. & SORKIN, R.D. (1988). Turning-point method for axisymmetric stability of rotating relativistic stars. *ApJ*, **325**, 722–724.

FRUCHTER, A.S., STINEBRING, D.R. & TAYLOR, J.H. (1988). A millisecond pulsar in an eclipsing binary. *Nature*, **333**, 237–239.

GALLOWAY, D.K., MORGAN, E.H. & LEVINE, A.M. (2004). A Frequency Glitch in an Accreting Pulsar. *ApJ*, **613**, 1164–1172.

GALLOWAY, D.K., LIN, J., CHAKRABARTY, D. & HARTMAN, J.M. (2010). Discovery of a 552 Hz Burst Oscillation in the Low-Mass X-Ray Binary EXO 0748-676. *ApJ*, **711**, L148–L151.

GAVRIIL, F.P., GONZALEZ, M.E., GOTTHELF, E.V., KASPI, V.M., LIVINGSTONE, M.A. & WOODS, P.M. (2008). Magnetar-Like Emission from the Young Pulsar in Kes 75. *Science*, **319**, 1802–.

GEPPERT, U. & URPIN, V. (1994). Accretion-driven magnetic field decay in neutron stars. *MNRAS*, **271**, 490–+.

GHOSH, P. & LAMB, F.K. (1979). Accretion by rotating magnetic neutron stars. III - Accretion torques and period changes in pulsating X-ray sources. *ApJ*, **234**, 296–316.

GLEN, G. & SUTHERLAND, P. (1980). On the cooling of neutron stars. *ApJ*, **239**, 671–684.

GLENDENNING, N. (1996). *Compact Stars. Nuclear Physics, Particle Physics and General Relativity.*. Springer-Verlag New York.

GNEDIN, O.Y., YAKOVLEV, D.G. & POTEKHIN, A.Y. (2001). Thermal relaxation in young neutron stars. *MNRAS*, **324**, 725–736.

GOLD, T. (1968). Rotating Neutron Stars as the Origin of the Pulsating Radio Sources. *Nature*, **218**, 731–732.

GOPAKUMAR, A., BAGCHI, M. & RAY, A. (2009). Ruling out Kozai resonance in highly eccentric galactic binary millisecond pulsar PSR J1903+0327. *MNRAS*, **399**, L123–L127.

GOURGOULHON, E. (1995a). Étoile en rotation lente avec intérieur fluide et croûte solide - cas newtonien et incompressible, notes de travail.

GOURGOULHON, E. (1995b). Rotating neutron stars with an elastic interior, preliminary work.

GOURGOULHON, E. (2005). "Objets Compacts", cours du Master 2 Recherche Astronomie, Astrophysique et Ingénierie Spatiale.

GOURGOULHON, E. (2007). 3+1 Formalism and Bases of Numerical Relativity. *ArXiv General Relativity and Quantum Cosmology e-prints 0703035*.

GOURGOULHON, E. (2010). An introduction to the theory of rotating relativistic stars. *ArXiv e-prints 1003.5015*.

GOURGOULHON, E. (2012). *3+1 Formalism in General Relativity - Bases of Numerical Relativity*. Lecture Notes in Physics, Springer.

GOURGOULHON, E. & BONAZZOLA, S. (1993). Noncircular axisymmetric stationary spacetimes. *Phys. Rev. D*, **48**, 2635–2652.

GOURGOULHON, E. & BONAZZOLA, S. (1994). A formulation of the virial theorem in general relativity. *Classical and Quantum Gravity*, **11**, 443–452.

GOURGOULHON, E., HAENSEL, P., LIVINE, R., PALUCH, E., BONAZZOLA, S. & MARCK, J.A. (1999). Fast rotation of strange stars. *A&A*, **349**, 851–862.

GRANDCLÉMENT, P. (2010). KADATH: A spectral solver for theoretical physics. *Journal of Computational Physics*, **229**, 3334–3357.

GRILL, F., MARGUERON, J. & SANDULESCU, N. (2011). Cluster structure of the inner crust of neutron stars in the Hartree-Fock-Bogoliubov approach. *Phys. Rev. C*, **84**, 065801.

GUDMUNDSSON, E.H., PETHICK, C.J. & EPSTEIN, R.I. (1983). Structure of neutron star envelopes. *ApJ*, **272**, 286–300.

GULMINELLI, F. (2011). "Dense matter", cours du master 2 Noyaux, Particules, Astroparticules et Cosmologie.

GUPTA, S., BROWN, E.F., SCHATZ, H., MÖLLER, P. & KRATZ, K.L. (2007). Heating in the Accreted Neutron Star Ocean: Implications for Superburst Ignition. *ApJ*, **662**, 1188–1197.

HAENSEL, P. (1997). Solid Interiors of Neutron Stars and Gravitational Radiation. In J.-A. Marck & J.-P. Lasota, ed., *Relativistic Gravitation and Gravitational Radiation*, 129.

HAENSEL, P. & ZDUNIK, J.L. (1990). Non-equilibrium processes in the crust of an accreting neutron star. *A&A*, **227**, 431–436.

HAENSEL, P. & ZDUNIK, J.L. (2003). Nuclear composition and heating in accreting neutron-star crusts. *A&A*, **404**, L33–L36.

HAENSEL, P. & ZDUNIK, J.L. (2008). Models of crustal heating in accreting neutron stars. *A&A*, **480**, 459–464.

HAENSEL, P., SALGADO, M. & BONAZZOLA, S. (1995). Equation of state of dense matter and maximum rotation frequency of neutron stars. *A&A*, **296**, 745.

HAENSEL, P., POTEKHIN, A.Y. & YAKOVLEV, D.G., eds. (2007). *Neutron Stars 1 : Equation of State and Structure*, vol. 326 of *Astrophysics and Space Science Library*.

HAENSEL, P., ZDUNIK, J.L., BEJGER, M. & LATTIMER, J.M. (2009). Keplerian frequency of uniformly rotating neutron stars and strange stars. *A&A*, **502**, 605–610.

HANAWA, T. & FUJIMOTO, M.Y. (1984). Thermal response of neutron stars to shell flashes. *PASJ*, **36**, 199–214.

HARRISON, B.K., THORNE, K.S., WAKANO, M. & WHEELER, J.A. (1965). *Gravitation Theory and Gravitational Collapse*. University of Chicago Press.

HARTLE, J.B. (1967a). Slowly Rotating Relativistic Stars. I. Equations of Structure. *ApJ*, **150**, 1005.

HARTLE, J.B. (1967b). Slowly Rotating Relativistic Stars. I. Equations of Structure. *ApJ*, **150**, 1005–+.

HARTLE, J.B. & THORNE, K.S. (1968). Slowly Rotating Relativistic Stars. II. Models for Neutron Stars and Supermassive Stars. *ApJ*, **153**, 807.

HASKELL, B., JONES, D.I. & ANDERSSON, N. (2006). Mountains on neutron stars: accreted versus non-accreted crusts. *MNRAS*, **373**, 1423–1439.

HEINKE, C.O. & HO, W.C.G. (2010). Direct Observation of the Cooling of the Cassiopeia A Neutron Star. *ApJ*, **719**, L167–L171.

HEINKE, C.O., WIJNANDS, R., COHN, H.N., LUGGER, P.M., GRINDLAY, J.E., POOLEY, D. & LEWIN, W.H.G. (2006). Faint X-Ray Sources in the Globular Cluster Terzan 5. *ApJ*, **651**, 1098–1111.

HEINTZMANN, H., HILLEBRANDT, W., KROTSCHECK, E. & KUNDT, W. (1973). Neutron star corequakes and crustquakes. *Annals of Physics*, **81**, 625–641.

HENYEY, L.G., FORBES, J.E. & GOULD, N.L. (1964). A New Method of Automatic Computation of Stellar Evolution. *ApJ*, **139**, 306.

HERNQUIST, L. & APPLEGATE, J.H. (1984). Analytical models of neutron star envelopes. *ApJ*, **287**, 244–254.

HESSELS, J., RANSOM, S., ROBERTS, M., KASPI, V., LIVINGSTONE, M., TAM, C. & CRAWFORD, F. (2005). Three New Binary Pulsars Discovered With Parkes. In F. A. Rasio & I. H. Stairs, ed., *Binary Radio Pulsars*, vol. 328 of *Astronomical Society of the Pacific Conference Series*, 395–+.

HESSELS, J.W.T., RANSOM, S.M., STAIRS, I.H., FREIRE, P.C.C., KASPI, V.M. & CAMILO, F. (2006). A Radio Pulsar Spinning at 716 Hz. *Science*, **311**, 1901–1904.

HEWISH, A., BELL, S.J., PILKINGTON, J.D.H., SCOTT, P.F. & COLLINS, R.A. (1968). Observation of a Rapidly Pulsating Radio Source. *Nature*, **217**, 709–713.

HO, W.C.G. (2011). Neutron star cooling: Theory and observations. Talk given at Mode-SNR-PWN workshop, November 21–24, 2011, Nançay radio observatory, France.

HO, W.C.G. & HEINKE, C.O. (2009). A neutron star with a carbon atmosphere in the Cassiopeia A supernova remnant. *Nature*, **462**, 71–73.

HOBBS, G., LYNE, A.G., JOSHI, B.C., KRAMER, M., STAIRS, I.H., CAMILO, F., MANCHESTER, R.N., D'AMICO, N., POSSENTI, A. & KASPI, V.M. (2002). A very large glitch in PSR J1806-2125. *MNRAS*, **333**, L7–L10.

HOFFBERG, M., GLASSGOLD, A.E., RICHARDSON, R.W. & RUDERMAN, M. (1970). Anisotropic Superfluidity in Neutron Star Matter. *Physical Review Letters*, **24**, 775–777.

HOMAN, J., VAN DER KLIS, M., WIJNANDS, R., BELLONI, T., FENDER, R., KLEIN-WOLT, M., CASELLA, P., MÉNDEZ, M., GALLO, E., LEWIN, W.H.G. & GEHRELS, N. (2007). Rossi X-Ray Timing Explorer Observations of the First Transient Z Source XTE J1701-462: Shedding New Light on Mass Accretion in Luminous Neutron Star X-Ray Binaries. *ApJ*, **656**, 420–430.

HULSE, R.A. & TAYLOR, J.H. (1975). Discovery of a pulsar in a binary system. *ApJ*, **195**, L51–L53.

IN 'T ZAND, J., HEISE, J., SMITH, M.J.S., COCCHI, M., NATALUCCI, L., CELIDONIO, G., AUGUSTEIJN, T. & FREYHAMMER, L. (1999). V2134 Ophiuchi = MXB 1659-29. *IAU Circ.*, **7138**, 1.

ITOH, N., HAYASHI, H., NISHIKAWA, A. & KOHYAMA, Y. (1996). Neutrino Energy Loss in Stellar Interiors. VII. Pair, Photo-, Plasma, Bremsstrahlung, and Recombination Neutrino Processes. *ApJS*, **102**, 411.

JACKSON, J.D. (1998). *Classical Electrodynamics, 3rd Edition*. Wiley.

JANKA, H.T., LANGANKE, K., MAREK, A., MARTÍNEZ-PINEDO, G. & MÜLLER, B. (2007). Theory of core-collapse supernovae. *Phys. Rep.*, **442**, 38–74.

JONKER, P.G., STEEGHS, D., CHAKRABARTY, D. & JUETT, A.M. (2007). The Cold Neutron Star in the Soft X-Ray Transient 1H 1905+000. *ApJ*, **665**, L147–L150.

KAARET, P., PRIESKORN, Z., IN 'T ZAND, J.J.M., BRANDT, S., LUND, N., MEREGHETTI, S., GÖTZ, D., KUULKERS, E. & TOMSICK, J.A. (2007). Evidence of 1122 Hz X-Ray Burst Oscillations from the Neutron Star X-Ray Transient XTE J1739-285. *ApJ*, **657**, L97–L100.

KARLOVINI, M. & SAMUELSSON, L. (2003). Elastic stars in general relativity: I. Foundations and equilibrium models. *Classical and Quantum Gravity*, **20**, 3613–3648.

KARLOVINI, M. & SAMUELSSON, L. (2004). Elastic stars in general relativity: III. Stiff ultrarigid exact solutions. *Classical and Quantum Gravity*, **21**, 4531–4548.

KARLOVINI, M. & SAMUELSSON, L. (2007). Elastic stars in general relativity: IV. Axial perturbations. *Classical and Quantum Gravity*, **24**, 3171–3189.

KARLOVINI, M., SAMUELSSON, L. & ZARROUG, M. (2004). Elastic stars in general relativity: II. Radial perturbations. *Classical and Quantum Gravity*, **21**, 1559–1581.

KASPI, V.M. (2010). Grand unification of neutron stars. *Proceedings of the National Academy of Science*, **107**, 7147–7152.

KASPI, V.M. & GAVRIIL, F.P. (2003). A Second Glitch from the "Anomalous" X-Ray Pulsar 1RXS J170849.0-4000910. *ApJ*, **596**, L71–L74.

KIEL, P.D., HURLEY, J.R., BAILES, M. & MURRAY, J.R. (2008). Populating the Galaxy with pulsars - I. Stellar and binary evolution. *MNRAS*, **388**, 393–415.

KIZILTAN, B., KOTTAS, A. & THORSETT, S.E. (2010). The Neutron Star Mass Distribution. *ArXiv e-prints 1011.4291*.

KLUŹNIAK, W. & RAPPAPORT, S. (2007). Magnetically Torqued Thin Accretion Disks. *ApJ*, **671**, 1990–2005.

KLUŹNIAK, W. & WAGONER, R.V. (1985). Evolution of the innermost stable orbits around accreting neutron stars. *ApJ*, **297**, 548–554.

KLUZNIAK, W., RUDERMAN, M., SHAHAM, J. & TAVANI, M. (1988). Nature and evolution of the eclipsing millisecond binary pulsar PSR1957 + 20. *Nature*, **334**, 225–227.

KONAR, S. & BHATTACHARYA, D. (1997). Magnetic field evolution of accreting neutron stars. *MNRAS*, **284**, 311–317.

KONAR, S. & BHATTACHARYA, D. (1999). Magnetic field evolution of accreting neutron stars - III. *MNRAS*, **308**, 795–798.

KOZAI, Y. (1962). Secular perturbations of asteroids with high inclination and eccentricity. *AJ*, **67**, 591–+.

KRAMER, M., STAIRS, I.H., MANCHESTER, R.N., MCLAUGHLIN, M.A., LYNE, A.G., FERDMAN, R.D., BURGAY, M., LORIMER, D.R., POSSENTI, A., D'AMICO, N., SARKISSIAN, J.M., HOBBS, G.B., REYNOLDS, J.E., FREIRE, P.C.C. & CAMILO, F. (2006). Tests of general relativity from timing the double pulsar. *Science*, **314**, 97–102.

KUTSCHERA, M. & WÓJCIK, W.Ł. (1995). Self-consistent proton crystallization in dense neutron-star matter. *Nuclear Physics A*, **581**, 706–724.

LANDAU, L.D. (1932). On the theory of stars. *Phys. Z. Sowjetunion*, **1**, 285–288.

LANDAU, L.D. & LIFSHIT'S, E.M. (1959). *Theory of elasticity*. Pergamon Press.

LATTIMER, J.M. & PRAKASH, M. (2004). The Physics of Neutron Stars. *Science*, **304**, 536–542.

LATTIMER, J.M. & PRAKASH, M. (2010). What a Two Solar Mass Neutron Star Really Means. *ArXiv e-prints 1012.3208*.

LATTIMER, J.M., PRAKASH, M., PETHICK, C.J. & HAENSEL, P. (1991). Direct URCA process in neutron stars. *Physical Review Letters*, **66**, 2701–2704.

LATTIMER, J.M., VAN RIPER, K.A., PRAKASH, M. & PRAKASH, M. (1994). Rapid cooling and the structure of neutron stars. *ApJ*, **425**, 802–813.

LEINSON, L.B. & PÉREZ, A. (2006a). Neutrino emission due to Cooper pairing in neutron stars. *ArXiv Astrophysics e-prints 0606653*.

LEINSON, L.B. & PÉREZ, A. (2006b). Vector current conservation and neutrino emission from singlet-paired baryons in neutron stars. *Physics Letters B*, **638**, 114–118.

LEVENFISH, K.P. & HAENSEL, P. (2007). Nucleon superfluidity versus thermal states of isolated and transiently accreting neutron stars. *Ap&SS*, **308**, 457–465.

LEVENFISH, K.P. & YAKOVLEV, D.G. (1994). Specific heat of neutron star cores with superfluid nucleons. *Astronomy Reports*, **38**, 247–251.

LEVINSON, A. & EICHLER, D. (1991). Can neutron stars ablate their companions? *ApJ*, **379**, 359–365.

LEWIN, W.H.G., HOFFMAN, J.A., DOTY, J. & LILLER, W. (1976). X-Ray Bursts. *IAU Circ.*, **2994**, 2.

LIN, J., ÖZEL, F., CHAKRABARTY, D. & PSALTIS, D. (2010). The Incompatibility of Rapid Rotation with Narrow Photospheric X-ray Lines in EXO 0748-676. *ApJ*, **723**, 1053–1056.

LIN, J., RAPPAPORT, S., PODSIADLOWSKI, P., NELSON, L., PAXTON, B. & TODOROV, P. (2011). LMXB and IMXB Evolution: I. The Binary Radio Pulsar PSR J1614-2230. *ApJ*, **732**, 70–+.

LINK, B. & EPSTEIN, R.I. (2001). Precession Interpretation of the Isolated Pulsar PSR B1828-11. *ApJ*, **556**, 392–398.

LIU, X.W. & LI, X.D. (2009). A Fallback Disk Accretion Involved Formation Channel to PSR J1903+0327. *ApJ*, **692**, 723–728.

LIVINGSTONE, M.A., KASPI, V.M., GOTTHELF, E.V. & KUIPER, L. (2006). A Braking Index for the Young, High Magnetic Field, Rotation-Powered Pulsar in Kesteven 75. *ApJ*, **647**, 1286–1292.

LOMBARDO, U. & SCHULZE, H.J. (2001). Superfluidity in Neutron Star Matter. In D. Blaschke, N. K. Glendenning, & A. Sedrakian, ed., *Physics of Neutron Star Interiors*, vol. 578 of *Lecture Notes in Physics, Berlin Springer Verlag*, 30.

LORIMER, D.R. (2008). Binary and Millisecond Pulsars. *Living Reviews in Relativity*, **11**, 8–+.

LOVE, A.E.H. (1911). *Some Problems of Geodynamics*. Cambridge University Press.

LOVE, A.E.H. (1944). *A treatise on the mathematical theory of elasticity*. Dover Publications.

LOVELACE, R.V.E., ROMANOVA, M.M. & BISNOVATYI-KOGAN, G.S. (2005). Screening of the Magnetic Field of Disk Accreting Stars. *ApJ*, **625**, 957–965.

LUNDGREN, S.C., ZEPKA, A.F. & CORDES, J.M. (1995). A Millisecond Pulsar in a 6 Hour Orbit: PSR J0751+1807. *ApJ*, **453**, 419–+.

LYNE, A.G. & GRAHAM-SMITH, F. (2005). *Pulsar Astronomy*. Cambridge University Press.

LYNE, A.G., BURGAY, M., KRAMER, M., POSSENTI, A., MANCHESTER, R.N., CAMILO, F., MCLAUGHLIN, M.A., LORIMER, D.R., D'AMICO, N., JOSHI, B.C., REYNOLDS, J. & FREIRE, P.C.C. (2004). A Double-Pulsar System: A Rare Laboratory for Relativistic Gravity and Plasma Physics. *Science*, **303**, 1153–1157.

MAGLI, G. & KIJOWSKI, J. (1992). A generalization of the relativistic equilibrium equations for a non-rotating star. *General Relativity and Gravitation*, **24**, 139–158.

MALONE, R.C. (1974). *Cooling of superfluid neutron stars*. Ph.D. thesis, Cornell Univ., Ithaca, NY.

MANCHESTER, R.N., HOBBS, G.B., TEOH, A. & HOBBS, M. (2005). The Australia Telescope National Facility Pulsar Catalogue. *AJ*, **129**, 1993–2006.

MAREK, A. & JANKA, H.T. (2009). Delayed Neutrino-Driven Supernova Explosions Aided by the Standing Accretion-Shock Instability. *ApJ*, **694**, 664–696.

MARSHALL, F.E., GOTTHELF, E.V., MIDDLEDITCH, J., WANG, Q.D. & ZHANG, W. (2004). The Big Glitcher: The Rotation History of PSR J0537-6910. *ApJ*, **603**, 682–689.

MIDDLEDITCH, J., PENNYPACKER, C., MORRIS, D.E., MULLER, R.A., PERLMUTTER, S., SASSEEN, T., KRISTIAN, J.A., KUNKEL, W.E., HAMMY, M.A., IMAMURA, J.N., STEIMAN-CAMERON, T.Y., SHELTON, I.K., TUOHY, I.R. & RAWLINGS, S. (1989). Sub-Millisecond Optical Pulsar in Supernova 1987A. *IAU Circ.*, **4735**, 1.

MIGDAL, A. (1959). Superfluidity and the moments of inertia of nuclei. *Nucl. Phys. A*, **13**, 655–674.

MIRALDA-ESCUDE, J., PACZYNSKI, B. & HAENSEL, P. (1990). Thermal structure of accreting neutron stars and strange stars. *ApJ*, **362**, 572–583.

MONROZEAU, C., MARGUERON, J. & SANDULESCU, N. (2007). Nuclear superfluidity and cooling time of neutron star crusts. *Phys. Rev. C*, **75**, 065807.

MORRISON, I.A., BAUMGARTE, T.W. & SHAPIRO, S.L. (2004). Effect of Differential Rotation on the Maximum Mass of Neutron Stars: Realistic Nuclear Equations of State. *ApJ*, **610**, 941–947.

MORTON, D.C. (1964). Neutron Stars as X-ray Sources. *Nature*, **201**, 1308–1309.

NEGELE, J.W. & VAUTHERIN, D. (1973). Neutron star matter at sub-nuclear densities. *Nuclear Physics A*, **207**, 298–320.

NICE, D.J., SPLAVER, E.M., STAIRS, I.H., LÖHMER, O., JESSNER, A., KRAMER, M. & CORDES, J.M. (2005). A 2.1 M_{solar} Pulsar Measured by Relativistic Orbital Decay. *ApJ*, **634**, 1242–1249.

NICE, D.J., STAIRS, I.H. & KASIAN, L.E. (2008). Masses of Neutron Stars in Binary Pulsar Systems. In C. Bassa, Z. Wang, A. Cumming, & V. M. Kaspi, ed., *40 Years of Pulsars: Millisecond Pulsars, Magnetars and More*, vol. 983 of *American Institute of Physics Conference Series*, 453–458.

OPPENHEIMER, J.R. & VOLKOFF, G.M. (1939). On Massive Neutron Cores. *Physical Review*, **55**, 374–381.

OSŁOWSKI, S., BULIK, T., GONDEK-ROSIŃSKA, D. & BELCZYŃSKI, K. (2011). Population synthesis of double neutron stars. *MNRAS*, **413**, 461–479.

ÖZEL, F. (2006). Soft equations of state for neutron-star matter ruled out by EXO 0748 - 676. *Nature*, **441**, 1115–1117.

PACZYŃSKI, B. (1971). Evolutionary Processes in Close Binary Systems. *ARA&A*, **9**, 183.

PAGE, D. (1998). Thermal Evolution of Isolated Neutron Stars. In N. Shibazaki, ed., *Neutron Stars and Pulsars: Thirty Years after the Discovery*, 183.

PAGE, D. (2009). Neutron Star Cooling: I. In W. Becker, ed., *Astrophysics and Space Science Library*, vol. 357 of *Astrophysics and Space Science Library*, 247.

PAGE, D. & APPLEGATE, J.H. (1992). The cooling of neutron stars by the direct URCA process. *ApJ*, **394**, L17–L20.

PAGE, D., LATTIMER, J.M., PRAKASH, M. & STEINER, A.W. (2004). Minimal Cooling of Neutron Stars: A New Paradigm. *ApJS*, **155**, 623–650.

PAGE, D., GEPPERT, U. & WEBER, F. (2006). The cooling of compact stars. *Nuclear Physics A*, **777**, 497–530.

PAGE, D., LATTIMER, J.M., PRAKASH, M. & STEINER, A.W. (2009). Neutrino Emission from Cooper Pairs and Minimal Cooling of Neutron Stars. *ApJ*, **707**, 1131–1140.

PAGE, D., PRAKASH, M., LATTIMER, J.M. & STEINER, A.W. (2011). Rapid Cooling of the Neutron Star in Cassiopeia A Triggered by Neutron Superfluidity in Dense Matter. *Physical Review Letters*, **106**, 081101–+.

PAPAPETROU, A. (1966). Champs gravitationnels stationnaires à symétrie axiale. *Ann. Inst. Henri Poincaré (A) Phys. théor.*, **4**, 83.

PAPITTO, A., D'AÌ, A., MOTTA, S., RIGGIO, A., BURDERI, L., DI SALVO, T., BELLONI, T. & IARIA, R. (2011). The spin and orbit of the newly discovered pulsar IGR J17480-2446. *A&A*, **526**, L3.

PARMAR, A.N., WHITE, N.E., GIOMMI, P., HABERL, F., PEDERSEN, H. & MAYOR, M. (1985). EXO 0748-676. *IAU Circ.*, **4039**, 1.

PAVLOV, G.G. & LUNA, G.J.M. (2009). A Dedicated Chandra ACIS Observation of the Central Compact Object in the Cassiopeia A Supernova Remnant. *ApJ*, **703**, 910–921.

PAVLOV, G.G., SANWAL, D. & TETER, M.A. (2004). Central Compact Objects in Supernova Remnants. In F. Camilo & B. M. Gaensler, ed., *Young Neutron Stars and Their Environments*, vol. 218 of *IAU Symposium*, 239.

PAYNE, D.J.B. & MELATOS, A. (2004). Burial of the polar magnetic field of an accreting neutron star - I. Self-consistent analytic and numerical equilibria. *MNRAS*, **351**, 569–584.

PENNER, A.J., ANDERSSON, N., SAMUELSSON, L., HAWKE, I. & JONES, D.I. (2011). Tidal deformations of neutron stars: The role of stratification and elasticity. *Phys. Rev. D*, **84**, 103006.

PÉREZ GARCÍA, M.A., CORTE RODRÍGUEZ, N., MORNAS, L., SUÁREZ CURIESES, J.P. & DÍAZ ALONSO, J. (2002). Formation of an ordered phase in neutron star matter. *Nuclear Physics A*, **699**, 939–962.

PINES, D. & SHAHAM, J. (1972). Neutron stars-Microquakes, macroquakes and glitches. *Nature*, **235**, 43.

PINES, D., SHAHAM, J. & RUDERMAN, M. (1972). Vela pulsar-Speedups explained in terms of corequakes. *Nature*, **237**, 83.

PIZZOCHERO, P.M. (2010). Neutron Stars, the Most Exotic Nuclear Lab in the Universe. *ArXiv e-prints 1001.1272*.

PLAVEC, M. & KRATOCHVIL, P. (1964). Tables for the Roche model of close binaries. *Bulletin of the Astronomical Institutes of Czechoslovakia*, **15**, 165.

PORTEGIES ZWART, S., VAN DEN HEUVEL, E.P.J., VAN LEEUWEN, J. & NELEMANS, G. (2011). The Formation of the Eccentric-orbit Millisecond Pulsar J1903+0327 and the Origin of Single Millisecond Pulsars. *ApJ*, **734**, 55–+.

POTEKHIN, A.Y. (1999). Electron conduction in magnetized neutron star envelopes. *A&A*, **351**, 787–797.

POTEKHIN, A.Y. & CHABRIER, G. (2010). Thermodynamic Functions of Dense Plasmas: Analytic Approximations for Astrophysical Applications. *Contributions to Plasma Physics*, **50**, 82–87.

POTEKHIN, A.Y. & YAKOVLEV, D.G. (2001). Thermal structure and cooling of neutron stars with magnetized envelopes. *A&A*, **374**, 213–226.

POTEKHIN, A.Y., CHABRIER, G. & YAKOVLEV, D.G. (1997). Internal temperatures and cooling of neutron stars with accreted envelopes. *A&A*, **323**, 415–428.

POTEKHIN, A.Y., BAIKO, D.A., HAENSEL, P. & YAKOVLEV, D.G. (1999). Transport properties of degenerate electrons in neutron star envelopes and white dwarf cores. *A&A*, **346**, 345–353.

POTEKHIN, A.Y., YAKOVLEV, D.G., CHABRIER, G. & GNEDIN, O.Y. (2003). Thermal Structure and Cooling of Superfluid Neutron Stars with Accreted Magnetized Envelopes. *ApJ*, **594**, 404–418.

PRIYMAK, M., MELATOS, A. & PAYNE, D.J.B. (2011). Quadrupole moment of a magnetically confined mountain on an accreting neutron star: effect of the equation of state. *MNRAS*, **417**, 2696–2713.

QUINTANA, H. (1976). The structure equations of a slowly rotating, fully relativistic solid star. *ApJ*, **207**, 279–288.

RADHAKRISHNAN, V. & MANCHESTER, R.N. (1969). Detection of a Change of State in the Pulsar PSR 0833-45. *Nature*, **222**, 228–229.

RADHAKRISHNAN, V. & SRINIVASAN, G. (1982). On the origin of the recently discovered ultra-rapid pulsar. *Current Science*, **51**, 1096–1099.

RAJAGOPAL, K. & SHARMA, R. (2006). Crystallography of three-flavor quark matter. *Phys. Rev. D*, **74**, 094019.

RAPPAPORT, S.A., FREGEAU, J.M. & SPRUIT, H. (2004). Accretion onto Fast X-Ray Pulsars. *ApJ*, **606**, 436–443.

RAVENHALL, D.G., PETHICK, C.J. & WILSON, J.R. (1983). Structure of Matter below Nuclear Saturation Density. *Physical Review Letters*, **50**, 2066–2069.

RAYNER, C.B. (1963). Elasticity in general relativity. *Proceedings of the Royal Society of London. Series A. Mathematical and Physical Sciences*, **272**, 44–53.

REED, J.E., HESTER, J.J., FABIAN, A.C. & WINKLER, P.F. (1995). The Three-dimensional Structure of the Cassiopeia A Supernova Remnant. I. The Spherical Shell. *ApJ*, **440**, 706.

REMILLARD, R.A., LIN, D., THE ASM TEAM AT MIT & NASA/GSFC (2006). New X-ray Transient, XTE J1701-462. *The Astronomer's Telegram*, **696**, 1.

REYNOLDS, A.P., PARMAR, A.N., HAKALA, P.J., POLLOCK, A.M.T., WILLIAMS, O.R., PEACOCK, A. & TAYLOR, B.G. (1999). The EXOSAT medium-energy slew survey catalog. *A&AS*, **134**, 287–300.

ROMANI, R.W. (1987). Model atmospheres for cooling neutron stars. *ApJ*, **313**, 718–726.

RUDERMAN, M. (1969). Neutron Starquakes and Pulsar Periods. *Nature*, **223**, 597–598.

RUTLEDGE, R.E., BILDSTEN, L., BROWN, E.F., PAVLOV, G.G. & ZAVLIN, V.E. (1999). The Thermal X-Ray Spectra of Centaurus X-4, Aquila X-1 , and 4U 1608-522 in Quiescence. *ApJ*, **514**, 945–951.

RUTLEDGE, R.E., BILDSTEN, L., BROWN, E.F., PAVLOV, G.G. & ZAVLIN, V.E. (2000). A Method for Distinguishing between Transiently Accreting Neutron Stars and Black Holes, in Quiescence. *ApJ*, **529**, 985–996.

RUTLEDGE, R.E., BILDSTEN, L., BROWN, E.F., PAVLOV, G.G., ZAVLIN, V.E. & USHOMIRSKY, G. (2002). Crustal Emission and the Quiescent Spectrum of the Neutron Star in KS 1731-260. *ApJ*, **580**, 413–422.

SANDULESCU, N. (2004). Nuclear superfluidity and specific heat in the inner crust of neutron stars. *Phys. Rev. C*, **70**, 025801.

SANDULESCU, N., VAN GIAI, N. & LIOTTA, R.J. (2004). Superfluid properties of the inner crust of neutron stars. *Phys. Rev. C*, **69**, 045802.

SCHAAB, C., SEDRAKIAN, A., WEBER, F. & WEIGEL, M.K. (1999). Impact of internal heating on the thermal evolution of neutron stars. *A&A*, **346**, 465–480.

SCHWENK, A., FRIMAN, B. & BROWN, G.E. (2003). Renormalization group approach to neutron matter: quasiparticle interactions, superfluid gaps and the equation of state. *Nuclear Physics A*, **713**, 191–216.

SHAPIRO, S.L. & TEUKOLSKY, S.A. (1983). *Black holes, white dwarfs, and neutron stars: The physics of compact objects*. Wiley-Interscience.

SHIBAZAKI, N., MURAKAMI, T., SHAHAM, J. & NOMOTO, K. (1989). Does mass accretion lead to field decay in neutron stars? *Nature*, **342**, 656–658.

SHTERNIN, P.S. & YAKOVLEV, D.G. (2006). Electron thermal conductivity owing to collisions between degenerate electrons. *Phys. Rev. D*, **74**, 043004.

SHTERNIN, P.S. & YAKOVLEV, D.G. (2007). Electron-muon heat conduction in neutron star cores via the exchange of transverse plasmons. *Phys. Rev. D*, **75**, 103004.

SHTERNIN, P.S., YAKOVLEV, D.G., HAENSEL, P. & POTEKHIN, A.Y. (2007). Neutron star cooling after deep crustal heating in the X-ray transient KS 1731-260. *MNRAS*, **382**, L43–L47.

SHTERNIN, P.S., YAKOVLEV, D.G., HEINKE, C.O., HO, W.C.G. & PATNAUDE, D.J. (2011). Cooling neutron star in the Cassiopeia A supernova remnant: evidence for superfluidity in the core. *MNRAS*, **412**, L108–L112.

SLATTERY, W.L., DOOLEN, G.D. & DEWITT, H.E. (1982). n dependence in the classical one-component plasma monte carlo calculations. *Phys. Rev. A*, **26**, 2255–2258.

SMITH, R.A. & PANDHARIPANDE, V.R. (1976). Nucleon-nucleon potentials including πNΔ coupling effects. *Nuclear Physics A*, **256**, 327–348.

SRINIVASAN, G., BHATTACHARYA, D., MUSLIMOV, A.G. & TSYGAN, A.J. (1990). A novel mechanism for the decay of neutron star magnetic fields. *Current Science*, **59**, 31–38.

STABLER, R.C. (1960). *Energy Loss Mechanisms from Very Dense Stars.*. Ph.D. thesis, CORNELL UNIVERSITY.

STAIRS, I.H., LYNE, A.G. & SHEMAR, S.L. (2000). Evidence for free precession in a pulsar. *Nature*, **406**, 484–486.

STERGIOULAS, N. (2003). Rotating Stars in Relativity. *Living Reviews in Relativity*, **6**, 3.

STROHMAYER, T.E. & MARKWARDT, C.B. (2010). EXO 1745-248 is an 11 Hz Eclipsing Pulsar. *The Astronomer's Telegram*, **2929**, 1.

SYNGE, J.L. (1959). A theory of elasticity in general relativity. *Mathematische Zeitschrift*, **72**, 82–87, 10.1007/BF01162939.

SYUNYAEV, R., GILFANOV, M., CHURAZOV, E., LOZNIKOV, V., YAMBURENKO, N., SKINNER, G.K., PATTERSON, T.G., WILLMORE, A.P., EMAM, O., BRINKMAN, A.C., HEISE, J., INTZAND, J. & JAGER, R. (1990). The New X-Ray Transient Burster KS:1731-260. *Soviet Astronomy Letters*, **16**, 59.

TAAM, R.E. & VAN DEN HEUVEL, E.P.J. (1986). Magnetic field decay and the origin of neutron star binaries. *ApJ*, **305**, 235–245.

TAKATSUKA, T. (1973). Proton Superfluidity in Neutron-Star Matter. *Progress of Theoretical Physics*, **50**, 1754–1755.

TAKATSUKA, T., TAMIYA, K., TATSUMI, T. & TAMAGAKI, R. (1978). Solidification and Pion Condensation in Nuclear Medium —Alternating-Layer-Spin Structure with One-Dimensional Localization Accompanying π^0 Condensate—. *Progress of Theoretical Physics*, **59**, 1933–1955.

TAKEMORI, M.T. & GUYER, R.A. (1975). Solid neutron matter. *Phys. Rev. D*, **11**, 2696–2723.

TANANBAUM, H. (1999). Cassiopeia A. *IAU Circ.*, **7246**, 1.

TAURIS, T.M. (2011). Five and a half roads to form a millisecond pulsar. *ArXiv e-prints 1106.0897*.

TAURIS, T.M. & VAN DEN HEUVEL, E.P.J. (2006). *Formation and evolution of compact stellar X-ray sources*, 623–665. Cambridge University Press.

TAURIS, T.M., LANGER, N. & KRAMER, M. (2011). Formation of millisecond pulsars with CO white dwarf companions - I. PSR J1614-2230: evidence for a neutron star born massive. *MNRAS*, **416**, 2130–2142.

TESSEMA, S.B. & TORKELSSON, U. (2010). The structure of thin accretion discs around magnetised stars. *A&A*, **509**, A45+.

THORNE, K.S. (1977). The relativistic equations of stellar structure and evolution. *ApJ*, **212**, 825–831.

TOLMAN, R.C. (1939). Static Solutions of Einstein's Field Equations for Spheres of Fluid. *Physical Review*, **55**, 364–373.

TSURUTA, S. (2009). Neutron Star Cooling: II. In W. Becker, ed., *Astrophysics and Space Science Library*, vol. 357 of *Astrophysics and Space Science Library*, 289.

TSURUTA, S. & CAMERON, A.G.W. (1966). Cooling and detectability of neutron stars. *Canadian Journal of Physics*, **44**, 1863.

VAN DEN HEUVEL, E.P.J. & BITZARAKI, O. (1995). The magnetic field strength versus orbital period relation for binary radio pulsars with low-mass companions: evidence for neutron-star formation by accretion-induced collapse? *A&A*, **297**, L41+.

VERBUNT, F. & LEWIN, W.H.G. (2004). Globular Cluster X-ray Sources. *ArXiv Astrophysics e-prints 0404136*.

WEBER, F., NEGREIROS, R. & ROSENFIELD, P. (2007). Neutron Star Interiors and the Equation of State of Superdense Matter. *ArXiv e-prints 0705.2708*.

WEBER, J. (1960). Detection and Generation of Gravitational Waves. *Physical Review*, **117**, 306–313.

WEISBERG, J.M., NICE, D.J. & TAYLOR, J.H. (2010). Timing Measurements of the Relativistic Binary Pulsar PSR B1913+16. *ApJ*, **722**, 1030–1034.

WEISSKOPF, M.C., KAROVSKA, M., PAVLOV, G.G., ZAVLIN, V.E. & CLARKE, T. (2007). Chandra observations of neutron stars: an overview. *Ap&SS*, **308**, 151–160.

WETTE, K., VIGELIUS, M. & MELATOS, A. (2010). Sinking of a magnetically confined mountain on an accreting neutron star. *MNRAS*, **402**, 1099–1110.

WHITE, N.E. & ZHANG, W. (1997). Millisecond X-Ray Pulsars in Low-mass X-Ray Binaries. *ApJ*, **490**, L87.

WIJERS, R.A.M.J. (1997). Evidence against field decay proportional to accreted mass in neutron stars. *MNRAS*, **287**, 607–614.

WIJNANDS, R. (2004). Crust cooling curves of accretion-heated neutron stars. *ArXiv Astrophysics e-prints 0405089*.

WIJNANDS, R. & VAN DER KLIS, M. (1998). A millisecond pulsar in an X-ray binary system. *Nature*, **394**, 344–346.

WIJNANDS, R., MILLER, J.M., MARKWARDT, C., LEWIN, W.H.G. & VAN DER KLIS, M. (2001). A Chandra Observation of the Long-Duration X-Ray Transient KS 1731-260 in Quiescence: Too Cold a Neutron Star? *ApJ*, **560**, L159–L162.

WIJNANDS, R., GUAINAZZI, M., VAN DER KLIS, M. & MÉNDEZ, M. (2002a). XMM-Newton Observations of the Neutron Star X-Ray Transient KS 1731-260 in Quiescence. *ApJ*, **573**, L45–L49.

WIJNANDS, R., HEINKE, C.O. & GRINDLAY, J.E. (2002b). A Chandra Observation of the Globular Cluster Terzan 1: The Neutron Star X-Ray Transient X1732-304 in Quiescence. *ApJ*, **572**, 1002–1005.

WOLF, R.A. (1966). Some Effects of the Strong Interactions on the Properties of Neutron-Star Matter. *ApJ*, **145**, 834.

WOLFF, M., RAY, P., WOOD, K. & WIJNANDS, R. (2008). RXTE and Swift Confirm Decay to Quiescence of EXO0748-676. *The Astronomer's Telegram*, **1812**, 1.

WOLFF, R.S., KESTENBAUM, H.L., KU, W. & NOVICK, R. (1975). Measurement of the spatial structure of the X-ray source in the Crab Nebula. I - Observation of the 1974 November 3 lunar occultation. II - Observation of the 1974 December 28 lunar occultation. *ApJ*, **202**, L15–L19.

WOLSZCZAN, A. & FRAIL, D.A. (1992). A planetary system around the millisecond pulsar PSR1257 + 12. *Nature*, **355**, 145–147.

WONG, T., BACKER, D.C. & LYNE, A.G. (2001). Observations of a Series of Six Recent Glitches in the Crab Pulsar. *ApJ*, **548**, 447–459.

WOOSLEY, S. & JANKA, T. (2005). The physics of core-collapse supernovae. *Nature Physics*, **1**, 147–154.

WOOSLEY, S.E., HEGER, A. & WEAVER, T.A. (2002). The evolution and explosion of massive stars. *Reviews of Modern Physics*, **74**, 1015–1071.

YAKOVLEV, D.G. & PETHICK, C.J. (2004). Neutron Star Cooling. *ARA&A*, **42**, 169–210.

YAKOVLEV, D.G., LEVENFISH, K.P. & SHIBANOV, Y.A. (1999). Cooling of neutron stars and superfluidity in their cores. *Soviet Physics Uspekhi*, **42**, 737–738.

YAKOVLEV, D.G., KAMINKER, A.D., GNEDIN, O.Y. & HAENSEL, P. (2001). Neutrino emission from neutron stars. *Phys. Rep.*, **354**, 1–155.

YAKOVLEV, D.G., LEVENFISH, K.P. & HAENSEL, P. (2003). Thermal state of transiently accreting neutron stars. *A&A*, **407**, 265–271.

ZDUNIK, J.L., HAENSEL, P., PACZYNSKI, B. & MIRALDA-ESCUDE, J. (1992). Thermal structure of neutron stars with very low accretion rates. *ApJ*, **384**, 129–135.

ZDUNIK, J.L., HAENSEL, P. & GOURGOULHON, E. (2002). Recycling strange stars to millisecond periods. *A&A*, **381**, 933–940.

ZDUNIK, J.L., BEJGER, M. & HAENSEL, P. (2008). Deformation and crustal rigidity of rotating neutron stars. *A&A*, **491**, 489–498.

ZHANG, G., MÉNDEZ, M., JONKER, P. & HIEMSTRA, B. (2011). The distance and internal composition of the neutron star in EXO 0748-676 with XMM-Newton. *MNRAS*, **414**, 1077–1081.